

HERIOT-WATT UNIVERSITY



**Local and Non-local Mathematical
Modelling of Signalling during Embryonic
Development**

Georgios Vasilopoulos

SUBMITTED FOR THE DEGREE OF
DOCTOR OF PHILOSOPHY IN MATHEMATICS
HERIOT-WATT UNIVERSITY
DEPARTMENT OF MATHEMATICS,
SCHOOL OF MATHEMATICAL AND COMPUTER SCIENCES.

July 2012

The copyright in this thesis is owned by the author. Any quotation from the thesis or use of any of the information contained in it must acknowledge this thesis as the source of the quotation or information.

Declaration

I hereby declare that the work presented in this thesis was carried out by myself at Heriot-Watt University, except where due acknowledgement is made, and not been submitted for any other degree.

Signature of Georgios Vasilopoulos:

Signature of Supervisor:

Abstract

Embryonic development requires cells to communicate as they arrange into the adult organs and tissues. The ability of cells to sense their environment, respond to signals and self-organise is of crucial importance. Patterns of cells adopting distinct states of differentiation arise in early development, as a result of cell signalling. Furthermore, cells interact with each other in order to form aggregations or rearrange themselves via cell-cell adhesion. The distance over which cells can detect their surroundings plays an important role to the form of patterns to be developed, as well as the time necessary for developmental processes to complete. Cells achieve long range communication through the use of extensions such as filopodia. In this work we formulate and analyse various mathematical models incorporating long-range signalling. We first consider a spatially discrete model for juxtacrine signalling extended to include filopodial action. We show that a wide variety of patterns can arise through this mechanism, including single isolated cells within a large region or contiguous blocks of cells selected for a specific fate. Cell-cell adhesion modelling is addressed in this work. We propose a variety of discrete models from which continuous models are derived. We examine the models' potential to describe cell-cell adhesion and the associated phenomena such as cell aggregation. By extending these models to consider long range cell interactions we were able to demonstrate their ability to reproduce biologically relevant patterns. Finally, we consider an application of cell adhesion modelling by attempting to reproduce a specific developmental event, the formation of sympathetic ganglia.

Στη γιαγιά μου, Στέλλα
To my grandmother, Stella

Acknowledgements

I primarily would like to thank my supervisor Dr. Kevin Painter, for showing great patience and care, both at an academic and personal level, and for providing me with constant support and critical feedback. Without his guidance I would not have been able to complete my thesis.

I am also grateful to my examiners, Dr Steven Webb and Dr Andy White, for taking the time to read my work in detail and offering valuable feedback.

A big thanks goes to all my friends in Edinburgh for sharing good and bad times with me. In particular, I'd like to thank Leticia Alvarez for being the best flat-mate, Patricia Ritter and Raphael Kominis for their "constructive pessimism", Elias Theocharopoulos, Myrto Petsota, Gabi Medero, George Gousetis, and Nikos Koulalis, for all the dinners, drinks and conversations we had and will continue to have. Giorgos Papageorgiou gets special mention, because he wouldn't submit my thesis for me otherwise, but also because he deserves it for being a true friend from the start. I also want to thank all my friends in Greece, Panos Ardas, Vasilis Vasonis, and Giannis Tzavellas, for staying close to me while I am away.

Thank you so much Despoina Nisyriou for living with me through the most stressful period of this work, and for being so loving and caring.

Finally, I want to thank my family for their love and unconditional support in every choice I have made: my parents Haris and Avgi, my brother Thanasis, my uncle Yorgos, and my grandparents Thanasis, Stella, and Eleni.

Contents

1	Introduction	1
1.1	Cell Signalling	3
1.2	Models for Pattern formation and morphogenesis	4
1.2.1	Morphogen models	4
1.2.2	Mechanical and Cell movement models	6
1.3	Thesis outline	8
2	Pattern formation via long-range filopodial cell-cell interaction	10
2.1	Introduction	10
2.1.1	Juxtacrine Signalling	11
2.1.2	Previous Modelling of Juxtacrine Signalling	12
2.1.3	Filopodia in cell-cell communication	14
2.2	Model Derivation	16
2.2.1	Model framework	16
2.2.2	System of Equations	16
2.3	Pattern Formation in a System with Lateral Inhibition	20
2.3.1	Linear Stability Analysis	21
2.4	Numerical Simulations	30
2.4.1	1-Dimensional line of cells	31
2.4.2	2-Dimensional arrays	40
2.5	Discussion	45
3	Modelling Contact Mediated Cell Movement	48
3.1	Introduction	49

3.2	Biology of Cellular Adhesion	50
3.2.1	Molecules in adhesion	50
3.2.2	Pattern generation through adhesion	52
3.3	Modelling of Cellular Movement	53
3.3.1	Discrete Modelling of Cell Adhesion	54
3.3.2	Continuous Modelling of Cell Adhesion	55
3.4	General Modelling Framework	56
3.5	Model Description	59
3.5.0	The Models	60
3.5.1	(M1) Strictly Local Sensing	60
3.5.2	(M2) Local Sensing with Crowding Effect	63
3.5.3	(M3) Sensing direction of movement	64
3.5.4	(M4) Sensing opposite to movement	65
3.5.5	(M5) Gradient Sensing	65
3.6	Summary of Models	66
4	Local Sensing Analysis	70
4.1	Strictly Local Sensing Analysis	71
4.1.1	Linear Stability Analysis	72
4.1.2	Strictly Local Model (M1) Bifurcation Analysis	78
4.1.3	Numerical Simulations	86
4.1.4	Summary and relation to aggregation of adhesive populations	89
4.2	Analysis of (M2): Local Sensing with Crowding	89
4.2.1	Linear Analysis	90
4.2.2	Bifurcation Analysis	92
4.2.3	Numerical Simulations	92
4.3	Analysis of (M3): Sensing into direction of movement.	94
4.3.1	Linear Analysis	95
4.3.2	Bifurcation Analysis	97
4.3.3	Numerical Simulations	98
4.4	Analysis of (M4): Sensing opposite to movement	100
4.4.1	Linear Analysis	101

4.4.2	Bifurcation Analysis	102
4.4.3	Numerical Simulations	104
4.5	Analysis of (M5): Gradient Sensing	107
4.5.1	Linear Analysis	107
4.5.2	Bifurcation Analysis	108
4.5.3	Numerical Simulations	109
4.6	Summary / Discussion	110
5	Sensing Radius	114
5.1	Model Derivation	115
5.1.1	Local Sensing	115
5.1.2	Other models	116
5.2	Local Sensing Model (R1)	118
5.2.1	Linear Analysis	118
5.2.2	Bifurcation Analysis	120
5.2.3	Numerical Simulations	122
5.3	Other Models	131
5.3.1	Linear Analysis	132
5.3.2	Bifurcation Analysis	134
5.3.3	Numerical Simulations	136
5.4	Summary	141
6	Application of adhesion modelling: Sympathetic ganglia formation	144
6.1	Introduction	144
6.1.1	Biological Background	144
6.1.2	Mathematical Background	147
6.2	Sympathetic ganglia formation modelling	150
6.2.1	Continuous Model	150
6.2.2	Discrete Model	151
6.3	Analysis	153
6.3.1	Continuous Model Analysis	153
6.3.2	Numerical simulations	155

6.4	Discrete modelling of sympathetic ganglia formation	160
6.5	Discussion/Summary	162
7	Conclusions	165
A	Numerical Methods	171
A.1	Juxtacrine Signalling	171
A.1.1	1-dimensional numerical simulations	171
A.1.2	2-dimensional numerical simulations	171
A.2	Cell Adhesion Modelling	172
A.3	Sympathetic Ganglia Formation	172
	Bibliography	173

Chapter 1

Introduction

Developmental biology studies the processes involved in the formation of an adult organism from a single cell. The sequence of events that lead to the formation of a multicellular organism is termed development (figure 1.1).

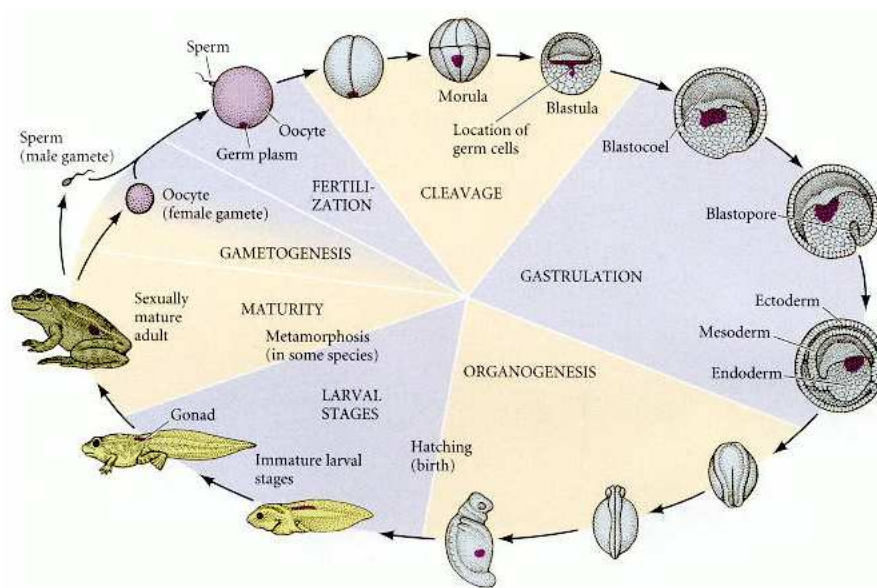


Figure 1.1: Developmental cycle of the frog, showing the different stages of embryogenesis. Taken from [34].

The process of fertilisation marks the beginning of development of a new living organism. Fusion of the two *gametes*, the sperm and the egg, activates the egg, and the nuclei of the two gametes merge and form a single diploid nucleus. Animal development following fertilisation is generally composed of four major stages [3, 34]:

1. *Cleavage* takes place immediately after fertilisation, and is characterised by a series of rapid cell divisions. Multiple smaller cells are thus created, called *blastomeres*, while the total mass remains constant, which ultimately form the *blastula*.
2. Following the slowing down of the rate of cell divisions, *Gastrulation* occurs. In this process, cells rearrange themselves forming three *germ layers*: the *ectoderm*, *endoderm*, and *mesoderm*, i.e. the outer, inner, and middle layers respectively. The three germ layers have different fates: The endoderm forms the lining of the digestive tube, and the respiratory tube and the associated organs and glands (pharynx, esophagus, stomach, intestines, liver, pancreas and lungs), the ectoderm produces epidermal cells and the nervous system, and mesoderm is responsible for the skeletal muscles, bones, the dermis, the heart, blood vessels and blood cells.
3. In the phase of *organogenesis*, cells that compose the three germ layers rearrange further, through interactions with one another to form the tissues and organs of the developing organism. During this process, numerous cell types can migrate over long distances to their appropriate destinations.
4. The process of *gametogenesis*, is the development of gametes, the cells that will eventually lead to the next generation of the organism. This process starts early in the embryo development, with the production of germ cells, yet is typically not completed until the organism reaches maturity. Germ cells migrate and differentiate into gametes.

The complex process of formation of a living organism requires the coordination of several fundamental mechanisms. Quoting from [34], principal questions faced in developmental biology are: (i) Cell differentiation - Understanding how different types of cells performing different tasks are generated; (ii) Growth and cell division - Revealing the mechanisms responsible for regulating cell division and consequently growth. (iii) Morphogenesis - the creation of form and how individual cells organise themselves in order to create properly functioning organs at the appropriate locations.

1.1 Cell Signalling

Development of a multicellular organism requires cell communication. Cells should be able to emit and receive signals which they interpret and act on accordingly, in order to self-organise and form the structures of a living organism. A variety of complex mechanisms are employed in order to control the signals that are emitted, the correct timing of signalling and the appropriate response of a cell to the signal.

Cell-cell signalling is achieved through the production of signalling molecules such as proteins. These molecules can either be secreted in the extracellular space and reach the target cells via diffusion or remain attached to the cell membrane and signal cells in direct contact with the signalling cell. A cell is capable of receiving and interpreting the signal through a receptor. Receptors are usually located in the surface of cell's membrane. The extracellular part of a receptor specifically binds the signalling molecule and becomes activated. Following receptor activation, the signal is relayed to the interior of the cell through activation of intracellular signalling molecules, and a response is generated. In some cases the receptors are located inside the cell and become activated by small signalling molecules entering the target cell [3].

Communication of cells through secreted signalling molecules is categorised depending on the distance the signal acts on. Thus, *paracrine* signalling refers to the case where the signalling molecules act locally, only stimulating cells located nearby. Cells may also respond to signals produced by themselves, a process termed *autocrine* signalling. The third category is *endocrine* signalling, in which the signalling molecules (hormones) travel long distances by entering the blood stream [3].

Cell signalling can also be achieved by cells directly contacting each other: In *juxtacrine* signalling both ligand and receptor molecules are attached to the cell membrane. We will discuss this mode of cell communication in more detail in chapter 2. Another form of direct cell-cell communication can be achieved by cells connecting to each other via GAP junctions and exchanging small molecules such as inorganic ions directly.

1.2 Models for Pattern formation and morphogenesis

Understanding and exploring the underlying mechanisms responsible for pattern formation in biology has been a major challenge. To this end, mathematical modelling can aid through offering explanations for experimental data and make predictions about the system that is being modelled. There exists a vast modelling literature of pattern formation during development, generally classified into two broad categories: chemical pre-pattern models, and mechanical models (see [11, 51, 52, 64] for reviews). The first class owes its existence to the pioneering work of Turing [97] and Wolpert [107]. Turing suggested that cells form patterns in response to a pre-pattern formed by chemicals which he termed *morphogens*, and showed how interactions between morphogens can result in spatial patterns. In the second class, patterns are generated from a homogeneous cell distribution due to mechanochemical interactions between cells and their environment.

1.2.1 Morphogen models

Wolpert's positional information theory [107] forms a chemical pre-pattern model. As the name suggests, Wolpert proposed that a cell somehow determines its position with respect to its neighbouring cells, and adopts a particular developmental fate accordingly. One simple such mechanism would be that a morphogen pre-pattern allows cells to differentiate according to the chemical's concentration at their position. The simplest pre-pattern model, involves a single morphogen, with source and sink cells generating a spatial gradient in the chemical's concentration. Once the gradient is established, cells differentiate according to a number of threshold values of concentration. Biological examples of this type of mechanism include Activin in xenopus embryos [38], and Sonic Hedgehog in the vertebrate neural tube [23].

In contrast, Turing [97] showed how a system of two or more morphogens can produce an inhomogeneous distribution without the need of a pre-pattern of source-sink type. In Turing's work, the patterned distribution of morphogens can emerge from homogeneity through chemical interactions and diffusion. Specifically, Turing

considered two morphogens that react with each other and diffuse in a domain of identical immobile cells, and was able to demonstrate that under a certain combination of these interactions, spatial patterns were possible due to the production of an instability. This is counter-intuitive since diffusion is considered a homogenising process, yet it is the interplay between the diffusivities of the chemicals that results in an instability of a homogeneous steady state, which in turn leads to patterning. In particular *diffusion-driven instability* comes as a result of ‘short-range activation, long-range inhibition’ dynamics, a term introduced by Gierer and Meinhardt [33]. In brief this means that one of the morphogens (the ‘activator’) self-promotes its own production, and has a smaller diffusion coefficient (i.e. ‘short range’), while the second chemical inhibits production of the activator. Turing-type models can exhibit a rich variety of patterns and have been extensively studied and applied in biological processes.

Similarly to the source-sink models, the pre-pattern of morphogens is first established, and cells are assumed to interpret the pre-pattern and differentiate according to the levels of chemical concentration they experience. Furthermore, the patterns predicted by reaction-diffusion systems have fixed wavelengths determined by the kinetics and diffusion coefficients.

The theoretical work of Turing has been verified experimentally in chemistry, and specifically in the CIMA (chlorite-iodide-malonic acid starch) reaction [16, 22]. Patterns predicted by the corresponding mathematical model [49] were shown to be in excellent agreement with experimental observations. However, the applicability of the mechanism in biological systems is still an open question, since the existence of morphogens and their precise function is not well established.

Turing considered a homogeneous medium in which morphogens diffuse and react. However, there exist other modes for cell-cell communication by signalling molecules, for example, active transport of molecules through channels between cells, or interactions between receptors and ligands of neighbouring cells. The latter mechanism is termed *juxtacrine signalling*, and has been identified as the mechanism for cell fate specification patterns in *Drosophila melanogaster*. In chapter 2 we discuss this phenomenon in more detail.

1.2.2 Mechanical and Cell movement models

As mentioned previously, in morphogen models it is assumed that the pre-pattern is established before the cells respond to it. There are instances however, in which self-organisation is achieved through the mechanical interactions between cells and their environment, for example instances of cell movement towards or away from a cue (taxis), or cell aggregation through adhesive interactions. Such aggregations can occur spontaneously from a uniform cell distribution due to an imbalance between homogenising factors such as diffusion, and aggregating factors. The latter include cell movement up gradients of chemical concentration (chemotaxis) or adhesive gradients (haptotaxis) among others.

Mechanochemical Models

The mechanochemical approach to morphogenesis developed by Murray and Oster [60] (see Murray [62] for an overview) offers an alternative view on pattern generation to the morphogen pre-pattern models. Models of this type take into account the various mechanical forces and chemical stimuli that act on the cells, which ultimately lead to cell aggregation and pattern formation. An advantage of this theory over pre-pattern models is that it is based in terms of measurable quantities. The disadvantage of the pre-pattern approach is that, as mentioned, the existence of morphogens is under debate.

Chemotactic Models

Chemotaxis is the preferential movement of cells or organisms up a chemical concentration gradient. The chemical in question may be a nutrient or a morphogen. The classical chemotaxis equation (or the Patlak-Keller-Segel (PKS) chemotaxis equation) has been used to model this phenomenon in a variety of different biological contexts. Patlak used a phenomenological approach in order to derive the chemotaxis equation [78]. He considered a random walk where an external bias from chemical cues gives the walker a preferred direction. Keller and Segel [46] used the derived equation along with a reaction-diffusion equation describing the evolution of a chemical signal

in order to model chemotactic movement of the amoebae of the slime mould *Dicystelium discoideum*. They proposed that amoebae aggregate due to an instability of the homogeneous steady state, a claim that was later proved incorrect. However, their work on modelling chemotaxis was a major contribution to the field.

Cell-Cell Adhesion

Cell adhesion is fundamental for a variety of developmental processes, such as cell migration, cell sorting, aggregation and subsequent formation of organs and tissues. Adhesive bonds can be created between cells or between cells and the extracellular matrix, thus providing a mechanism for the attachment of cells in specific locations. Adhesion mechanisms are responsible for providing guidance to migrating cells along their paths, in order for them to reach their destination and assemble with other cells and create organ structures. Furthermore, *selective adhesion* allows cells of the same type to form stronger bonds with each other. This gives the cells of different populations the ability to sort out and form structured arrangements, which is of crucial importance for the correct formation of organs. In chapter 3 we discuss in further detail the biology of cell-cell adhesion, as well as its potential for driving pattern formation. Several attempts to mathematically model cell adhesion and its role in pattern formation under different circumstances have been recorded, using a variety of modelling approaches, which we discuss in section 3.3.

The ability of cells to sense their environment, receive and emit signals to which they respond in a variety of manners is essential for development. The range over which cells can detect their surroundings plays an important role in morphogenetic pattern formation. Cells extend thin protrusions (lamellipodia, filopodia) which assist them in both moving and detecting chemical signals. In doing so, they are able to communicate with each other over larger distances than their average cell radius permits. By being capable of gathering information about their environment over larger distances, cells can react, transmit and relay chemical or mechanical signals faster and over a greater number of their neighbouring cells. This has large implications on pattern formation, since long range communication allows cells to form a variety of long wavelength patterns. Furthermore, long range signalling can accelerate the

patterning process and provide the correct pattern in the time available for certain developmental events. Including long range signalling in mathematical modelling of pattern formation, and investigating its implications is the central theme of this work.

1.3 Thesis outline

The overall aim of this thesis is to consider the manner in which cell-cell signalling, and in particular non local signalling, can lead to pattern formation during embryonic development.

In chapter 2 we consider a model for cell differentiation and pattern formation via juxtacrine signalling. We have extended an existing model for this phenomenon in order to include long range signalling. The original model proposed in [20] is capable of producing fine grain patterns of cells with alternating cell fate. By considering several manners in which cells can sense their environment over larger distances, we show that a variety of long wavelength patterns are possible.

In chapter 3 a framework for modelling cell-cell adhesion is introduced. A set of discrete models is proposed by considering a biased random walk, in a similar fashion to the derivation of chemotaxis equations [66]. The bias introduced varies according to the assumptions made for the nature of the adhesive mechanism. In this family of models, only next neighbour interactions are assumed. Through the use of appropriate scalings continuous models for cellular adhesion are derived and assessed. Analysis of the adhesion models derived in chapter 3 is undertaken in chapter 4. Using techniques such as linear stability analysis, bifurcation analysis and numerical simulations, we draw conclusions of the capabilities and drawbacks of each model.

Extension of the models of cellular adhesion in order to allow for long range signalling is considered in chapter 5. Here we introduce the notion of a sensing radius in this context, and alter the models of chapter 3 accordingly. The extended models are analysed using similar methods as in chapter 4, as well as insight obtained from the analysis of the simpler models. We show that aggregations comprised of multiple cells are possible as a direct result of the long-range signalling regime employed.

In chapter 6 we consider a specific biological application of cellular adhesion mod-

elling. We model the formation of sympathetic ganglia in developing chick embryos. Both cellular adhesion and chemical cues have been experimentally shown to play important roles in the process we attempt to model. We employ both discrete and continuous modelling formulations to address the problem. The continuum model presented in [8] is coupled with a chemotaxis-type contribution in order to provide the continuous model for sympathetic ganglia formation. For the discrete modelling approach we use a modification of one of the models analysed in chapter 5.

Chapter 2

Pattern formation via long-range filopodial cell-cell interaction

2.1 Introduction

Developmental biology studies the mechanisms by which complex living organisms are constructed from a single cell. The cell is the structural unit of every living organism and the mechanisms that control its behaviour are of crucial importance. In particular, the emergence of spatial organisation is required for an organism to be built: cells must be able to communicate with each other to arrange the organs and tissues that form the adult organism.

Cell differentiation is taking place in early embryonic development. During this process cells adopt a cell fate whereby different genes are activated. Regulation of cell fates is achieved by a variety of mechanisms involving the interaction of signalling molecules. These molecules bind to specific sites triggering a response. This can be achieved via diffusion of the molecules in the extracellular space, molecules passing directly from cell to cell through channels or *Juxtacrine* signalling (cf. Figure 2.1)[3].

Many theoretical and mathematical approaches have been proposed in order to investigate spatial pattern formation. As briefly discussed in chapter 1, Turing [97] demonstrated that reaction and diffusion of chemicals can result, under certain circumstances, in heterogeneous spatial patterns of concentration. A pre-pattern of chemical concentration is thus generated and cell fate specification is regulated through

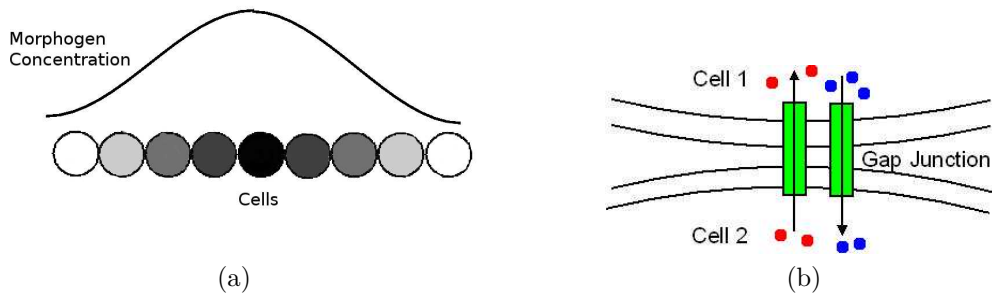


Figure 2.1: Schematic representation of two of the mechanisms responsible for cell fate regulation. (a): Diffusion of a signalling molecule into extracellular space. Cell fate (represented by different shading) is determined according to the concentration of the chemical represented by the curve. (b): GAP junction: Chemicals pass directly from cell to cell.

the different reaction of the cells to the chemical according to their location. Such chemicals are therefore termed *morphogens*. A different suggestion was made by Wolpert [107] who proposed that diffusion of a morphogen can generate a gradient in morphogen concentration. Cells were assumed to be pre-programmed to react to such a gradient and adopt different fates according to their distance from the source of the morphogen. Such morphogen gradients do exist, for example the Sonic Hedgehog protein in the neural tube [23] and activin in *Xenopus* [38].

2.1.1 Juxtacrine Signalling

In juxtacrine signalling, the signalling molecules are situated in the cell's membrane and bind to the membrane-bound receptors of immediate neighbouring cells and activate them. Juxtacrine signalling can play an important role in cell fate specification through the response in the neighbouring cell to receptor activation. For example, in the process of *lateral inhibition*, a cell that commits to a specific fate prevents its neighbouring cells from adopting the same fate, for example, see [17], [50]. In lateral induction, the signal stimulates the production of receptors and ligands.

One of the most widely studied examples of juxtacrine signalling and lateral inhibition is *Drosophila* neurogenesis. In early development, cells in a *proneural* cluster are equivalent in the sense that they all have the same potential of developing into a neural cell. In practice, a pattern is generated in which only a few selected cells adopt the (primary) neural fate and they are surrounded by cells adopting the (secondary)

epidermal. Biological experiments showed that developing neuroblasts are equally spaced between them, and if one of them is ablated with a laser beam, an adjacent cell that would normally have adopted the epidermal fate instead differentiates to a neuroblast [24]. It was suggested that this is a consequence of the absence of inhibition that would normally take place if the ablated neuroblast was present. This suggestion contrasted with the original theory that cells are competing for a diffusible substance which promotes the primary fate.

A set of genes was identified that mediates lateral inhibition. Experiments demonstrated that there is an overproduction of neural cells when the initial cells are defective in these genes (figure 2.2). These experiments served both to prove the lateral inhibition process, as well as identifying the genes that mediate it. Specifically, the products of the genes Notch and Delta were identified as receptor and ligand for lateral inhibition in *Drosophila*. It has been demonstrated that when a cell expresses Delta, its neighbours are forced to downregulate Delta expression via binding to Notch. Therefore, small differences in Delta activity in neighbouring cells are amplified.

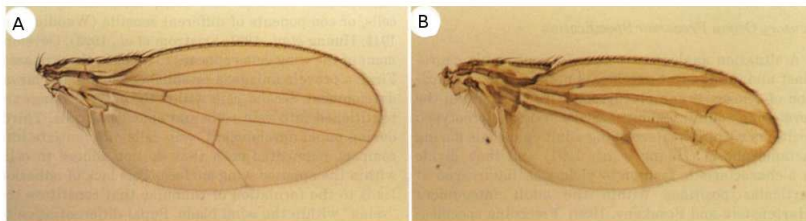


Figure 2.2: A: Adult wing blade from a wild type fly. B: Adult wing blade from a fly with cells made defective of neurogenic genes which resulted to overcommitment to the vein cell fate and reduction of epidermal cells. (Taken from [63])

2.1.2 Previous Modelling of Juxtacrine Signalling

To mathematically model juxtacrine signalling, a spatially discrete approach is typical, in contrast to the continuum models classically used to describe reaction-diffusion systems. The latter treat the cells as a continuous and homogeneous medium, the former assumes each cell as a distinct object. For juxtacrine signalling, this allows direct interaction between individual cells to be incorporated. In biological systems relevant to this study, the nature of the signalling demands a discrete model, whereby

the variables representing levels of activity of the relevant factors are recorded in each cell. Othmer and Scriven [65] considered such a set-up in order to pattern a population in a manner similar to a Turing system.

An early attempt to model juxtacrine signalling specifically, was made by Collier et al. [20]. Through the use of a simplified model for Notch-Delta interactions they were able to derive the conditions under which patterns arise. Their analysis predicts small spatial scale patterns (wavelength of two and three cells for a linear array and a hexagonal array of cells respectively). This model, despite its simplifications demonstrates the basic process of lateral inhibition, yet is unable to robustly generate the longer-range patterns (i.e. of wavelength greater than 2) observed in the proneural field. The assumption is that additional mechanisms may operate.

Plahte [79] and Plahte and Øyehaug [80] further explored the model and highlighted the importance of the feedback structure of the model in favouring the alternating pattern seen in [20]. Furthermore, travelling waves that generate pattern by invading into a homogeneous region were explored.

In [27] the Collier et al. model was extended in order to include a diffusible form of the ligand which contributes to signalling in addition to the juxtacrine signalling process. It was demonstrated that including diffusion of the ligand in the system has both stabilising effects that counteract the pattern formation process, as well as eliminating the imperfections of the patterns seen in [20].

An alternative model for juxtacrine signalling was proposed by Owen and Sherratt [68] and formed the basis for a number of further studies [69, 100, 101]. Rather than the more phenomenological approach of describing general levels of “activity” in these models an explicit representation of ligand/receptor binding was incorporated. Ligand molecules are assumed to bind to receptors of adjacent cells and the variables are the numbers of ligand molecules and the bound and free receptors. A further difference from the Collier et al. [20] model is that lateral induction is also considered. This is the reverse mechanism of lateral inhibition studied in [20]. When ligand molecules bind to cell receptors, the occupied receptors generate a signal which leads to activating (instead of inhibiting) the production of ligands and receptors. This alternative model predicts a wider range of long wavelength patterns in contrast to

those produced by the model of Collier et al. [20]

A further extension to the model of Owen and Sherratt [68] and Wearing et al [100, 101] was developed by Webb and Owen [102, 103]. They investigated the behaviour of the model using different geometries and including both lateral induction and inhibition. In a subsequent paper, Webb and Owen [102], further amended the model to account for non uniform distributions of proteins and receptors within a cell. Hence, interactions between segments of cell membranes were considered (e.g. each side of a square). They also include diffusive transport of proteins and receptors between segments of cell membranes. Additionally, they suggest that production of ligand or receptor may be localised to distinct parts of a cell membrane.

The potential of a juxtacrine model to give rise to travelling wave solutions as well as graded solutions was investigated by Monk [58] who studied a juxtacrine system using a 3-variable model and demonstrated that both behaviours can be observed, depending on the strength of the signalling feedback. Owen [67] studied the production and propagation of waves of initiation of pattern formation in a general framework and applied the study to the model developed in [68, 69, 100].

2.1.3 Filopodia in cell-cell communication

A number of studies [21, 54, 83, 84] have revealed that cells extend finger-like protrusions named *filopodia* to signal to cells located further away. Ramirez-Weber and Kronberg [83, 84] discovered long ($\sim 100\mu m$) and thin ($\sim 0.2\mu m$ in diameter) filopodia on drosophila imaginal discs which they named *cytonemes*. Such protrusions were previously found in other organisms such as the sea urchin embryo [39] and have recently been associated with long range cell-cell interactions [55]. The suggestion that cytonemes take part in transferring signalling molecules was further supported by experiments showing *Decapentaplegic* receptors travelling along the length of a filopodium [43].

de Joussineau et al. [21] studied epithelial sheets of cells in fruitflies. During embryonic development, cells with the same potential for a particular fate develop into sense organ precursors (SOPs) and signal to their surrounding cells to inhibit them from adopting the same fate. The question of how an inhibition signal is transmitted

over long distances arises. The authors conducted experiments that ruled out a relay transport of the system. Another alternative for long range action of lateral inhibition is signal transduction via diffusion. Indeed, a soluble form of Delta exists [82], but this was found to be unable to activate Notch, as a relevant study suggests [56].

The authors [21] found that filopodia contain the Delta protein and therefore are able to activate Notch in distant cells by direct contact. They performed experiments that demonstrated that disrupting filopodium formation resulted in too many cells adopting the primary fate, an indication that long range lateral inhibition failed. They also studied SOP formation and showed that a new SOP is always formed outside the reach of the filopodia of a preexisting SOP. Furthermore, it was observed that overexpression of Delta leads to an increase in filopodium formation.

In a recent paper, Cohen et al. [19] observed that the SOP pattern undergoes a refinement process in which the “unorganised” pattern that initially emerges gradually becomes well ordered. Additionally, the authors in [19] tested the role of filopodia in pattern formation using a combination of imaging and modelling techniques. They were able to demonstrate that filopodial signalling is responsible for the long-scale patterns observed and reveal their role in the process of pattern refinement by highlighting the importance of filopodial length and lifetime.

These studies therefore provide a novel mechanism for how communication over larger distances can be achieved with lateral inhibition and thus how longer wavelength patterns can arise.

The aim of this study is to incorporate the action of filopodia into a mathematical model for juxtacrine signalling with lateral inhibition. We shall begin by discussing the original model of Collier et al. [20] for Delta and Notch. Whilst the later models describe the biology of receptor-ligand activation more realistically, the simple nature of the Collier et al. model makes it more amenable to analysis. Following a brief review of the Collier et al. model we extend it to include the filopodial action and investigate its potential for pattern formation.

2.2 Model Derivation

2.2.1 Model framework

To mathematically model juxtacrine signalling, a spatially discrete approach is appropriate, in which each cell is represented as a distinct object, allowing direct interaction between individual cells to be incorporated.

Incorporation of filopodia is taken into account in this model, offering a mechanism for long-range signalling between cells. We have considered several distinct scenarios for the mechanism of sensing. Figure 2.3a shows a generic signalling scenario, in which a cell extends filopodia of different lengths and signals cells in its vicinity, and no specific assumptions are made about the nature of signalling. In our analysis we first consider the fully generic scenario of figure 2.3a, and then study two “extreme” cases for the nature of signalling. In the first case (figure (2.3A)) each cell equally signals all cells from its immediate neighbours to those at the maximum filopodial reach. In the second case, (figure (2.3B)) it is assumed that each cell only signals to cells located at the full distance a filopodium is assumed to reach. These first two scenarios would respectively model idealised scenarios in which all filopodia grow to the same length and, in the first case contact cells uniformly along their length, and, in the second case only contact cells at the tips of their filopodia. Finally, we address a more general and realistic case, shown in figure (2.3C), where it is assumed that neighbouring cells receive more signal due to the increased likelihood of contact. This latter supposition is supported by evidence provided in [21].

2.2.2 System of Equations

General framework

To study the role of filopodia we adopt the model of Collier et al. [20]. This model describes the activation levels of receptors and ligands in each cell. While, more realistic models have been developed, incorporating details of receptor-ligand binding [68, 69, 100, 101, 102, 103], the simpler model of Collier et al. [20] is more amenable to analysis.

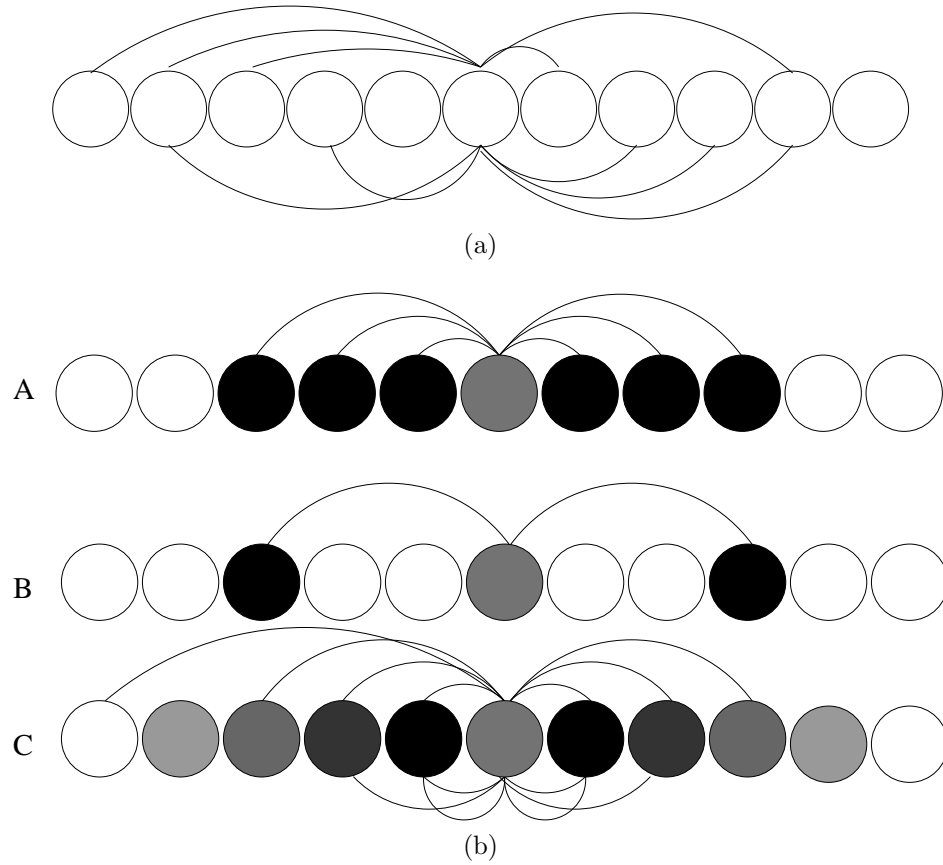


Figure 2.3: Schematic diagram of cell signalling through filopodia. (a): General case. A cell extends filopodia of different lengths to all directions and communicates with cells in its neighbourhood. No specific assumptions are made about the nature of signalling. (b): Three specific signalling scenarios considered in this work. A: The cell in the centre signals to all the cells within the filopodial radius. All cells receive equal amount of signal. B: Only cells located in the maximum distance filopodia can reach are signalled. C: Cells located in the vicinity of the source are receiving more signal.

The system of equations is given by the coupled set of equations:

$$\frac{d(R_j/R_0)}{d\tau} = F(\bar{L}_j/L_0) - \mu R_j/R_0, \quad (2.1)$$

$$\frac{d(L_j/L_0)}{d\tau} = G(R_j/R_0) - \rho L_j/L_0, \quad (2.2)$$

where R_j and L_j are respectively the levels of receptor and ligand activity in cell j , and τ is the time. R_0 and L_0 are typical levels of ligand and receptor activity. The

assumptions made were as follows:

1. Cells interact with neighbours within the range that filopodia extend. We define \bar{L}_j to be the mean level of ligand activity in the neighbouring cells of cell j over the filopodial signalling range.
2. Functions F and G are continuous functions $F, G : [0, \infty) \rightarrow [0, \infty)$ that model the nature of interaction between cells (e.g. lateral inhibition). Their specific form depends on the case study considered and will be detailed below.
3. μ and ρ are the rate constants for decay of receptor and ligand activity.
4. Cell division is neglected
5. Low levels of receptor activity in a cell lead it to adopt the primary fate, while high levels lead it to adopt the secondary fate

Defining $f := F/\mu$ and $g := G/\rho$, where f and g are of order 1, setting $r_j = R_j/R_0$, $l_j = L_j/L_0$, $t = \mu\tau$ and $v = \rho/\mu$, we obtain the non-dimensional system:

$$\frac{dr_j}{dt} = f(\bar{l}_j) - r_j, \quad (2.3)$$

$$\frac{dl_j}{dt} = v[g(r_j) - l_j]. \quad (2.4)$$

The specific form of \bar{l}_j will be dictated by the geometry of the array of cells being considered and the assumptions made about the nature of filopodial interactions, as we describe later. The action of filopodia alters the averaging term so as to include more cells in the signalling process. This is a simple assumption, and a more detailed model should consider the filopodial mechanism as a dynamic process since, as relevant studies reveal, filopodia are promoted by Delta [21].

Filopodia sensing functions

Since the exact nature of the action of filopodia is not known, a theoretical approach is considered here. In a general framework we may expect closer cells to receive greater signal due to the increased likelihood of contact. This can be taken into account by

applying a weighting on the contributions of cells to the averaging term according to their location. The general form of \bar{l}_j is assumed to take the following form for a 1-dimensional line of cells:

$$\bar{l}_j = \frac{\sum_{i=-m, i \neq 0}^m B_i l_{j+i}}{\sum_{i=-m, i \neq 0} B_i}, \quad (2.5)$$

where i denotes the distance of a cell from cell j , m is the maximum distance filopodia can reach, and B_i are the values of a weighting function applied to a cell located at a distance of i cell diameters. In the following we assume $B_i = B_{-i}$, reflecting that filopodial distribution is symmetrical with respect to the signalling source. However, it is worth noting that in certain biological situations signalling is polarised towards some direction [83], and the above framework can be extended to model such scenarios. We briefly consider polarised signalling in section 2.4.2. Equation (2.5) is a generalised form of the averaging term for juxtacrine signalling employed by Collier et al. [20]. The term in the denominator acts as a normalisation ensuring that \bar{l}_j describes the mean level of ligand activity in the neighbouring cells of cell j . Filopodia have been reported to span several cell diameters and Ramirez-Weber and Kronberg reported cytonemes of $700\mu m$ in length [83]. In the following we allow m to vary up to a value of 10 cell diameters, or approximately $100\mu m$ assuming an average cell diameter of $10\mu m$.

To model the specific cases of figure (2.3), we assume for the case of figure 2.3A:

$$B_i = \begin{cases} 1 & -m \leq i \leq m, i \neq 0 \\ 0 & \text{elsewhere,} \end{cases} \quad (2.6)$$

for the case of figure (2.3B):

$$B_i = \begin{cases} 1 & i = \pm m, \\ 0 & \text{elsewhere,} \end{cases} \quad (2.7)$$

and a decreasing function of $|i|$ for case C.

To understand the potential contribution of filopodial signalling, we consider its

impact on both pattern formation as well as travelling waves and signal propagation.

2.3 Pattern Formation in a System with Lateral Inhibition

In the following sections we will analyse the extended model given by equations (2.3) - (2.4) using (2.5) for the averaging term \bar{l}_j , with the various assumptions for B_i outlined in the previous section. It was shown in [21] that long-range signalling through filopodial extensions is responsible for the long wavelength patterns of organ precursors observed experimentally. By disrupting filopodial formation, the authors were able to show how the resulting pattern is affected. Specifically, it is reported that restriction of the range of operation of lateral inhibition (by disruption of filopodial extensions) results in overexpression of SOPs, i.e. in a shorter wavelength pattern. Our aim is to model the experimental findings of de Jossineau et al. [21] and investigate the potential for long-range pattern formation. Through the use of different assumptions for the nature of filopodial signalling we study the conditions under which long scale patterns are possible, and analyse the different patterns that result depending on the signalling regime.

We first consider the system (2.3) - (2.4) for the different cases of filopodial signalling using a lateral inhibition mechanism. In a lateral inhibition mechanism, external ligand from a neighbour bound to a receptor in a cell is assumed to result in a downregulation of the cell's ligand activity. Receptor activity in a cell is assumed to increase with the level of ligand activity in adjacent cells. To model this we adopt the approach of Collier et al.[20] by assuming $F : [0, \infty) \rightarrow [0, \infty)$, to be a continuous increasing function. Similarly, $G : [0, \infty) \rightarrow [0, \infty)$ is a continuous decreasing function accounting for the fact that ligand activity in a cell is a decreasing function of the level of receptor activity in the same cell (fig. (2.4)). With respect to equations (2.3) & (2.4) we take the Hill type functions

$$f(x) = \frac{x^{h_1}}{\alpha + x^{h_1}}, \text{ and } g(x) = \frac{1}{1 + \beta x^{h_2}}, \quad (2.8)$$

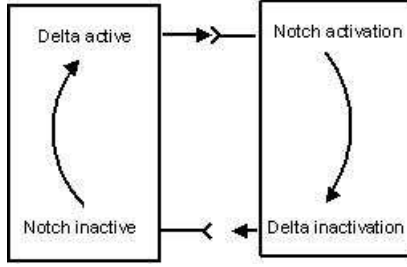


Figure 2.4: Diagram showing the lateral inhibition mechanism taking place between interacting ligands and receptors of neighbouring cells. Figure adapted from [20].

where $\alpha, \beta > 0$ and $h_1, h_2 \geq 1$. The system of equations (2.3)- (2.4) becomes:

$$\frac{dr_j}{dt} = \frac{\bar{l}_j^{h_1}}{\alpha + \bar{l}_j^{h_1}} - r_j \quad (2.9)$$

$$\frac{dl_j}{dt} = v \left[\frac{1}{1 + \beta r_j^{h_2}} - l_j \right], \quad (2.10)$$

Figure (2.5) depicts the manner by which the feedback functions vary with respect to the parameters. The form of the feedback functions (eq. (2.8)) was chosen such that both functions are monotonic, and saturating. Biologically, this means that the level of activation cannot increase indefinitely and there is a limit to the production of signalling molecules.

2.3.1 Linear Stability Analysis

The system of equations (2.9) and (2.10) possesses a single homogeneous steady state (r^*, l^*) . That is, a state in which the levels of Notch and Delta activity have the same value in every cell of the system. This is given by: $f(g(r^*)) = r^*$, $l^* = g(r^*)$. Since $f(g(r))$ is monotonically decreasing $\forall r \geq 0$, there can only exist one homogeneous steady state. We need to examine the stability of this steady state to spatially varying perturbations. If it is stable, that means that no pattern is formed since the rates of production of Notch and Delta activity are in equilibrium with their rates of decay, and any disturbance from the equilibrium will die out and the system will return to homogeneity. If the steady state is unstable, however, any small perturbations will be magnified and the system will evolve to a different inhomogeneous steady state

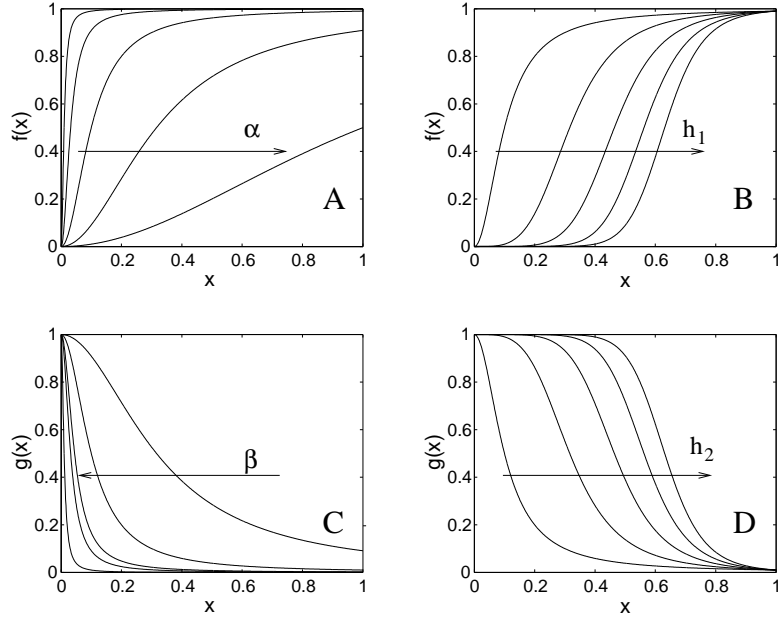


Figure 2.5: Feedback functions $f(x)$ and $g(x)$ for the lateral inhibition system plotted against parameters of the model (eq. (2.8)). Arrows indicate direction of increasing parameter values. A: plot of $f(x)$ with fixed $h_1 = 2$ and (from left to right) $\alpha = 10^{-4}, 10^{-3}, 10^{-2}, 10^{-1}, 1$. B: plot of $f(x)$ with $\alpha = 0.01$ and $h_1 = 2, 4, 6, 8, 10$. C: plot of $g(x)$ with $h_2 = 2$ and $\beta = 10000, 1000, 500, 100, 10$. D: plot of $g(x)$ with $\beta = 100$ and $h_2 = 2, 4, 6, 8, 10$.

which allows pattern formation. If we consider small perturbations from the steady state we can disregard the non-linear terms of the equations on the basis that their contribution is negligible. Studying the stability of the resulting linearised system gives valuable information about the behaviour of the full non-linear system.

For the 1-D case, we start by setting: $\hat{r}_j = r_j + x_0$ and $\hat{l}_j = l_j + g(x_0)$, where $r_j^* = x_0, l_j^* = g(x_0)$ is the homogeneous steady state. Thus, the new variables give a measure of the disturbance from the steady state. The linearised equations read:

$$\dot{r}_j = a\bar{l}_j - r_j, \quad (2.11)$$

$$\dot{l}_j = vbr_j - vl_j, \quad (2.12)$$

where r_j, l_j denote the new variables, and $\dot{\cdot}$ denotes the time derivative. $a := f'(g(x_0))$

and $b := g'(x_0)$, with $r_j^* := x_0$ and $l_j^* := g(x_0)$ being the homogeneous steady state of the system. We first consider the fully generic scenario of figure 2.3a. The general form of the averaging term in 1-dimension is:

$$\bar{l}_j = \frac{\sum_{i=1}^m B_i (l_{j+i} + l_{j-i})}{2 \sum_{i=1}^m B_i}. \quad (2.13)$$

In the above, B_i are the values of the weighting function applied to a cell located at a distance of i cell diameters. As mentioned, we assume a symmetrical filopodial distribution, so that $B_{-i} = B_i$. Through use of the appropriate weighting function we obtain the averaging terms for each of the cases depicted in figure 2.3. Thus, using $B_i = 1$ for all i we obtain \bar{l}_j for the scenario in which all cells within the filopodial reach receive equal amount of signal (figure 2.3A):

$$\bar{l}_j = \frac{1}{2m} \sum_{i=1}^m (l_{j+i} + l_{j-i}). \quad (2.14)$$

Considering the case where only the cells located at the maximum filopodial distance are being signalled (figure 2.3B), we obtain:

$$\bar{l}_j = \frac{l_{j+m} + l_{j-m}}{2}. \quad (2.15)$$

Notably, both cases collapse into the simple juxtacrine signalling model of Collier et al. [20] for $m = 1$. In the case of figure 2.3C, the averaging term \bar{l}_j is obtained by (2.13) with B_i a decreasing function of i .

Following standard stability analysis, e.g. [61], we look for solutions of the form: $l_j = l e^{\lambda t + i k j}$ and $r_j = r e^{\lambda t + i k j}$, where l and r are constants, λ is the temporal growth and k the wavenumber. Substitution into (2.11) yields:

$$\begin{pmatrix} -1 - \lambda & aK \\ vb & -v - \lambda \end{pmatrix} \begin{pmatrix} r \\ l \end{pmatrix} = \begin{pmatrix} 0 \\ 0 \end{pmatrix},$$

where K is a function of the wavenumber (k), and differs according to the averaging

term. In general:

$$K = \frac{\sum_{j=1}^m B_j \cos(jk)}{\sum_{j=1}^m B_j}, \quad (2.16)$$

with $|K| \leq 1$. Thus, $K = \frac{1}{m} \sum_{j=1}^m \cos(jk)$ for the first case (fig. 2.3A) while $K = \cos(mk)$ for the second (fig. 2.3B). Note once again that for $m = 1$ we have $K = \cos(k)$ as for the Collier et al. model [20].

For non-trivial solutions we require the determinant of this matrix to be zero, i.e. for the eigenvalues λ to satisfy:

$$\lambda^\pm = \frac{1}{2} \left[-(v+1) \pm \sqrt{(v-1)^2 + 4vabK} \right]. \quad (2.17)$$

Considering stability to homogeneous perturbations ($k = 0$), we require all λ to have a negative real part. Therefore, we require $ab < 1$ for both cases (since $K = 1$), which is automatically satisfied for the choices for f and g . Considering inhomogeneous perturbations, we look for regions where the steady state is unstable, for $k \neq 0$, i.e. for regions where $Re(\lambda^+) > 0$. Equation (2.17) yields $abK > 1$. The criterion for patterned solutions to arise is therefore:

$$ab < \frac{1}{K_{min}} \leq -1 \quad (2.18)$$

where K_{min} is the minimum value of K . Note that for both the Collier et al. model and the scenario depicted in figure 2.3B, $K_{min} = -1$, and the condition for patterning simplifies to: $ab < -1$. The eigenvalue with the largest real part is given by:

$$\lambda^+ = \frac{1}{2} \left[-(v+1) + \sqrt{(v-1)^2 + 4vabK_{min}} \right],$$

since $ab < 0$ from the assumption that f is monotonically increasing and g is monotonically decreasing. The fastest growing mode will be the wavenumber k_m that minimises K and the pattern that is expected to arise (for random initial data and

at least initially) will be the one with wavelength $w = \frac{2\pi}{k_m}$. Due to the discrete nature of the grid, for spatial patterns to arise we need to look for patterns of wavelength 2 cells or greater. Thus, patterns will only emerge if there are unstable wavenumbers $k \in [0, \pi]$. Figure 2.6 illustrates the relation between $Re(\lambda)$ and the wavelength for the two cases illustrated in figure 2.3A and 2.3B, when $m = 3$.

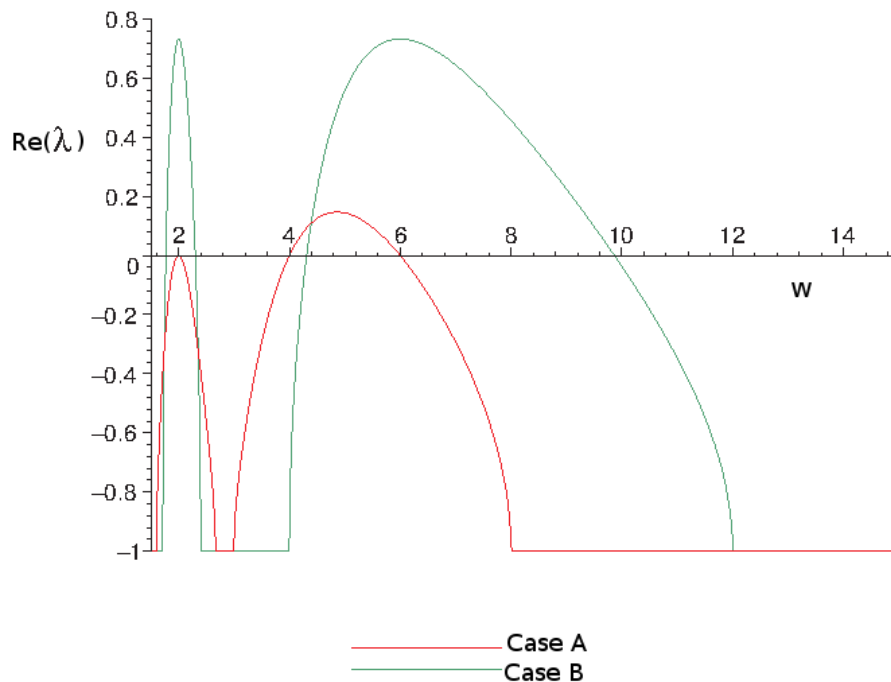


Figure 2.6: Dispersion relation for the two distinct cases of figure 2.3. The real part of the eigenvalue is plotted against the wavelength w . The homogeneous steady state is unstable in regions where $Re(\lambda) > 0$. Multiple ranges of unstable modes can be observed for both cases. For case A there always exists one mode that grows faster than any other, while for case B we observe a number of modes growing equally fast.

a and b as defined above, are the slopes of the feedback functions f and g at the homogeneous steady state respectively. Condition (2.18) above demonstrates that the feedback mechanism should be sufficiently strong for patterns to emerge. If the feedback is weak, the system will not diverge from its homogeneous steady state, and small perturbations from it will eventually die out.

In order to predict the pattern that will result if condition (2.18) is met, we can compute the range of unstable wavenumbers in each case. Thus, we can determine the modes of pattern that may result. The range of unstable wavenumbers is generally

given by: $abK > 1$. This implies that for both the extreme cases considered, if 2.18 holds, we obtain multiple ranges of unstable wavenumbers separated by stable ones, for $m > 2$, depending on the parameter choices. The fastest growing mode will be the one expected to dominate and is given by the wavenumber k_m that minimises K . Thus, the pattern expected to be observed will be the one with a wavelength (in terms of number of cells): $w = \frac{2\pi}{k_m}$.

Case A

Figure 2.7 shows the relation between the absolute value of ab required for pattern formation, as computed by criterion (2.18), and m , the filopodial range for the case of figure 2.3A. In this case, as m is increased, more cells are signalled. As can be observed in figure 2.7, as more cells are included the value of $|ab|$ that is needed to satisfy the criterion in (2.18) is increased. In other words, as the number of cells receiving signal increases, a stronger feedback is required for patterning. An explanation for this result is that the more cells are being signalled, the available amount of Delta has to be distributed among more cells. Thus, a stronger feedback is required to sustain pattern formation. Therefore, the analysis suggests that long wavelength patterns are possible, on the condition that the feedback mechanism is sufficiently strong. From a biological point of view, this result shows that there is a limit on the scale of pattern that can be produced, even in the event where filopodial interactions are artificially enhanced.

Inspecting figure 2.7, we observe that the feedback strength needed for pattern formation seems to be saturating for large values of m . For biologically realistic large values of the filopodial range, $|ab|$ is approaching the value $3\pi/2$, and $k_m \approx \frac{2\pi}{3m}$. The feedback strength is controlled by the parameters α , β , h_1 , and h_2 appearing in the chosen form of the feedback functions f and g as given by equation (2.8). It can be shown that $|ab|$ cannot exceed the value h_1h_2 . Here we present the case for $h_1 = h_2 = 2$ for simplicity, but the result can be generalised for larger values of h_1, h_2 . Additionally we assume $\alpha\beta = \rho = const..$ The system (2.3)- (2.4) has a unique

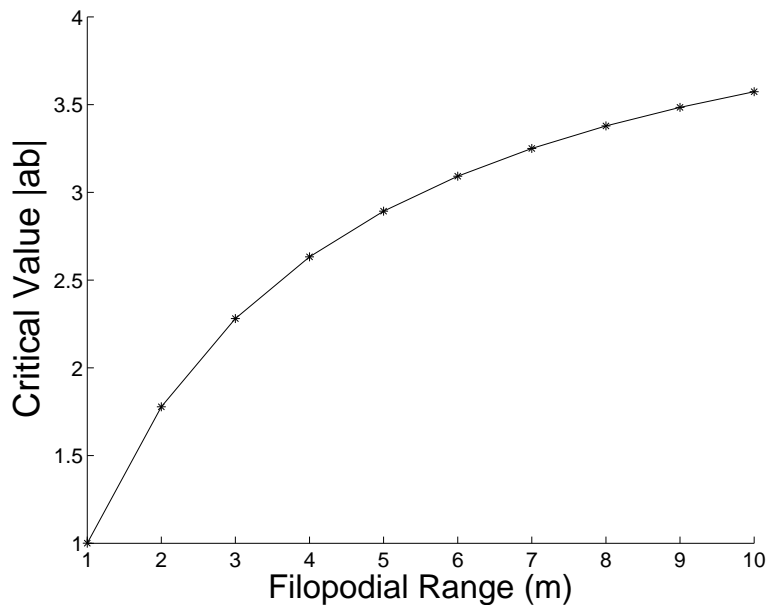


Figure 2.7: Critical value of $|ab|$ needed for pattern formation as a function of m (the distance that filopodia can cover), for the scenario of figure 2.3A. As m increases, more cells are signalled and therefore a stronger feedback is required for pattern formation.

homogeneous steady state r_0, l_0 , which can be determined by solving:

$$\frac{l_0^2}{\alpha + l_0^2} = r_0 \quad (2.19)$$

$$\frac{1}{1 + \beta r_0^2} = l_0. \quad (2.20)$$

Substituting (2.20) into (2.19) and rearranging yields:

$$\alpha r_0 + r_0 + 2\alpha\beta r_0^3 + \alpha\beta^2 r_0^5 = 1. \quad (2.21)$$

We require the homogeneous steady state to exist $\forall \alpha, \beta$ and therefore equation (2.21) to hold $\forall \alpha, \beta$. In the limit $\alpha \rightarrow 0$ ($\beta \rightarrow \infty$):

$$\lim_{\beta \rightarrow \infty} (r_0 + 2\beta r_0^3 + \beta^2 r_0^5) = 1, \quad (2.22)$$

which implies

$$\lim_{\beta \rightarrow \infty} \beta r_0^5 = 1,$$

and thus, for large enough β , we can therefore approximate

$$r_0 \sim \frac{1}{\rho} \beta^{-1/5}. \quad (2.23)$$

From (2.20) we obtain $l_0 + \beta r_0^2 l_0 = 1$. Taking the limit $\beta \rightarrow \infty$, and using (2.23) yields:

$$\lim_{\beta \rightarrow \infty} \beta^{3/5} l_0 = \rho^2,$$

so that, for large enough β :

$$l_0 \sim \frac{1}{\rho^2} \beta^{-3/5}. \quad (2.24)$$

Now

$$ab = f'(l_0)g'(r_0) = -\frac{2\alpha l_0}{(\alpha + l_0^2)^2} \frac{2\beta r_0}{(1 + \beta r_0^2)^2}.$$

Using $\alpha\beta = \rho$ and equations (2.23) and (2.24), we obtain the result:

$$\lim_{\beta \rightarrow \infty} ab = -4. \quad (2.25)$$

Combined with the result discussed previously, that the greater the number of cells signalled the stronger the feedback required for patterns to emerge, the consequence of this result is that in a setup where a large number of cells are being signalled, one needs to consider $h_1 > 2$ or $h_2 > 2$ in order for inhomogeneous patterns to be obtained. For example, in the case of large protrusions such as reported in [83]. From a biological point of view, this result suggests that there may be limitations to the scale of patterns that can be generated.

Case B

As mentioned, in the case depicted in figure 2.3B, the instability criterion (2.18) simplifies to $ab < -1$ and does not depend on the filopodial length. As we have discussed, the feedback strength needed for patterning depends on the number of cells receiving the signal, which in this case is 2 for any m .

In the situation reflected in fig 2.3B there are modes that grow equally fast, the number of which increases with filopodial range. For example when $m = 3$, the

analysis shows that the 2 and 6 wavelength modes are growing equally fast (see the dispersion relation in figure 2.6). This is depicted in figure 2.8, where the fastest growing modes are plotted as a function of the maximum distance that filopodia can reach. As shown, multiple fastest growing modes appear as filopodial range increases. In contrast, in the case of figure 2.7A, there is always a single mode that grows faster than any other.

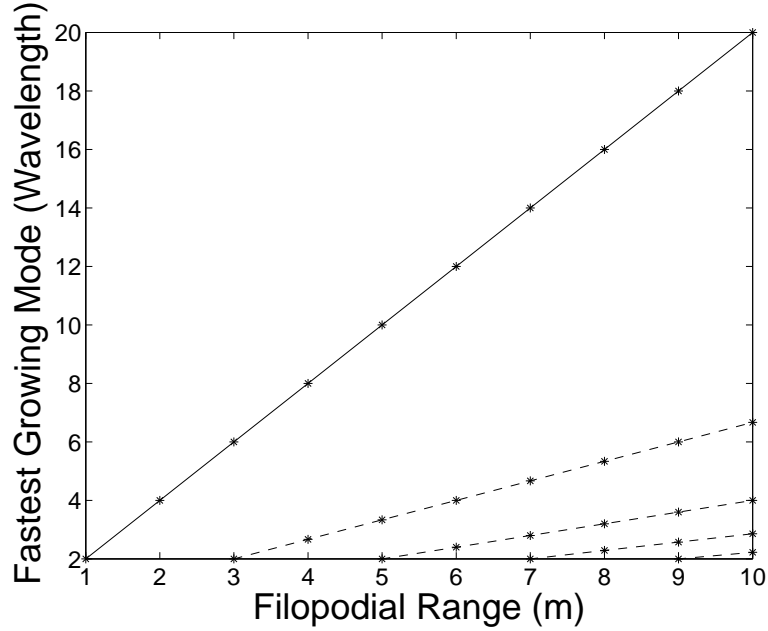


Figure 2.8: Plot of the fastest growing modes as a function of m , the maximum filopodial reach (case B in fig. 2.3). The number of dominant modes that grow equally fast increases with the filopodial length. Solid line indicates the uppermost fastest growing mode, dominating in numerical simulations (see section 2.4).

2-dimensional arrays

The linear stability analysis for two-dimensional (hexagonal) cells, is similar to the one-dimensional case described above. For the Collier et al. model [20], the averaging term is given by:

$$\bar{l}_{i,j} = \frac{l_{i,j-1} + l_{i,j+1} + l_{i-1,j} + l_{i+1,j} + l_{i+1,j+1} + l_{i-1,j-1}}{6}, \quad (2.26)$$

which, after repeating the procedure outlined above, leads to:

$$K = \frac{1}{3} (\cos(k_1) + \cos(k_2) + \cos(k_1 + k_2)), \quad (2.27)$$

where k_1, k_2 are the wavenumbers. Therefore, the patterning criterion becomes more strict than the one-dimensional case. Specifically, we require $ab < -2$ for patterns to form, since $K_{min} = -\frac{1}{2}$. The reason for this is that, as discussed, a single cell now possesses six neighbours that receive signalling. The fastest growing mode corresponds to $k_1 = k_2 = \frac{2\pi}{3}$ and therefore patterns of wavelengths $w_1 = w_2 = 3$ are observed. Introducing filopodial signalling in this system increases the number of cells contacted and therefore leads to a stronger feedback requirement in order for patterns to emerge. Similarly to the one-dimensional case, incorporation of long-range signalling results in longer wavelength modes becoming unstable and therefore we expect to obtain longer wavelength patterns than in the Collier et al. model.

2.4 Numerical Simulations

In order to investigate the behaviour of the system, equations (2.3) and (2.4) were solved numerically using a 4th order Runge-Kutta method (see Appendix A.1 for details). Simulations were performed using either periodic boundary conditions, or such that there is no contribution to the averaging term from cells located outside the boundary. That is, we assume, for example with $m = 2$, $\bar{l}_1 = \frac{l_2 + l_3}{2}$. Periodic boundary conditions model a ring of cells, or can be interpreted as modelling an infinite line of cells. The system is initially close to homogeneity, with small ($\sim 1\%$) random perturbations applied around the homogeneous steady state. We can thus investigate how the system evolves from initially almost identical cells to pattern formation. We begin by presenting numerical simulations carried out for the two “extreme” cases of figure 2.3.

2.4.1 1-Dimensional line of cells

Figures 2.9- 2.13 show simulations carried out for the two extreme cases discussed in the previous section. With the major change being the introduction of long-range filopodial mediated sensing, we choose to concentrate on the sensing range m as our parameter for investigation. The levels of receptor activity are depicted in each case at a time point for which equilibrium has been reached, for 100-cell lines. As mentioned, cells adopt the primary fate when the levels of receptor activity in that cell are low.

Case A: Sensing all cells

Figures 2.9a and 2.10a show the simulations carried out (for $h_1 = h_2 = 2$ and $h_1 = h_2 = 3$ respectively) with $m = 1$, which corresponds to the Collier et al. model to allow comparison with subsequent simulations. Figures 2.9b, c, and d and 2.10b, c, and d show the simulations performed for the first case of fig. 2.3 with a filopodial range of $m = 3, 5$ and 10. The choice of parameters was such that the instability criterion (2.18) is satisfied. We have chosen to use $v = 1$, assuming equal ligand and receptor rates of decay. The choice $v \neq 1$ does not alter the final pattern produced, but does affect the time needed for the inhomogeneous equilibrium to be reached. The linear analysis dictates (figure 2.7A) that the more cells are being signalled, the stronger the feedback needs to be in order to produce inhomogeneous patterns. For large values of m therefore, such as the system with $m = 10$ considered below, we either need to use parameter values $\alpha \sim 10^{-6}, \beta \sim 10^6$, or choose $h_1 = h_2 = 3$ in the feedback functions. Both these choices however, are somewhat problematic for reasons that will be discussed in the following.

All the numerical simulations for this model exhibit a basic common feature: The small initial perturbations from homogeneity initially diminish, and the system approaches the homogeneous steady state before pattern formation occurs. Collier et al. [20] have also observed this behaviour in their simulations. The time evolution of a system of 50 cells for $m = 3$ is depicted in figure 2.11.

The pattern observed in figure 2.9b is a combination of the modes with $w = 4$ and $w = 5$, which are predicted by the linear analysis, the $w = 5$ mode being the fastest growing. Additionally, the linear analysis predicts that the modes with $w = 2$ and

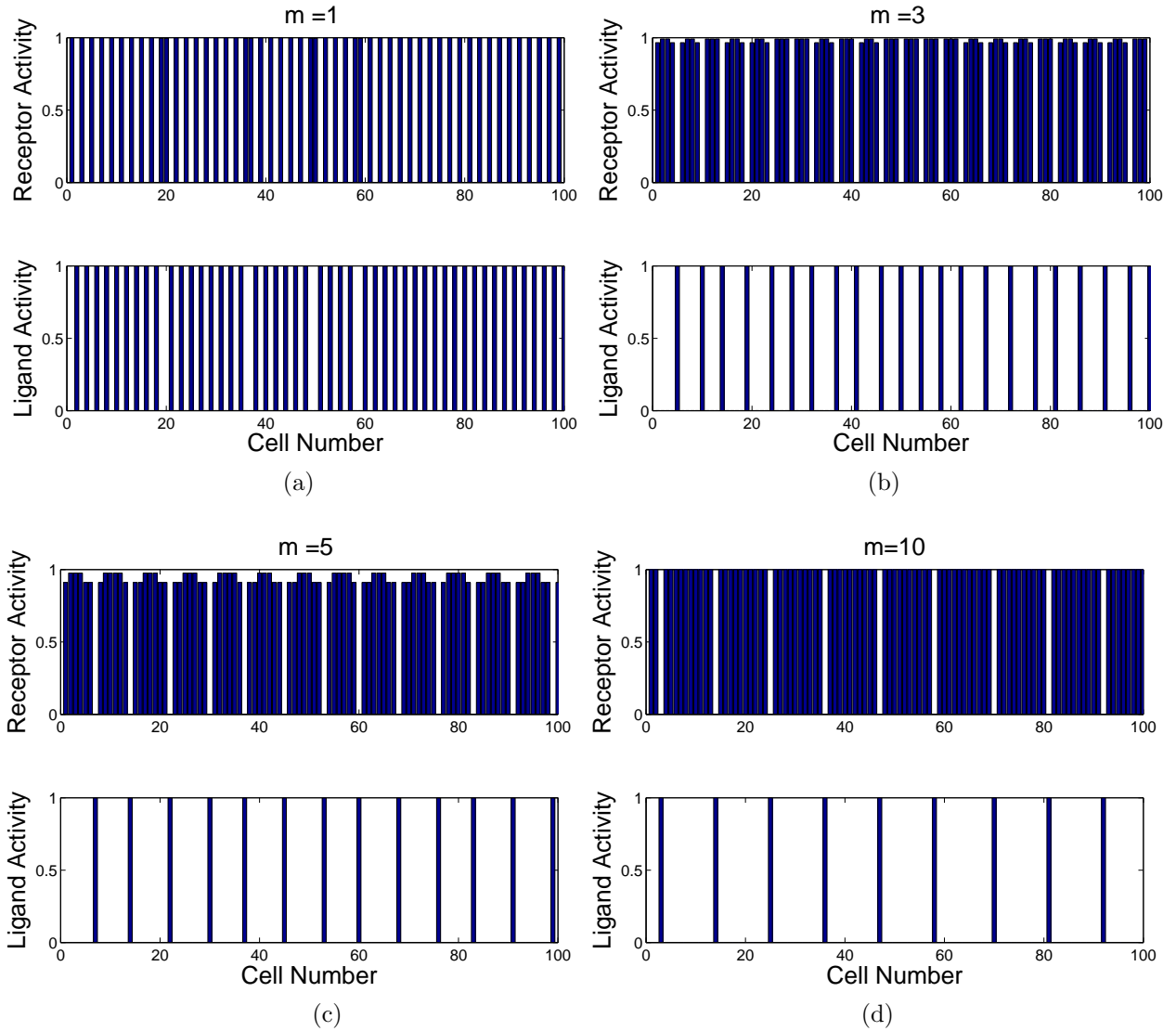


Figure 2.9: Numerical simulations for the first case of figure 2.3 for various values of the filopodial length m . Periodic boundary conditions were employed. Parameters used: (a)-(c): $\alpha = 0.001, \beta = 1000, v = 1$, (d): $\alpha = 10^{-8}, \beta = 10^8, v = 1$, with $h_1 = h_2 = 2$. All the pictures show the levels of Notch (receptor) and Delta (ligand) activity when equilibrium has been reached. (a): $m = 1$ (Collier et al. model). (b): $m = 3$. (c): $m = 5$. (d): $m = 10$. The pattern obtained for $m = 10$ is the minimum wavelength pattern, not predicted by the linear analysis due to the choices of α and β (see main text).

$w = 6$ are also expected to grow for the parameters used. Using initial conditions that favour these modes show that the $w = 2$ mode initially grows, but ultimately cannot be sustained, as it appears to be unstable, and the system evolves to a pattern similar to that seen in figure 2.9b. The $w = 6$ pattern however, appears to be stable and the system will evolve to it when selected initial conditions are applied. The same is

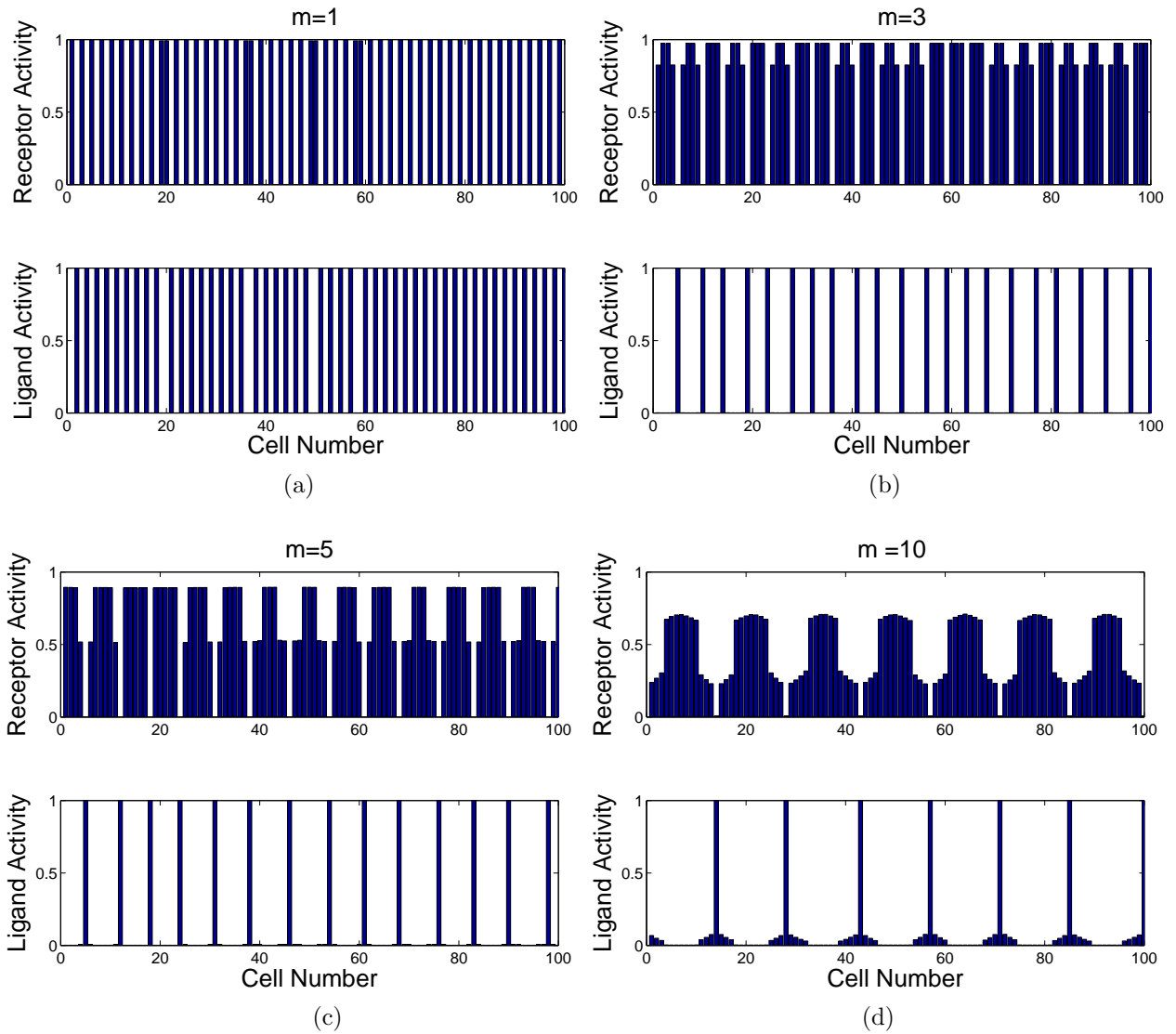


Figure 2.10: Numerical simulations for the first case of figure 2.3 for various values of the filopodial length m , using $h_1 = h_2 = 3$ to avoid phenomena seen in figure 2.9d. Periodic boundary conditions were employed. Parameters used: $\alpha = 0.001, \beta = 1000, v = 1$, with $h_1 = h_2 = 3$. All the pictures show the levels of Notch (receptor) and Delta (ligand) activity when equilibrium has been reached. (a): $m = 1$ (Collier et al. model). (b): $m = 3$. (c): $m = 5$. (d): $m = 10$

true for the cases were initial conditions force the system towards the $w = 4$ or the $w = 5$ patterns. Similar conclusions can be drawn from simulations with different values of m . We can expect therefore, from figure 2.6, that inhomogeneous steady states corresponding to the fastest growing mode range of unstable wavenumbers are likely to be stable.

In simulations using $m = 10$, we need to choose the parameters such that a

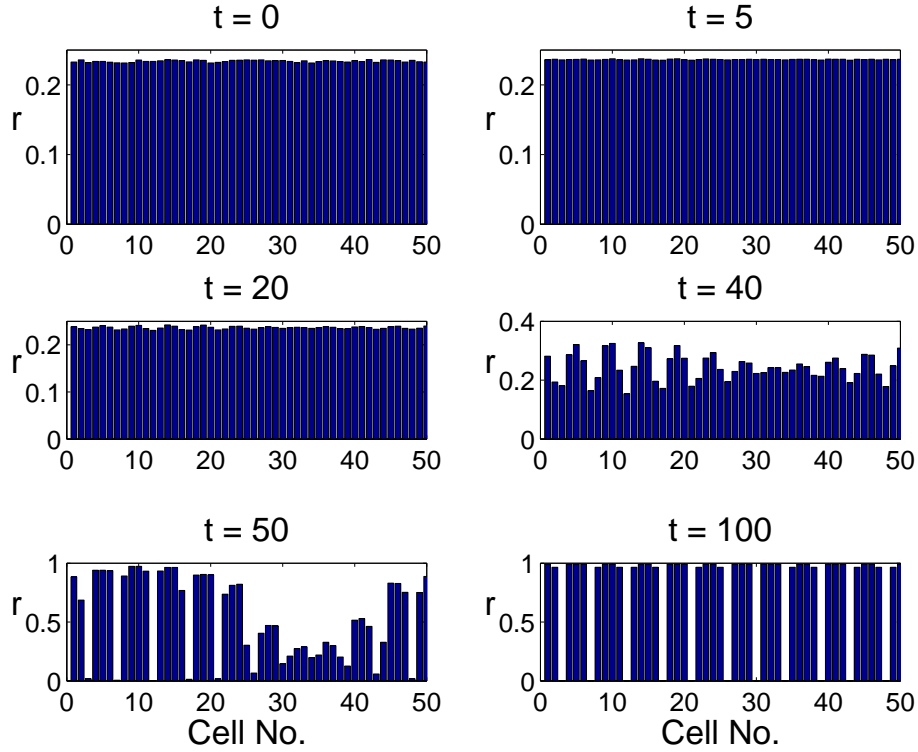


Figure 2.11: Time evolution of the system of figure 2.3A for $m = 3$, in a 50-cell line. Periodic boundary conditions were used. Initial conditions are shown in the top left figure. Only receptor activity is shown. The initial perturbations die out and the system approaches the homogeneous steady state. As time progresses, peaks of activity emerge corresponding to the fastest growing mode predicted by the linear analysis. These peaks grow until an inhomogeneous equilibrium is established. Parameters used: $\alpha = 0.001, \beta = 1000, v = 1, h_1 = h_2 = 2$.

strong feedback is produced. Choosing $\alpha = 10^{-6}, \beta = 10^6$ has the desirable effect, and the system does evolve initially as predicted by the linear analysis. That is, we observe peaks of activity being formed corresponding to the fastest growing mode. However, this choice of parameters ultimately leads to negligible levels of activity that are numerically indistinguishable from zero. The very steep slopes of the feedback functions imply that once the activity at a certain cell p exceeds a threshold, it grows almost instantaneously to $l_p = 1$. This renders the lateral inhibition imposed by any other small peaks in its neighbourhood insignificant. As a consequence, the evolution of the pattern breaks down, and the pattern that the simulation evolves to is the minimum wavelength pattern ($w = 11$ in this case), composed of cells exhibiting either maximum or zero activity (figure 2.9d). In order to avoid this behaviour we chose $h_1 = h_2 = 3$, such that $f(l) = \frac{l^3}{\alpha + l^3}$, and $g(r) = \frac{1}{1 + \beta r^3}$. The resulting simulation

is depicted in figure 2.10d.

Another important finding of Collier et al. is that in their simulations, adjacent cells never adopt the primary fate. That is, adjacent cells never exhibit low receptor activity. However, they report that the alternating pattern was found to contain “defects” where two adjacent cells have high levels of receptor activity. Plahte [79] and Plahte and Øyehaug [80] argue that the alternating pattern of the Collier et al. model can be a result of travelling waves: A small perturbation in receptor or ligand activity of a cell in a string of cells at the homogeneous steady state, results in the perturbation spreading from its origin, and establishing the predominant pattern in its passage. It is argued that the evolution of a randomly perturbed system can be considered as a superposition of waves spreading from the most perturbed cells. Therefore, the defects in the alternating pattern seen in [20] occur as a result of two travelling waves originating from different spatial points with opposite directions meeting in equal phases.

The authors in [20] remark that boundary conditions in their simulations do not play as an important role as the initial conditions, in the time evolution of their model. Additionally they report that the pattern usually starts forming close to the boundaries and spreads inwards. The zero activity boundary conditions used in [20] do produce boundary effects, in the sense that there is always a patterning wave emanating from the boundaries due to the boundary conditions. In the case where m is small, these effects are not very significant, since their magnitude is similar to the perturbations applied initially. However, for larger values of m , this particular type of boundary conditions results in large perturbations forming at the boundaries and spreading inwards. The consequences of this phenomenon are more apparent in the case described in the following section.

The fact reported in [20] that two cells never adopt the primary fate generally holds for our simulations. However, using parameter values that marginally satisfy the instability criterion, we were able to produce patterns in which the levels of ligand and receptor activity vary in a gradient-like manner. The resulting pattern does involve adjacent cells expressing comparably low levels of receptor activity. Whether this can be regarded as two adjacent cells adopting the primary fate depends on the threshold

of receptor activity needed. This type of pattern can be observed for relatively large values of m , and is more prominent when higher order feedback functions are used. Figure 2.12 shows two examples for $m = 3$ and $m = 10$. These patterns are a result of travelling waves occurring from different points within the lattice and meeting. We note that the marginal instability requirement may indicate that patterns such as the ones presented in figure 2.12 are not likely to be robust.

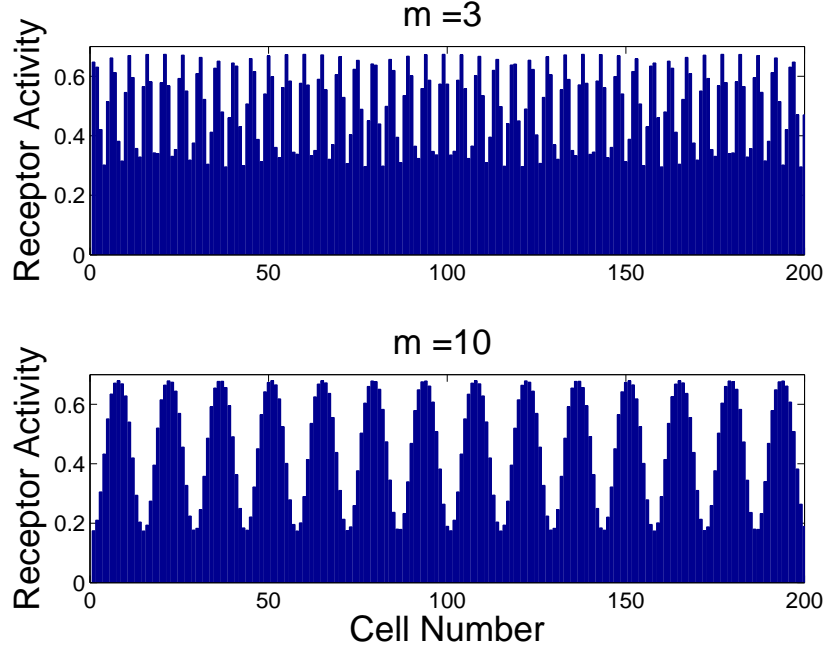


Figure 2.12: Numerical simulations showing the ability to produce patterns in which receptor activity varies in a gradient-like manner, when using parameters that marginally satisfy the instability criteria. Parameters: $h_1 = h_2 = 3$ (a): $m = 3, \alpha = 0.1, \beta = 10$, (b): $m = 10, \alpha = 0.01, \beta = 100$.

Case B: Sensing cells in the maximum distance

Simulations for the second case depicted in fig. 2.3 are shown in figure 2.13. In this case, we assume that there is a set filopodial length, and only cells at the tip of the filopodia are contacted. The linear analysis for this scenario predicts multiple modes growing equally fast. Since $K = \cos(mk) = \cos(\frac{2\pi}{w})$, modes with wavelengths $w = \frac{2\pi m}{2n+1}, n = 0, 1, 2, \dots$ are expected to dominate. This is in fact what the simulations of figure 2.13a depict. Observation of figure (2.13a) (where $m = 3$) reveals that the dominating pattern is a combination of patterns with wavelengths $w = 6$ and $w = 7$,

as well as the alternating cell fate pattern. This should be expected, since the fastest growing mode is 6, but the mode with $w = 7$ is growing almost as fast. As shown by the stability analysis, the $w = 2$ mode is also unstable (fig. 2.8).

It should be noted that simulations carried out for this case have been found to be sensitive to the size of the domain used and the boundary conditions, unlike the corresponding simulations of the previous sections. The alternating cell fate pattern does not always emerge. As the value of m increases, so does the number of unstable modes. Thus, for large m , using random small perturbations from homogeneity as initial conditions results in a steady state composed by blocks of cells of various sizes being selected.

Furthermore, using periodic boundary conditions and small random initial perturbations favours the shorter wavelength modes. However, the system evolves to a pattern of alternating cell fates ($w = 2$), as in the simulations performed by Collier et al. [20] (figure 2.9a), or indeed any pattern corresponding to the modes plotted in figure 2.8 when using initial conditions biased towards them. On the other hand, when using boundary conditions supposing zero ligand activity outside the domain ($l_0 = l_{N+1} = 0$, etc.), in line with [20], we observe patterns consistent with the uppermost growing mode (solid line in figure 2.8). These patterns always first emerge near the boundaries and spread inwards. As mentioned in the analysis of the previous case, this is a direct result from the relatively large perturbations generated at the boundaries due to the imposed conditions. The domain size is a significant factor concerning the final pattern in this case. As the pattern spreads inwards, patterning fronts spreading from the boundaries meet in the middle of the domain. Therefore, if the domain size is of the appropriate size, a regular pattern of equal blocks of cells will emerge, otherwise the pattern will be defective, and at the point of intersection of the two fronts a defect similar to the ones seen in [20] will appear (figure 2.13b).

The numerical simulations reveal that in this case it is possible to observe neighbouring cells adopting the primary fate. This is to be expected, because of the assumption made about the nature of the signalling: here immediate neighbour signalling only occurs for $m = 1$ and communication is, as mentioned above, only with cells located at the maximum distance of the filopodium reach. This may generate a sit-

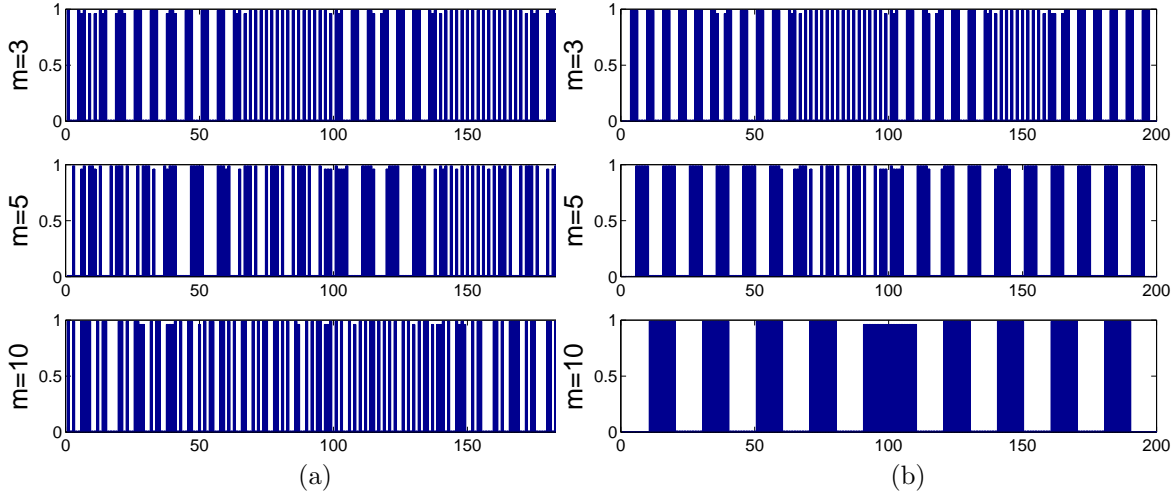


Figure 2.13: Numerical simulations for the case of fig. 2.3B. This case is sensitive to the domain size and boundary conditions. Simulations in 200-cell lines. (a): Periodic boundary conditions, and small random perturbations from homogeneity as initial condition were used. The number of unstable modes increases with m and the pattern reached is composed of blocks of cells of various sizes being selected. Shorter wavelength modes are favoured. (b): Boundary conditions such that ligand activity is zero outside the domain. In this case the pattern spreads from the boundaries inwards and its wavelength corresponds to the largest fastest growing mode (solid line in figure 2.8). “Defects” form at the areas where the patterning waves meet, so that the resulting pattern depends on the exact domain length. Parameters: $\alpha = 0.01, \beta = 100, h_1 = h_2 = 2$.

uation where a cluster of cells is selected to adopt a certain fate, while its adjacent cluster adopts a different one.

Case C: Weighted sensing

Investigation of the two extreme cases (figure 2.3A and B) is instructional, as it reveals fundamental aspects of juxtacrine signalling incorporating long-range signalling through direct contact with filopodia. In this section we examine the scenario depicted in figure 2.3C: Specifically, we assume that cells located in the vicinity of the signalling cell are receiving a stronger signal. This case is more biologically realistic and is supported by experimental data reported in [21]. To model this scenario we use smoother weighting functions. We choose a Gaussian type function for the weighting function, so that the averaging term is given by (2.13):

$$\bar{l}_j = \frac{\sum_{i=1}^m B_i (l_{j+i} + l_{j-i})}{2 \sum_{i=1}^m B_i},$$

with:

$$B_i = e^{-\frac{(i-\mu)^2}{(2\sigma^2)}}, \quad (2.28)$$

where i denotes the distance from the signalling source, $\mu = 1$ so that the immediate neighbours receive maximum signal, and σ is varied. Division by $2 \sum_{i=1}^m B_i$ normalises the weighting so that \bar{l}_j is an averaging term. The weighting functions used are depicted in figure 2.14.

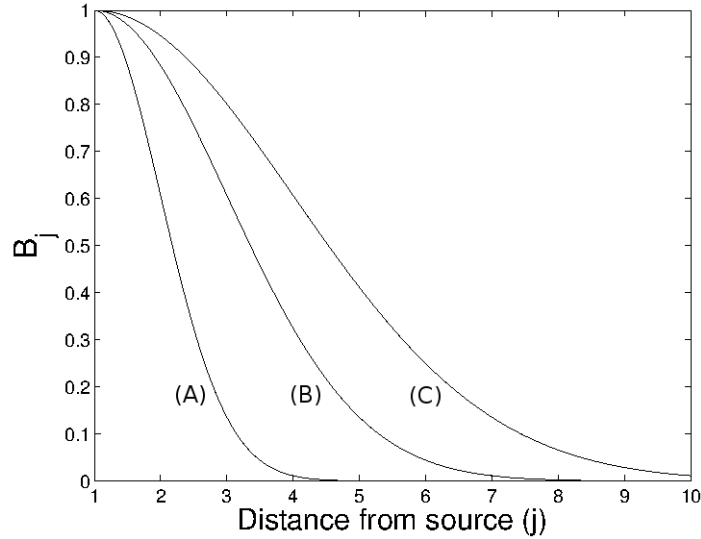


Figure 2.14: plot of (2.28) against j , with $\mu = 1$: (A) $\sigma = 1$, (B) $\sigma = 2$, (C) $\sigma = 3$.

Figure 2.15a shows the simulations carried out. We have used periodic boundary conditions and the system is initially perturbed from homogeneity. The maximum filopodial length was taken to be $m = 10$ in all cases. By varying σ in equation 2.28 we are able to control the relative weights in the averaging term. The linear analysis for this case indicates that a strong feedback is needed in order for inhomogeneities to grow. By increasing σ , the wavelength of the corresponding pattern rises, since cells located at longer distances receive more significant inhibition signals. The patterns depicted in figure 2.15 are consistent with the predictions of the linear analysis, and

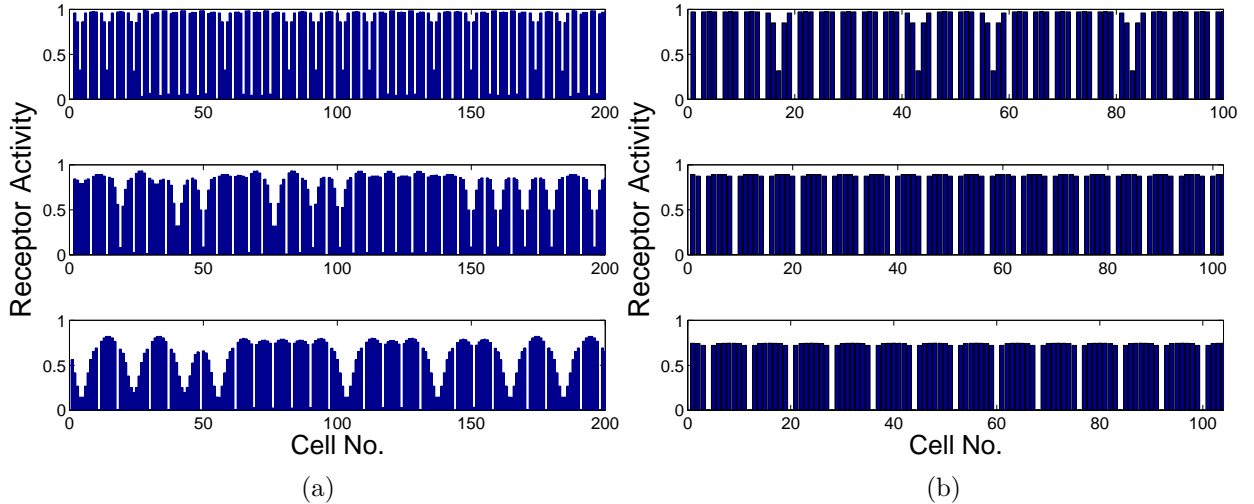


Figure 2.15: Numerical simulations using (2.28) as the weighting function. Simulations shown correspond to the curves (A), (B), and (C) of fig. (2.14) from top to bottom. Periodic boundary conditions used. (a) Initial conditions were small random perturbations from homogeneity. (b) The activity of the receptor of a single cell is initially perturbed from homogeneity. The pattern then spreads from that cell. Domain sizes are 100, 102, 104 from top to bottom. Parameters used: $h_1 = h_2 = 3$, $\alpha = 0.001$, $\beta = 5000$.

correspond to the fastest growing mode in each case. However, the patterns seen here show irregularities due to the domain size and the strong feedback that has been used. Regular patterns can be obtained, provided the domain is of the appropriate size. In figure 2.15b, such regular patterns are shown for the same parameters as in figure 2.15a. The domain size along with the initial conditions were altered.

Our simulations show that by increasing σ , thus increasing the filopodial length, results in patterns with increasing spacing between the cells selected to adopt the primary fate. Therefore, our analysis can reproduce the experimental procedures undertaken in [21] and [19], in which perturbing filopodia formation results in patterns of decreased spacing.

2.4.2 2-Dimensional arrays

In the preceding sections we have analysed distinct signalling scenarios for one-dimensional arrays, which are more amenable to analysis. In this section we present simulations performed for hexagonal arrays of cells. This offers a more realistic repre-

sentation of cells, making the resulting patterns more easily comparable to the actual patterns seen in a biological system. The equivalent scenarios as in the 1-D case were considered. That is, cells signalling every cell in a set radius, cells contacting cells located in the maximum filopodial distance, and weighted signalling relative to distance. Figure 2.16 shows the signalling regime for the equivalent of the two cases studied in one dimensional arrays: (A) signalling all cells within a set radius and (B) signalling cells located at the maximum filopodial length. Linear analysis demonstrated that the criterion for inhomogeneous solutions should be more strict than in the equivalent 1-dimensional case. i.e. the feedback should be stronger in order for inhomogeneities to grow. This is to be expected since a signalling source must communicate with more cells.

Case A: Signalling all cells

The first simulation depicted in figure 2.17 shows the pattern obtained when all cells within a radius of $m = 3, 5$ and 10 cell diameters from the source are signalled (figure 2.16A). Regular patterns are produced for this case for different values of m .

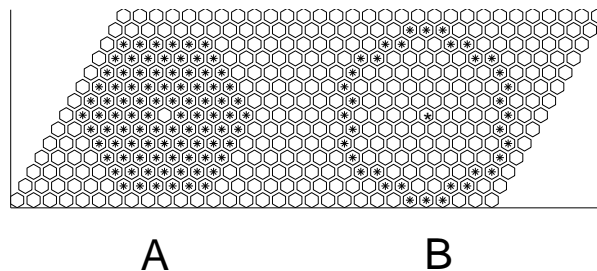


Figure 2.16: Representation of the signalling regime for the simulations carried out in hexagonal arrays. Depending on the different cases under investigation, it was assumed that a cell either communicates with all its neighbours within a set radius or with the cells located at the maximum distance the filopodia can reach. That is, the signal is received by cells forming a disc or a ring around the source. In the latter case we set the radius to be: $r = m \pm 0.5$. The cell in the centre signals to all the cells marked with a star. A: All cells are included. B: Only the cells in the perimeter are being signalled.

As in the 1-dimensional case, the wavelength being observed is a combination of the wavelengths that are predicted by the linear analysis. Therefore, extending the Collier et al [20] model by including filopodia results in isolated cells being singled out to adopt the primary fate. Similarly to the equivalent 1-dimensional case, the distance that separates these cells depends on the filopodial length.

de Joussineau et al. [21] performed experiments where they disrupted filopodial formation. They showed that not allowing filopodia to grow as long as they normally would leads to overproduction of SOPs. We can reinterpret our results in order to confirm their findings. If we suppose that filopodia can grow up to 10 cell diameters (figure 2.17c), then the results shown in figures 2.17a and 2.17b can be interpreted as situations where filopodia were artificially disrupted, leading to a shorter wavelength pattern.

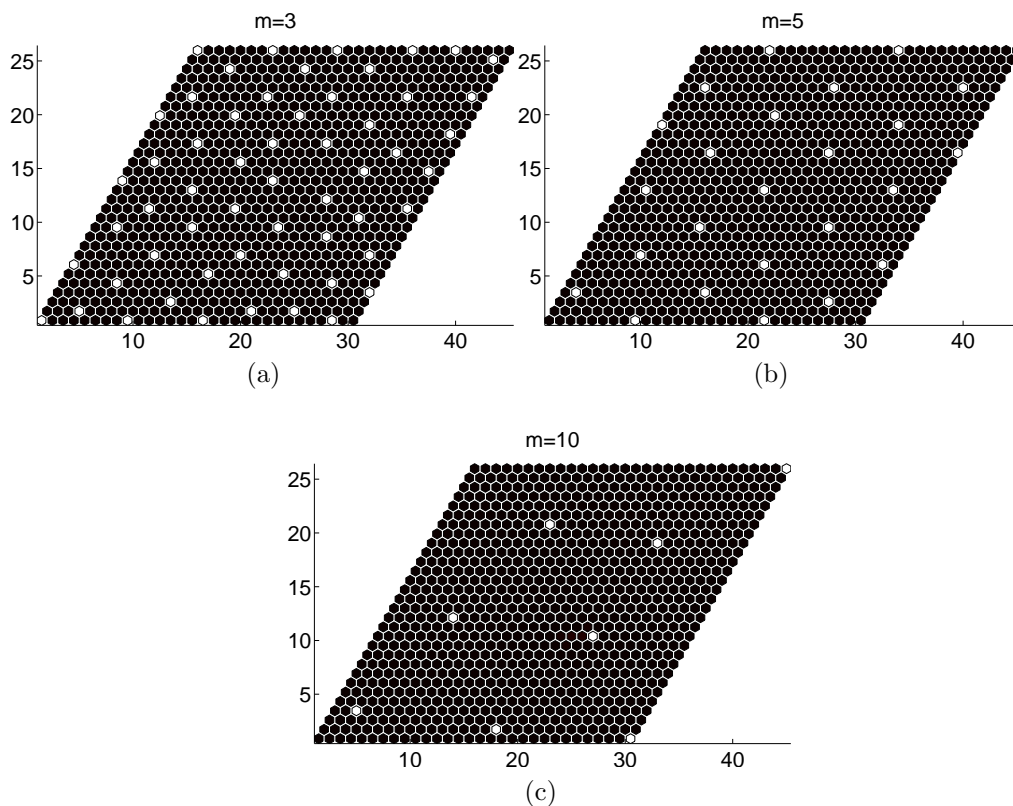


Figure 2.17: Numerical simulation of the case where all cells within a radius of 3, 5, and 10 cell diameters are signalled, according to the signalling regime shown in figure 2.16A, performed on a 30×30 hexagonal grid. Receptor activity shown only. Black indicates high activity (secondary fate) and white indicates low activity (primary fate). Parameters: $h_1 = h_2 = 3, \alpha = 10^{-7}, \beta = 10^7$

Case B: Sensing cells in the maximum distance

In the case shown in figure 2.18, simulations were performed where the signalling radius was varied. As can be observed, blocks of cells are being selected, the size of

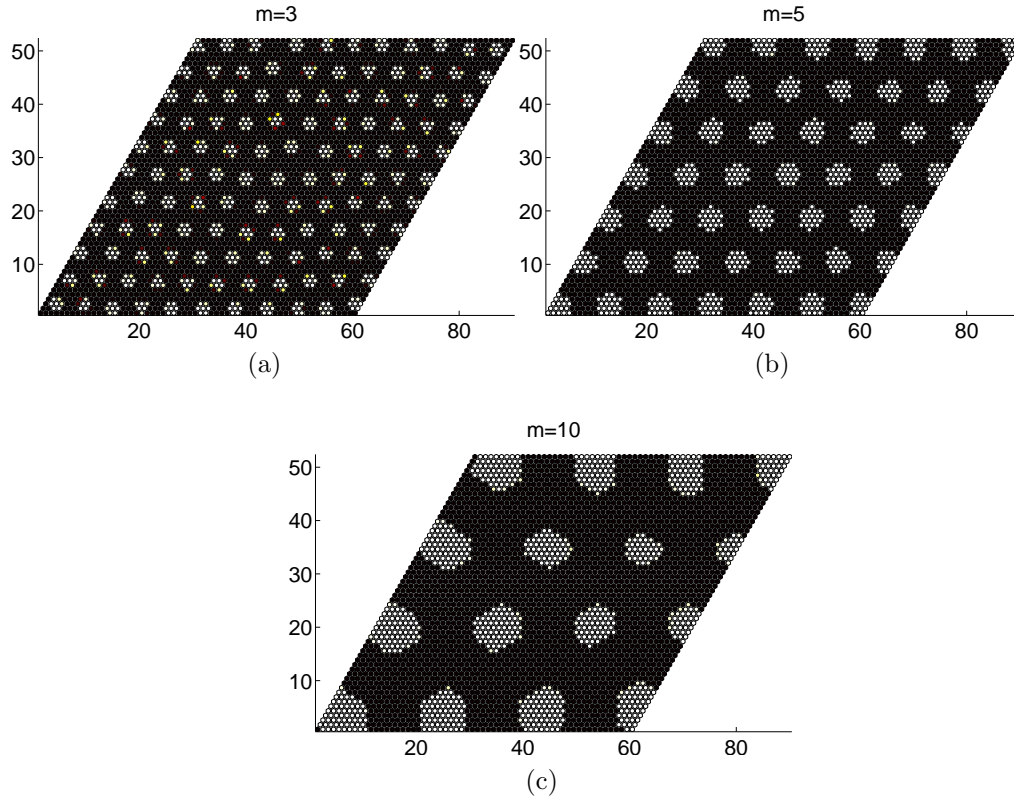
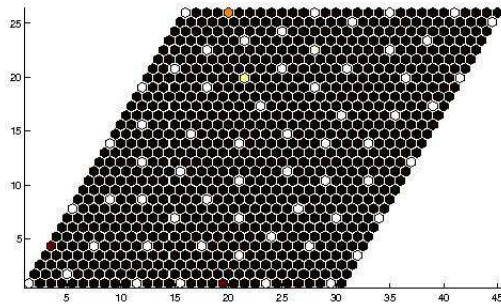


Figure 2.18: Receptor activity levels when only cells in a maximum filopodial distance of 3, 5, or 10 cells are receiving the signal. Blocks of cells are singled out to adopt the primary fate as opposed to isolated cells seen in previous simulations (fig. 2.17). Parameters: $h_1 = h_2 = 2$, $\alpha = 10^{-3}$, $\beta = 10^3$.

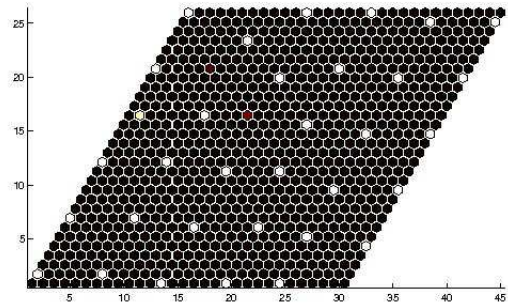
which depends on the distance that filopodia are allowed to reach. Regular patterns are also found here, and similarly to the 1-dimensional case, the alternating fate mode can sometimes be observed. In both cases, the system is perturbed from homogeneity. The perturbations seem to die out initially and the system returns to the homogeneous steady state temporarily, before the patterns start to emerge. It should also be noted that the patterns spread from the boundaries inwards, an observation also made in [20].

Case C: Weighted Sensing

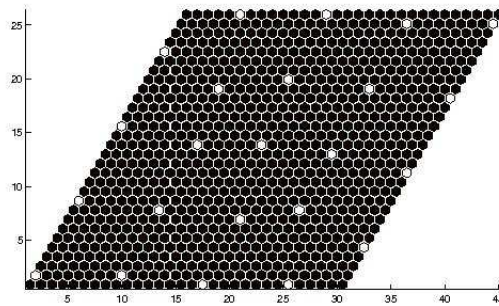
Figure 2.19 shows the simulations carried out using the 2-dimensional equivalent of the averaging term and weighting function used in section 2.4.1 (equation (2.28)). Here, i represents the distance of a cell from the signalling source. The patterns



(a) $\sigma = 1$



(b) $\sigma = 2$



(c) $\sigma = 3$

Figure 2.19: Simulation when the strength of the signal depends on the distance from the source, using (2.28) as the weighting function. Parameters: $h_1 = h_2 = 5, \alpha = 10^{-8}, \beta = 10^8$.

obtained for three different choices of parameter σ are shown. By increasing σ we allow more cells to be contacted by effectively increasing the number and length of filopodia. By increasing σ therefore, the range in which lateral inhibition is operating is also increased, leading to more sparse patterns. The results shown mirror the experimental procedures undertaken in [21]: Disrupting filopodial formation leads

to an overexpression of the primary fate in cells, which is what can be observed in figure 2.19 for reducing σ .

Polarised signalling

The authors [21] also report that filopodia are mainly oriented along one axis. In the simulations presented so far a symmetrical distribution of filopodia was assumed. We took that fact into account and performed simulations where signalling is polarised, for the equivalent of the two “extreme” cases. The simulations are shown in figure 2.21. It was assumed that the orientation of the filopodia is mainly along the x-axis. This was achieved by reducing the reach of filopodia along the y-axis to half the value of the equivalent x-axis range (see figure 2.20 for a schematic representation of the signalling regime employed, and compare with figure 2.16). We can observe striped patterns for both cases. Figure 2.21a can be compared with fig. 2.17. We observe that while the wavelength along one axis is preserved, cells adopting the primary fate emerge along the second axis of the pattern. Similarly, in figure 2.21b we observe alternating stripes of equal thickness of cells adopting different fates.

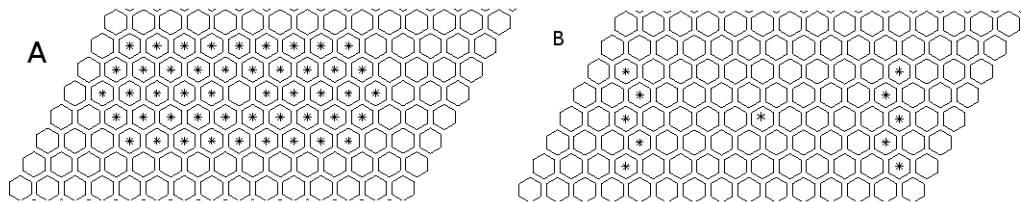


Figure 2.20: Schematic representation of the signalling regime under the assumption that filopodial growth is polarised. We assume that filopodial orientation is mainly along the x-axis. The equivalent of cases I and II were addressed (cf. figure 2.16). A: All cells within the filopodial reach are signalled. B: The cell in the centre signals the cells located at the tip of each filopodium. $m = 5$ in both cases.

2.5 Discussion

We have studied a discrete receptor-ligand model for long range intercellular signalling in early development, and investigated its behaviour under different assumptions. Collier et al. [20] considered such a model taking into account juxtacrine (nearest

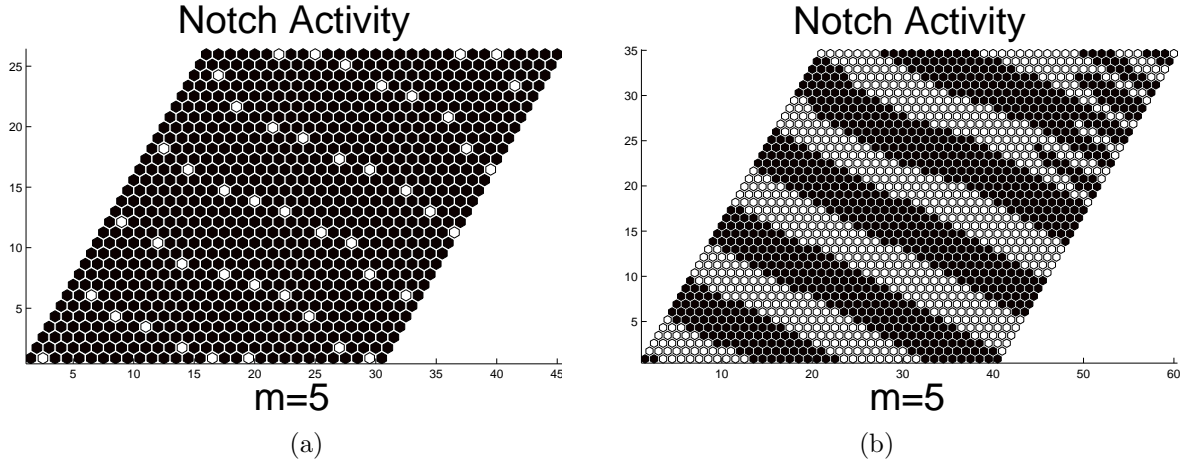


Figure 2.21: Patterns emerging when polarisation of the orientation of filopodia is accounted for. In both simulations filopodia are growing along the x-axis. (a): all cells within a radius $m = 5$ are signalled. Two distinct wavelengths are observed along each axis of the pattern. Parameters: $h_1 = h_2 = 3, \alpha = 10^{-5}, \beta = 10^5$. (b): Only the cells in the maximum distance are signalled. Stripes of alternating blocks of cells are produced. Parameters: $h_1 = h_2 = 2, \alpha = 10^{-2}, \beta = 10^2$.

neighbour) signalling only, assuming that lateral inhibition takes place. This model however, only predicts patterns of short wavelength. The authors suggested that longer scale patterns can emerge as a result of cell division occurring after the pattern is set up. Long wavelength patterns were predicted by other models when a positive feedback in ligand and receptor activation levels (lateral induction) was coupled with juxtacrine signalling [68, 69, 100, 101].

In this work we considered long range cell signalling via the inclusion of filopodial action into a system of juxtacrine signalling, as supported by experimental findings [21, 54, 83]. Linear stability analysis and numerical simulations in a system with lateral inhibition, revealed that a variety of long wavelength patterns can be obtained when filopodial signalling is taken into account. Using techniques similar to the investigation of diffusion driven instability by Turing [97] we derived conditions for pattern formation and showed that these depend on parameters of the feedback functions. Different long-scale patterns were observed in our simulations under different assumptions for the nature of signalling, reflecting different biological situations. It was demonstrated that in order for longer wavelength patterns to emerge, more cells have to be signalled and the available resources of ligand have to be shared be-

tween them. The pattern formation criteria therefore, reflect the fact that a stronger feedback is needed for patterned solutions to emerge. However, linear analysis cannot always accurately predict the dominating pattern, making a non-linear study of this model an interesting direction for future research.

In a recent study [19], the model of Collier et al. [20] was extended in a similar fashion to our work, in order to include nonlocal filopodial sensing. The authors combined experimental procedures and mathematical modelling in their work, and were able to demonstrate the impact of filopodial signalling both for producing the correct spacing between SOPs and the patterning refinement process. In their modelling work they considered randomly distributed dynamic filopodia and highlighted the impact of the filopodial length and lifetime. Our work consists of a more detailed theoretical approach in which we perform a comprehensive analysis of the various signalling scenarios, investigate the underlying mechanisms of pattern formation, as well as analysing the resulting long-scale patterns.

Studying two distinct cases we were able to reveal the basic characteristics of the model and showed that the filopodial signalling mechanism is sufficient to produce long-range patterns if coupled to a system in which lateral inhibition alone is operating. Patterns emerge from small random fluctuations without the need of a pre-pattern, or a diffusion mechanism, while lateral induction was not considered in the study of this particular system. Regular patterns of several cell diameters in wavelength can be generated in which a single cell is singled out to commit to the primary fate surrounded by neighbouring cells adopting the secondary fate, a situation that has been observed in various biological situations, like the organisation of bristles in the *Drosophila notum* [89]. Our results can reproduce the experiments [19, 21] in which the formation of filopodia is disrupted. These experiments have shown that if filopodial extension is perturbed, the distance between successive SOPs is significantly reduced.

We have also demonstrated that considering polarised filopodia orientation has a dramatic effect on the patterns produced. A potential direction for further study therefore, would be to explore polarised signalling in more detail.

Chapter 3

Modelling Contact Mediated Cell Movement

In this chapter we examine self-aggregation behaviour and patterning in a population of cells driven by a contact mediated process such as cellular adhesion. Aggregation of cells occurs as a result of their ability to sense their environment and preferentially move towards higher cell density areas in order, for example, to establish and sustain adhesive bonds. In the following sections we discuss the biological motivation and present previous attempts to model similar systems. By providing simple movement rules, we devise discrete models for cell movement, and derive their continuous counterparts. The models presented in this chapter are then analysed in chapter 4. Our aim is to explore whether these models are capable of predicting behaviours seen in real biological situations, such as the cell-aggregation phenomena shown in figure 3.1. In particular, we are interested in assessing: (i) the capability of a model to capture cell-aggregation, (ii) if a model can exhibit multiple such aggregations, and (iii) whether cell aggregations spanning over multiple cell diameters can be produced. These three fundamental questions are tabulated in table 3.1.

Table 3.1: Fundamental Questions

(i) Aggregating behaviour
(ii) Multiple/Regularly spaced aggregations
(iii) Multi-cell width aggregates

In this and the following chapter we consider models of cell movement based on

cells only being capable of sensing their immediate environment. In chapter 5, the models presented here are extended in order to allow long-range signalling.

3.1 Introduction

Modelling cell movement has been the focus of numerous studies due to its importance and involvement in a variety of biological processes such as tumour invasion or aggregation of bacteria [61, 62]. Cell movement plays a very important role in development, as many cells must migrate in order to organise themselves and form organs. Cells can interact with each other and exhibit aggregating or cell-sorting behaviour via various contact mediated processes, such as cell-cell adhesion. Numerous attempts have been made to mathematically model cell-cell adhesion and cell movement. One approach is to devise a discrete model for cell movement wherein the position of each individual cell is tracked, with rules for cell movement defined according to the phenomenon under investigation (for a review of random walks in biology see [18]). In certain cases a continuous model can then be derived by considering an appropriate scaling (e.g. [66]).

In this chapter we will follow this approach and present and analyse a number of mathematical models that incorporate non local information and derive their contin-

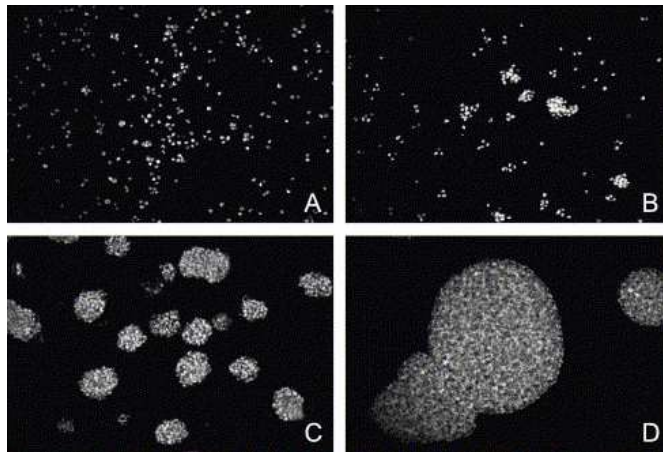


Figure 3.1: Cell aggregations due to adhesive bonds. Pictures show cell aggregations forming with increasing levels of N-cadherin expression. Note that the average size of the aggregates increases with increasing cadherin expression. Taken from [29]. To give an indication of size, the authors in [29] remark that the aggregations shown in figures 3.1C and D are visible to the unaided eye.

uous counterparts. Given its importance to a wide range of biological processes we concentrate on cell adhesion, although we note that the framework is generic and can describe other types of movement. We therefore outline adhesion below.

3.2 Biology of Cellular Adhesion

Adhesion plays a crucial role in a number of important processes in biology. During early embryonic stages, cells move and arrange themselves into the specific configurations that will form tissues and organs. Cell-cell and cell-matrix adhesion play a key role for these processes to take place [94]. Adhesive bonds are also essential for the tissue stability of the adult organism. During development, adhesive molecules located both at cell surfaces and in the extracellular matrix guide cells to the appropriate location [3].

Adhesion is mediated by the cell adhesion molecules (CAMs), which are located on the cell membrane. CAMs can be divided into two classes, Ca^{2+} -dependent, and Ca^{2+} -independent molecules. In general, CAMs are transmembrane molecules in which the extracellular domain binds to molecules located on other cells or the ECM. The intracellular domain is linked with molecules inside the cell that form a signalling pathway [3]. Adhesion molecules bind to each other by a variety of mechanisms. They can form a *homophylic* bond, in which molecules of the same type in neighbouring cells form a bond (figure 3.2A), a *heterophylic* bond, when molecules of different type are bound to each other (figure 3.2B), or binding can be achieved through secretion of a linker molecule (figure 3.2C) [3].

3.2.1 Molecules in adhesion

Cadherins

Cadherins form the principle family of CAMs of the Calcium-dependent class, and are the proteins principally responsible for cell-cell adhesion [81, 105]. Their large extracellular domain is composed by five similar domains (*cadherin repeats*) and calcium ions are responsible for holding the repeats together, thus stabilising the

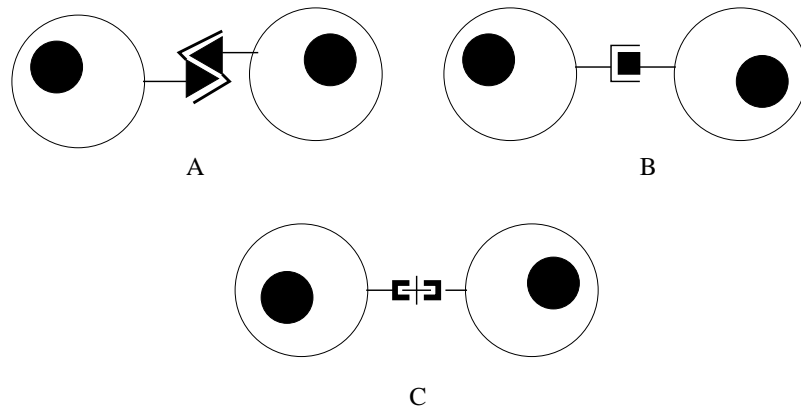


Figure 3.2: Illustration of the three possible mechanisms by which cell-cell adhesion is mediated. A: Homophylic bond. B: Heterophylic bond. C: Binding through extracellular linker molecule. Figure adapted from [3].

molecules [3, 77]. The importance of Ca^{2+} becomes apparent by their removal, leading to the degradation of the cadherins by proteolysis. Cadherins principally form homophylic bonds, however heterophylic bonds do form (e.g. P-cadherin - E-cadherin bonds), with different adhesive intensity [26]. Many members of the Cadherins family have been identified (e.g. E-cadherin in epithelial cells, N-cadherin in mesenchymal cells [106]), and it was demonstrated that when different types of cadherins are mixed, they tend to bind to their own type, and cells expressing different proteins sort out. Roth et al. [86] have shown that if dissociated cells from liver and retina are mixed together, they will eventually sort out into aggregates of cells of the same type. Takeichi [93] then demonstrated that this sorting out occurs because of the difference in cadherin type expression between the two cell types. Experiments have demonstrated that changes in cadherin expression coincide with the formation of specific tissues during development [37]. Multiple molecules on adjacent cells bind to each other simultaneously, in a zipper manner, thus increasing the strength of the bond. The intracellular domain of the cadherins interacts with a number of intracellular attachment proteins, the most important of which are the *catenins*. An adherens junction is then formed by the cadherin-catenin complex, which connects cells together [96]. Catenins interact with and bind to the actin cytoskeleton. It has been shown that cell-cell adhesion fails without the cadherin-catenin interaction. Cadherin molecules must be attached to the cytoskeleton as well as to one another in order for the adhesive

bonds to function properly.

Integrins

Integrins also mediate Ca^{2+} -dependent adhesion, and are mainly involved in the regulation of adhesion between cells and the components of the extracellular matrix [12]. Integrins are heterodimeric receptors that form much weaker bonds with their ligands in comparison to other signalling molecules, but 10 to 100 times the number of bonds are created. In this manner, cells can remain connected to the ECM while, since bonds can be easily broken, still having the freedom to move. Integrins are so called because they unite the extracellular matrix, by binding to their appropriate ligands, and the cytoskeleton by binding to actin filaments inside the cell, with the use of attachment proteins *talin* and α -*actinin* [42].

3.2.2 Pattern generation through adhesion

As mentioned earlier, when different types of dissociated cells are artificially mixed together, they reorganise and form aggregates of cells of the same type. This was first demonstrated experimentally by Townes and Holtfeter [95]. Steinberg performed a series of experiments and formulated the *Differential Adhesion Hypothesis* (DAH) [90, 91, 92], reviewed in [29]. The experiments show that cells sort-out into separate aggregates the configuration of which is preserved. Furthermore, it was shown that a hierarchy between cell populations exists: If cells of type A ultimately surround cells of type B and cells of type B engulf cells of type C, then cells A will also engulf cells C. In order to explain the experimental findings Steinberg proposed a model based on thermodynamic principles. His assumption was that cells interact and form aggregates while minimising their free interfacial energy, which leads to a thermodynamic equilibrium. Using the DAH one can predict the final configuration of a mixture of cells of different types A and B with different adhesive strengths (see figure 3.3). If S_{AA} , the adhesive strength of the binding between two A-type cells, is greater than the equivalent strength for cells of type B (S_{BB}) and the strength with which two cells of different type connect (S_{AB}), then sorting will occur with the cells that form the strongest bonds (A, in this case) engulfed (figures 3.3B and C).

No sorting will occur if the “cross-adhesion” S_{AB} strength is greater or equal to the average “self-adhesion” strengths and the cells will be randomly mixed, because such a scenario will consist a thermodynamic equilibrium (figure 3.3A). Finally, if cells of different type do not adhere to one another (i.e. if $S_{AB} = 0$), then complete sorting will occur and two separate aggregates of each type will form (figure 3.3D).

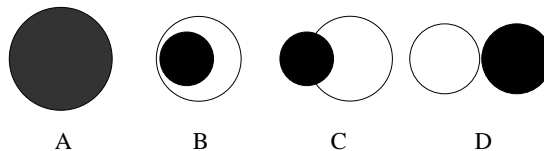


Figure 3.3: Illustration of the possible results of mixing two cell populations, A , shown in black, and B , in white. A: Cross adhesion strength S_{AB} is greater than the average self-adhesion strengths S_{AA} and S_{BB} : The two cell populations are mixed, no sorting occurs. B: Cells of type B engulf cells of type A if $S_{AA} > S_{AB} > S_{BB}$. That is, the cross-adhesion strength is greater than the self-adhesion strength of one of the cell types and weaker than the other. C: If the cross-adhesion term is weaker than both self-adhesion strengths, partial engulfment occurs. D: The two populations do not adhere to each other ($S_{AB} = 0$). Complete sorting occurs. Figure adapted from [28].

3.3 Modelling of Cellular Movement

Models for cell movement can generally be classified into two principal classes. Discrete models study the behaviour of individual cells and their interactions with each other and their surroundings. Continuous models consider cell densities rather than isolated cells and model phenomena at a larger length scale. The latter class of models has the advantage that it is easier to analyse both analytically and computationally due to the large number of variables that a realistic discrete model would require. On the other hand, the use of a discrete model enables the tracking of individual cells and ease of setting up movement rules.

Both modelling approaches should yield similar results at their overlapping area of applicability. A number of papers (e.g. [7, 66, 70, 74]) start from a discrete model that incorporates movement rules for a biased random walk at the microscopic level and subsequently derive the corresponding continuous model. Specifically, the approach is to develop a discrete-space, continuous-time master equation and then use a scaling

in order to obtain a continuous partial differential equation model.

3.3.1 Discrete Modelling of Cell Adhesion

There are a large variety of discrete modelling approaches that take cellular adhesion into account (see [32] for a mini review). Discrete models can often be subdivided into lattice-based and lattice-free models. Cellular automata models fall into the former category: generally, in these models the cells occupy a single site on a lattice in which evolution is governed by specified rules. An example of this type of model is found in [59] where a cellular automaton model is employed to study pigmentation stripes in zebrafish generated by differential adhesion.

A significant modelling approach is the Cellular Potts Model (CPM), an extension of the Potts model from statistical mechanics adapted to model cell populations by Graner and coworkers [35, 36]. In the CPM a cell is represented by a number of points on a lattice. The type of cell is also defined, so that cells of different type can be differentiated. A Hamiltonian function of the system can then be defined which describes the total energy of cell interactions. The energy terms describe surface energy due to binding of adhesive receptors and ligands of neighbouring cells, of the same or of different type, and the energy required for the deformation of cells. Depending on the model, other contributions can be included, for example, due to chemotactic interactions. A Monte Carlo scheme is employed for the evolution of the system with the aim to reduce its total energy. The cellular Potts model has been used to model cell sorting [57], in agreement with the experimental work of Steinberg [90, 91, 92], and has been extended to model different biological processes such as solid tumour growth [98] or cellular slime mould morphogenesis [53]. Alber et al. [1, 2] and Turner et al. [99] were able to derive continuous models of cell interactions beginning with a Potts model.

A “hybrid” model was proposed by Anderson [6] to model tumour invasion. In this model, cells are discrete entities which interact with continuous variables representing the extracellular matrix, oxygen, and enzymes. The movement of cells is dictated by these interactions (including cell-ECM adhesion) through appropriate probability assignments.

In a family of models for the movement of *Dictyostelium discoideum* cells [75, 76], each cell is considered to be a deformable ellipsoid and its movement calculated according to its location and the forces exerted on it. Models of this type have the advantage that the movement occurs in a continuous medium and no pre-imposed grid is necessary.

Immersed boundary models (e.g. [85]) treat cells as individual elastic entities immersed in an incompressible fluid. The forces exerted between cells and a fluid representing the extracellular medium and cytoplasm are studied in order to describe cell behaviour.

3.3.2 Continuous Modelling of Cell Adhesion

As mentioned previously, continuous models for cell adhesion can be derived by taking discrete models to their continuum limit (e.g. see [99], where a Cellular Potts Model was taken to its continuous limit). The same approach was used by Anguige and Schmeiser [7]. They proposed a discrete model for cell adhesion by imposing cell movement rules and by taking its continuum limit they were able to derive a continuous model for cell-cell adhesion including volume filling effects. Khain and Sander [47] developed a continuous model that incorporates cell movement, cell proliferation and cellular adhesion, in order to study propagating cell fronts invading a wound. These authors have used an extended Cahn-Hilliard equation and compared its behaviour to a discrete model of the same phenomenon [48]. Armstrong et al. [8] (see also [32]) proposed a phenomenological continuous model for cell-cell adhesion, by considering the response of cells to adhesive forces, and incorporating a non-local adhesion term. Their model exhibits aggregating behaviour, and when extended to consider multiple cell populations, it was shown to be able to replicate different types of cell sorting. This model was then used in further work [9] in order to adapt a model of somite formation to include cellular adhesion. In [71] and [31] it was used in models for cancer invasion.

3.4 General Modelling Framework

Clearly, there have been many attempts to derive continuous models for cell movement from an underlying discrete lattice-based model. In this chapter we will use the framework employed by Othmer and Stevens [66] which we outline below. We derive mathematical models for cell adhesion, starting from discrete models and considering their continuous limit.

Othmer and Stevens [66] employed this approach in order to derive a variety of continuous PDE models. By making several assumptions about the ways that cells can communicate with their neighbours and sense their environment, the authors were able to define distinct movement rules in a biased random walk on a discrete lattice. Through deriving the corresponding continuous-time discrete-space master equation and applying an appropriate scaling, they could derive the continuous models in the limit. Models considered in [66] were classified into (a) strictly local models, in which a walker only bases its movement on local information, (b) “barrier” models, where movement occurs as a result of information gathered at a neighbouring site and (c) gradient models where the walker detects a local gradient and chooses the most favourable direction accordingly. Studying these models, the authors were able to demonstrate that they exhibit a range of behaviours, from aggregation to blow-up to collapse to homogeneity. Painter and Hillen [72] used this framework of a biased random walk in order to derive continuous models for chemotactic movement incorporating volume filling and quorum-sensing effects. In [40] a variety of continuous chemotactic models were derived based on several assumptions on the jump probability of random walkers. Painter et al. [73] and Horstmann et al. [41] focused on the first class of models as classified in [66], i.e. strictly local sensing models, and performed analyses for both the discrete and the continuous model derived from it. Painter and Sherratt [74] also used this approach in order to derive continuous models for cell migration of multiple interacting cell populations, and in [70] the same technique was used in order to derive a PDE model for the movement of tissue composed by different cell types. Anguige and Schmeiser [7] were able to derive a continuous model for cell-cell adhesion starting with a discrete model incorporating volume filling

effects. Baker et al. [10] also derived similar PDE models by considering the limit of a lattice-based random walk model, and incorporated the effect of growing domains.

We begin by introducing the framework of Othmer and Stevens [66]. For a one-dimensional discrete lattice we define $u_n(\tau)$ to be the probability of a walker being at a point n at time τ , conditioned on beginning at $n = 0$ at $\tau = 0$. Considering T_n^\pm to be the transitional probabilities per unit time of a jump from n to $n \pm 1$ (cf. figure 3.4), we can write down the master equation for the evolution of u_n as

$$\frac{\partial u_n}{\partial \tau} = T_{n-1}^+ u_{n-1} + T_{n+1}^- u_{n+1} - (T_n^+ + T_n^-) u_n. \quad (3.1)$$

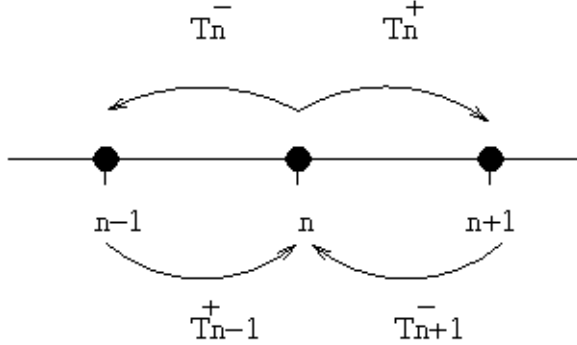


Figure 3.4: Schematic diagram showing a particle moving on a 1-dimensional grid, and the transitional probabilities

To begin with, we outline a few distinct assumptions for the rules of movement. These are purposefully simplistic, in order to provide insight into how the different rules can impact on the expected model behaviour. We consider a discrete lattice divided into subintervals of length h , and set $x = ih$. To model a system in which our particle executes an unbiased random walk, we can assume that $T_n^\pm = a$, a constant. i.e. the probability of jumping to the left or right is the same. Then equation (3.1) becomes:

$$\frac{\partial u_n}{\partial \tau} = a(u_{n-1} + u_{n+1} - 2u_n). \quad (3.2)$$

By expanding the right-hand side as a function of x to second order in h we obtain:

$$\frac{\partial u}{\partial \tau} = ah^2 \frac{\partial^2 u}{\partial x^2} + \mathcal{O}(h^4). \quad (3.3)$$

Finally, introducing the scaling $\tau = \lambda t$ and assuming that $\lim_{\substack{\lambda \rightarrow \infty \\ h \rightarrow 0}} a\lambda h^2 = D$ (a constant), we obtain the continuous diffusion equation:

$$\frac{\partial u}{\partial t} = D \frac{\partial^2 u}{\partial x^2}, \quad (3.4)$$

with constant diffusion coefficient D .

Next, we demonstrate the impact of a bias in the transitional probabilities, such that the probability to jump away from a site now depends on the particle density at the site in question: for example, $T_n^\pm = a + bu_n$. For $b < 0$, this models the case in which a particle is less likely to move away from a site of high particle density, while for $b > 0$ a particle moves away from sites at high density. Both cases can be found to have parallels in real life scenarios. For example, the former case could be considered a crude approximation for a cell-cell adhesion type phenomenon, in which particles stick to one another, while the latter case could, for example represent dispersion induced by overcrowding. Substituting this expression into the master equation (3.1), expanding, and neglecting the higher order terms, we now obtain:

$$\frac{\partial u}{\partial \tau} = ah^2 \frac{\partial^2 u}{\partial x^2} - 2bh^2 \frac{\partial}{\partial x} \left(u \frac{\partial u}{\partial x} \right), \quad (3.5)$$

which, after using the same scaling as above, $\tau = \lambda t$ and assuming that $\lim_{\substack{\lambda \rightarrow \infty \\ h \rightarrow 0}} \lambda h^2 = D$, yields:

$$\begin{aligned} \frac{\partial u}{\partial t} &= D \left[a \frac{\partial^2 u}{\partial x^2} - 2b \frac{\partial}{\partial x} \left(u \frac{\partial u}{\partial x} \right) \right] \\ &= D \frac{\partial}{\partial x} \left[(a - 2bu) \frac{\partial u}{\partial x} \right]. \end{aligned} \quad (3.6)$$

Comparing the resulting equation to the diffusion equation (3.4), one can observe that by including a bias, an additional term is produced, that either counteracts or

enhances the diffusion process depending on the sign of b . It should be mentioned however, that in the case $a - 2bu < 0$ the problem becomes ill-posed (i.e. negative diffusion).

In the following section we will be applying these techniques in order to derive a variety of simple “short range” models for cell-cell adhesion and other processes in which movement is affected by the local cell density. In these models we assume that cells are capable to communicate with each other within a limited region that defines their local neighbourhood. In the following chapter we will proceed to analyse both the discrete/ master equation and the corresponding continuum models. In chapter 5, these models are extended in order to allow for cell communication over longer distances.

The aim of this study is to present a variety of models that can be used to model cell adhesion, and assess their capability of capturing the behaviour of cells in real biological systems, such as the ability of cells to sort and rearrange themselves into patterns of distinct cell aggregations separated by low cell density areas. We are particularly interested in the models’ capability of producing such patterns, and by studying the resulting patterns we can obtain further understanding of the mechanisms that drive pattern generation through cell-cell adhesion.

3.5 Model Description

Applying the techniques previously discussed, and similarly to the work of Othmer and Stevens [66], we make several simple assumptions for the nature of movement and examine their behaviour. The discrete/master equation approach employed in [66] allows a variety of different possibilities for the mechanisms cells use to sense and respond to their environment. As shown in [66], the precise form of the underlying sensing mechanism of a chemical signal greatly affects the behaviour of the system. Consequently, in order to explore the suitability of a model to describe an adhesion-type process, we perform a comprehensive analysis by looking at a number of plausible forms by which a cell can locally respond to the environment. In the next section we present a preliminary description of the models that will be formally presented and

analysed in this and the following chapter.

3.5.0 The Models

We begin by assuming that a cell occupies a single point on a linear grid (figure 3.4), although we note that this will be relaxed in chapter 5. A schematic representation of the various models we consider is given in figure 3.5. The probability of performing a one-site jump depends on information gathered by the cells from their immediate surroundings. Figure 3.5 shows the existing or prospective adhesive bonds (represented by straight lines). Based on the information gathered, cells move with an assigned probability in the direction marked by the arrows.

First, we will look at two strictly local models ((M1)-(M2)), the first of which is the simplest scenario describing a myopic walker basing its decision to move on information gathered locally, i.e. at the site that it is located and regardless of the status of the sites to which it will move (figure 3.5a). The second form of local model we consider is a modification of the strictly local model, where we introduce a “volume filling” effect as in [72]. That is, we assume the decision to move depends on local information as before, but now movement is impeded if the target site has reached a saturation level of cell density (figure 3.5b). Secondly, we will look at two distinct models in which movement is dictated by information gathered from a cell’s near neighbourhood: (i) a cell senses an adjacent site and moves to it (model (M3), figure 3.5c) and (ii) a cell senses an adjacent site and moves away from it (model (M4), figure 3.5d). Finally, we will consider a gradient-based model (M5), where the decision to move depends on computing local differences in information (figure 3.5e). Models (M1)-(M5) will be presented in more detail in the following sections.

3.5.1 (M1) Strictly Local Sensing

Using the underlying motivating problem of cell-cell adhesion, we suppose that the capacity of cells to migrate is dictated by whether they can break the bonds necessary to leave a site. That is, movement is dictated only by information gathered at the location the cell currently occupies. If the cell density at the specific site is high, then

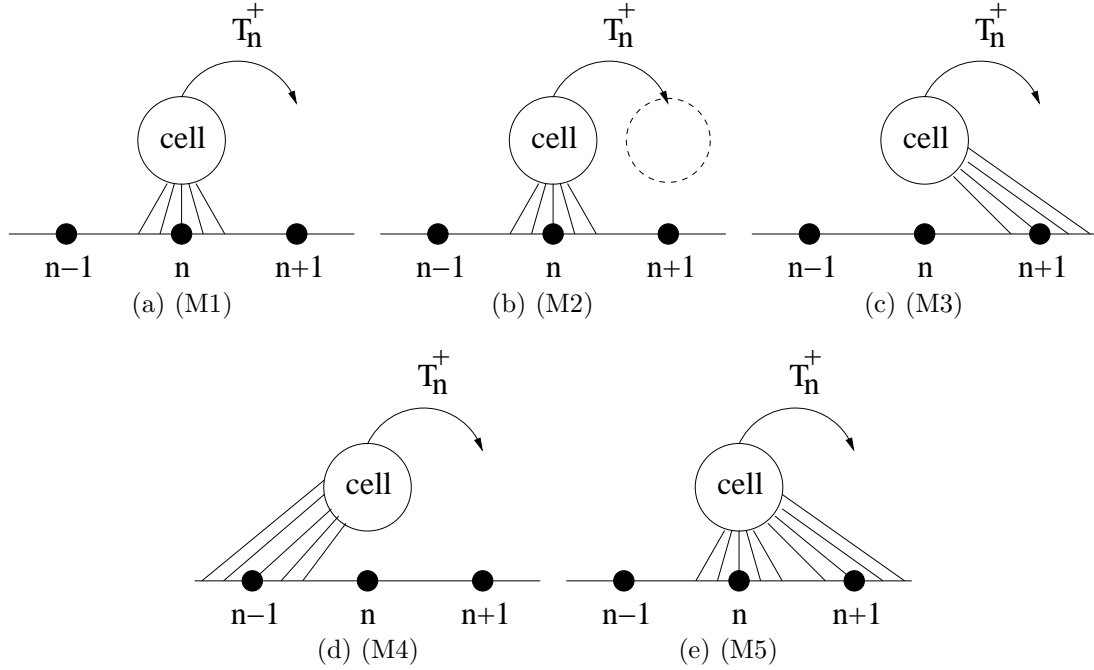


Figure 3.5: Schematic representation of the models considered in this chapter. A cell occupies a single lattice point. Straight lines connecting the cell to the lattice show the point(s) from which information is gathered. Arrows represent the probability of a cell moving in the direction shown based on that information. (a): Strictly local sensing model (M1). The decision to move depends only on the site a cell occupies. (b): Local sensing with crowding (M2). Same as in (a) but movement is impeded by the presence of cells in the target site (represented by the dashed circle). (c): Sensing into direction of movement (M3). Cells sense the target site and move towards it. (d): Sensing into direction opposite of movement (M4). Cells sense an adjacent site and move away from it. (e): gradient sensing (M5). Information at both the current and target site is computed and compared.

the cell is likely to have formed a large number of adhesive bonds and will be less likely to move from that site, but if the bonds are broken movement is assumed to occur in either direction with equal probability. Effectively, cells are assumed to have no longer range communication with its surroundings. This is modelled by:

$$T_n^\pm = a + bf(u_n) \quad (3.7)$$

where f is assumed to be a decreasing function of u_n . Substituting into the master equation (3.1), we obtain:

$$\frac{\partial u_n}{\partial \tau} = (a + bf(u_{n-1}))u_{n-1} + (a + bf(u_{n+1}))u_{n+1} - 2(a + bf(u_n))u_n. \quad (3.8)$$

Considering a grid of mesh size h and setting $x = nh$, we can expand the right hand side of (3.8) as a function of x to second order in h to obtain:

$$\begin{aligned} \frac{\partial u}{\partial \tau} &= \left(a + bf(u) - bh \frac{\partial f(u)}{\partial x} + \frac{1}{2}bh^2 \frac{\partial^2 f(u)}{\partial x^2} \right) \left(u - h \frac{\partial u}{\partial x} + \frac{1}{2}h^2 \frac{\partial^2 u}{\partial x^2} \right) \\ &+ \left(a + bf(u) + bh \frac{\partial f(u)}{\partial x} + \frac{1}{2}bh^2 \frac{\partial^2 f(u)}{\partial x^2} \right) \left(u + h \frac{\partial u}{\partial x} + \frac{1}{2}h^2 \frac{\partial^2 u}{\partial x^2} \right) \\ &- 2(a + bf(u))u, \end{aligned} \quad (3.9)$$

which after some manipulation leads to:

$$\frac{\partial u}{\partial \tau} = h^2 a \frac{\partial^2 u}{\partial x^2} + h^2 b \frac{\partial^2}{\partial x^2} (f(u)u) + \mathcal{O}(h^4). \quad (3.10)$$

Finally, introducing the scaling $\tau = \lambda t$ and assuming that $\lim_{\substack{\lambda \rightarrow \infty \\ h \rightarrow 0}} \lambda h^2 = D$, we obtain the continuous model:

$$\frac{\partial u}{\partial t} = D \left(a \frac{\partial^2 u}{\partial x^2} + b \frac{\partial^2}{\partial x^2} (fu) \right), \quad (3.11)$$

which can be written in the alternative form

$$\frac{\partial u}{\partial t} = D \frac{\partial}{\partial x} \left((a + bf) \frac{\partial u}{\partial x} + b \frac{\partial f}{\partial x} u \right). \quad (3.12)$$

Equation 3.11 can also be written as:

$$\frac{\partial u}{\partial t} = D \frac{\partial}{\partial x} \left((a + bf + buf') \frac{\partial u}{\partial x} \right) = D \frac{\partial^2}{\partial x^2} (au + buf). \quad (3.13)$$

where f' denotes the first derivative of f with respect to u . Equation 3.13 is the form of a non-linear diffusion equation and if $(a + bf + buf') < 0$, then the equation is not well posed and we would expect blow up to occur. As we shall see in chapter 4, $(a + bf + buf') < 0$ is precisely the condition required for patterning. The system is expected to converge to homogeneity if $a + bf + buf' > 0$. The form of model (3.12) suggests that there is a competition between the two terms inside the brackets. The

first of these terms will have a dampening effect since $a + bf > 0$, whereas the second term is favouring self-aggregating behaviour since $\frac{\partial f}{\partial u} < 0$. We expect that depending on the initial data, this system will exhibit blow-up in finite time or convergence to homogeneity. Studies on similar models have indeed demonstrated this [41, 73].

3.5.2 (M2) Local Sensing with Crowding Effect

The continuous local sensing model derived above is problematic since, depending on the parameters, it can be ill-posed or cannot exhibit aggregating behaviour. Equation (3.13) predicts blow-up behaviour since there is no restriction on cell density. In an attempt to prevent blow-up from occurring we introduce an additional bias such that a “crowding” or “volume filling” effect is taken into account, similarly to [40]. Thus, we assume that if the cell density at a site reaches a certain maximum, no more cells can be attracted to that site. To model this behaviour, we assume:

$$T_n^\pm = [a + bf(u_n)](1 - u_{n\pm 1}), \quad (3.14)$$

with f , again, a decreasing function of u . Proceeding as before, we obtain the continuous model:

$$\frac{\partial u}{\partial t} = D \left[\left\{ a \frac{\partial^2 u}{\partial x^2} + b \frac{\partial^2}{\partial x^2} (fu) \right\} - b \frac{\partial}{\partial x} \left(u^2 \frac{\partial f}{\partial x} \right) \right], \quad (3.15)$$

or

$$\frac{\partial u}{\partial t} = D \frac{\partial}{\partial x} \left((a + bf) \frac{\partial u}{\partial x} + b \frac{\partial f}{\partial x} (1 - u)u \right). \quad (3.16)$$

This can again also be written as a diffusion equation:

$$\frac{\partial u}{\partial t} = D \frac{\partial}{\partial x} \left((a + bf + bu(1 - u)f') \frac{\partial u}{\partial x} \right). \quad (3.17)$$

Comparing (3.16) to the strictly local model (3.12) we observe the inclusion of the term $(1 - u)$. Similarly to the remarks of the previous section, there is a competition between dampening terms and terms favouring aggregation. Intuitively, we could expect that the extra term prevents aggregates from growing above a certain density

threshold. However, the continuous model derived here can still be ill-posed if $a + bf + bu(1 - u)f' < 0$, which according to the analysis of chapter 4 is the region where pattern formation is expected. Thus, even after including volume filling effects we still obtain blowup.

3.5.3 (M3) Sensing direction of movement

Next, we assume that a particle will move from site n to $n + 1$ according to how many new adhesion bonds it can create at the potential new site. For this model we have:

$$T_n^\pm = a + bg(u_{n\pm 1}), \quad (3.18)$$

where g is now assumed to be an increasing function of u , reflecting that the probability of a cell moving to a specific site increases with the cell density of that site. The continuum limit of (3.1) with (3.18) is then:

$$\frac{\partial u}{\partial t} = D \left[\left\{ a \frac{\partial^2 u}{\partial x^2} + b \frac{\partial^2}{\partial x^2} (gu) \right\} - 2b \frac{\partial}{\partial x} \left(u \frac{\partial g}{\partial x} \right) \right], \quad (3.19)$$

or

$$\begin{aligned} \frac{\partial u}{\partial t} &= D \frac{\partial}{\partial x} \left((a + bg) \frac{\partial u}{\partial x} - b \frac{\partial g}{\partial x} u \right) \\ &= D \frac{\partial}{\partial x} \left((a + bg - bug') \frac{\partial u}{\partial x} \right). \end{aligned} \quad (3.20)$$

Comparing with previous models, we would expect this model to yield similar results to the strictly local model (3.12): We again obtain two terms with opposite sign, since $\partial g / \partial u > 0$. In the absence of random diffusion, ($a = 0$), and with g an increasing function we would expect dampening of perturbations to occur at relatively high cell densities. Similarly to the previous remarks, this model will behave as a non-linear diffusion equation if $a + bg - bug' > 0$ and we therefore expect evolution to a homogeneous distribution. In contrast when $a + bg - bug' < 0$ we obtain a backward diffusion equation and the problem is ill-posed.

3.5.4 (M4) Sensing opposite to movement

Mirrored to the previous case our next model assumes that a cell senses a site in its immediate neighbourhood, but moves in the opposite direction. Hence, if the site to a cell's right is empty or the cell density at it is low, we assume that the cell will move to the left:

$$T_n^\pm = a + bf(u_{n\mp 1}). \quad (3.21)$$

Where f is taken to be a decreasing function. Substituting into (3.1) and expanding the right-hand side, the continuous model derived is given by:

$$\frac{\partial u}{\partial t} = D \left[\left\{ a \frac{\partial^2 u}{\partial x^2} + b \frac{\partial^2}{\partial x^2} (fu) \right\} + 2b \frac{\partial}{\partial x} \left(u \frac{\partial f}{\partial x} \right) \right], \quad (3.22)$$

or

$$\begin{aligned} \frac{\partial u}{\partial t} &= D \frac{\partial}{\partial x} \left((a + bf) \frac{\partial u}{\partial x} + 3b \frac{\partial f}{\partial x} u \right) \\ &= D \frac{\partial}{\partial x} \left((a + bf + 3b f') \frac{\partial u}{\partial x} \right). \end{aligned} \quad (3.23)$$

Similarly to the previous sections, in the continuous model derived in this case there is a competition between terms of opposite signs (since $f'(u) \leq 0$). Furthermore, if $a + bf + 3b f' > 0$ the system is expected to only obtain a stable homogeneous solution. Conversely, if $a + bf + 3b f' < 0$ blow up is expected.

3.5.5 (M5) Gradient Sensing

Our final model incorporates elements of the previous models in that now cell movement is determined by information gathered both at the site the cell resides and the site it may move to. Therefore, cells decide whether to move to a specific location based on the difference in cell density between its current and neighbouring location. Thus we use an increasing function g and write down the model:

$$T_n^\pm = a + b[g(u_{n\pm 1}) - g(u_n)], \quad (3.24)$$

where it should be noted that (since T^\pm denote probabilities) we should demand $T^\pm \geq 0$. Proceeding as before and upon substitution in the master equation (3.1), expansion to second order terms and taking the diffusion limit we obtain the continuous gradient model:

$$\frac{\partial u}{\partial t} = D \left[\left\{ a \frac{\partial^2 u}{\partial x^2} - b \frac{\partial^2}{\partial x^2} (gu) \right\} + b \left(g \frac{\partial^2 u}{\partial x^2} - u \frac{\partial^2 g}{\partial x^2} \right) \right], \quad (3.25)$$

or

$$\begin{aligned} \frac{\partial u}{\partial t} &= D \frac{\partial}{\partial x} \left(a \frac{\partial u}{\partial x} - 2b \frac{\partial g}{\partial x} u \right) \\ &= D \frac{\partial}{\partial x} \left((a - 2bug') \frac{\partial u}{\partial x} \right). \end{aligned} \quad (3.26)$$

The continuum model thus derived (eq. 3.26) is not well-posed if $a < 2bug'$ and will remain homogeneous otherwise.

3.6 Summary of Models

Table 3.2 below summarises the derived continuous models of the preceding sections. The general form of all the models derived is given as

$$\frac{\partial u}{\partial t} = \frac{\partial}{\partial x} \left[(A(u) + B(u)u) \frac{\partial u}{\partial x} \right]. \quad (3.27)$$

The table also shows the sign of the first derivative of the function F with respect to u , (where F is either f or g) in order to indicate whether an increasing or a decreasing function of the cell density is used in each model.

Table 3.3 shows typical simulations performed for each discrete model, in order to provide a preview of the results and assist in clarifying the differences between the models. It also illustrates the importance of the random diffusion component (a), since its inclusion in the model can have a drastic effect on the final pattern reached. Note that for the gradient model we need to impose $a \geq b$ since we require $T_n^\pm \geq 0$. Consequently, a small random migration term is necessary, rendering the case $a = 0$ non-applicable.

Model	Section	T_n^\pm	$A(u)$	$B(u)$	$\partial F/\partial u$
(M1)	(3.5.1)	$a + bf(u_n)$	$a + bf$	bf'	–
(M2)	(3.5.2)	$[a + bf(u_n)](1 - u_{n\pm 1})$	$a + bf$	$bf'(1 - u)$	–
(M3)	(3.5.3)	$a + bg(u_{n\pm 1})$	$a + bg$	$-bg'$	+
(M4)	(3.5.4)	$a + bf(u_{n\mp 1})$	$a + bf$	$3bf'$	–
(M5)	(3.5.5)	$a + b[g(u_{n\pm 1}) - g(u_n)]$	a	$-2bg'$	+

Table 3.2: Summary of the models proposed in this section. The table shows the transitional probabilities of the discrete models and the corresponding continuous models written in the form: $\frac{\partial u}{\partial t} = \frac{\partial}{\partial x} [(A(u) + B(u)u)\frac{\partial u}{\partial x}]$. Both increasing and decreasing functions of cell density were used depending on the model’s assumptions. The sign of $\frac{\partial F}{\partial u}$ is shown to indicate which function type is being considered.

In summary, in this section we have proposed a number of discrete models, (M1)-(M5), to describe cell movement and aggregation due to cell density. We have considered biased random walks in one-dimensional discrete lattices. The specific nature of the introduced bias differs according to the assumptions of each model, but in general movement towards higher cell densities (or away from low cell densities) is favoured. By applying techniques similar to [66] we have derived the corresponding continuous models, and demonstrated that the models thus derived take the form of a non-linear diffusion equation, given in general by equation (3.27). The behaviour of each of the models considered depends on the interplay between stabilising terms (denoted by $A(u)$ in (3.27)) and aggregating terms ($B(u)u$ in (3.27)). The condition for inhomogeneous solutions to evolve is therefore: $A(u) + B(u)u < 0$. However, this is precisely the condition under which the problem becomes ill-posed. Consequently, with the expectation of blow up in the continuous versions of the models, it is doubtful whether these could provide a “useful” model for biological adhesion.

In the following chapter, we will mainly concentrate on the analysis of the discrete models proposed in this section. However, a part of the chapter is dedicated to analysing the continuous models since they do offer some valuable information about the behaviour of the system. We will use techniques such as linear stability analysis, bifurcation analysis and numerical simulations for each of the discrete models in order to illustrate their main properties, and assess their validity. In particular we are interested in assessing whether, (i) the model is capable of producing self-aggregating behaviour, (ii) it produces multiple and regularly spaced aggregations, and (iii) the

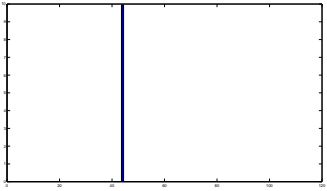
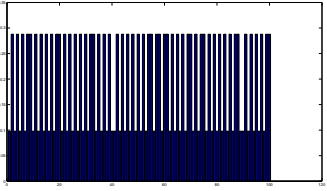
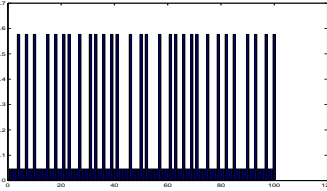

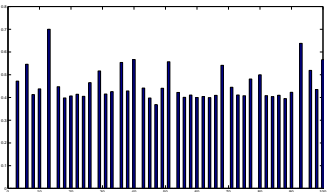
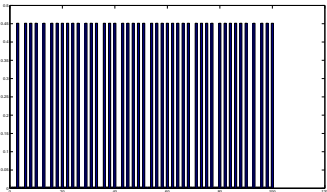
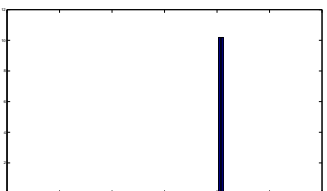
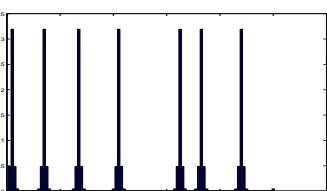

Model	$a = 0$	$a \neq 0$
(M1)		
(M2)		
(M3)		
(M4)		
(M5)	N/A	

Table 3.3: Typical simulations for the discrete models studied in subsequent sections. All simulations show the systems at rest. Note the effect a small random migration term ($a \neq 0$) can have to the patterns observed. The case $a = 0$ in the gradient model (Model 5) is not applicable since it leads to negative transition probabilities. Function $f = \frac{1}{1+qu^2}$ was used in (M1), (M2), (M4), $g = \frac{u^2}{\gamma+u^2}$ in (M3), and $g = \frac{u^3}{\gamma+u^3}$ in (M5). All simulations shown were performed in 100-site lattices with periodic boundary conditions. A small random perturbation from homogeneity was used as initial condition. Parameters used: (a): $b = 1.0, q = 100, M = 10$. (b): $a = 0.1, b = 1.0, q = 100, M = 20$. (c): $b = 1.0, q = 100, M = 20$. (d): $a = 0.01, b = 1.0, q = 100, M = 20$. (e): $b = 2.0, \gamma = 0.1, M = 20$. (f): $a = 0.01, b = 2.0, \gamma = 0.1, M = 20$. (g): $b = 1.0, q = 100, M = 20$. (h): $a = 0.1, b = 1.0, q = 100, M = 30$. (i): $a = 1.1, b = 1.0, \gamma = 0.1, M = 30$.

model can produce cell aggregates of multiple cell widths.

Chapter 4

Local Sensing Analysis

In this chapter we analyse the models presented in section 3.5. The discrete models are generally given by (3.1):

$$\frac{\partial u_n}{\partial t} = T_{n-1}^+ u_{n-1} + T_{n+1}^- u_{n+1} - (T_n^+ + T_n^-) u_n,$$

where the form of the transitional probabilities T_n^\pm varies for each model (see table 3.2). The continuous models take the form:

$$\frac{\partial u}{\partial t} = \frac{\partial}{\partial x} \left[(A(u) + B(u)u) \frac{\partial u}{\partial x} \right],$$

where functions $A(u)$ and $B(u)$ differ according to the specific model. We will study both types of models subject to periodic boundary conditions, so that total cell density is conserved and the impact from the boundaries is minimal. We study the discrete system in one-dimensional domains comprised of N sites, whereas for the continuous system $x \in [0, L]$. Small ($\approx 0.5\%$) random perturbations from a homogeneous distribution were used as initial conditions, unless otherwise stated.

We initially perform a linear stability analysis for both the discrete and continuous models in order to obtain predictions of the behaviour of the systems as well as to compare them to each other. Since as we have seen in chapter 3 that the continuous models can be ill-posed, we concentrate our investigation on the discrete models.

A bifurcation analysis is then performed in discrete systems of a limited number of sites. In order to obtain detailed understanding of the system, we first study

the behaviour for small sized grids, comprising only a few sites. We investigate the behaviour of the steady state stability as the total density increases in lines of two, three and five sites, using periodic boundary conditions to limit boundary induced artifacts. Bifurcation analyses for all models were carried out in order to calculate the stability of the homogeneous steady state as well as to trace inhomogeneous solutions, characterise them, and calculate their stability, similarly to the work undertaken in [73]. This was achieved using the numerical package AUTO [25].

Finally, numerical simulations of the discrete systems discussed in the previous sections have been performed. Our aim is to further explore the systems behaviour in order to confirm the analysis and reveal aspects of the models that cannot be determined analytically. We performed numerical simulations in systems of 100 or more lattice sites. Small perturbations from a homogeneous distribution were used as initial condition, unless otherwise noted. Additionally, the initial cell density is chosen such that any criterion for instability, as derived from the linear analysis, is met for each case studied. Periodic boundary conditions were employed throughout.

The analysis undertaken in the following sections serves as a tool for understanding the properties of each model. The aim, from a biological point of view, is to test whether a particular model is capable of reproducing behaviours found in real biological systems, and to what extent. Analysis of each model can reveal its drawbacks and limitations in that aspect. Furthermore, the mathematical models proposed here, are approximations of biological systems and analysing their properties can help improve our understanding of the underlying mechanisms of the real systems in question.

4.1 Strictly Local Sensing Analysis

In this section we perform a detailed stability, bifurcation, and numerical analysis of the strictly local model. This will highlight the methodologies being performed in a transparent manner aided by the relatively tractable nature of the model. Our principal aim is to understand the capacity of the model to predict aggregation in a population of cells.

4.1.1 Linear Stability Analysis

We begin by focusing on the strictly local sensing model (sec. 3.5.1). We linearise both the discrete and continuous models. As implied in the preceding chapter, the continuous models derived are shown to be ill-posed whenever deviation from homogeneity is expected. By linearising the continuous models however, we can both confirm this point, and further our investigation by obtaining a general stability condition, which we can then compare to the equivalent stability condition of the discrete model and explore the correspondence between them.

Continuous model

The continuous model derived for the strictly local case (equation (3.11)) possesses a single homogeneous steady state u_0 , where $u_0 = \frac{1}{L} \int_0^L u(x, 0) dx$. We are interested in determining the stability of the homogeneous steady state in order to derive the conditions under which patterns can emerge. Furthermore, linear stability analysis about the homogeneous equilibrium can provide useful information about the system's evolution. The model (3.11) reads:

$$\begin{aligned} \frac{\partial u}{\partial t} &= D \frac{\partial}{\partial x} \left((a + bf) \frac{\partial u}{\partial x} + b \frac{\partial f}{\partial x} u \right) \\ &= D \frac{\partial}{\partial x} \left((a + bf) \frac{\partial u}{\partial x} + bf' \frac{\partial u}{\partial x} u \right), \end{aligned} \quad (4.1)$$

where $f' = \frac{\partial f}{\partial u}$. We linearise around the homogeneous steady state u_0 , and set $u = u_0 + \tilde{u}$, where \tilde{u} is a small perturbation from the steady state:

$$\begin{aligned} \frac{\partial \tilde{u}}{\partial t} &= D \frac{\partial}{\partial x} \left[\frac{\partial \tilde{u}}{\partial x} (a + bf_0 + b\tilde{u}f'_0) + b(f'_0 + \tilde{u}f''_0)(\tilde{u} + u_0) \frac{\partial \tilde{u}}{\partial x} \right] \\ &= D \frac{\partial}{\partial x} \left[\frac{\partial \tilde{u}}{\partial x} (a + bf_0 + 2b\tilde{u}f'_0 + bu_0f'_0 + b\tilde{u}^2f''_0 + b\tilde{u}u_0f''_0) \right]. \end{aligned} \quad (4.2)$$

where f_0 , f'_0 , and f''_0 represent the function f and its first two derivatives evaluated at u_0 . Ignoring any non-linear terms, we obtain:

$$\frac{\partial \tilde{u}}{\partial t} = D \frac{\partial^2 \tilde{u}}{\partial x^2} (a + bf_0 + bu_0 f'_0). \quad (4.3)$$

Finally we assume solutions of the form $\tilde{u} = ue^{ikx+\lambda t}$, which yields the following dispersion relation:

$$\lambda = -D(a + bf_0 + bu_0 f'_0)k^2 \quad (4.4)$$

where, f_0 and f'_0 are the values of f and its first derivative evaluated at u_0 , the homogeneous steady state, and λ and k are the eigenvalues and wavenumbers of the system. As mentioned in the preceding sections, we presume f to be a decreasing and saturating function. Biologically, this reflects the fact that a large number of adhesive bonds will form at high densities, making a cell less likely to move away from densely populated sites. Saturation of f prevents negative values, as this will not make sense from a biological point of view. Furthermore, equation (4.4) yields the condition:

$$a + bf_0 + bu_0 f'_0 < 0, \quad (4.5)$$

for inhomogeneous patterns to develop, or

$$f'_0 < -\frac{a + bf_0}{bu_0},$$

which implies that f must be sufficiently steep at the homogeneous steady state for patterning to occur.

We observe therefore from equation (4.4) that the equilibrium is always stable or unstable for every wavenumber. When it is unstable, the fastest growing modes correspond to the shortest wavelengths. Note that the unstable case corresponds exactly to a backward diffusion equation, and is hence an ill posed problem. Consequently, blowup behaviour can be expected and the model can be considered unsuitable as a model for cells, since the density will tend to infinity at blowup locations.

Discrete model

The continuous model is ill-posed in the region of instability of the homogeneous steady state. Linear stability analysis was also performed on the discrete model, to establish the correspondence between the two models, and to obtain predictions about the behaviour of the discrete system which will be further explored in the following sections.

Equations (3.7) and (3.1) read:

$$\frac{\partial u_n}{\partial t} = [a + bf(u_{n-1})]u_{n-1} + [a + bf(u_{n+1})]u_{n+1} - 2[a + bf(u_n)]u_n. \quad (4.6)$$

Proceeding as with the continuous case, we examine perturbations from the homogeneous steady state u_0 , where in the discrete case, $u_0 = \frac{1}{N} \sum_{i=1}^N u_i$. By setting $u_n = \tilde{u}_n + u_0$, and expanding with Taylor's series ignoring higher order terms, equation (4.6) yields:

$$\begin{aligned} \frac{\partial \tilde{u}_n}{\partial t} &= [a + bf(\tilde{u}_{n-1} + u_0)](\tilde{u}_{n-1} + u_0) + [a + bf(\tilde{u}_{n+1} + u_0)](\tilde{u}_{n+1} + u_0) \\ &\quad - 2[a + bf(\tilde{u}_n + u_0)](\tilde{u}_n + u_0) \\ &= (a + bf_0 + b\tilde{u}_{n-1}f'_0)(\tilde{u}_{n-1} + u_0) + (a + bf_0 + b\tilde{u}_{n+1}f'_0)(\tilde{u}_{n+1} + u_0) \\ &\quad - 2(a + bf_0 + b\tilde{u}_nf'_0)(\tilde{u}_n + u_0) \\ &= (\tilde{u}_{n-1} + \tilde{u}_{n+1} - 2\tilde{u}_n)bu_0f'_0 + (a + bf_0 + b\tilde{u}_{n-1}f'_0)\tilde{u}_{n-1} \\ &\quad + (a + bf_0 + b\tilde{u}_{n+1}f'_0)\tilde{u}_{n+1} - 2(a + bf_0 + b\tilde{u}_nf'_0)\tilde{u}_n. \end{aligned} \quad (4.7)$$

Ignoring non-linear terms, we obtain:

$$\frac{\partial \tilde{u}_n}{\partial t} = (a + bf_0 + bf'_0)(\tilde{u}_{n-1} + \tilde{u}_{n+1} - 2\tilde{u}_n). \quad (4.8)$$

In the discrete case we look for solutions of the form $\tilde{u}_n = ue^{ink+\lambda t}$, yielding the

corresponding discrete dispersion relation:

$$\lambda = 2(\cos k - 1)(a + bf_0 + bu_0f'_0), \quad (4.9)$$

which, upon expanding the cosine term to second order in k is in accordance with the continuous case dispersion relation (eq. (4.4)), and both yield the same condition for λ to be positive for all wavenumbers k . That is, we require:

$$a + bf_0 + bu_0f'_0 < 0. \quad (4.10)$$

We should note here that in the discrete version of the model, we consider a discrete lattice and therefore the admissible modes are also discrete. Furthermore, we are only interested in discrete wavenumbers that correspond to the effective wavelengths of $w = \frac{2\pi}{k} = 2, 3, 4$ cells etc. Thus, we only consider values of $k \leq \pi$, since values of $k > \pi$ correspond to wavelengths smaller than 2 cells, which is the lowest relevant wavelength for patterning on a discrete lattice. Taking the periodic boundary conditions into account, the admissible discrete modes are given by $k = \frac{2\pi n}{N}$, $n = 0, 1, 2, \dots, N/2$. Figure 4.1 shows a plot of the dispersion relation (equation (4.9)) under a specific patterning scenario (i.e. equation (4.10) is satisfied). Modes corresponding to integer values of wavelength w are indicated.

As previously discussed, we presume f to be a decreasing and saturating function. Functions of the form $f = \frac{1}{1+qu^m}$, with $m > 1$, with q a positive constant, meet the general requirements. We note that according to (4.10), if $m \leq 1$ the homogeneous steady state remains stable. In the following sections we are using the analytically convenient form: $f = \frac{1}{1+qu^2}$. Another suitable form is $f = e^{-qu}$ and simulations using the latter function have shown the same qualitative behaviour as with $f = \frac{1}{1+qu^2}$. Under these assumptions for f , it follows from (4.10) that the necessary condition for the homogeneous steady state to be unstable is:

$$Q \equiv a + aq^2 \frac{M^4}{N^4} + q \frac{M^2}{N^2} (2a - b) + b < 0 \quad (4.11)$$

where we have used $f = \frac{1}{1+qu^2}$, N is the total number of grid points and M is the total

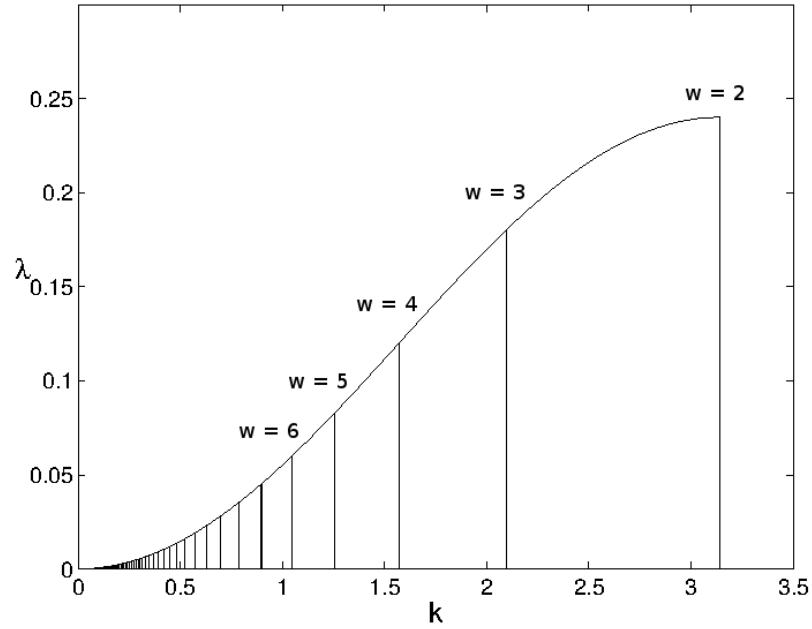


Figure 4.1: Plot of the dispersion relation (equation (4.9)) for the discrete model in the range of values of $k \in [0, \pi]$. Parameters were chosen such that condition (4.10) is satisfied, and the homogeneous steady state is unstable to all modes. Vertical lines indicate the modes corresponding to wavelengths of $w = 2, 3, 4, \dots$ cells. (Only the modes of wavelength up to 6 cells are annotated for clarity). We plot equation (4.9) with $f = \frac{1}{1+qu^2}$. Parameters: $a = 0.1, b = 2, q = 100, u_0 = M/N = 0.3$

cell density over the lattice, such that $u_0 = M/N$ is the homogeneous steady state. Figure 4.2 shows a plot of the above expression as a function of the total cell density for a representative set of parameters. We can observe that the homogeneous steady state is unstable for values of M greater than ≈ 11 and smaller than ≈ 41 with the parameters used. We observe therefore, that the homogeneous equilibrium becomes unstable once the total cell density exceeds a certain threshold, and is stable for high densities. As mentioned in the derivation of the model (section 3.5.1), equation (3.12) suggests that there is a competition between terms of opposite sign. At low cell densities the diffusive terms dominate. Considering the discrete model, the decision to move depends on local information and if the cell density is low, cells will move with greater probability in a random direction. Conversely, if the total cell density is high, cells will generally remain “stuck”, and small perturbations from homogeneity will die out due to diffusion. In the special case $a = 0$, the condition (4.11) reduces

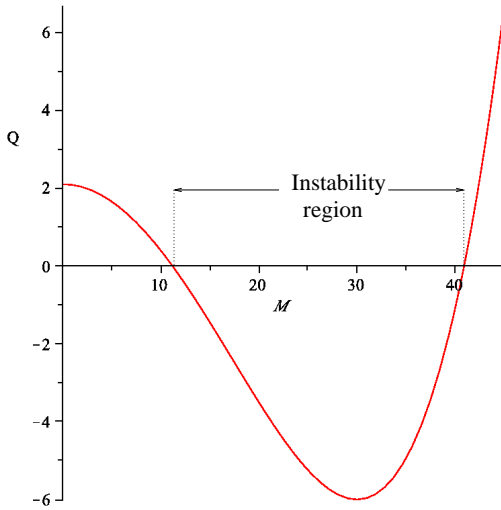


Figure 4.2: Plot to illustrate the stability criterion of eq. (4.11) for the strictly local model of section 3.5.1. The quantity Q is plotted against M , the total cell density. The sign of Q indicates whether the homogeneous steady state is stable. When $Q < 0$, the homogeneous steady state is unstable. Parameters used: $a = 0.1, b = 2, q = 100, N = 100$.

to:

$$M > N \sqrt{\frac{1}{q}}. \quad (4.12)$$

In this case therefore, the steady state is stable only below a certain threshold of the cell density and unstable above it, suggesting that for high densities in the absence of random diffusion, small perturbations from the homogeneous steady state are magnified. Figure 4.3 shows a plot of Q with respect to M for different values of a to illustrate its effect on the instability criterion. It follows from equation (4.11) that a necessary condition for the steady state to become unstable in a certain region (i.e. for equation (4.11) to hold) is $b < 8a$. In other words, with reference to equation (3.11), we can see that by increasing a the diffusivity of the system increases, and when a reaches a critical value, diffusion dominates and the system remains homogeneous. Furthermore, (4.9) suggests that as long as (4.11) holds, the fastest growing modes will be the ones with the shortest wavelengths $w = \frac{2\pi}{k}$ (see also figure 4.1).

Both the discrete and continuous linear stability analysis therefore, yield the same condition for instability of the homogeneous steady state (equation (4.10)).

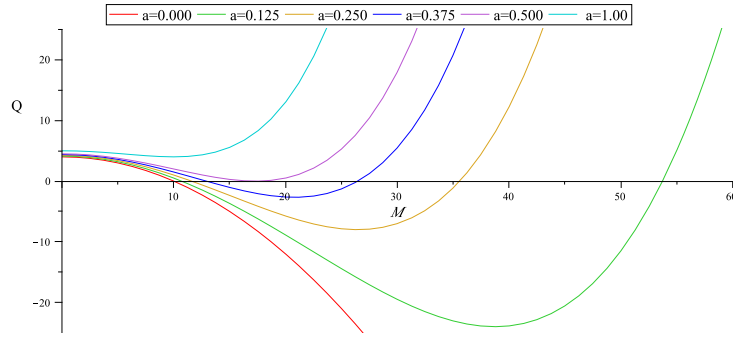


Figure 4.3: Plot of Q versus the total cell density M , according to eq. (4.11), for different values of a , Parameters: number of sites $N = 100$, $q = 100$ and $b = 4$. The homogeneous steady state becomes unstable when $Q < 0$. The region of instability is reduced as a increases due to the increasing dominance of diffusion. When a reaches the critical value $a = b/8$ the region of instability ceases to exist. Note that for the specific case $a = 0$, $Q < 0 \forall M > M^*$, where $Q(M^*) = 0$.

4.1.2 Strictly Local Model (M1) Bifurcation Analysis

In this section we perform a detailed bifurcation analysis in small lattices. As shown from the linear analysis, the stability of the homogeneous steady state depends on the total cell density M . We therefore have chosen M to be the varying parameter, and explored the stability properties of the homogeneous equilibrium as well as the existence, form, and stability properties of any inhomogeneous steady states. A classification of the steady states encountered in the following sections is presented in table 4.1. The inhomogeneous steady states found in the systems under consideration are generally characterised by two levels of cell density, although we note that steady states consisting of more than two density levels can also exist, as we demonstrate later. We have therefore classified the inhomogeneous steady states in terms of the number of sites at high (H) and low (L) cell density. For example, ($HHLL$) denotes a family of steady states, in a 4-site lattice, composed of two sites at high density and two sites at low, regardless of their position on the lattice.

Case I: $a = 0$

We begin by first examining the case where $a = 0$. This case has been studied by Painter et al. [73] and is reviewed here for completeness. Linear stability analysis showed that in this case we expect the homogeneous equilibrium to be unstable above







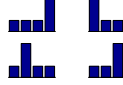
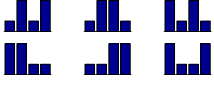
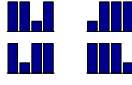
Lattice	Homogeneous	Inhomogeneous		
2 sites		(<i>HL</i>) 		
3 sites		(<i>HLL</i>) 	(<i>HHL</i>) 	
4 sites		(<i>HLLL</i>) 	(<i>HHLL</i>) 	(<i>HHHL</i>) 

Table 4.1: Classification of the steady states found in 2, 3, and 4-site lattices. Inhomogeneous equilibria consist of two levels of cell density. The number of sites at each level characterises the class of equilibria. As we discuss in the following sections, steady states of the same class share their stability properties: For example, the three steady states that form the class (*HLL*) in a 3-site lattice coexist in the same parameter space and are either all stable or all unstable depending on the parameters. Thus, in the following, there is no distinction between members of the same class.

a certain level of the total cell density (fig. 4.3 in section 4.1.1). In the bifurcation diagrams of this and the following sections the cell density of a site at all possible steady states (u^*) is shown as the total cell mass (M) is varied. The stability of a steady state is also traced, and indicated by a solid line (stable steady state), or a dashed line (unstable steady state).

As can be observed in figure 4.4, the system possesses only one homogeneous steady state, $u_0 = \frac{M}{N}$ which is stable, when the total density is below the threshold dictated by the criterion of (4.10). Once the threshold is reached, the homogeneous equilibrium loses its stability and further steady states appear. In the 2-sites case (figure 4.4a), an inhomogeneous equilibrium is reached, where one site has high cell density while the other site low. We can analytically determine all steady states of the system in this case. The system reads:

$$\frac{\partial u_1}{\partial t} = 2bf(u_2)u_2 - 2bf(u_1)u_1 \quad (4.13)$$

$$\frac{\partial u_2}{\partial t} = 2bf(u_1)u_1 - 2bf(u_2)u_2, \quad (4.14)$$

where we have used periodic boundary conditions. At steady state the two equations

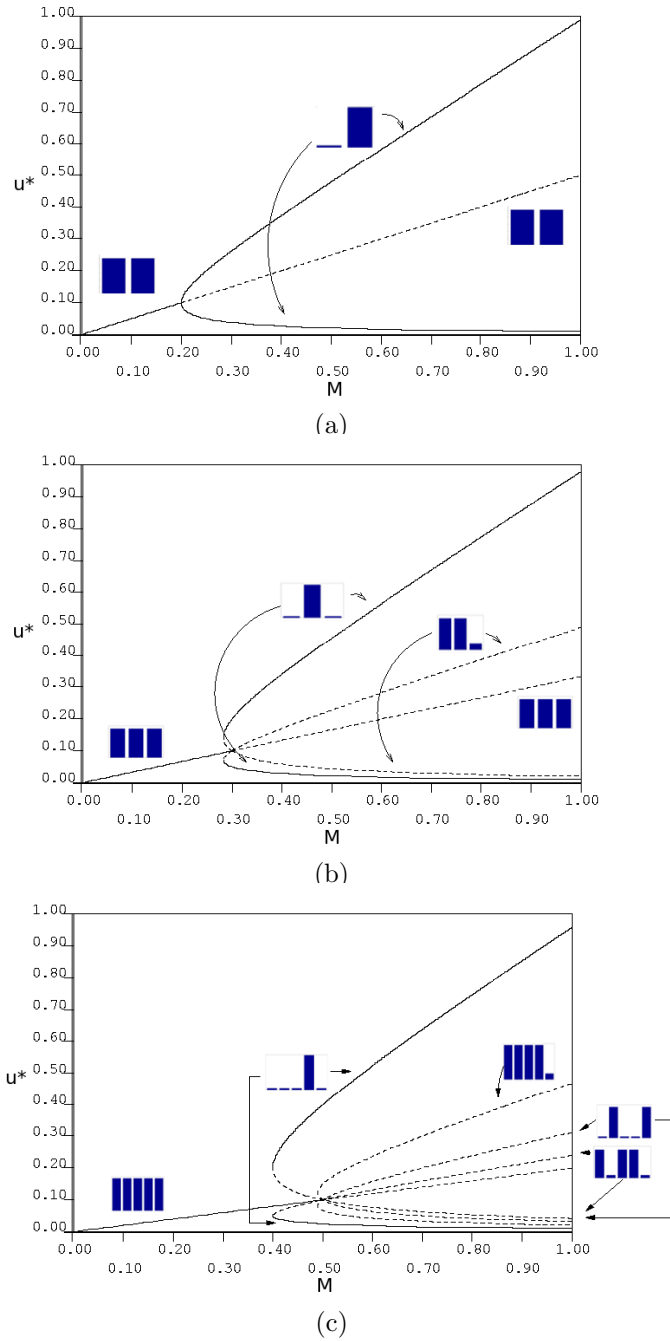


Figure 4.4: Bifurcation diagrams for the strictly local model of section 3.5.1. Steady states (u^*) are plotted versus the bifurcation parameter M , the total cell mass for (a) a 2-sites system, (b) a 3-sites system and (c) a 5-sites system. Parameters used throughout: $a = 0, b = 1, q = 100$. Solid lines indicate stable steady states and dotted lines unstable steady states. Also shown are the forms of the steady states the different lines of the diagram correspond to.

collapse into:

$$bf(u_1)u_1 = bf(u_2)u_2, \quad (4.15)$$

which is coupled with the mass conservation constraint:

$$u_1 + u_2 = M. \quad (4.16)$$

The system (4.15)- (4.16) can be analytically solved. Using $f = \frac{1}{1+qu^2}$, the solutions are: $u_1 = u_2 = M/2$ (the homogeneous steady state) and

$$u_i^\pm = \frac{M \pm \sqrt{M^2 - 4/q}}{2}, \quad (4.17)$$

where $i = 1, 2$, and which are paired $(u_1^+, u_2^-), (u_1^-, u_2^+)$. We can observe that the bifurcation occurs for $M = 2/\sqrt{q}$. For $M < 2/\sqrt{q}$, the only real solution is the homogeneous one, whereas for $M > 2/\sqrt{q}$, the inhomogeneous solutions (4.17) become real. This behaviour is shown in figure 4.4a.

In the 3-sites case (figure (4.4b)), there appear two new branches and at equilibrium, the density is low at two of the sites and high at the third. The unstable branch corresponds to a steady state where there is high density at two of the sites. As the number of sites increases, the situation becomes more complicated. Figure 4.4c shows the bifurcation diagram obtained for a system of 5 sites. As shown, the stable equilibrium is inhomogeneous and corresponds to a state where there is relatively high cell density at one of the sites and low density at the other four (HLLLL). The unstable branches shown correspond to steady states where: four sites have high density and one site low (HHHHL), three sites with high density and two with low (HHHLL), and two sites with high density and three with low (HHLLL). As a final outcome therefore, when in the region where the homogeneous steady state is unstable, the system will evolve to a state where there is global aggregation of all cells at a unique site. Further increasing of the lattice size will not alter the final outcome, but further unstable solutions will emerge that can play a role in the temporal evolution of the system, as will be shown in the numerical simulations of the following section.

Figure 4.5 below shows some preliminary simulations on 5-site grids to further

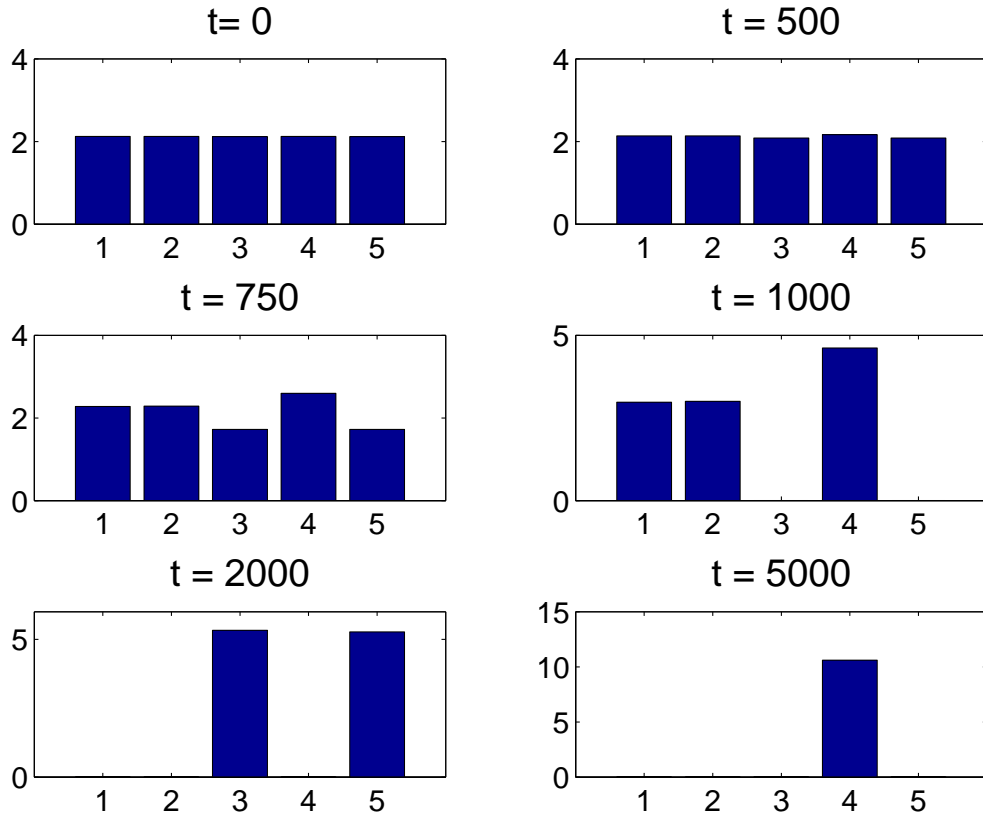


Figure 4.5: Time evolution of the strictly local model (M1) with $a = 0$ on a 5-site lattice. Parameters used $b = 1, q = 100, M = 10.6$

illustrate the bifurcation analysis carried out in this section. Periodic boundary conditions were used. The system was given a small perturbation from homogeneity and, as can be seen in figure 4.5, the system transiently passes from the homogeneous steady state to one where three peaks appear, to one with only two peaks remaining before finally reaching one of the five possible stable inhomogeneous steady states where almost all the cell mass is located at one of the sites. It is also shown that the pattern with alternating high and low cell density is the first to appear. This can be expected from the linear analysis, where patterned modes with the shortest wavelength (2 for discrete lattices), are the fastest growing.

Case II: $a > 0$

In the case where $a \neq 0$ the homogeneous steady state is stable for both low and high cell densities according to the linear analysis. Bifurcation analysis shown in the figures below confirms this. However, the main difference between this case and when $a = 0$

is that, in the absence of random migration, there are just two fundamental forms of stable equilibria, given the total cell density: a uniformly dispersed population and a unique localised aggregation. For $a \neq 0$ there are many possible stable steady states as the total density varies. Comparing figures 4.4b and 4.6b for the 3-sites case for example, we can observe that in the former case the only possible steady state for $M > 0.3$ is (HLL). In the second figure however, the steady state (HHL) is also stable for a certain range of values of M . This feature becomes more prominent as the number of sites increases. In the 5-sites case of fig. 4.6d, in the range of M for which the homogeneous equilibrium is unstable, four stable branches emerge corresponding to four different stable inhomogeneous steady states. In contrast to the case where $a = 0$ (fig. 4.4c), the equilibria (HHHHL), (HHLLL), and (HHHLL) can now be stable. This is also shown by Painter et al. [73], where by adding a small random diffusion component in the system studied, they showed that it evolved to stable multiple peak solutions rather than a unique aggregation, although no further analysis was performed. We can also observe in figures 4.4b - 4.4c and 4.6b - 4.6d that there are some areas of bistability. It should also be noted that inhomogeneous steady states of the same form share the same stability properties. For example in the 4-sites case (figure 4.6c), both (HHLL) and (HLHL) equilibria as well as the permutations of these are either all stable or all unstable depending on the parameters. However, we expect the pattern with alternating high and low cell density between sites to emerge from simulations, with random initial data. That is because, as shown by the linear analysis (section 4.1.1), the fastest growing modes are those with the shortest wavelength, and specifically with wavelength $w = 2$.

In order to illustrate the bifurcation analysis for this case, simulations on a 5 site grid were performed. Figure 4.7, shows the results of a series of simulations with varying total cell mass. The pictures show the system following evolution to equilibrium, and it can be used as an accompaniment to figure 4.6d. It shows the progression of the stable steady states reached as the total mass M is increased.

It is also interesting to note that when $a \neq 0$ steady states exist in which there are three distinct levels of cell density, albeit these have always been found to be unstable. Figures 4.8a and 4.8b show details from fig. 4.6d. Two unstable solutions

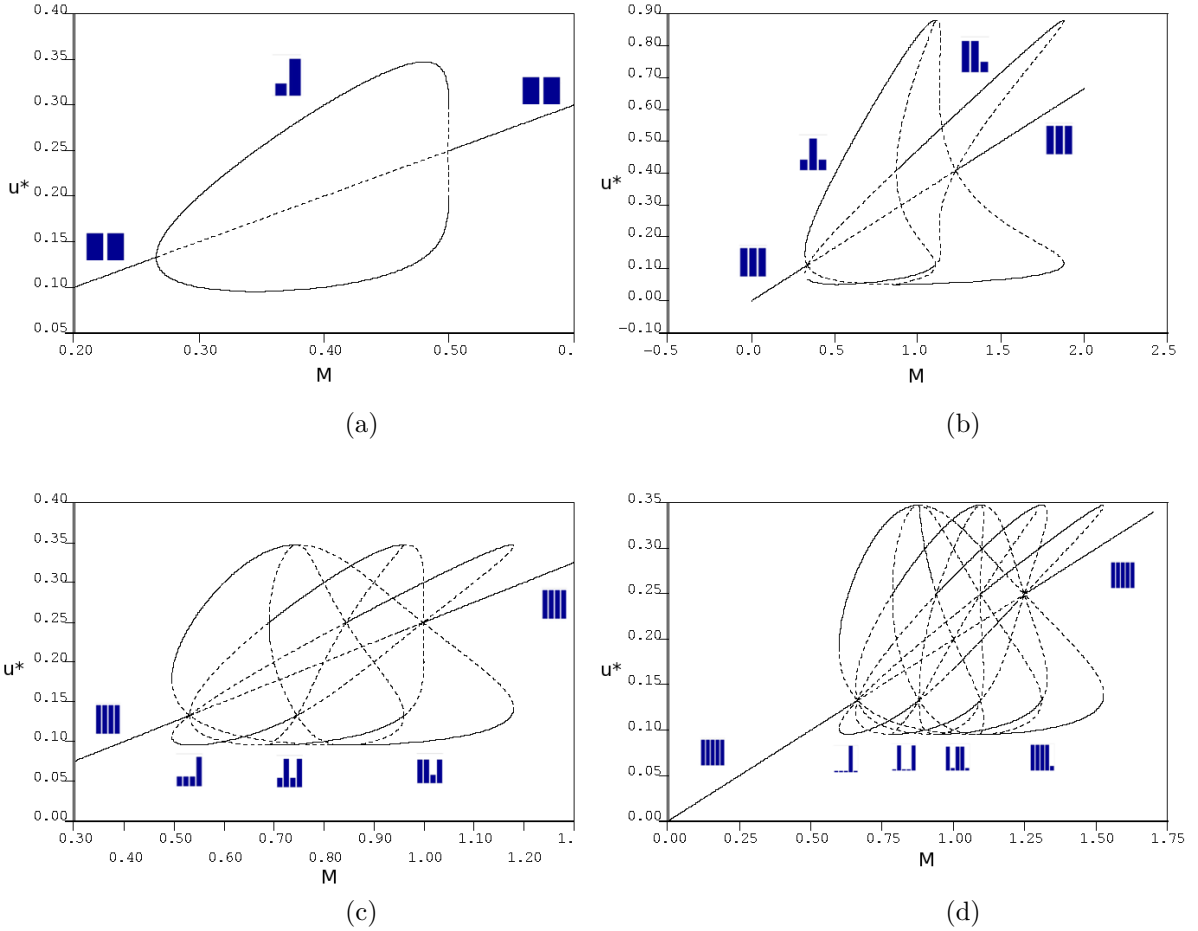


Figure 4.6: Bifurcation diagrams for the strictly local model of section 3.5.1 for (a) a 2-sites system, (b) a 3-sites system, (c) a 4-sites system and (d) a 5-sites system for the case where a random diffusion component is added ($a \neq 0$). $f = 1/(1 + qx^2)$ was used throughout with $q = 100$, and the varying bifurcation parameter is the total cell density M . Parameters: (a) $a = 0.1, b = 1$, (b) $a = 0.1, b = 2$, (c) $a = 0.1, b = 1$, (d) $a = 0.1, b = 1$. Solid line: stable steady state. Dotted line: unstable steady state. The form of each steady state is shown at the parameter area where it is stable.

are plotted. If, for example, we examine the vertical line where $M = 0.90$ in fig. 4.8a we can observe that there is a steady state where $u = 0.10$ in two of the sites, $u = 0.20$ in another two and $u = 0.30$ in the remaining one. Such steady states do not occur at all in the case where $a = 0$.

Summary of bifurcation analysis

In this section we have performed bifurcation analysis of the strictly local sensing model (M1). Based on the predictions of the linear stability analysis (section 4.1.1),

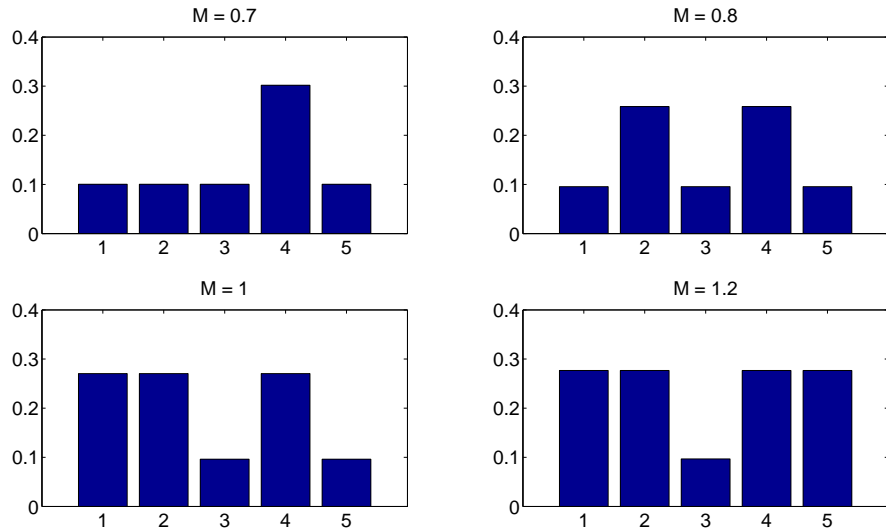


Figure 4.7: Simulations on a 5-site lattice of the strictly local model in order to further illustrate the bifurcation diagrams. Four different simulations are shown when equilibrium is reached, for varying total cell density. Periodic boundary conditions were employed. Parameters used $a = 0.1, b = 1, q = 100$

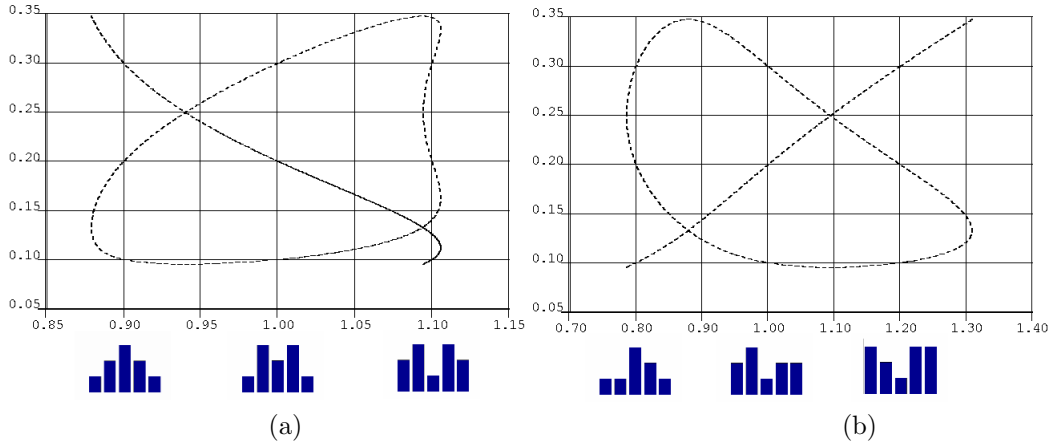


Figure 4.8: Details from figure 4.6d, the bifurcation diagram of a 5-site system with $a > 0$. Each figure shows the existence of steady states with three distinct levels of cell density among the 5 sites. Also shown are the forms of the steady states in question. Steady states of this form do not exist when $a = 0$, and are not expected to be observed in simulations with random initial conditions, since they are always unstable (as indicated by the dashed line).

we considered the cases $a = 0$ (no random cell motility) and $a \neq 0$ separately.

In the first case, we have shown that the unique homogeneous steady state is stable for relatively low values of the total cell density and unstable otherwise. If the total

cell density is higher than a threshold specified by the parameters, the system can only evolve to a family of inhomogeneous steady states, where almost all cells aggregate at a single site. Increasing the lattice size results in more inhomogeneous steady states emerging. However, these are all unstable and do not alter the final outcome of global aggregation at a single site. It is expected however, that the time evolution of a system from small perturbations from homogeneity to global aggregation will be affected.

When a small random cell motility term is added to the system, global aggregation can be prevented. The bifurcation analysis shows that in this case the homogeneous steady state is stable for both low and high total cell densities. In the region where it is unstable, there are now multiple stable inhomogeneous steady states, the number of which increases with the domain size. These equilibria are composed of two levels of cell density, and the ratio of sites at high density to sites at low density is dictated by the total available cell density M . The stability of the inhomogeneous steady states, and therefore the pattern the system will evolve to also depends on M . We therefore expect that in a large domain system, a large variety of stable inhomogeneous equilibria exists, and the model is capable of producing a number of different patterns. In order to confirm this prediction and further investigate our model we have performed the numerical simulations presented in the following section.

4.1.3 Numerical Simulations

The bifurcation analysis presented in the previous section allows insight into the properties of the system and the various forms of patterns that can be obtained in a system with small size. However, as the domain size is increased, studying the models with bifurcation analysis techniques becomes increasingly difficult. Therefore, in order to study larger domains we resort to a numerical investigation to see whether the insight gained can be further explored.

The simulations shown in this section concern the model (M1) discussed in section 3.5.1 and analysed in 4.1.1 (for details of the numerical methods used, see section A.2 of the appendix). This is the simplest model where only local sensing is assumed. We begin by exploring the special case where $a = 0$. We have seen that the homogeneous steady state is always unstable provided that the total cell density

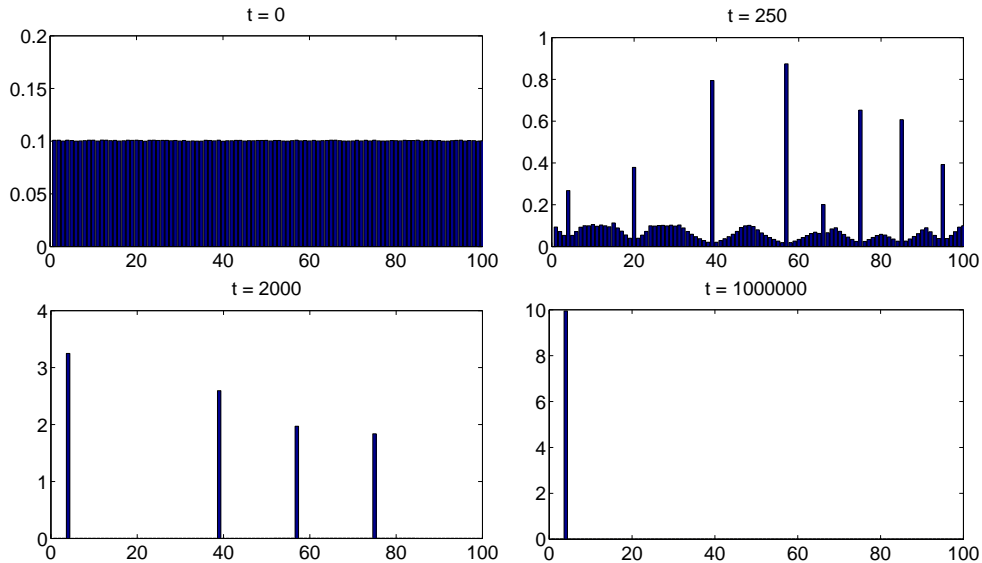


Figure 4.9: Time evolution of the strictly local model with $a = 0$, in a 100-site domain. The system was initially perturbed from homogeneity. Perturbations are magnified and multiple peaks appear. In the course of the simulation the peaks merge until finally equilibrium is reached with almost every cell gathered at a single site. Parameters: $b=1.0$, $q=100$. Numerical method details in A.1.2

exceeds a certain threshold (eq. (4.10)). The bifurcation diagrams of section 4.1.2 have shown that in this case it is expected that if the parameter regime is such that the homogeneous steady state is unstable, then in the resulting inhomogeneous equilibrium, a single site on the lattice will have high cell density. To test this prediction we have performed the simulation displayed in figure 4.9. $f = \frac{1}{1+qu^2}$ was used, and the parameters were: $a = 0, b = 1, q = 100$. The simulation reveals that the final pattern is indeed one with a single site attracting a high cell density, while the rest of the sites have a low cell density. Transiently, the perturbations initially given are magnified and as a result spikes appear. Gradually, the spikes become larger and further apart as cells move. Eventually all peaks but one disappear and the system reaches equilibrium. This coarsening effect is reported in [41] and [73] and can be predicted from the bifurcation analysis carried out above: as the lattice size is increased, multi-peaked patterns correspond to saddle points which may transiently attract solutions.

Further simulations were performed in order to explore the general case in which $a \neq 0$. The analysis previously undertaken predicts that there are now stable solutions where multiple peaks appear. When $a = 0$ the system evolves to either the

homogeneous equilibrium or to a steady state where all the cells aggregate at a single site, depending on the total cell density. In this case however, the inhomogeneous equilibria correspond to a number of sites being at a relatively high cell density while the rest at a relatively low density. We expect that for a given set of parameters, the number of peaks at equilibrium will be increasing as the total cell mass M increases. This can be seen in fig. 4.10, which shows the simulations performed for six different values of the total cell density M . The bifurcation analysis of a 5-site system in section 4.1.2 showed that as M is increased, the system evolves in succession from the homogeneous steady state to $(HLLLL)$, to $(HHLLL)$, to $(HHHLL)$, to $(HHHHL)$, and finally to homogeneity (cf. figure 4.7). Figure 4.10 shows the equivalent behaviour for a system of 100 sites.

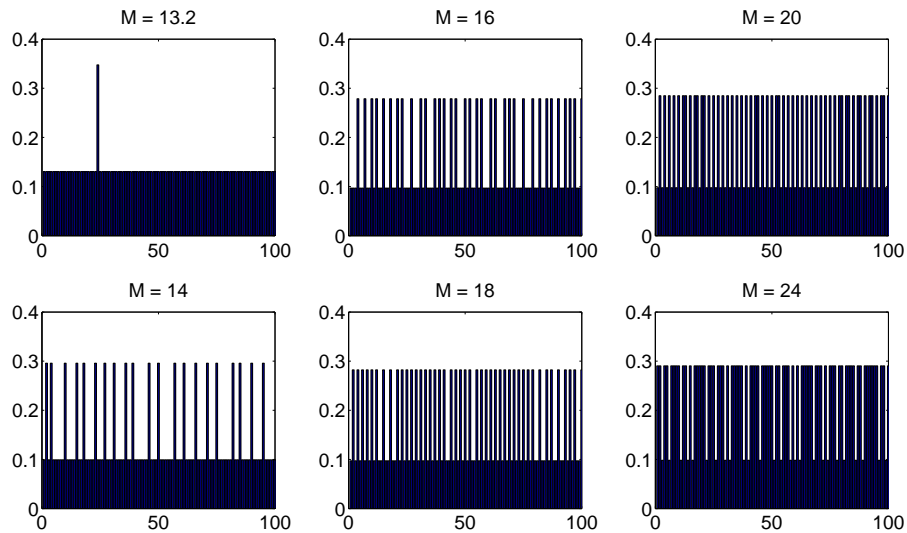


Figure 4.10: Simulations for the full strictly local model where diffusion is included ($a > 0$). The different plots show the equilibria reached for different values of the total cell density M . In each case, each site can be at either of two possible levels of cell density. As the total density increases, the fraction of sites at high density rises. Parameters: $a = 0.1, b = 1.0, q = 100$. (see A.1.2 for details)

4.1.4 Summary and relation to aggregation of adhesive populations

In summary, we have seen that global aggregation of all the cells at a single site occurs unless a small element of random diffusion is added to the system. Such behaviour is typically not desirable, since the model is incapable of capturing the regular aggregation patterns observed in real systems. Including random migration prevents global aggregation and produces regular patterns. However, the analysis showed that these are short wavelength patterns, meaning that instead of cell aggregations we obtain patterns at the scale of individual cells. In order to obtain blocks of sites at high cell density, a system with high total cell density is needed. In this case, the aggregations form as a result of the high cell density forcing high density sites in proximity, rather than the model's properties. Furthermore, the aggregations formed in this way are separated by single site regions of low cell density, and are therefore not good approximations of a natural system since at a macroscopic scale, such regions would be indistinguishable. Therefore, with reference to the fundamental questions outlined in table 3.1, the model (M1) is capable of: (i) producing aggregating behaviour, (ii) producing multiple aggregations provided there is a non-zero random migration element, but (iii) these aggregations are of single cell width.

4.2 Analysis of (M2): Local Sensing with Crowding

In this section, the local sensing model with crowding effect is analysed. The model is presented in section 3.5.2, where the assumptions for cell movement are described. In summary, a cell moves according to information gathered locally. That is, a cell is more likely to move away from a site when the cell density at that site is low. Additionally, a restriction in cell movement is imposed. It is assumed that there exists a certain maximum capacity at each site, and when it is reached no more cells can move to this particular site.

4.2.1 Linear Analysis

We have performed linear stability analysis for the case of section 3.5.2. That is, the case where strictly local sensing is assumed and a crowding effect is taken into account. By linearising the continuous model derived (eq. (3.15)) we obtain the following dispersion relation:

$$\lambda = -D(a + bf_0 + bu_0f'_0 - bu_0^2f'_0)k^2, \quad (4.18)$$

which implies that for inhomogeneities to grow we require

$$a + bf_0 + bu_0f'_0 - bu_0^2f'_0 < 0. \quad (4.19)$$

Performing the corresponding linear analysis for the discrete case of the model yields:

$$\lambda = 2(\cos k - 1)(a + bf_0 + bu_0f'_0 - bu_0^2f'_0) \quad (4.20)$$

which is equivalent to the continuous dispersion relation eq. (4.18) upon expansion of the cosine term to second order, and yields the same condition for stability of the homogeneous equilibrium (equation (4.19)). Again we note that the instability condition in the continuous model corresponds to the region where the model is an ill posed/backward diffusion model. As such, we expect blowup and concentrate on the discrete model.

Similarly to the previous case, assuming $f = \frac{1}{1+qu^2}$, we obtain the following criterion for the homogeneous steady state to be unstable in the discrete case:

$$Q = a + b + aq^2\frac{M^4}{N^4} + 2bq\frac{M^3}{N^3} + q\frac{M^2}{N^2}(2a - b) < 0 \quad (4.21)$$

which is illustrated in figure 4.11 using the same parameters as with the simple local sensing case. Comparing this plot with figure 4.2 we observe a far smaller region in which the homogeneous steady state is unstable for the same parameters. This difference can be intuitively explained by comparing equation (3.15) and equation (3.11) for the strictly local case: here we observe the introduction of the term $-b\frac{\partial}{\partial x}(u^2\frac{\partial f}{\partial x})$.

The inclusion of this term has a dampening effect explaining the smaller region of instability observed. For the same reason, the homogeneous steady state remains stable for smaller a than in the previous case. It is also worth noticing that in this case the homogeneous steady state is stable for large values of M , even in the extreme case of $a = 0$, in contrast to the strictly local sensing scenario discussed in the previous section. Again, this can be intuitively expected from the crowding term, which will restrict cell movement at higher levels. As can be seen from table 3.2 the $B(u)$ term of the strictly local sensing case is multiplied by a saturation factor of $(1 - u)$, which becomes more significant in high densities and impedes the movement of cells. Similarly to the local sensing scenario, provided that the homogeneous equilibrium is unstable, the fastest growing modes will be those with the short wavelength modes and we would expect these to dominate initial patterning from the steady state.

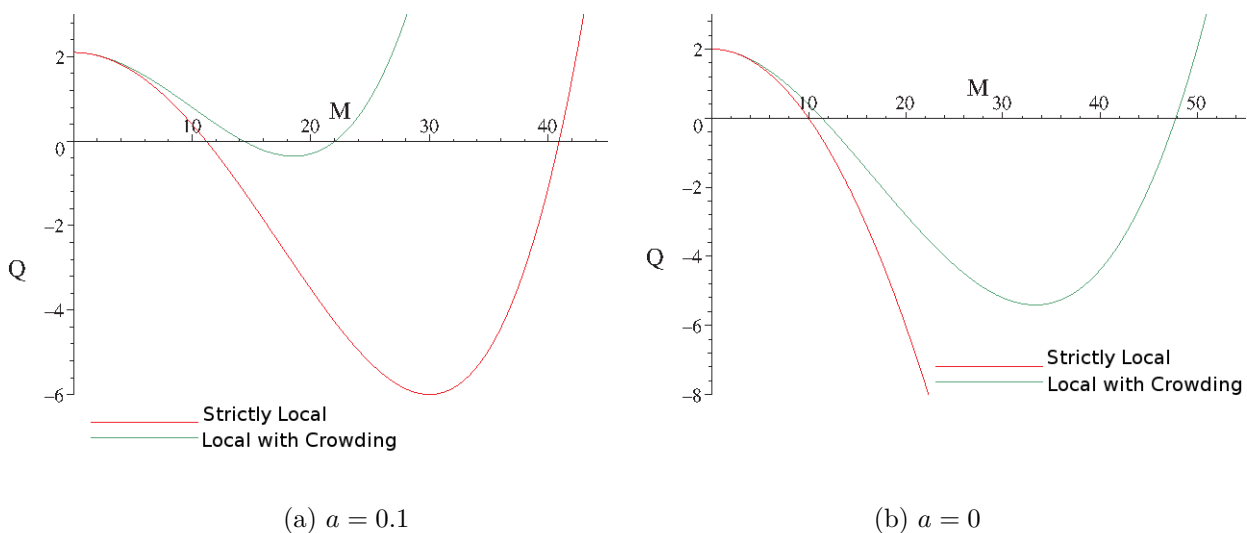


Figure 4.11: Plot to illustrate the stability criterion of eq. (4.21) for the local sensing with crowding model of section 3.5.2. The equivalent criterion for the strictly local case (eq. (4.11)) is also plotted here for comparison. The quantity Q is plotted against M , the total cell density. The sign of Q indicates whether the homogeneous steady state is stable: When $Q < 0$, the homogeneous steady state is unstable. (a): The homogeneous equilibrium is shown to be unstable for both low and high values of M , for sufficiently low a . (b): The region of stability for high total density exists even for $a = 0$, in contrast to the case of the strictly local sensing model as a result of the crowding term included. Parameters used: $b = 2, q = 100, N = 100$.

4.2.2 Bifurcation Analysis

Figures 4.12a and 4.12b below show the bifurcation diagrams obtained for the model (M2), for a system of three lattice sites and for $a = 0$ and $a \neq 0$ respectively. In contrast to the case discussed in the previous section, we observe that, when $a = 0$ the homogeneous equilibrium can now become stable both below and above a certain threshold of the total cell density. This was also shown by the linear analysis undertaken in section 3.5.2. Figure 4.12a also reveals that the “secondary” inhomogeneous solution (where two sites have high cell density (HHL)) also becomes stable for some values of M , and the system is bi-stable. This becomes clearer when the lattice size is increased Figure 4.12c shows the case for a 4-site lattice. The situation for $a \neq 0$ is qualitatively the same, in that the system possesses the same stable steady states, and only the region in which the homogeneous steady state is unstable changes. Note also that, as in the case for strictly local sensing, steady states with sites in more than two levels of cell density exist but are always unstable.

4.2.3 Numerical Simulations

In this section we investigate the model numerically, using the method outlined in A.2. We have mentioned previously that there is a competition between terms of opposite sign in the model, where both the crowding term and the random migration term have a stabilising effect. This was examined further in the analysis undertaken in the previous sections. In this section we make no distinction between the $a = 0$ (no random migration) and $a \neq 0$ cases, since they are qualitatively identical.

The simulation depicted in figure 4.13 illustrates how the final pattern depends on the total cell density. We note that multiple simulations were undertaken with varying initial cell density. The model shows qualitatively the same behaviour to the strictly local sensing model (with $a \neq 0$) analysed in the preceding section: as the total cell density increases, the number of sites at high cell density found at the final stable pattern increases in line with the predictions of the bifurcation analysis for small lattice size (section 4.2.2). As the domain size is increased, further stable branches appear at higher densities. Figure 4.13 depicts the progression from homogeneity at

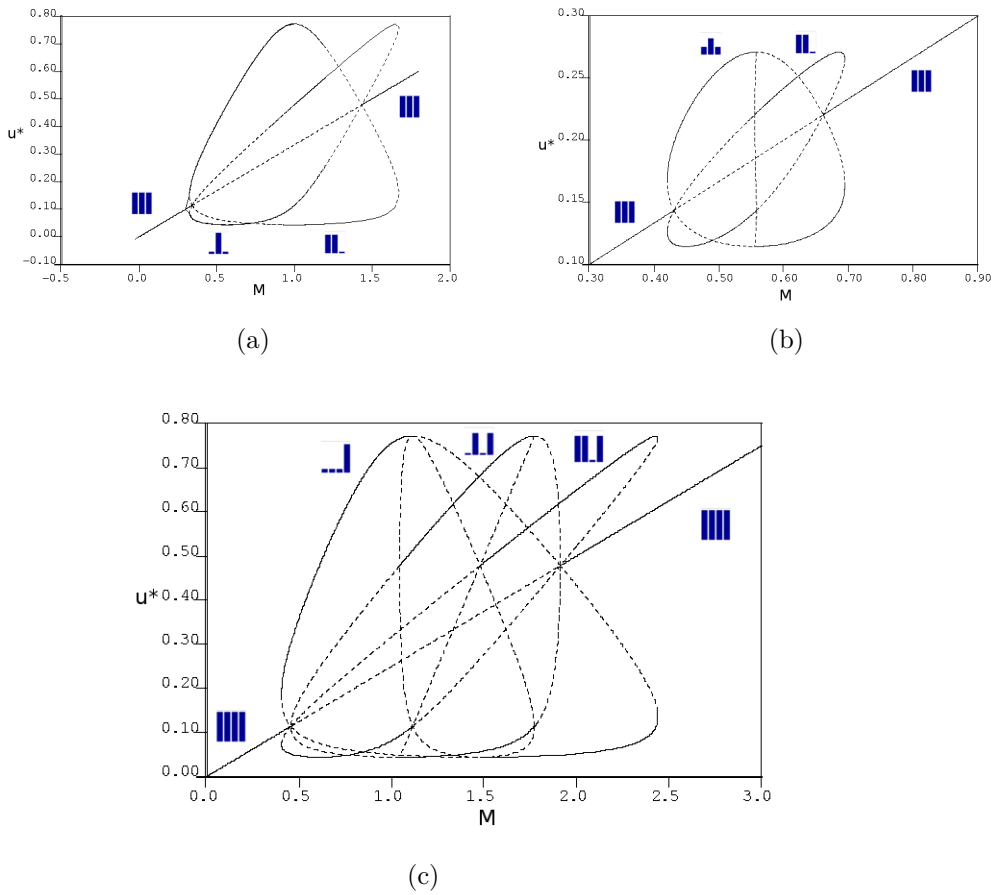


Figure 4.12: Bifurcation diagrams for the local sensing model with crowding effect of section 3.5.2. Steady states are plotted versus the bifurcation parameter M , the total cell mass for (a) a 3-sites system with no random diffusion, $a = 0$, (b) a 3-sites system for $a \neq 0$, and (c) a 4-sites system. Parameters used : (a) $a = 0, b = 2, q = 100$, (b) $a = 0.1, b = 2, q = 100$, (c) $a = 0, b = 2, q = 100$. Solid lines indicate stable steady states and dotted lines unstable steady states. Also shown are the forms of the steady states the different lines of the diagram correspond to.

low cell density (not shown) to patterns with scattered high density sites, to large numbers of sites at high density, and back to homogeneity for large total cell mass (not shown).

Figure 4.14 shows the time evolution of the system for a particular choice of the total cell mass M , for $a = 0$. The system is shown to follow a similar course as with the strictly local scenario with $a \neq 0$. Small perturbations from a uniform density are magnified, and provided the total density is low enough, the system evolves into a fine pattern where high density sites are separated from low density sites. This is consistent with the predictions made from the linear analysis, where it was shown

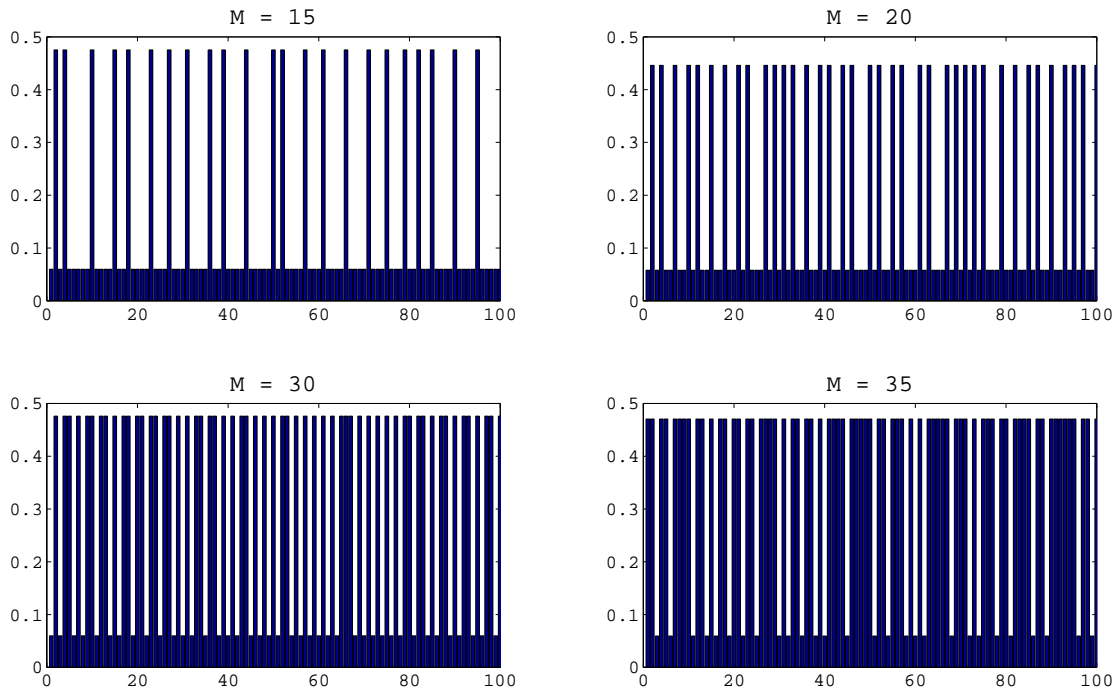


Figure 4.13: Numerical simulations of the local sensing model with crowding effects. Figures show the dependence of the pattern on the total cell density M . Each site can be at either of two possible density states. The number of sites at high density increases with M . Parameters used: $q = 100, N = 100, a = 0.01, b = 1.0$. Details of numerical methods can be found in A.1.2

that the shorter wavelength modes are the fastest growing.

In summary, inclusion of crowding effects prevents global aggregation to a single site, and has a similar impact to the inclusion of a small random migration element. However, similarly to the strictly local case, this model only appears to produce patterns with alternating high and low cell densities and there is no evidence of reproducing the multicell width patterns often found in biological cases of cell aggregation.

4.3 Analysis of (M3): Sensing into direction of movement.

Here, we analyse the model (M3) described in section 3.5.3. The assumption for this model was that a cell's decision to move is based on the cell density of the destination site. Cells probe their adjacent neighbourhood and move to a particular site if the

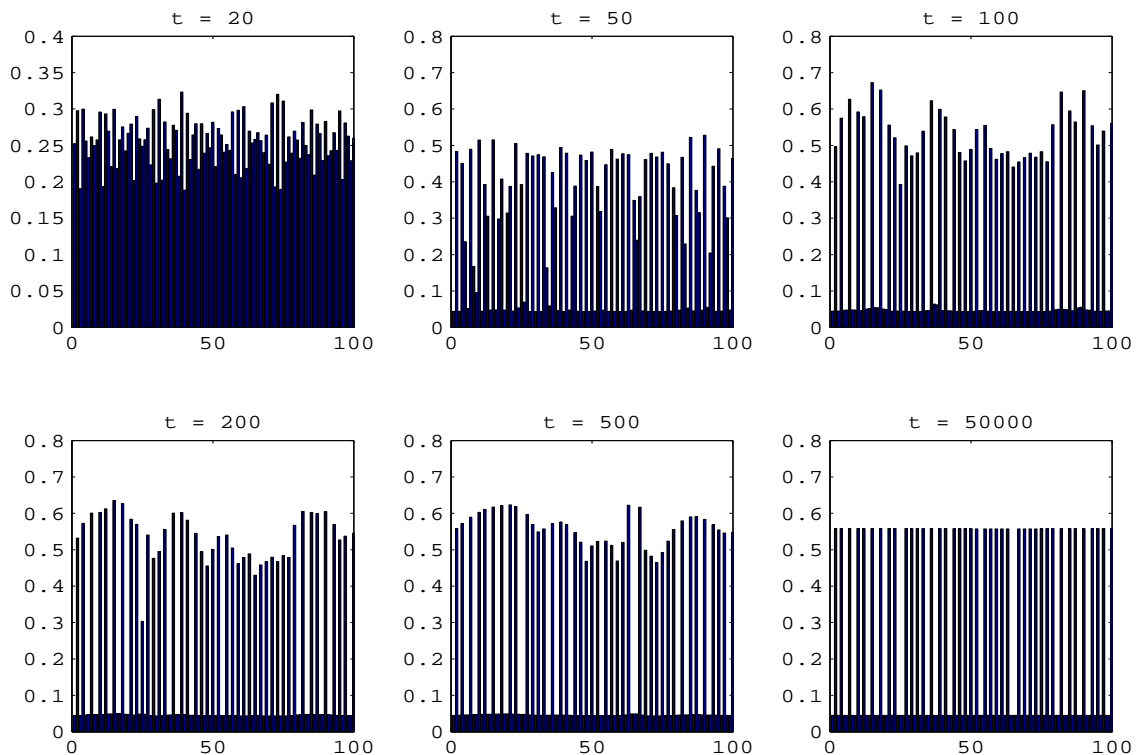


Figure 4.14: Time evolution of the crowding effects model. Small initial perturbations are magnified and the system diverges from homogeneity. Parameters used: $q = 100$, $N = 100$, $M = 25$, $a = 0.0$, $b = 1.0$. See A.2 for details

conditions at that site are favourable. In this case, to model an adhesion type process, the probability of a cell moving to a site is assumed to increase with its cell density.

4.3.1 Linear Analysis

Linearising equation (3.19), the continuous model for the assumptions made in section (3.5.3) we obtain:

$$\lambda = -D(a + bg_0 - bu_0g'_0)k^2. \quad (4.22)$$

Linearising the discrete model yields a dispersion relation which results in the equivalent criterion for instability as the continuous case:

$$\lambda = 2(\cos k - 1)(a + bg_0 - bu_0g'_0). \quad (4.23)$$

Both equation (4.22) and (4.23) imply that the stability of the homogeneous steady state depends on the sign of $a + bg_0 - bu_0g'_0$. Similarly to the cases previously described,

this condition indicates that the homogeneous steady state is either stable or unstable to all modes. We again note that in the continuous case, the condition for instability coincides with the region where the model is ill-posed, and we will concentrate on the discrete model. g is an increasing function of u , as mentioned previously. This is motivated from a biological point of view: The higher the cell density at the target site, the more adhesive bonds will be formed. However, we require g to be saturating at high cell densities in order to impose a limit on the number of adhesive bonds that can be formed. A suitable form is: $g = \frac{u^m}{\gamma + u^m}$, with $\gamma > 0$, and $m > 1$ since the system will always remain homogeneous otherwise. In the following we use $g = \frac{u^2}{\gamma + u^2}$ for analytical convenience. The criterion for instability in the discrete case reads:

$$Q = a\gamma^2 + (a + b)\frac{M^4}{N^4} + \gamma\frac{M^2}{N^2}(2a - b) < 0, \quad (4.24)$$

which has at most two positive real roots. A plot of (4.24) for a specific set of parameters can be seen in figure 4.15. By setting $a = 0$ in (4.24), the condition reduces to: $M < N\sqrt{\gamma}$, which gives the value of the threshold below which the steady state is unstable. We observe that in this case there is at most one positive root for $Q = 0$ and, that in contrast to the cases analysed previously, the homogeneous steady state is unstable for all densities up to some threshold (figure 4.15b).

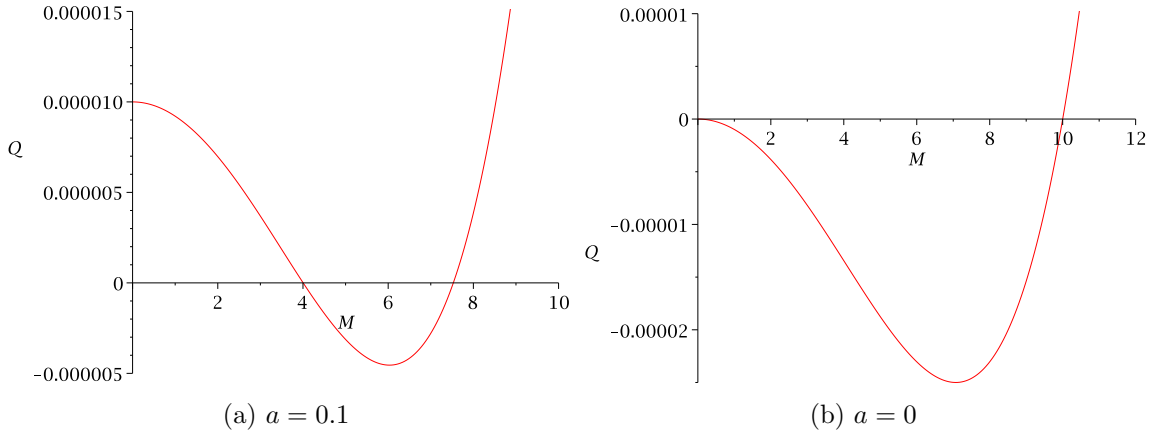


Figure 4.15: Plot to illustrate the stability criterion of eq. (4.24). (a): Similarly to previous models for $a \neq 0$ the homogeneous steady state is stable for both low and high densities. (b) For $a = 0$ the homogeneous equilibrium is stable only at high densities. Parameters used: $b = 1, \gamma = 0.01, N = 100$, and $a = 0.1$ in (a).

4.3.2 Bifurcation Analysis

Case I: No random diffusion. $a = 0$

Figures 4.16a and 4.16b show the bifurcation analysis diagrams of the model presented in section 3.5.3 for a system of 3 sites. Figure 4.16a is the bifurcation diagram obtained for the case $a = 0$. The stable steady states besides the homogeneous one are $(M/2, M/2, 0)$ and $(M, 0, 0)$, whereas unstable inhomogeneous equilibria shown in figure 4.16a correspond to (HHL), (HLL), and (HL0). Effectively, the only heterogeneous steady states are those in which one site has become completely devoid of cells. Intuitively, we expect that for larger domains the system evolves to steady states strongly dependent on the initial conditions: initial variation in cell density between adjacent sites can lead to sites being depleted of cells and, in the absence of random diffusion ($a = 0$), once a site has become depleted, then the probability of cells moving to it becomes zero, since $T_n^\pm = a + bg(u_{n\pm 1})$ and $g(0) = 0$. Therefore, if alternating sites have zero cell density then all the equations of the system are automatically satisfied, leaving only the constraint of mass conservation. In a system of 4 sites for example, $u_1 = u_3 = 0$ and $u_4 = M - u_2$ is a steady state for any u_2 . In larger arrays therefore, the system can evolve into an infinite number of steady states. As seen with the previous cases, the linear analysis predicts that the shortest wavelength modes ($w = 2$) are the fastest growing, corresponding to alternating sites of high and low density. As such we again initially observe evolution to steady states with peaks separated by empty sites. Once a zero cell density is established in alternate sites, no further evolution can take place. The steady state the system evolves to therefore depends on the initial random perturbation from homogeneity, and therefore is impossible to predict exactly (see the numerical simulations, sec. 4.3.3).

Case II: Including random diffusion. $a \neq 0$

For $a \neq 0$, the bifurcation diagrams obtained (represented in figure 4.16b for a 3-site system) are similar to cases previously described in that there is an area of instability of the homogeneous equilibrium for intermediate values of the total density (as predicted from the linear stability analysis of section 4.3), and multiple stable

inhomogeneous steady states, depending on the total density M . Inclusion of random diffusion stabilises the homogeneous steady states at low densities in contrast to when $a = 0$. Furthermore, it allows movement to empty sites and therefore “regular” patterns are formed.

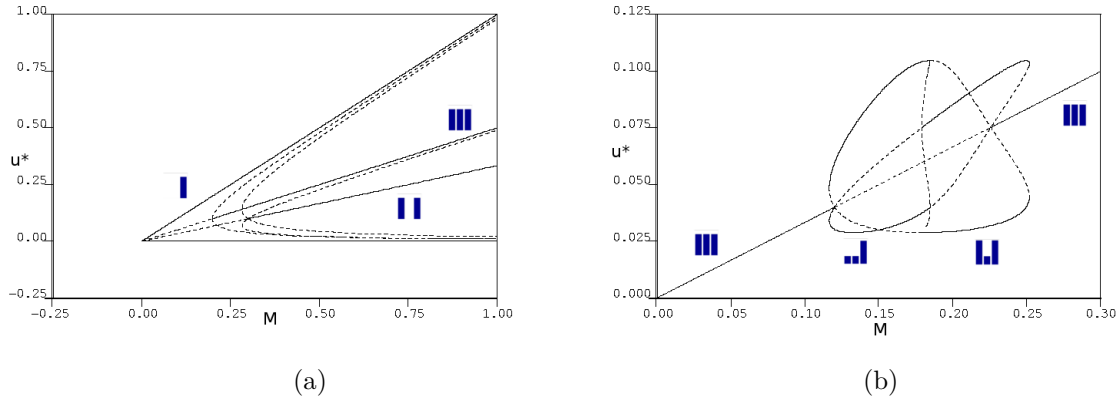


Figure 4.16: Bifurcation diagrams for the closest neighbour sensing model of section 3.5.3. Steady states are plotted versus the bifurcation parameter M , the total cell density for (a) a 3-sites system with no random diffusion, $a = 0$, and (b) a 3-sites system for $a \neq 0$. Parameters used : (a) $a = 0, b = 1, \gamma = 0.01$, (b) $a = 0.1, b = 1, \gamma = 0.01$. Solid lines indicate stable steady states and dotted lines unstable steady states. Also shown are the forms of the stable steady states the different lines of the diagram correspond to.

4.3.3 Numerical Simulations

In this section, numerical simulations performed for the closest neighbour sensing model are presented. Figure 4.17 shows a series of simulations performed in an array of 100 sites for different values of the total density M , with $a = 0$ and periodic boundary conditions. $g(u) = \frac{u^2}{\gamma + u^2}$ was used as above. The figure demonstrates the same properties as in the cases analysed in the previous sections. That is, as the total initial cell density is increased, more sites are populated by cells. In this particular case, as shown in the bifurcation diagrams of section 4.3.2 the patterns that emerge show sites that are completely empty, and others with varying levels of cell density. When M is relatively low, the stable patterns that can be observed are ones with alternating sites of zero and non-zero cell density. As M increases, neighbouring sites can be found having equal non-zero density, and the resulting pattern is comprised by blocks of sites

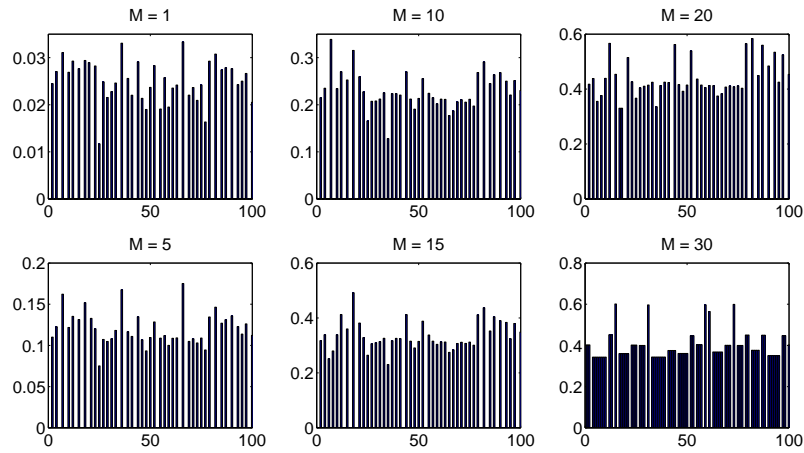


Figure 4.17: Numerical simulations for the model where cells sense their adjacent neighbours, section 3.5.3. No random migration was taken into account ($a = 0$). Six different simulations are shown for different values of the total cell density, are shown at final equilibrium. Simulations show that the steady states reached are comprised of peaks of cell density separated by completely empty sites. Parameters: $\gamma = 0.1, b = 2, a = 0$. Numerical details in A.2.

populated by cells. The location of the peaks in the final pattern as well as the level of cell density exhibited cannot be predicted: as explained in the previous section, these are critically dependent on the initial conditions. Figure 4.18 below demonstrates two simulations carried out using the same value for the total density M but given slightly different random perturbations from the homogeneous steady state. These perturbations were of the same magnitude and drawn from a uniform distribution with a different seeding. The two simulations of figure 4.18 demonstrate the dependence on the initial conditions. However, we can also observe that the patterns obtained are qualitatively similar. Both the average spacing between aggregates and the average cell density of the aggregates are the same in the two simulations. Thus, although the pattern reached cannot be predetermined quantitatively, similar initial conditions will yield similar patterns, which from a biological point of view are indistinguishable.

By including a random diffusion component, cell movement is allowed into sites containing no cells. The system can now evolve to a regular steady state comprised of two levels of cell density, see figure 4.19.

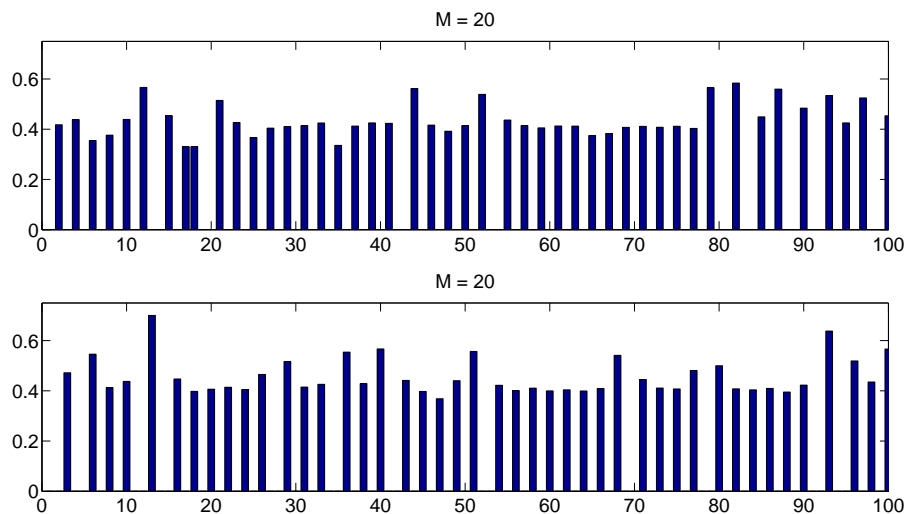


Figure 4.18: Simulations for the closest neighbour sensing model, in order to illustrate the dependence on initial conditions. The figures show the equilibria reached for two simulations of the same system with slightly different initial conditions given. The total cell density is $M = 20$ in both cases. Parameters used: $\gamma = 0.1, b = 2, a = 0$.

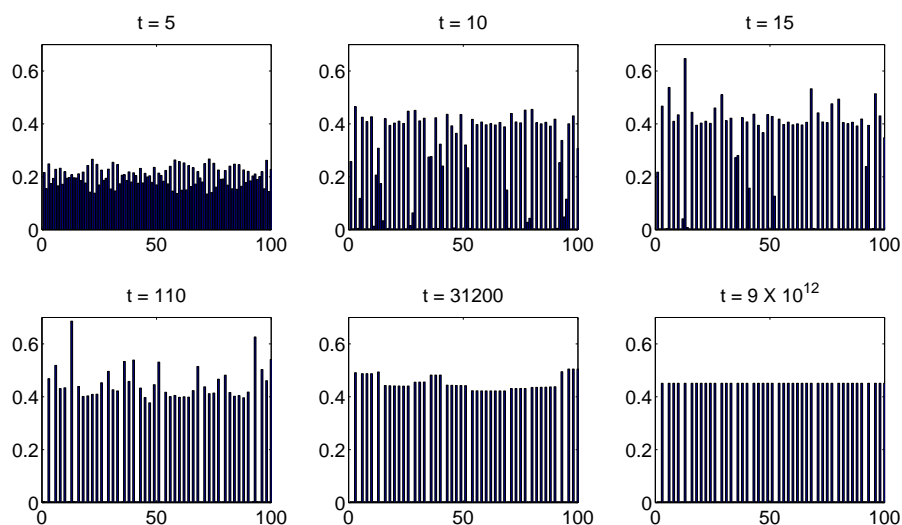


Figure 4.19: Time evolution of the full closest neighbour sensing model. Random diffusion was taken into account. Small initial perturbations are magnified and eventually the system evolves to a steady state where two different cell density levels exist. Parameters: $M = 20, \gamma = 0.1, b = 2, a = 0.01$.

4.4 Analysis of (M4): Sensing opposite to movement

The model of section 3.5.4 is examined in the following sections. Here, we assume that cell movement is dictated by the site opposite to movement. Thus, a cell will

now be more likely to move away from an adjacent site with low cell density.

4.4.1 Linear Analysis

Linearisation of the continuous model of section 3.5.4 yields the equation below for the eigenvalues of the system:

$$\lambda = -D(a + bf_0 + 3bu_0f'_0)k^2. \quad (4.25)$$

The criterion for instability, assuming $f = \frac{1}{1+qu^2}$ as before, in this case reads:

$$Q = a + b + aq^2u_0^4 + qu_0^2(2a - 5b) < 0, \quad (4.26)$$

which as can be seen in figure 4.20, exhibits similar behaviour as discussed above. Once more, if the criterion (4.25) is satisfied, the continuous model is not well-posed.

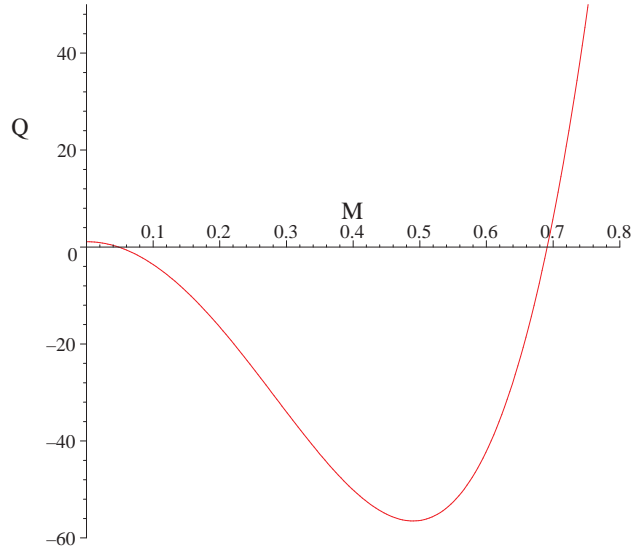


Figure 4.20: Plot to illustrate the stability criterion of eq. (4.26). Parameters used: $a = 0.1, b = 1, q = 100, L = 1$.

The linearised discrete model yields the dispersion relation below.

$$\lambda = 2(\cos k - 1)(a + bf_0) + 2bu_0f'_0(2 \cos^2 k - \cos k - 1), \quad (4.27)$$

which upon expansion of the cosine terms to second order agrees with (4.25).

Condition (4.26) is sufficient to predict instability for the continuous model, as the corresponding dispersion relation (equation (4.25)) from which it is derived generates either $\lambda \geq 0$ or $\lambda \leq 0$ for every k . However, in contrast to previous cases analysed, linear analysis of the discrete model does not generate the same result to the continuous model. While $Q < 0$ still yields the condition for which the homogeneous steady state is unstable, only a range of unstable wavenumbers exists. To illustrate this, the dispersion relation (4.27) is plotted as a function of k for different values of M (shown in figure 4.21 for $a = 0$). The inequality given in (4.26) for $a = 0$ yields: $M_{critical} = \frac{N}{\sqrt{5q}}$ which is the value below which we obtain strictly negative eigenvalues for the discrete dispersion relation (4.27) for every value of k ($M = 0.2$ for the parameters used in figure 4.21). However, we should impose a second restriction for pattern formation to occur. Periodic boundary conditions suggest that only wavenumbers of the form $k = \frac{2\pi n}{N}$, $n = 0, 1, 2, \dots$ are admitted. Therefore the critical value for M , which allows patterns to occur emerges from (4.27) with $k = k_{critical} = \frac{2\pi}{N}$. For example, for a system with 4 sites, $k_{critical} = \pi/2$ and the condition for patterns to emerge becomes:

$$M > \frac{N}{\sqrt{q}}. \quad (4.28)$$

As the number of lattice sites N increases, the condition of instability for the discrete model approaches that of the continuous model.

4.4.2 Bifurcation Analysis

Figure 4.22a demonstrates the bifurcation diagram for the model (M4) for a system comprised of four lattice sites, with $a = 0$. Similarly to the previous cases, the homogeneous steady state loses stability once the total mass M exceeds a certain threshold and remains unstable for larger values of M . The inhomogeneous steady states that emerge correspond to (HHLL), i.e. a steady state where two sites are in high density while the remaining two are in low density, which is stable, and to an unstable steady state where there exist three levels of cell density. The same classification of steady states can be observed in figure 4.22b (where $a \neq 0$). In the

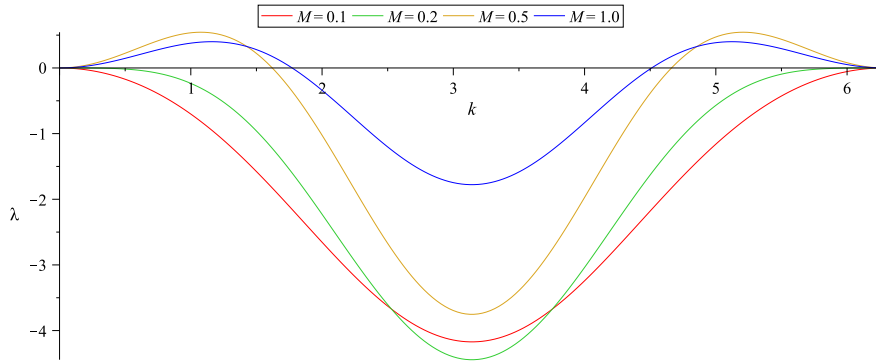


Figure 4.21: Dispersion relation for the discrete model (equation (4.27)). In contrast to previously analysed models, when the criterion for instability is satisfied, a range of unstable wavenumbers exists. $M = 0.2$ is the critical value predicted from (4.26), the continuous model dispersion relation. However, when periodic boundary conditions are taken into account, the critical value increases for the discrete model. Parameters: $a = 0.0, b = 1.0, q = 80, N = 4$.

latter case, similar to previous cases, the homogeneous equilibrium becomes stable for large values of M . As the domain size increases, we observe that the stable steady state that emerges in the area of instability, for $a = 0$, is an equilibrium comprised of three distinct cell densities (fig. 4.22c, for a 5-site system), where two of the sites are at high density, one in low and two at intermediate cell density (HHMML). This is distinct from all previous models to date, where the only stable steady states found in the bifurcation analysis correspond to sites in one of just two densities. Numerical simulations confirm this holds also for larger domains (see section 4.4.3 below). A typical bifurcation diagram for $a \neq 0$, is shown in figure 4.22d. In addition to the homogeneous steady state, there is an inhomogeneous equilibrium (HHMML), as previously, but also a stable steady state (for a small range of values of M), in which all 5 sites have distinct levels of cell density. Furthermore, at high range of values of M , the system becomes bistable, since along with the homogeneous steady state, there is a stable steady state characterised by 1 site with high density, two with intermediate density, and two with low (HMMLL).

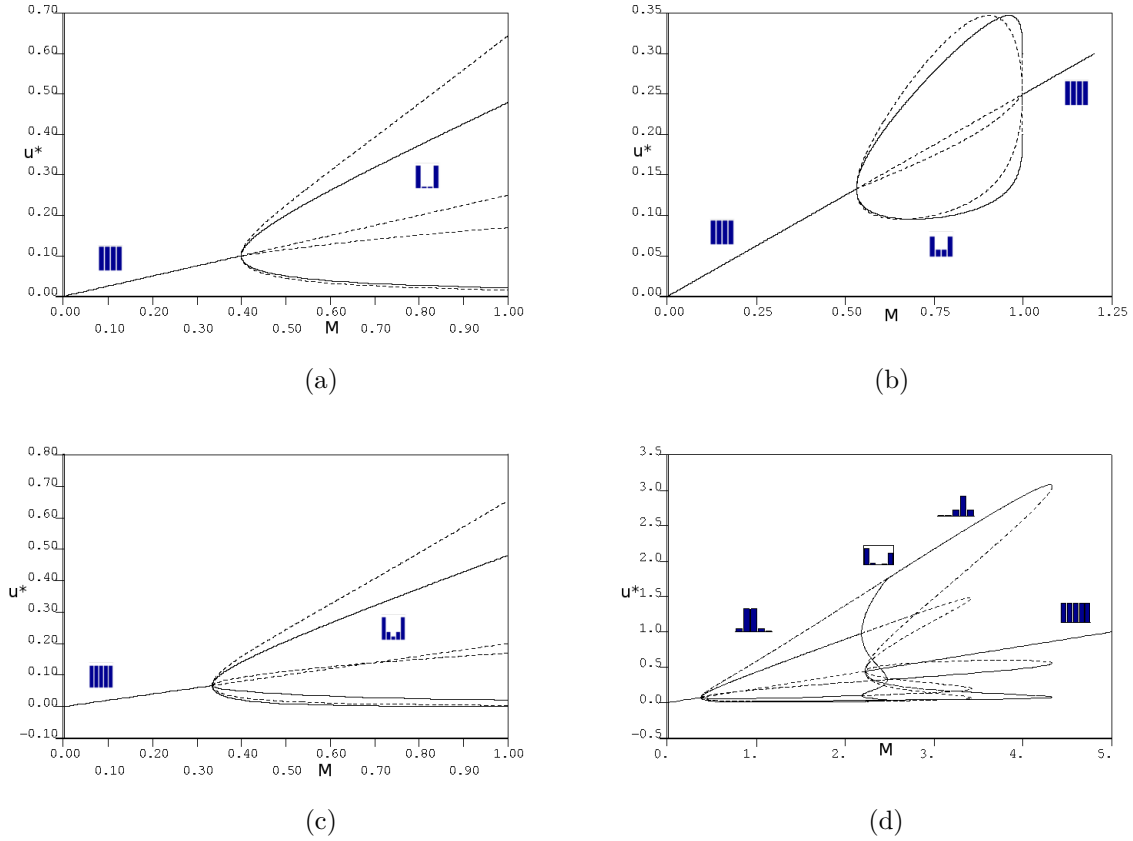


Figure 4.22: Bifurcation diagrams for the sensing opposite to movement model of section 3.5.4. Steady states are plotted versus the bifurcation parameter M , the total cell mass for (a) a 4-sites system with no random diffusion, $a = 0$, (b) a 4-sites system for $a \neq 0$, (c) a 5-sites system for $a = 0$. and (d) a 5-sites system for $a \neq 0$. Parameters used : (a) $a = 0, b = 1, q = 100$, (b) $a = 0.1, b = 1, q = 100$, (c) $a = 0, b = 1, q = 100$, (d) $a = 0.1, b = 1, q = 100$. Solid lines indicate stable steady states and dotted lines unstable steady states. Also shown are the forms of the stable steady states the different lines of the diagram correspond to, in the region where they are stable.

4.4.3 Numerical Simulations

Numerical simulations performed for the model described in section 3.5.4 are presented in this section. As above, we used 100-site domains and periodic boundary conditions (for details, see section A.2 of the appendix). The initial condition imposed is a small random fluctuation from the homogeneous steady state, while the parameters used ensure that the criterion for instability (eq. (4.26)) derived in section 4.4.1 is met. Figure 4.23 shows the progression from a small random perturbation to the final steady state reached for $a = 0$. Similarly to the strictly local sensing scenario investigated in 4.1.3, the initial perturbations are magnified, leading to the appearance

of peaks and troughs of cell density. The setup of the model is such that cells located adjacently to a site with relatively high population will be less likely to move away from it. Additionally, if the site located in the opposite direction is scarcely populated, the cells will tend to move towards the highly populated region. This leads to the transient appearance of pairs of sites with relatively high cell densities. The system finally relaxes to a pattern where almost all cells are aggregated at two adjacent sites. Technically speaking, there are three levels of cell density as shown by the bifurcation analysis of section 4.4.2, as besides the two prominent peaks of figure 4.23 there are another two sites with non-zero cell density located on each side of the aggregation, so that the final pattern has the form of a very abrupt gradient of cell density.

Figure 4.24 demonstrates the same progression from small perturbations applied to the homogeneous equilibrium to the stable pattern with the inclusion of diffusion ($a \neq 0$). Resembling the $a = 0$ case, small aggregations start to appear as time progresses with the gradient-like structure more apparent. Including diffusion in the model plays a stabilising role and prevents global aggregation.

The final pattern (figure 4.24, bottom right) is distinctly different from the patterns emerging in the previous models. To date, we have generally encountered aggregations consisting of alternating high and low cell density. Here however, the equilibrium reached takes the form of distinct small, but multi-cell aggregates, more closely corresponding to cell aggregations in real biological systems. In order to explain this behaviour, we re-examine the basic underlying assumption of the model in section 3.5.4. In this model, it is assumed that movement occurs according to the information gathered by cells from the site opposite to the direction in which they move: $T_n^\pm = a + bf(u_{n\mp 1})$. Therefore, a longer range sensing element is introduced here. A jump between two adjacent sites involves three sites in this case: the site of origin, the destination site, and the site at which the walker bases its decision to move. In contrast, in the previous models only the site of origin and the destination are involved. The results presented here therefore, give a strong indication that by allowing long range sensing distinct cell aggregations can occur, in contrast to the local sensing cases of the preceding sections.

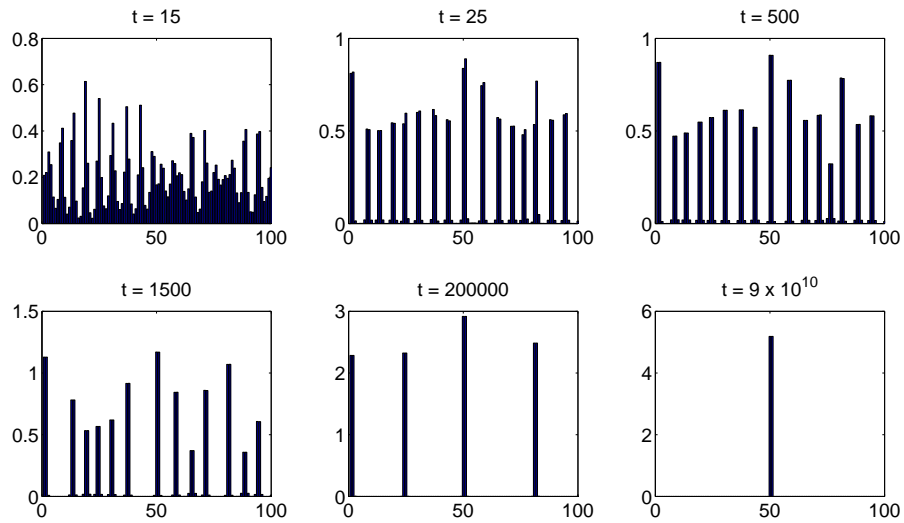


Figure 4.23: Time evolution of a 100-site system for the discrete model of section 3.5.4, with $a = 0$ (for numerical details see A.2). Small perturbations from the homogeneous steady state, given initially, are magnified, leading to the appearance of pairs of adjacent sites at high densities separated by low density gaps. The peaks eventually merge, and the system rests to a steady state. Note that the global aggregation that occurs consists of a high density at 2 neighbouring sites. Parameters: $b = 1.0, q = 100, M = 10$.

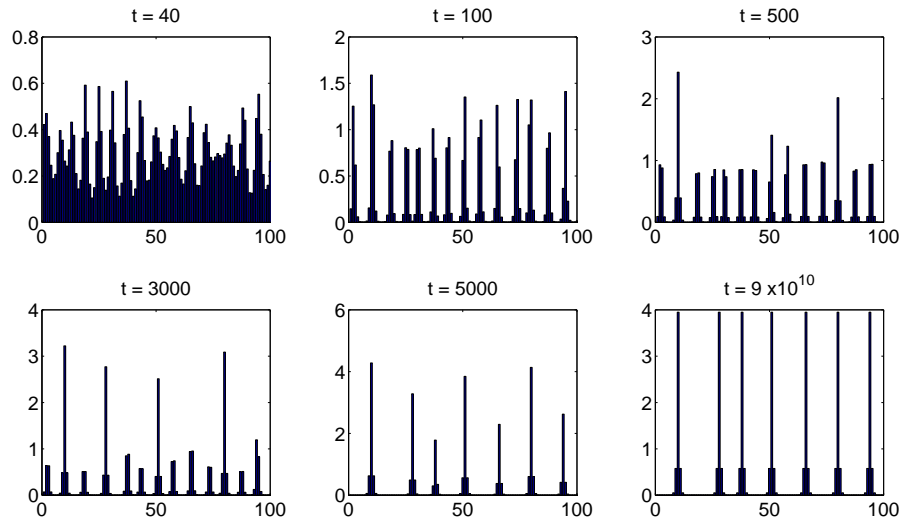


Figure 4.24: Time evolution of a 100-site system for the discrete model of section 3.5.4, with $a \neq 0$. Similarly to when $a = 0$, small perturbations are magnified, but now cells aggregate in gradient-like structures. The final pattern comprises of a number of cell aggregations, depending on the total cell density. Parameters: $a = 0.1, b = 1.0, q = 100, M = 35$.

4.5 Analysis of (M5): Gradient Sensing

Finally, we explore the gradient model of section 3.5.5. In this model, a cell senses its immediate environment, and chooses to move if the conditions at its new position are favourable in relation to the original site. In other words, a cell computes a local gradient in the cell density and moves according to this information.

4.5.1 Linear Analysis

Linearising the continuous gradient model (equation (3.26)) of section 3.5.5 yields the following dispersion relation:

$$\lambda = -D(a - 2bu_0g'_0)k^2, \quad (4.29)$$

while linearising the discrete model yields:

$$\lambda = 2(a - 2bu_0g'_0)(\cos k - 1). \quad (4.30)$$

Both equations imply that the homogeneous steady state is unstable if $a - 2bu_0g'_0 < 0$. This condition for aggregation exactly corresponds to the condition for the continuous model becoming ill-posed. In common with all previous models, we therefore concentrate on the analysis of the discrete model.

In this case, because of the extra condition that needs to be imposed in order to keep the transition probabilities positive ($a \geq b$), the general form $g(u) = u^2/(\gamma + u^2)$ does not allow patterning. Therefore, we consider $g(u) = u^3/(\gamma + u^3)$. Substitution into (4.29) yields the criterion for instability in this case:

$$Q = a\gamma^2 + a\frac{M^6}{N^6} + 2\gamma\frac{M^3}{N^3}(a - 3b) < 0 \quad (4.31)$$

which possesses exactly two positive real roots for M , for $b \leq a < 3b/2$ and no positive roots for $a > 3b/2$. A plot of (4.31) is shown in figure 4.25 for different values of a . We can deduce that, similarly to some of the cases previously analysed, the homogeneous steady state is stable for both low and high values of the total cell density, and unstable

for intermediate values. Additionally, equation (4.30) shows that as long as (4.31) is satisfied ($a < 2bu_0g'_0$), the largest positive eigenvalue corresponds to $k = \pi$. Therefore, the fastest growing mode is expected to have a wavelength $w = 2\pi/k = 2$. In other words, we expect the pattern to emerge to possess alternating high and low cell densities.

4.5.2 Bifurcation Analysis

Bifurcation analysis undertaken for the gradient model (M5) reveals similar behaviour to other models covered previously. According to the linear analysis of section 4.5.1 we expect that for a certain set of parameters, the homogeneous equilibrium will be stable for low and high total cell densities. When the homogeneity cannot be sustained, the system can evolve to a variety of stable steady states depending on the total cell density. Figure 4.26 below shows the bifurcation diagram for this model for a 3-site system. Once the threshold of total density M for instability is exceeded, two branches appear, corresponding to the (HLL) and (HHL) steady states. Similarly to the strictly local sensing case, there exists a steady state where all three of the sites are occupied by different cell densities (see figure 4.8). This steady state however, is always unstable and is not expected to be observed in a simulation. We expect that as the size of the domain increases, more inhomogeneous steady states arise, similarly to the cases previously described. Note that in this case, since we have used

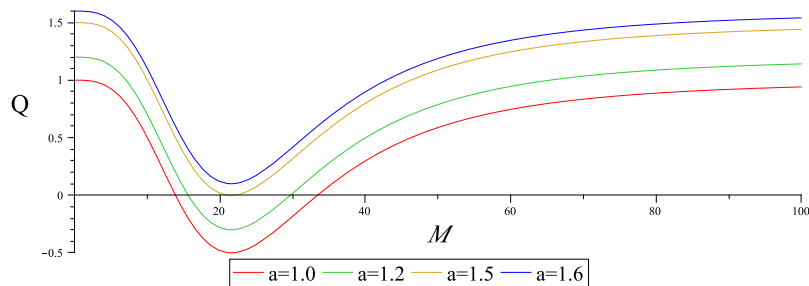


Figure 4.25: Plot to illustrate the criterion for instability of the homogeneous steady state, resulting from linearising the gradient model of section 3.5.5. The quantity Q is plotted against the total cell density for different values of parameter a . When $Q < 0$, the homogeneous equilibrium is unstable. Parameters: $b = 1.0$, $\gamma = 0.01$, $N = 100$. The critical value for a , above which the instability region does not exist is $a = 3b/2$.

$g = u^3/(\gamma + u^3)$, there is another family of steady states that correspond to at least one of the sites having negative cell density. These steady states are always unstable and do not make sense biologically. Therefore, the bifurcation analysis predicts that the system will evolve to a steady state where all sites are at either of two levels of cell density, and that the fraction of sites at high density will depend on the total cell density.

4.5.3 Numerical Simulations

As with the previous models, we conclude the analysis of the gradient model with a numerical investigation for systems comprised of multiple lattice sites. We begin by investigating the effect the total cell density has on the emerging patterns. To this end, the simulations depicted in figure 4.27 were undertaken. The results shown do not differ from the equivalent investigations undertaken for the models discussed previously. The bifurcation analysis of the previous section implies that as the total cell density M increases, the stable steady states consist of a larger fraction of sites at

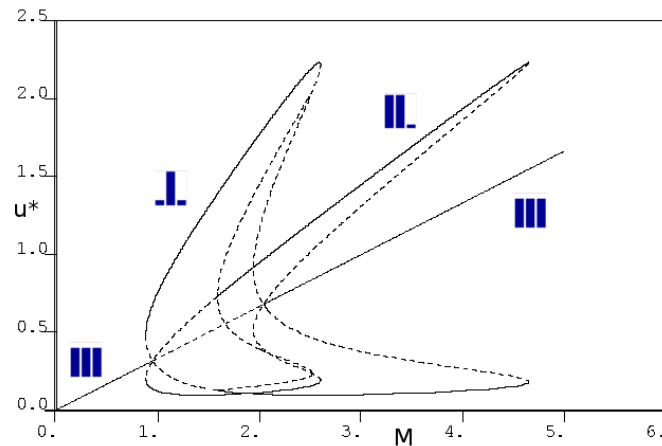


Figure 4.26: Bifurcation diagram for a system of 3 sites for the gradient model of section 3.5.5. The homogeneous steady state is stable for low and high total cell density. For intermediate values, the system can evolve to two inhomogeneous equilibria depending on the cell density. Both possible stable equilibria are comprised of two levels of cell density. A steady state where all three sites are in different cell densities exists, but is always unstable. Similarly to previous models, increasing the domain size yields more stable steady states. Parameters used $a = 1.1, b = 1.0, \gamma = 0.1$.

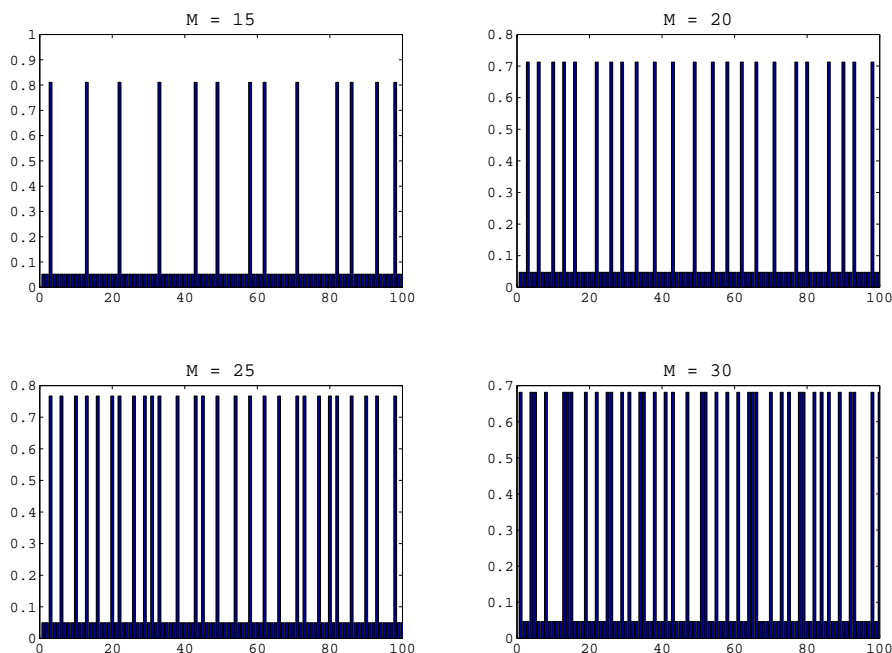


Figure 4.27: Numerical simulations for the gradient model of section (3.5.5). Figures depict the equilibria reached for various values of M , the total cell density. The fraction of lattice sites at high density is proportional to the total initial density. Parameters: $a = 1.1, b = 1.0, \gamma = 0.01$. Numerical details in A.2

high density. This is confirmed by the numerical simulations. While M is relatively low, we obtain patterns in which high cell density is found at isolated lattice sites. As the total cell density is increased, the low density gaps between peaks shrink, and only for relatively high values of u_0 , we observe neighbouring sites in high density.

The time evolution of the system for a particular choice of M is shown in figure 4.28. Initial perturbations from a uniform density are magnified and as expected from the linear analysis a pattern with alternating high and low densities emerges initially. The system rests at a steady state where a fine pattern is created.

4.6 Summary / Discussion

We have presented and analysed a variety of models for a cell-cell adhesion type process. The models were developed in chapter 3 with a cell described as occupying a single site on a discrete one-dimensional lattice. Cells perform one site jumps along the lattice with transition probabilities prescribed according to rules specific to each

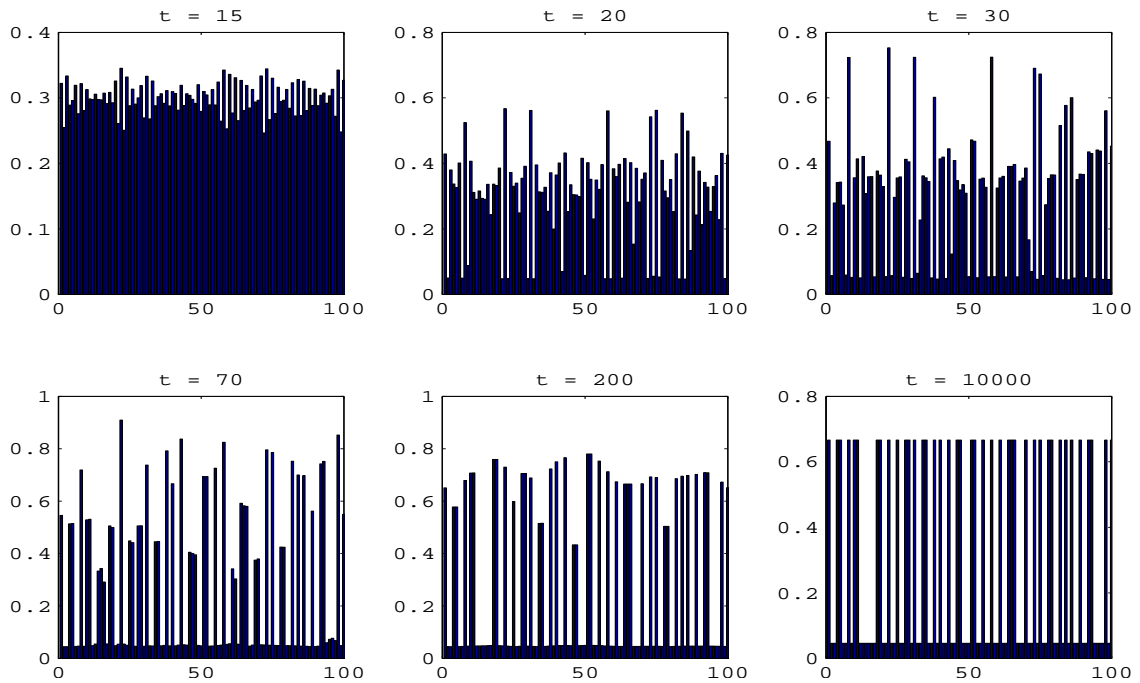


Figure 4.28: Time evolution of the gradient model for a total cell density $M = 30$. Parameters: $a = 1.1, b = 1.0, \gamma = 0.01$. Numerical details in A.2

model. Given the large flexibility of choices for the discrete model, we performed a comprehensive analysis of a variety of models based on different plausible forms for environmental interactions, models (M1)-(M5). The discrete models formed in this way, were taken to their continuum limit in order to yield the corresponding continuous model.

A consistent feature repeatedly found, however, is that the continuous models are generally ill-posed in the region where we expect patterning, and therefore lead only to either blow-up or convergence to homogeneity. Thus, any information inherent in the discrete model was lost after the approximation needed in order to derive the continuous model. Nevertheless they provided helpful insight into the requirements of the movement rules needed to generate distinct forms of behaviour. However, in terms of a suitable model for cell-cell adhesion, we focus on the discrete models

Analysis of the various discrete models is instructional since their relative simplicity offers insight into their potential for pattern formation and renders them amenable to explore. Furthermore, one can argue that at the level of a cell population, a discrete model is more appropriate: Supposing a cell diameter of $10 \mu m$, a lattice of 100

sites is equivalent to a domain of 1mm, which is a relevant length to biological spatial scales, particularly in embryonic development, cancer invasion etc. We have provided a comprehensive analysis of the different models allowing us to draw conclusions of their merit and disadvantages as a model for patterning, as well as make predictions and further our understanding for the development of a more complicated model.

Table 4.2 summarises the models’ capabilities in relation to the three fundamental properties we outlined in chapter 3 (see table 3.1), in which the models were introduced. In particular, we were interested in a model that: (i) is able to exhibit aggregating behaviour, (ii) produce multiple and regularly spaced distinct cell aggregates, and (iii) produce multiple cell width aggregations.

Notably, despite the different underlying assumptions on how the cells interact with the environment, all of the models (M1)-(M5) explored tended to generate very similar behaviour. In contrast, in the case of cell movement and aggregation due to chemical signalling studied by Othmer and Stevens [66], the precise mechanism of signal detection had a large impact in the behaviour of the system. Our results suggest that the general model of adhesion type processes is relatively robust against the precise mode of environment sensing.

Model	Section	Aggregation	Multiple/ Regularly spaced	Multicell width
(M1)	(3.5.1)	Yes	Yes if $a \neq 0$	No
(M2)	(3.5.2)	Yes	Yes	No
(M3)	(3.5.3)	Yes	Yes	No
(M4)	(3.5.4)	Yes	Yes if $a \neq 0$	Yes
(M5)	(3.5.5)	Yes	Yes	No

Table 4.2: Comparison of the models analysed in this chapter. The ability of the models to exhibit the three fundamental properties of table 3.1 is assessed: (i) All models are capable of aggregating behaviour. Global aggregation at a single lattice point is generally observed, unless a small random migration term $a > 0$ or a crowding term (model (M2)) are introduced. (ii) When global aggregation is prevented, multiple aggregations are produced. However, (iii) these aggregations are at the level of individual cells, with the exception of the “sensing opposite model” (model (M4)), in which a longer-range signalling regime is assumed.

A feature common to all the models considered is that their behaviour ultimately depends on competition between stabilising terms, and terms that favour aggregation. It is also shown that global aggregation to a single site occurs unless a small

random diffusion term, or a crowding term is included in the model. Inclusion of such terms generally results in regular patterns, i.e. patterns that are composed of multiple aggregations which are equally spaced. However, in nearly all the cases, these are patterns at the scale of individual cells which is often not the case for many biological instances of cell aggregation (for example sympathetic ganglia formation [44], which we discuss in chapter 6, see also figure 3.1). A notable exception is the model (M4) in which a cell decides to move away from the site adjacent to it (presented in section 3.5.4 and analysed in 4.4). Simulations of this model exhibit regular patterns composed of distinct small cell aggregations of a few cell widths. This phenomenon can be attributed to a “longer-range” element in this model. In the next chapter we take this a step further, exploring whether inclusion of long-range sensing can generate much larger cell aggregates, i.e. of the spatial scale corresponding to aggregates observed in biological instances of patterning.

Chapter 5

Sensing Radius

In this chapter we extend the models of section 3.5 to incorporate a “sensing radius”. This can be the physical boundary of a cell, which extends over several grid points, or can also be larger than the average cell radius if cell protrusions are taken into account. In general, the sensing radius defines a neighbourhood over which a cell can sense its environment.

As we have seen in the previous chapter, while all the “short-range” models generated aggregations, such aggregations were typically of the dimension of a single site, rather than the larger scale (multicell diameters) aggregations, characteristic of adhesive populations (figure 3.1). This is chiefly attributed to the short range signalling itself. In the “sensing opposite” model (M4), we found aggregations spanning multiple lattice sites, which we attributed to the somewhat long-range signalling regime incorporated into this model. We expect that by allowing cells to communicate over longer distances, the resulting patterns will more closely reflect real biological systems.

We have also seen in chapter 4 that the continuous models can become ill-posed. Furthermore, linear stability analysis showed that the condition for aggregation for each model converges to the condition for ill-posedness. The continuous models therefore are not capable of exhibiting the desirable aggregating behaviour. Consequently, an important question that arises is whether incorporating longer range information can result in a continuous model that allows aggregating behaviour while remaining well posed.

In the following sections, we first present the extended models before analysing

them as previously, i.e. through a combination of linear stability analysis, bifurcation analysis, and numerical simulations.

5.1 Model Derivation

5.1.1 Local Sensing

We begin by extending the strictly local sensing model presented in section 3.5.1. The general assumption for the earlier model is that a cell is only capable of detecting information at the site it occupies, and decides to move based on that information. Extending the model, we assume that now a cell extends over multiple grid points. In other words, the physical size of a cell is taken into account. With reference to section 3.5.1, we now write:

$$T_n^\pm = a + bf(U_n), \quad (5.1)$$

where $\bar{U}_n = \sum_{i=n-r}^{n+r} \frac{u_i}{2r+1}$ now denotes the average cell density within an area of sensing radius r centred at n . To describe an adhesive type process, in which cells are limited in their migratory capacity when localised with other cells, we assume f to be a decreasing function of U as in 3.5.1. Now the master equation (3.1) becomes:

$$\frac{\partial u_n}{\partial \tau} = (a + bf(U_{n-1}))u_{n-1} + (a + bf(U_{n+1}))u_{n+1} - 2(a + bf(U_n))u_n. \quad (5.2)$$

Expanding the right-hand side as before, we need the expansions of $f(U_n)$, $f(U_{n-1})$, and $f(U_{n+1})$ as a function of x to second order in h . These are as follows:

$$\begin{aligned} f(U_n) &\approx f(u) + \mu f' h^2 \frac{\partial^2 u}{\partial x^2}, \\ f(U_{n-1}) &\approx f(u) + \mu f' h^2 \frac{\partial^2 u}{\partial x^2} - h \frac{\partial f}{\partial x} + \frac{1}{2} h^2 \frac{\partial^2 f}{\partial x^2}, \\ f(U_{n+1}) &\approx f(u) + \mu f' h^2 \frac{\partial^2 u}{\partial x^2} + h \frac{\partial f}{\partial x} + \frac{1}{2} h^2 \frac{\partial^2 f}{\partial x^2}, \end{aligned} \quad (5.3)$$

where $\mu = \sum_{j=1}^r j^2 \frac{1}{2r+1}$ and f' denotes the first derivative of f with respect to u . Equation (5.2) becomes:

$$\begin{aligned} \frac{\partial u}{\partial \tau} &= \left(a + bf + \mu bf' h^2 \frac{\partial^2 u}{\partial x^2} - hb \frac{\partial f}{\partial x} + \frac{1}{2} bh^2 \frac{\partial^2 f}{\partial x^2} \right) \left(u - h \frac{\partial u}{\partial x} + \frac{1}{2} \frac{\partial^2 u}{\partial x^2} \right) + \\ &+ \left(a + bf + \mu bf' h^2 \frac{\partial^2 u}{\partial x^2} + hb \frac{\partial f}{\partial x} + \frac{1}{2} bh^2 \frac{\partial^2 f}{\partial x^2} \right) \left(u - h \frac{\partial u}{\partial x} + \frac{1}{2} \frac{\partial^2 u}{\partial x^2} \right) + \\ &- \left(2a + 2bf + 2\mu bf' h^2 \frac{\partial^2 u}{\partial x^2} \right) u, \end{aligned}$$

which collapses to

$$\frac{\partial u}{\partial \tau} = h^2 a \frac{\partial^2 u}{\partial x^2} + h^2 b \frac{\partial^2}{\partial x^2} (fu) + \mathcal{O}(h^4). \quad (5.4)$$

Note that this is exactly equation (3.10) of sec. 3.5.1. Finally, introducing the scaling $\tau = \lambda t$ and assuming that $\lim_{\substack{\lambda \rightarrow \infty \\ h \rightarrow 0}} \lambda h^2 = D$, as in section 3.5 we obtain the continuous model:

$$\frac{\partial u}{\partial t} = D \left(a \frac{\partial^2 u}{\partial x^2} + b \frac{\partial^2}{\partial x^2} (fu) \right) \quad (5.5)$$

or

$$\frac{\partial u}{\partial t} = D \frac{\partial}{\partial x} \left((a + bf) \frac{\partial u}{\partial x} + b \frac{\partial f}{\partial x} u \right) \quad (5.6)$$

Notably, the continuous model derived here (equation (5.6)) is exactly as for the strictly local continuous model derived in section 3.5.1 (equation (3.12)): The extra “information” provided by the non local sensing is lost as $h \rightarrow 0$ and we can expect similar behaviour (for the continuous model) as before.

5.1.2 Other models

The local models of chapter 3 have all been extended to incorporate a sensing radius. By undergoing similar procedures as in the preceding section, we were able to present the equivalent non-local discrete models and derive their continuous counterparts. These models are summarised in table 5.1. We present both the original local models of chapter 3 and their extended non-local version. The discrete models are given by the master equation (3.1): $\frac{\partial u_n}{\partial t} = T_{n-1}^+ u_{n-1} + T_{n+1}^- u_{n+1} - (T_n^+ + T_n^-) u_n$. Table 5.1 shows the transitional probabilities T_n^\pm from which the discrete models are derived.

The continuous models take the form: $\frac{\partial u}{\partial t} = \frac{\partial}{\partial x} [(A(u) + B(u)u)\frac{\partial u}{\partial x}]$. Functions $A(u)$ and $B(u)$ are tabulated for each case. Any difference between the local and nonlocal continuous models is also shown to highlight the effect of incorporating a sensing radius in the models. Note that the continuous models (R1)-(R5) can still be ill-posed despite the differences from their local counterparts (M1)-(M5).

Model	T_n^\pm	$A(u)$	$B(u)$	Difference
(M1)	$a + bf(u_n)$	$a + bf$	bf'	0
(R1)	$a + bf(U_n)$	$a + bf$	bf'	0
(M2)	$[a + bf(u_n)](1 - u_{n\pm 1})$	$a + bf$	$bf'(1 - u)$	0
(R2)	$[a + bf(U_n)](1 - u_{n\pm 1})$	$a + bf$	$bf'(1 - u)$	0
(M3)	$a + bg(u_{n\pm 1})$	$a + bg$	$-bg'$	$-2br \frac{\partial}{\partial x} (ug' \frac{\partial u}{\partial x})$
(R3)	$a + bg(u_{n\pm r\pm 1})$	$a + bg$	$-bg'(1 - 2r)$	$-2br \frac{\partial}{\partial x} (ug' \frac{\partial u}{\partial x})$
(M4)	$a + bf(u_{n\mp 1})$	$a + bf$	$3bf'$	$2br \frac{\partial}{\partial x} (uf' \frac{\partial u}{\partial x})$
(R4)	$a + bf(u_{n\mp r\mp 1})$	$a + bf$	$bf'(3 - 2r)$	$2br \frac{\partial}{\partial x} (uf' \frac{\partial u}{\partial x})$
(M5)	$a + b[g(u_{n\pm 1}) - g(u_n)]$	a	$-2bg'$	$-4br \frac{\partial}{\partial x} (ug' \frac{\partial u}{\partial x})$
(R5)	$a + b[g(u_{n\pm 1}) - g(u_n)]$	a	$-2bg'(1 - 2r)$	$-4br \frac{\partial}{\partial x} (ug' \frac{\partial u}{\partial x})$

Table 5.1: Summary of all local and nonlocal models. The local models of chapter 3 ((M1)-(M5)) are shown for comparison. The nonlocal models are denoted by (R1)-(R5). The transitional probabilities T_n^\pm are shown for the discrete models, and functions $A(u)$ and $B(u)$ for the continuous models. The last column shows the extra term (if any) generated by incorporating a sensing radius.

5.2 Local Sensing Model (R1)

In the following we analyse the extended long-range models presented in the preceding sections. We proceed using the techniques employed in chapter 4.

First, linear stability analysis is undertaken, in order to determine the conditions under which stable heterogeneous solutions exist, and extract some information about the form of the patterns expected to be observed. Linear stability analysis is performed for both the discrete and continuous versions of the models in order to identify potential differences. Similarly to the short range models we linearise around the homogeneous steady state. $u_0 = \frac{1}{N} \sum_{i=1}^N u_i$ is the homogeneous steady state for the discrete model, where N is the total number of sites in the lattice, and u_i , the cell density at site i . The homogeneous steady state for the continuous model studied on a one-dimensional line of length L , with $u(x)$ being the cell density at x is given by: $u_0 = \frac{1}{L} \int_0^L u(x) dx$. The stability of this steady state in both cases depends on the total initial cell density, for a given set of parameters.

A bifurcation analysis on lattices of small size is then presented for each case. We study the various models using the bifurcation software AUTO [25] and show how the steady states and their stability vary according to the total cell density available. Finally, numerical simulations for larger domains were performed to reveal aspects of the models that are analytically intractable.

5.2.1 Linear Analysis

In this section we perform linear stability analysis for the spatially extended equivalent of the model (M1). We have seen that the continuous model (R1) derived is identical to the strictly local sensing model (M1) derived in section 3.5.1. Therefore, linear analysis of the continuous model (R1) yields the exact same results as in section 4.1.1. In particular, the model becomes ill-posed in the region where the homogeneous steady state is unstable. Linear stability analysis performed on the discrete model, however, reveals a different situation. The dispersion relation now reads:

$$\lambda = 2(a + bf_0)(\cos k - 1) + \frac{2bu_0f'_0}{2r + 1} \left(\cos[(r + 1)k] - \cos(rk) \right) \quad (5.7)$$

where f_0 and f'_0 are the values of f and its first derivative evaluated at u_0 , the homogeneous steady state, and λ and k are the eigenvalues and wavenumbers of the system as before. When $r = 0$, this reduces to:

$$\lambda = 2(\cos k - 1)(a + bf_0 + bu_0f'_0) \quad (5.8)$$

which is consistent with the dispersion relation for the strictly local case (eq. (4.9)), as expected. As shown in section 4.1.1, in the case of the strictly local sensing scenario ($r = 0$) the uniform steady state can be either stable or unstable for every wavenumber. However, if $r \neq 0$ there is a range of unstable wavenumbers: figure (5.1) depicts the dispersion relation for $r = 0, r = 2, r = 5$, and $r = 10$. The common feature in the case $r \neq 0$ is that the modes corresponding to larger wavelengths are unstable

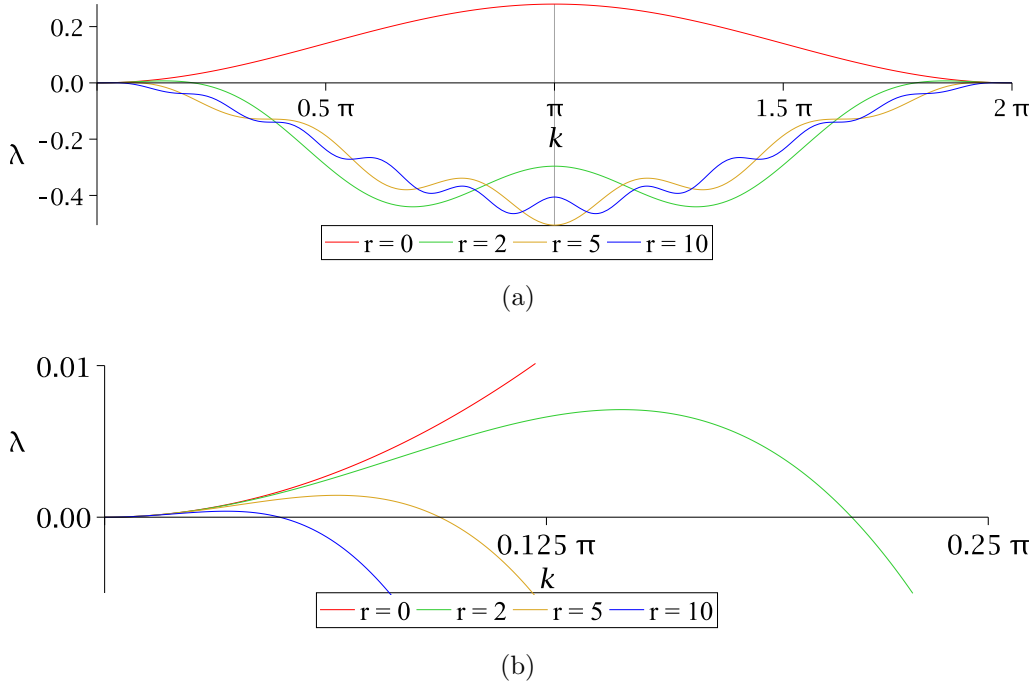


Figure 5.1: Dispersion relation for the long-range discrete local sensing model. The eigenvalues of the system λ are plotted as a function of the wavenumber k for different values of the sensing radius. (a): Plot for the range $k \in [0, 2\pi]$. Note that the range of values of $k > \pi$ corresponds to wavelengths of less than two cells and are therefore not taken into account. The common feature of all three plots with $r \neq 0$ is that low wavenumbers (large wavelengths) are unstable. (b): In order to further illustrate this point, the dispersion relation is plotted for $k \in [0, \pi/4]$. We plot equation (5.7) with $f = \frac{1}{1+qu^2}$, and $u_0 = M/N$ is the homogeneous steady state. Parameters used: $b = 1, q = 100, M = 30, N = 100, a = 0.01$.

while lower wavelengths are stable. This is in contrast to the strictly local sensing model ($r = 0$), where only the shorter wavelength patterns are favoured. One could intuitively expect therefore to obtain patterns with larger cell aggregates.

5.2.2 Bifurcation Analysis

In this section we perform bifurcation analysis on small sized grids, as was done in the strictly local case. Note that in the long range sensing, while a five sites system provides some level of detail, in order to study the different steady states possible and compare to the case $r = 0$, we would need to study systems with even more sites. This however poses limitations, since larger systems quickly become analytically intractable. Therefore, such analysis will be limited to numerical simulations.

Case I: $a = 0$.

We begin by first examining the case where the random diffusion component is set to zero. In order to investigate the behaviour of the system when the sensing radius $r = 1$, we study a line of 5 sites. The resulting bifurcation diagram is shown in figure 5.2b, next to the corresponding diagram for the strictly local case ($r = 0$), replotted here in order to facilitate comparison. As the total density exceeds a critical value the homogeneous steady state becomes unstable and six further branches appear. The stable branches correspond to an inhomogeneous steady state to which the system evolves. Figure (5.3b) demonstrates the numerical simulation performed showing the steady state reached: *(HMMLL)*. Also plotted (figure 5.3a) is the steady state reached for the case where $r = 0$, showing global aggregation at one site.

Case II: $a > 0$.

Figure 5.4 below depicts the bifurcation diagram obtained for a system comprised of five sites in the case where $a \neq 0$. The inhomogeneous stable steady state corresponds to the case depicted in figure 5.3. That is, three different levels of cell density, as in the case where $a = 0$. The critical difference between here and above is that, as in the strictly local case, the homogeneous steady state is stable for both high and low cell densities.

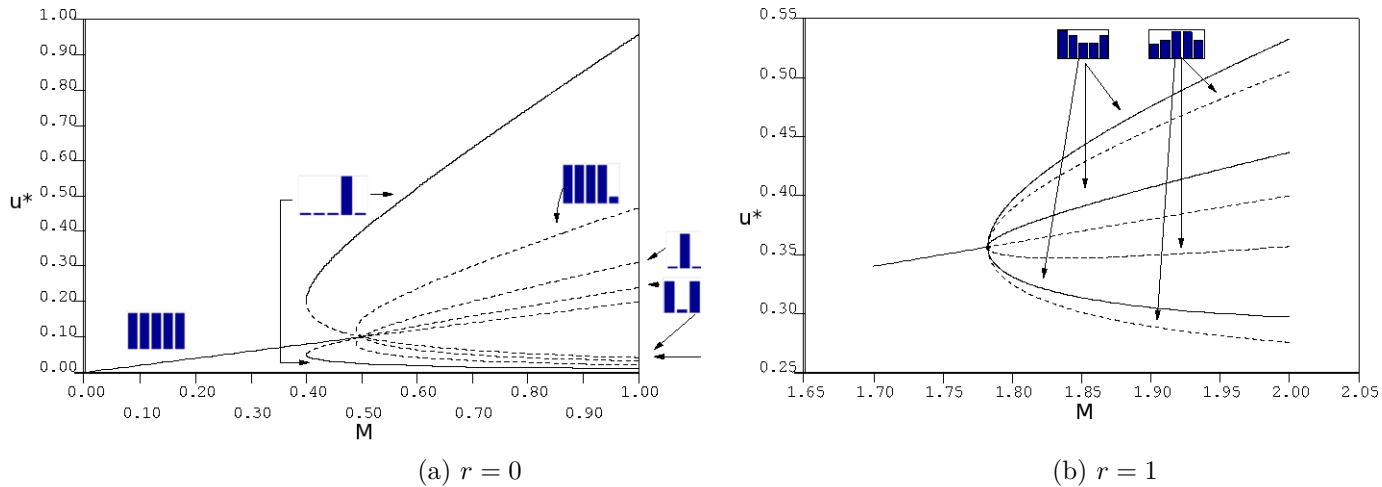


Figure 5.2: Bifurcation diagrams for the local sensing model. (a) Bifurcation diagram for $r = 0$, presented in section (4.1.2), to allow comparison. (b) Bifurcation diagram for the extended model, with $r = 1$. The stable branches (solid lines) correspond to the steady state shown in fig. 5.3b. Parameters: $a = 0.0, b = 1.0, q = 100$.

The main conclusion to be drawn from the bifurcation analysis shown in this section is that it demonstrates, despite its limitations discussed above, that introduction of nonlocal sensing allows the possibility of nonlocal aggregations.

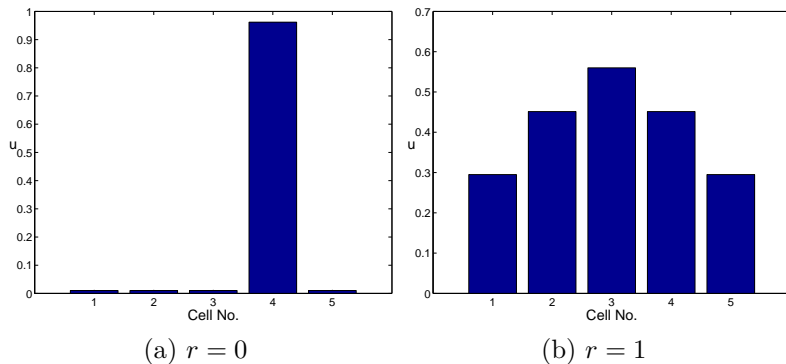


Figure 5.3: Simulations in 5-site domains for the local sensing model with (a) $r = 0$, strictly local sensing and (b) $r = 1$, extended model. Parameters as in figure 5.2 with $M = 1.0$ in (a) and $M = 2.0$ in (b). The system was initially given a small random perturbation from homogeneity ($\sim 0.5\%$).

5.2.3 Numerical Simulations

Case I: $a = 0$.

Simulations for various lattice sizes were performed with the same parameters as given in figure 5.2, and for different values of the radius r . In section 5.2.2, a bifurcation analysis was performed for $r = 1$ for a 5-site lattice. It was shown that when the homogeneous steady state becomes unstable, three stable branches appear, corresponding to three different levels of cell density, such that the resulting pattern has the characteristics of a gradient of density. We expect more stable branches to appear as the domain size increases. To confirm this, simulations for lattices of 5, 7, 9, and 15 grid points were performed for the case where $r = 1$. The results are shown in figure 5.5. As can be seen, the patterns emerging are gradients of cell density. In the 5-site case, there are 3 levels of cell density corresponding to the stable branches of figure 5.2b in section 5.2.2. As we increase the size of the domain, the density levels that compose the equilibrium reached increase as well.

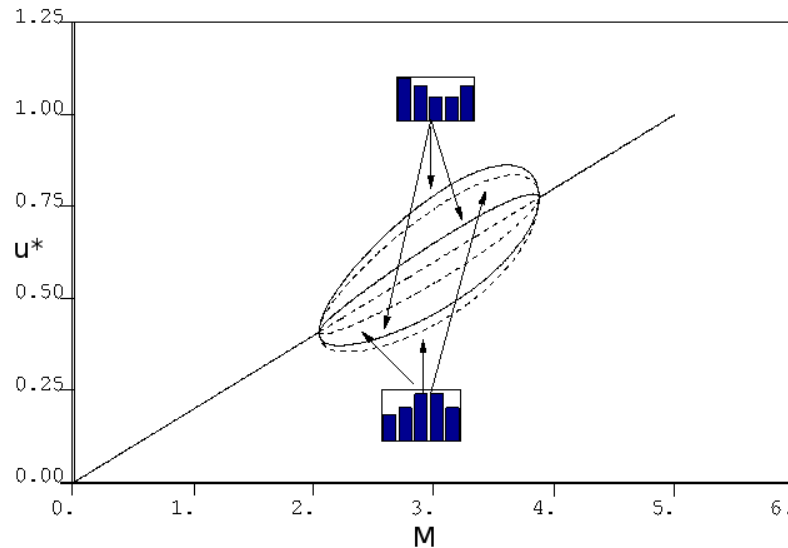


Figure 5.4: Bifurcation analysis of the extended local sensing model, when a small random diffusion element is added ($a \neq 0$). A 5-site system is considered. The homogeneous steady state is stable for both low and high total cell density. For intermediate values the system evolves to a steady state comprised of three levels of cell density (HMMLL). In the same region, an unstable steady state exists (HHMML). Parameters: $a = 0.001$, $b = 1.0$, $q = 100$.

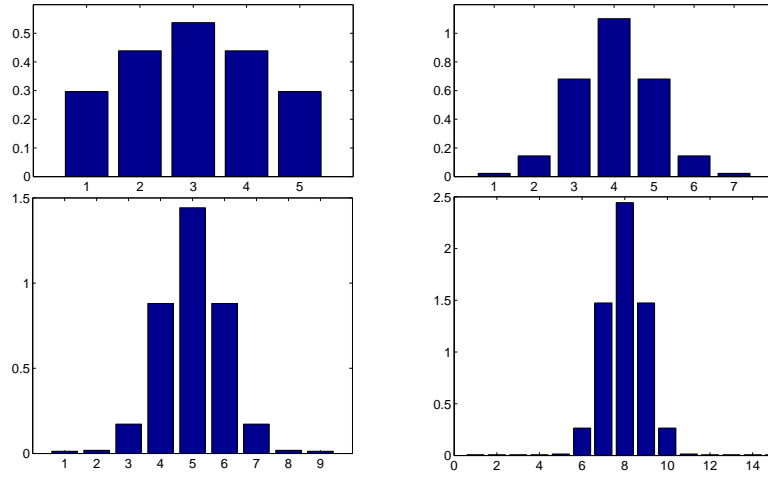


Figure 5.5: Numerical simulations for the extended local sensing model. The pictures show how domain size affects the final pattern. Lattices of 5, 7, 9, and 15 sites are shown. As the domain size increases the gradient-like patterns that emerge involve more cells.

Simulations performed in a 100-site lattice showed the same coarsening type behaviour observed for $r = 0$. That is, starting from small perturbations of the homogeneous equilibrium, we observe multiple aggregations appearing which decrease in number until one dominates and the system is at equilibrium. Significantly different, however is that the sensing radius allows smoother and multiscale aggregates to appear instead. Figure 5.6 depicts the evolution of the system.

In order to study the effect the sampling region has on the resulting pattern, we have performed simulations over a range of values of the sensing radius. Figure 5.7 shows simulations carried out for $r = 1, r = 2, r = 3$, and $r = 5$. The evolution of each system has the same characteristics mentioned above, and we can observe that as the radius increases, the resulting aggregates become distributed over an increasing number of lattice sites.

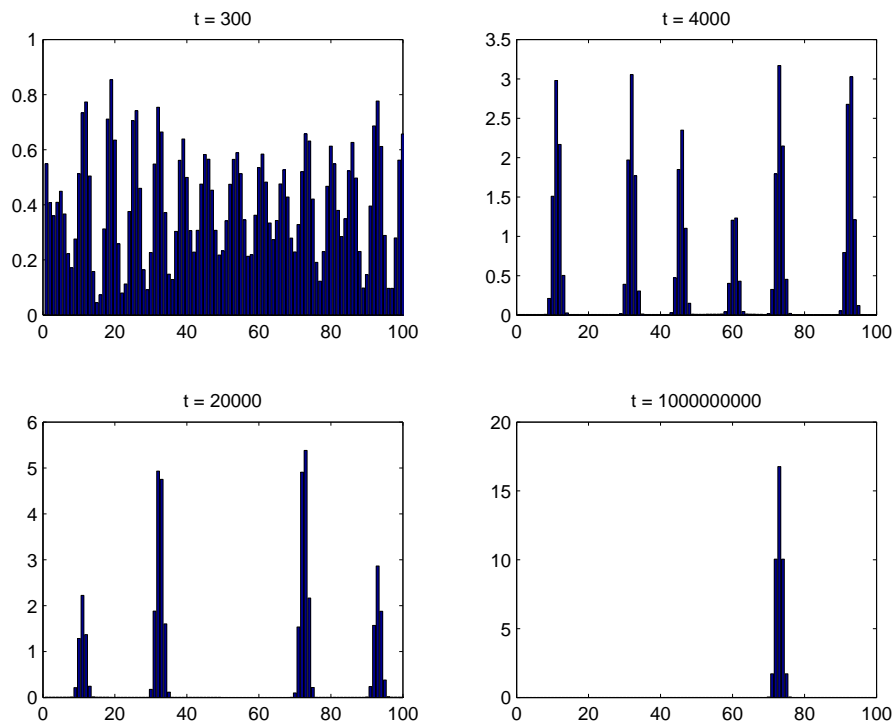


Figure 5.6: Time evolution of the extended local sensing model with no random migration. The system was started from a slightly perturbed uniform cell density. The perturbations are magnified initially and peaks appear. The peaks subsequently merge and become broader, until the system finally rests to a steady state where a single aggregation exists. Parameters: $r = 1, b = 1.0, q = 100, M = 40$. Numerical method details in A.2.

Case II: $a > 0$

The following set of simulations were performed in order to reveal the effect of adding a small random diffusion component to the system. Figure 5.8 depicts the patterned steady states reached for different values of the sensing radius. All simulations were performed on 200-site domains, with the same parameters, using periodic boundary conditions. Initially the system is perturbed from a homogeneous distribution. We can observe that by adding a random migration element to the system, global aggregation can be prevented. As seen in the analyses of the short range models of chapter 4, choosing $a > 0$ results in multiple-peaked patterns emerging, since the interplay between diffusion and the attraction of cells by adhesive forces leads to a stable equilibrium. The final patterns are formed by distinct cell aggregations that occupy more space and are fewer as the sensing radius is increased. If a is further increased,

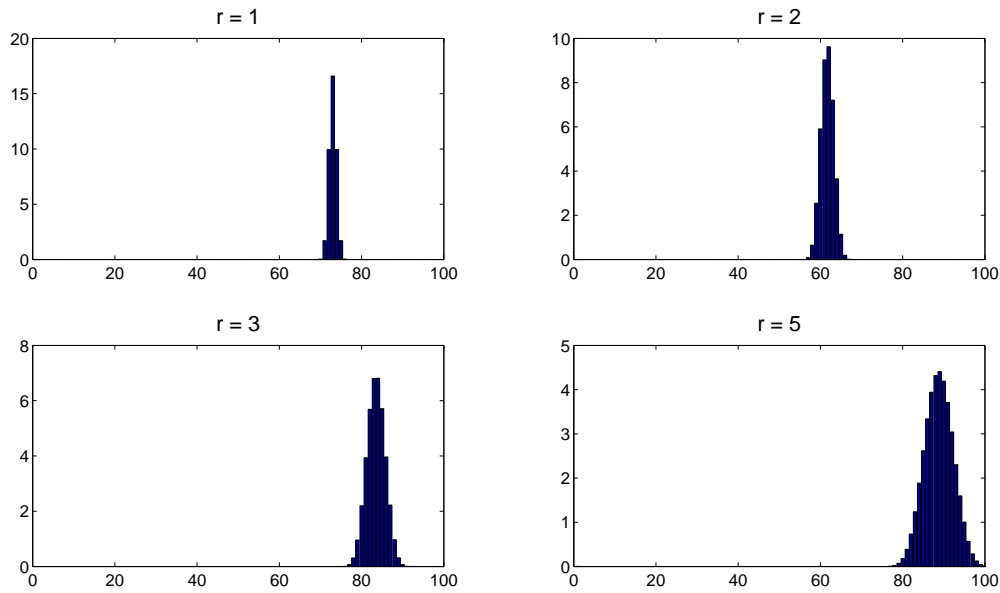


Figure 5.7: Effect of the sampling radius on the system. All figures show the systems at equilibrium. Global aggregation is observed for every value of the sensing radius r . As r increases, the aggregates formed become distributed over an increasing number of lattice sites. Parameters: $q = 100, b = 1, M = 40$. Numerical method details can be found in A.2

the result is a pattern with more and broader aggregates. Furthermore, the difference in cell density between low and high density regions of the final pattern decreases with increasing a .

Time evolution

In order to study the time evolution of the system further, we have examined the system with $r = 3$ using the same parameters as in figure 5.8, using the initial condition: $u_i(0) = \frac{M}{N} - 0.01 \cos(\frac{4\pi}{N}i)$. We have seen that a stable inhomogeneous solution comprised of two cell aggregates exists in this case (figure 5.8). The initial condition described above provides a bias towards this steady state. The two small peaks created initially, shown in figure 5.9 (top left), are magnified as the simulation progresses. However, each of the two peaks breaks up into smaller aggregates, and a pattern with 8 aggregates is formed. Subsequently, these aggregates begin to merge, producing a pattern comprised of four cell-aggregations. Finally, after further merging, a stable steady state with two aggregations is formed. The linear analysis for this system, pre-

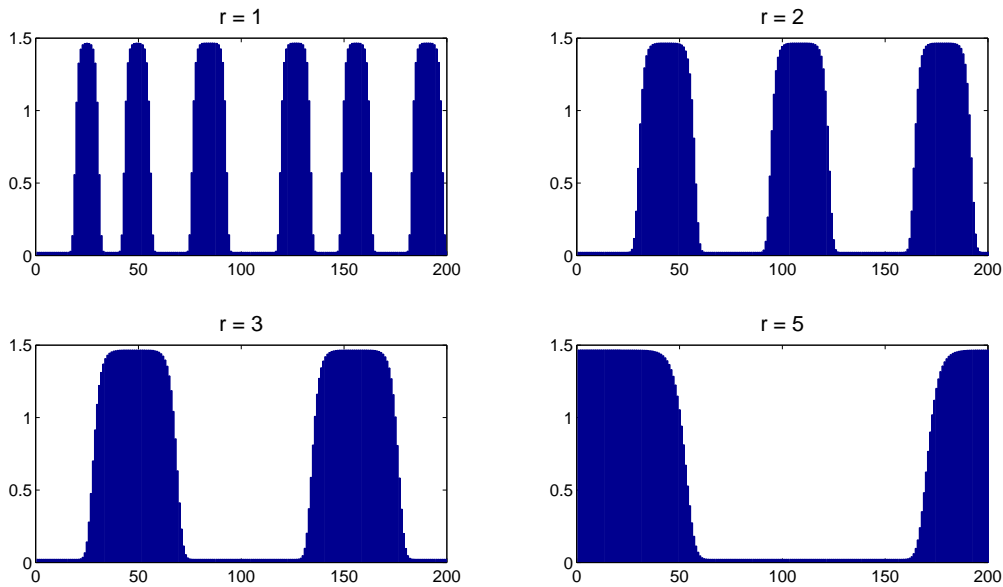


Figure 5.8: Effect of the sensing radius on a system of 200 lattice sites with a small random diffusion element ($a \neq 0$). The stable inhomogeneous equilibrium is comprised of multiple aggregations in this case. As we allow the sensing radius to include more sites, the final aggregations become fewer and larger. Parameters: $b = 1$, $a = 0.01$, $M = 120$. For numerical method details, see A.2.

dicts that the homogeneous steady state is stable for modes with wavelengths $w < 16$ and unstable to all other modes. According to the linear analysis, the fastest growing mode corresponds to a wavelength $w = 22$, which corresponds to the pattern of 8 cell aggregations initially seen in the simulation. This time evolution is persistent and observed in simulations with different initial conditions. In addition, simulations for different parameter sets show that the fastest growing mode is the one observed initially, as predicted by the linear analysis, but the systems eventually evolve to a pattern of larger wavelength.

The bifurcation analysis for both the long range model with $r = 1$ (figure 5.4) and the short range case (figure 4.6) give an indication for this behaviour. They reveal the existence of numerous unstable inhomogeneous steady states, the number of which increases with the available total cell density. Furthermore, they seem to suggest that, for given total cell mass, there are at most two families of steady states that are stable. Transiently, saddle points of multiple aggregations, like the one observed here, attract solutions, and after a relatively long time period, the effect of coarsening

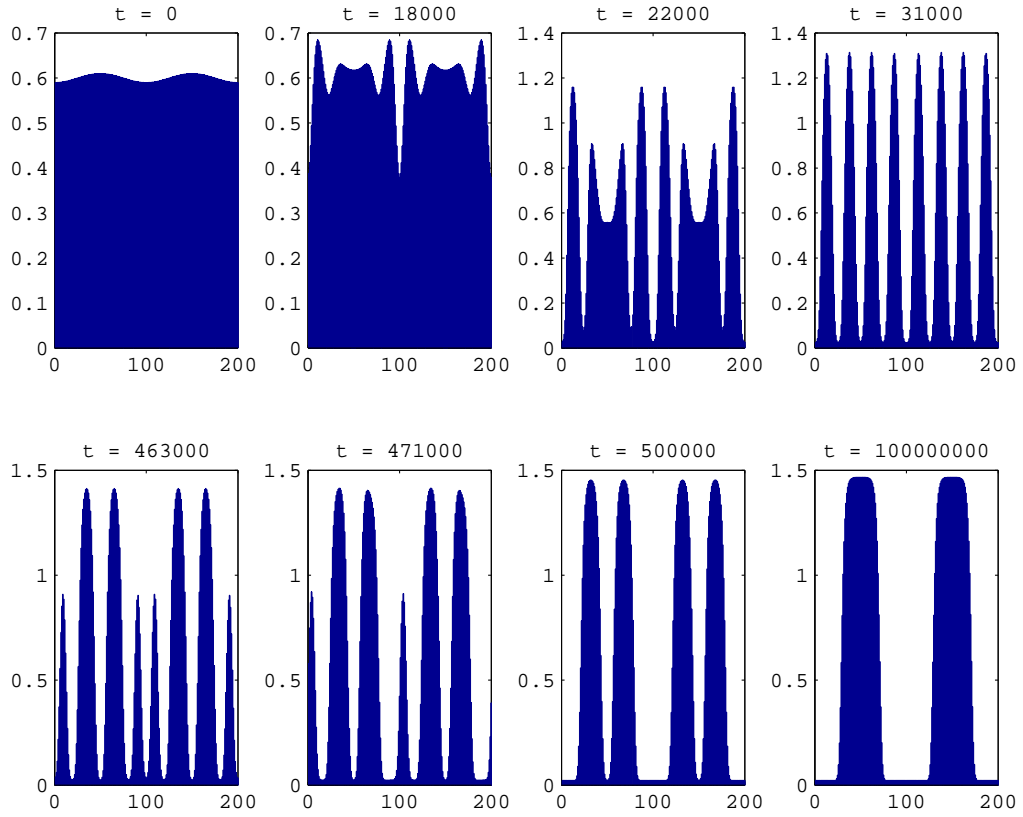


Figure 5.9: Time evolution of the long-range local-sensing model with sensing radius $r = 3$ in a 200-site domain. The initial condition $u_i(0) = \frac{M}{N} - 0.01 \cos(\frac{4\pi i}{N})$ forces two small peaks to appear which become magnified. A patterned solution with 8 peaks appears transiently. The system undergoes a process of coarsening of the cell aggregates and finally rests at a stable equilibrium with two distinct aggregations. Parameters: $b = 1, a = 0.01, M = 120$.

of cell aggregates takes place, until the system reaches a stable steady state (here a 2-peaked solution, $w = 100$ in this case) of fewer aggregates.

From a biological point of view, this behaviour can be explained as follows: In a randomly distributed population of cells, small aggregations start to form relatively quickly as adhesive bonds form between cells located within a small neighbourhood. After these initial aggregations are formed, they attract one another, but this process is much slower due to the competing forces exerted on cells by adhesion bonds that are already formed. Ultimately, the small cell aggregations move towards each other and form larger aggregations located in sufficiently large distances such that an equilibrium is reached.

Pattern dependence on total cell density

The total available cell density also plays an important role in the form of the final stable patterns. In order to illustrate its effect, figure 5.10 was plotted, showing the stable equilibria reached for systems of 200 sites in the same parameter regime for four values of the total cell mass M .

It is demonstrated that the number of cell aggregates that compose the final steady state increases with cell density. This is an effect also observed in the strictly local sensing case, and can be attributed to the assumptions of the model. At relatively low cell densities, the random diffusion component becomes more significant. Therefore, cells are able to move more freely along the grid. Once aggregations start to form, they attract more cells. Subsequently, merging and coarsening of the peaks occurs, and the number of aggregates is decreased. Since cell movement is not significantly constrained, small density differences in the remaining peaks will cause the cells to be attracted to the higher density regions over time. Increasing the total cell density is shown to have a similar effect as when decreasing the random migration term, since competition between the adhesive attraction forces and diffusion determines the

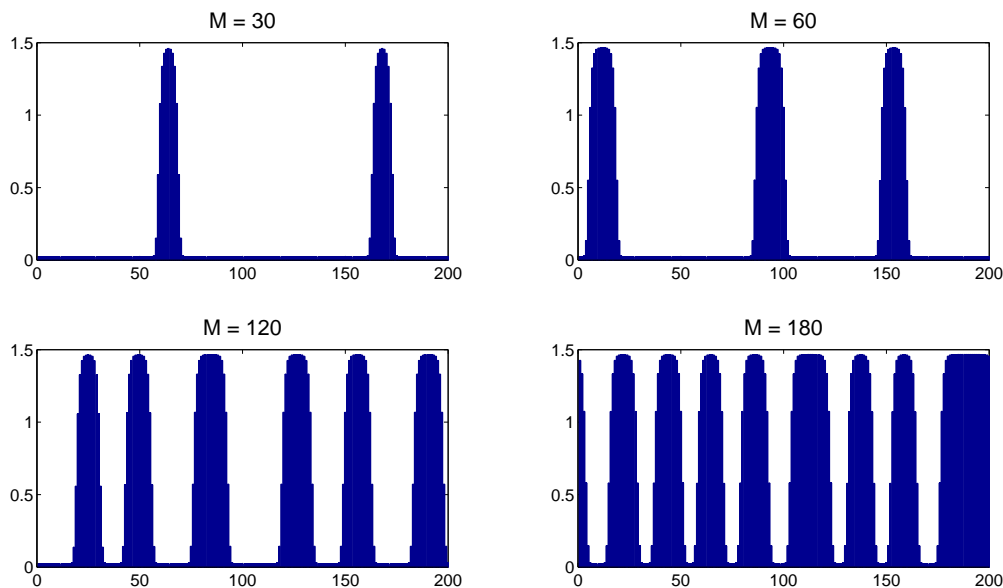


Figure 5.10: Effect of the total cell density on the final pattern reached. The number of cell aggregations observed at equilibrium rises with the number of available cells. Parameters: $b = 1$, $a = 0.01$, $r = 1$.

form of the resulting pattern. The linear analysis shows that increasing the total cell density results in the solution of $\lambda(w) = 0$ as well as the fastest growing mode moving towards higher values of w . This however, does not greatly affect the final pattern obtained since, as discussed earlier, it is the large wavelength steady states that are stable.

Minimum and Maximum cell density

It is also interesting to note another feature revealed by the simulations presented: As can be observed by the time-evolution simulation (figure 5.9), the aggregations formed are growing initially until they reach a certain maximum level of cell density. During the course of the simulation, aggregations merge, but this results in broader aggregates while the maximum cell density at any one site remains constant. The same holds for the minimum cell density a single site can accommodate. Furthermore, as can be seen in figures 5.8 and 5.10 both the maximum and minimum cell density are independent of the sensing radius and the total cell density as long as the remaining parameters are fixed. Simulations were carried out in which cells were added at a system that was already at an inhomogeneous equilibrium. The additional cell density was distributed within the previously established aggregates and the resulting pattern consisted of broader aggregates, but both the maximum and minimum cell density were not altered.

Insight to this phenomenon can be gained by focusing on the bifurcation analysis of the strictly local model. Figure 4.6 shows the bifurcation diagrams obtained for systems of 2, 3, 4, and 5 sites, in absence of a sensing radius. One can observe that every branch of the bifurcation diagram reaches the same maximum and minimum values, which seem to be independent of the lattice's size. Furthermore, the change in stability for every branch corresponds to the same values of u . As the lattice size is increased, more branches emerge corresponding to different steady states. For large lattices, these branches are sufficiently close to each other such that the range of values of the total cell mass M in which each equilibrium dominates becomes significantly small. Thus, as the total cell density increases, the system switches from one family of steady states to another, so that both the maximum and minimum cell density at any

site remain almost constant. It should be noted that this behaviour is only possible for $a \neq 0$ since, as we have demonstrated, global aggregation occurs otherwise and the maximum cell density can grow as large as the total cell density allows.

Size dependence with sensing radius

We have previously discussed the effect of the magnitude of the sampling radius to the final patterns for the case where no random diffusion term was taken into account (see figure 5.7). As discussed above, introducing a small random migration element into the system prevents global aggregation phenomena and results in wider cell aggregations. In the $a = 0$ case, the size of the unique aggregation is the minimum allowed by the sensing radius, irrespectively of the total cell density.

Figure 5.11 is a set of graphs that show the relationship between the size of the aggregations formed (S) and the sensing radius (r), for $a \neq 0$. We define the aggre-

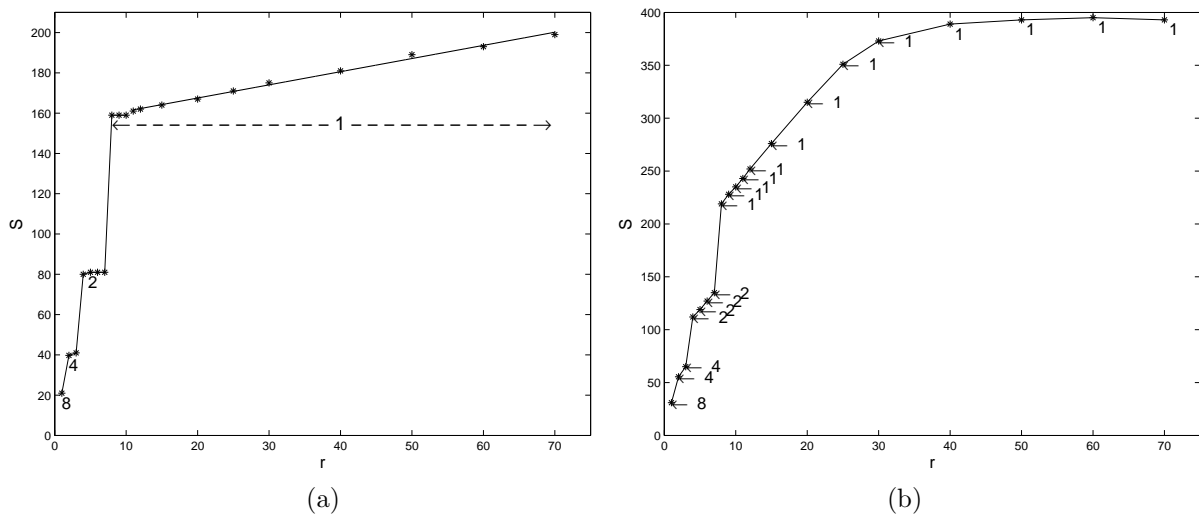


Figure 5.11: Plots of the aggregation size S as a function of the sensing radius r for the two different definitions of S explained in the main text. The number of aggregations formed in each case are indicated. All data points were obtained from numerical simulations with parameters: $a = 0.05$, $b = 1.0$, $q = 100$, $M = 100$, $N = 400$, and show the aggregation sizes at equilibrium. S is shown to be a piece-wise linear function of r . S grows linearly with r for r -values that produce the same number of peaks.

gation size S as the total number of lattice sites at which the cell density exceeds a certain threshold. We can choose this threshold to be M/N , the homogeneous steady state, or we can exclude from the aggregation the sites at densities within a set toler-

ance of the minimum cell density within the lattice. In the first graph (fig. 5.11a), S is defined as the number of sites at density $u \geq M/N$, whereas in the second graph (fig. 5.11b), S is the sum of sites at densities $u \geq u_{min} + 10^{-4}$, where u_{min} is the minimum cell density. The data plotted refers to the size of one of the aggregations in the cases multiple peaks exist. The number shown at each data point indicates the number of peaks formed at equilibrium for each case (e.g. for $r = 2$ we obtain 4 identical aggregations).

As expected, the size of the aggregations rises with r . We can observe that S increases linearly within ranges of r that result in the same number of aggregations, whereas S increases abruptly when the change in r alters the form of the equilibrium reached. In this case however, the total number of sites above the set threshold actually decreases. As r is increased, the aggregations grow in size until their magnitude renders the previously stable steady state unstable. Therefore, the peaks merge and produce a pattern composed of fewer and more compact aggregates. The piecewise linear nature of $S = S(r)$ is more apparent in figure 5.11b, and in figure 5.11a for large values of r . That behaviour cannot be captured in the case of figure 5.11a when small steps in r are considered due to the stricter definition of S . However, in the case of figure 5.11b, linearity breaks down at high r values, since almost every site in the domain is considered a part of the aggregation.

In conclusion, the long range model shares a number of properties with its short range counterpart, in the sense that competition between two terms in the models determine the evolution of the system. In the case where no random diffusion is taken into account ($a = 0$), both models exhibit global aggregation. However, the long range sensing version of the model is capable of producing relatively large distinct cell aggregations which are more relevant from a biological point of view. In contrast, the strictly local model gives rise to patterns of alternating high and low cell density.

5.3 Other Models

In this section we use the techniques applied in chapter 4 and section 5.2 in order to investigate the non-local models (R2)-(R5) derived by extending the models (M2)-

(M5) of chapter 3 (see table 5.1). Extensive analysis of the equivalent local models has been presented in chapter 4. The non-local models analysed in this section share many of their properties and behaviours with the long-range local sensing model (R1) analysed in the previous section. Here we will restrict our analysis to the basic details of the remaining models, and show some representative results.

5.3.1 Linear Analysis

Linearisation of the continuous models (R2)-(R5) revealed that, similarly to the models (M1)-(M5) analysed in chapter 4, the patterning condition in each case corresponds to the region in which the models are ill-posed. Therefore, incorporating non-local information in the models under this framework was not sufficient in producing a well posed continuous model that allows aggregating behaviour. For this reason we limit our analysis to the discrete models.

We have linearised the discrete long range models (R2)-(R5) around the homogeneous steady state. The dispersion relation for each model is given by:

$$\lambda = \begin{cases} 2(a + bf_0)(\cos k - 1) + \frac{2bu_0f'_0}{2r+1}(1 - u_0)\left(\cos[(r+1)k] - \cos(rk)\right), & \text{(R2)} \\ 2(a + bg_0)(\cos k - 1) + 2bu_0g'_0\left(\cos(rk) - \cos[(r+1)k]\right), & \text{(R3)} \\ 2(a + bf_0)(\cos k - 1) + 2bu_0f'_0\left(\cos[(r+2)k] - \cos[(r+1)k]\right), & \text{(R4)} \\ 2a(\cos k - 1) + 4bu_0g'_0\left(\cos(rk) - \cos[(r+1)k]\right), & \text{(R5)} \end{cases} \quad (5.9)$$

where, λ is the temporal growth, k is the wavenumber, u_0 denotes the homogeneous steady state, and r is the sensing radius. f_0, g_0, f'_0 and g'_0 are the functions modelling adhesive processes for each case and their first derivatives, evaluated at u_0 . For $r = 0$, equations (5.9) reduce to the dispersion relations for the local models, as to be expected.

The most notable common characteristic of equations (5.9) is that they predict the existence of a range of unstable modes. In contrast, the dispersion relations obtained for the equivalent local models revealed that the homogeneous steady state is either stable or unstable to all modes. To further illustrate this property, we have plotted λ against the wavelength $w = 2\pi/k$, in figure 5.12, using the same functions f, g as in

chapter 4.

Figure 5.12a shows the dispersion relation for the extended local sensing model with crowding effects (R2), in which we observe the same behaviour qualitatively as in the simpler model that does not include crowding effects. Similarly to the local sensing case, we note that including crowding effects results in a smaller instability region, due to the $1 - u_0$ term of equation (5.9 (R2)). The fastest growing modes correspond to relatively large wavelengths ($w = 2\pi/k$). However, we should note that for a certain range of parameters, and for large values of the total cell density, the reverse can be observed. That is, the homogeneous steady state becomes unstable for short wavelength modes.

In contrast, we can observe that in each of the three remaining models (R3)-(R5)

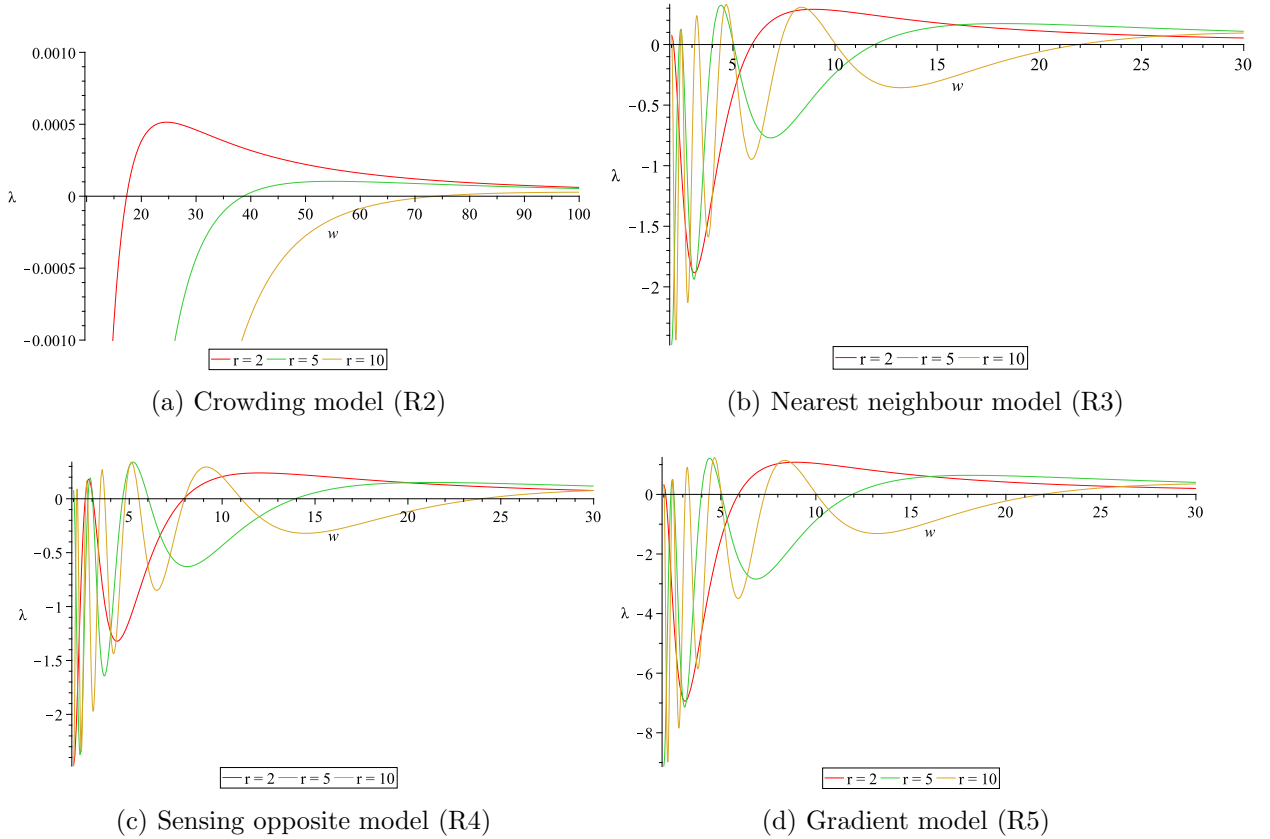


Figure 5.12: Plots of the eigenvalue λ against the wavelength w for the non-local models (R2)-(R5). In the crowding model case long wavelength modes are unstable, while in the remaining three cases there exist intermittent ranges of unstable modes. Parameters: (a): $a = 0.01, b = 1.0, q = 100, u_0 = M/N = 0.3$, (b): $a = 0.1, b = 1.0, \gamma = 0.01, u_0 = M/N = 0.05$, (c): $a = 0.1, b = 1.0, q = 100, u_0 = M/N = 0.2$, (d): $a = 1.1, b = 1.0, \gamma = 0.01, u_0 = M/N = 0.01$.

and under the chosen parameter regimes, the homogeneous steady state is unstable to an intermittent range of values of the wavenumber k . Therefore, under certain circumstances dictated by the parameters used, different modes can become unstable. Both short and long wavelength modes are growing, in contrast to the cases previously discussed where either exclusively short or exclusively long wavelengths are favoured. By increasing the sensing radius, we allow for more modes to become unstable.

5.3.2 Bifurcation Analysis

Figure 5.13 shows the bifurcation analysis undertaken for the long-range crowding model (R2) and the closest neighbour model (R3) for systems of 5 sites with sensing radius $r = 1$.

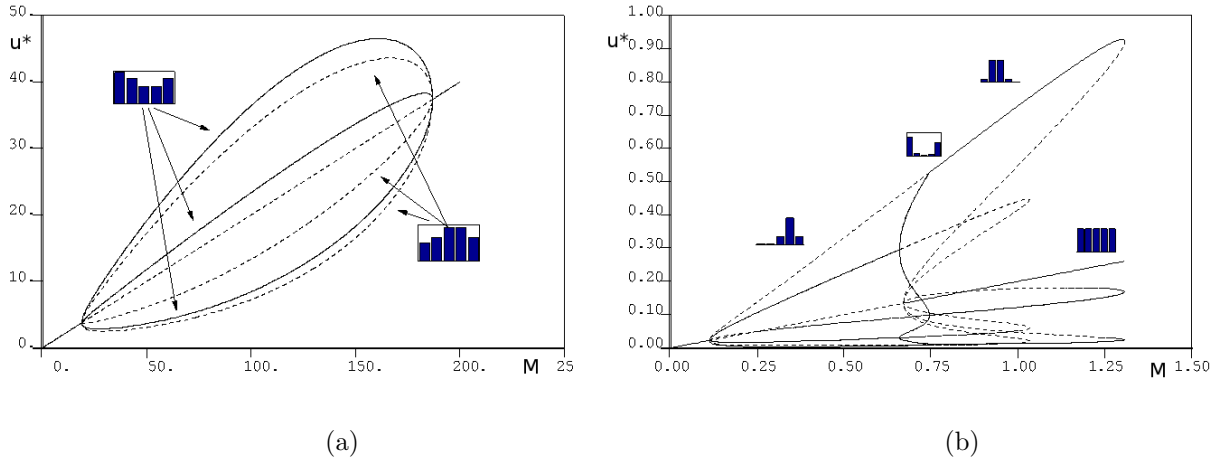


Figure 5.13: Bifurcation diagrams for: (a) the long-range sensing model with crowding effects, and (b) the extended neighbour sensing model. The homogeneous equilibrium is stable for both low and high cell densities in both cases. (a): Stable inhomogeneous steady states, existing for intermediate values of M , are of the form: $(HMMLL)$. Unstable equilibria of the form $(HHMML)$ exist in the same region. Parameters used: $a = 0.001, b = 10, q = 100$. (b): Three forms of inhomogeneous equilibria exist: $(HMMLL)$, $(HHMML)$, and one in which all 5 sites are at different cell density levels. Out of these, the former is expected to arise from simulations since it is stable in the area of instability of the homogeneous steady state. The two remaining are stable in the region where the homogeneous equilibrium is also stable, and are therefore expected to arise should the initial conditions favour them. Parameters used: $b = 1, \gamma = 0.01, a = 0.1$.

As in chapter 4, the bifurcation diagram of figure 5.13a, for the model incorporating crowding effects (R2), is qualitatively the same for (R1) with the same steady

states observed. In this case the only possible stable inhomogeneous steady state is the one corresponding to figure 5.3: One site with high cell density, two sites with low cell density, and two with a cell density level between the two extremes. We should expect therefore, to observe the same general behaviour. Specifically we expect gradient-like structures, the size of which will depend on the sampling radius. Similarly to the case $r = 0$, the homogeneous steady state becomes stable for high cell densities even in the absence of random migration.

Figure 5.13b depicts the bifurcation diagram of the neighbour sensing model. Similarly to the equivalent short-range model, the homogeneous steady state is stable for both low and high cell densities. For intermediate values of the total cell mass M , stable inhomogeneous steady states emerge. In this specific system three inhomogeneous equilibria exist, only one of which can be stable for a given value of M . Two of these equilibria, shown in figure 5.13b, correspond to steady states where three distinct levels of cell density exist between the five sites: $(HHMML)$, and $(HMMLL)$. The third one, corresponds to a steady state where all sites are occupied by cells at different density levels. In the parameter region where the uniform steady state is unstable, the $(HMMLL)$ equilibrium becomes stable, and therefore is the one expected to be observed in simulations. Both remaining inhomogeneous equilibria are stable in the region of stability of the homogeneous steady state, making the system bi-stable in these areas. The patterned solutions of this type therefore will be observed depending on whether the initial conditions favour them instead of homogeneity.

It should be noted however, that the small size of the lattices along with the periodic boundary conditions imposed pose limitations to the parameters that can be used in order for the uniform steady state to be unstable. As can be seen in figure 5.13a, the homogeneous equilibrium loses stability for considerably higher cell densities due to the parameter regime employed. The boundary conditions also reinforce stability at lower cell densities. As the domain size is increased, the boundary conditions' stabilising effect becomes less significant and we can expect the conditions for instability to be satisfied for the range of parameter values used previously. The linear stability analysis suggests that for the parameters used in this section, and for a relatively large domain size, one should observe two separate regions of instability.

Due to these limitations, we omit the bifurcation diagrams for the remaining two models. Even though they do suggest that multiple cell width patterns are admissible, they are incapable of reproducing the behaviour of larger systems or providing any additional information to the diagrams shown, offering very limited insight. Thus, we have to resort to numerical simulations in order to examine larger systems.

5.3.3 Numerical Simulations

In this section we present numerical simulations undertaken for the nonlocal models (R2)-(R5).

Time evolution

All models studied here exhibit similar general behaviour, as far as their time evolution is concerned, to the long-range local sensing model (section 5.2): Multiple peaks appear initially, the number of which is predicted by the linear analysis, since the transient pattern corresponds to the fastest growing mode. The aggregates formed initially merge and grow during the course of the simulation until a final stable pattern is produced. In particular, the time evolution of the model incorporating crowding effects is qualitatively the same as in figure 5.9 for the local sensing model. The difference between the two models is that the aggregates formed in this case are not as sharp and are elongated. This is due to the crowding effect of the model, which does not allow lattice sites to become densely populated. Thus, we obtain patterns with plateaus of cell aggregations rather than spikes. For that reason, we generally observe a larger number of aggregates being formed, which are less pronounced and occupy more lattice sites than in the previous case.

Figure 5.14 shows the time evolution of the nonlocal closest neighbour model (R3), which demonstrates the common characteristics described above: The system deviates from homogeneity and initially sharp peaks appear. As time progresses, these peaks coarsen and ultimately the system rests at a patterned equilibrium. The top left picture of figure 5.14 shows a pattern with wavelength $w \approx 5$, whereas after coarsening of the peaks has ensued ($t = 130$, second frame shown) the approximate wavelength of the pattern is $w \approx 8$. Finally, after a long period of time has elapsed, the system

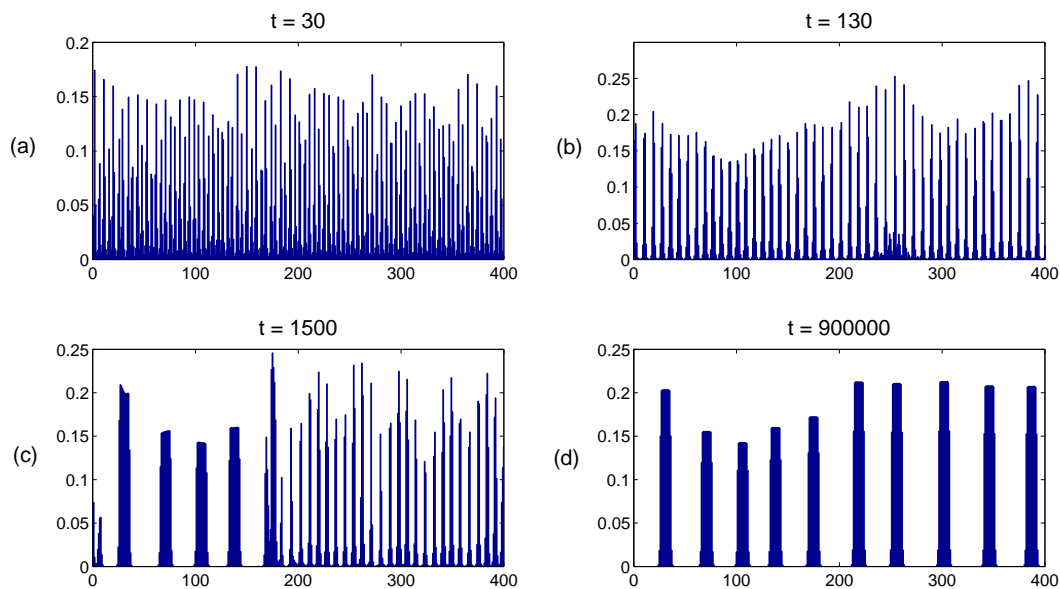


Figure 5.14: Time evolution of model (R3). (a): Initially small aggregations appear corresponding to the fastest growing mode as dictated from the linear analysis. (b): The aggregates start to coarsen as time progresses, in common with all the models considered. (c): Further coarsening of the peaks occurs until (d): the system reaches equilibrium, forming a pattern in which the cell aggregations are separated by a distance of at least $2r + 1$ sites. Parameters: $b = 1, \gamma = 0.01, a = 0.1, r = 10, M=20, N=400$.

relaxes forming a pattern with $w \approx 40$. The linear stability analysis undertaken in section 5.3.1 predicts that the first two modes mentioned are the ones growing most rapidly (figure 5.12b). However, the simulations reveal that they are unstable, and the system further evolves to a stable solution. As mentioned, this behaviour is common in all our models. We note however, that in the case of the nonlocal sensing opposite model (R4), simulations reveal that there exist multiple stable steady states and the evolution of the system depends largely on the initial conditions used.

Concentrating on the time evolution of the closest neighbour model we can observe that when the initial aggregations start merging in order to form the final pattern, they do so in a wave-like fashion. That is, some of the cell aggregations of figure 5.14(b) begin to merge forming the aggregates shown on the left hand side of figure 5.14(c). This forces the cell aggregates adjacent to these peaks to follow the same process and merge as well. This is a consequence of the model's assumptions: cells sense their environment and decide to move to a new site if the density at it is relatively high.

After the initial aggregations have been formed, the system is in a pseudo-steady state, where cells move to either direction with almost equal probability, because the characteristics of this intermediate pattern roughly correspond to the sensing radius. However, once the first few peaks merge, they attract almost every cell in their local environment, defined by the sensing radius. That in turn leads to a break in symmetry, in the sense that now cells in an aggregate obtain a favourable direction in which to move. The final pattern is composed by a number of large cell aggregates separated by sites at very low cell density. The distance between sites located in the aggregates is always more than twice the value of the sensing radius, making cell aggregates unable to communicate between them, and therefore the system rests.

Relation to sensing radius

Here we consider the effect of the sensing radius to the aggregations formed in each model. Another common feature of all the models we have analysed is that increasing the sensing radius results in patterns with fewer and larger aggregations, i.e. patterns composed of aggregates of multiple sites in width.

Figure 5.15 depicts a set of simulations carried out for different sensing radii for the long-range crowding model. By increasing the sensing radius, the aggregations forming the final pattern involve more lattice sites as expected. They are broader than the corresponding aggregations of the simpler long-range local sensing model, since the crowding term prevents cells from further aggregating at a specific site.

Figure 5.16 is a plot of the magnitude of the final aggregations as a function of the sensing radius for the long-range gradient model (R5). Similar behaviour is also observed for the neighbour sensing and the sensing opposite models. This plot is produced using data of numerical simulations performed for each case, using random small perturbations from a homogeneous cell distribution. The size of the aggregate S is defined here as the number of consecutive lattice sites in which the density is above the value of the homogeneous steady state M/N . Also shown is the number of aggregates in equilibrium for each value of r . Thus, for example for $r = 3$, we obtain 8 aggregations of size $S = 4$. Note that shortly after the first peaks merge, the width of each aggregation reaches a set number of sites dictated by the value of

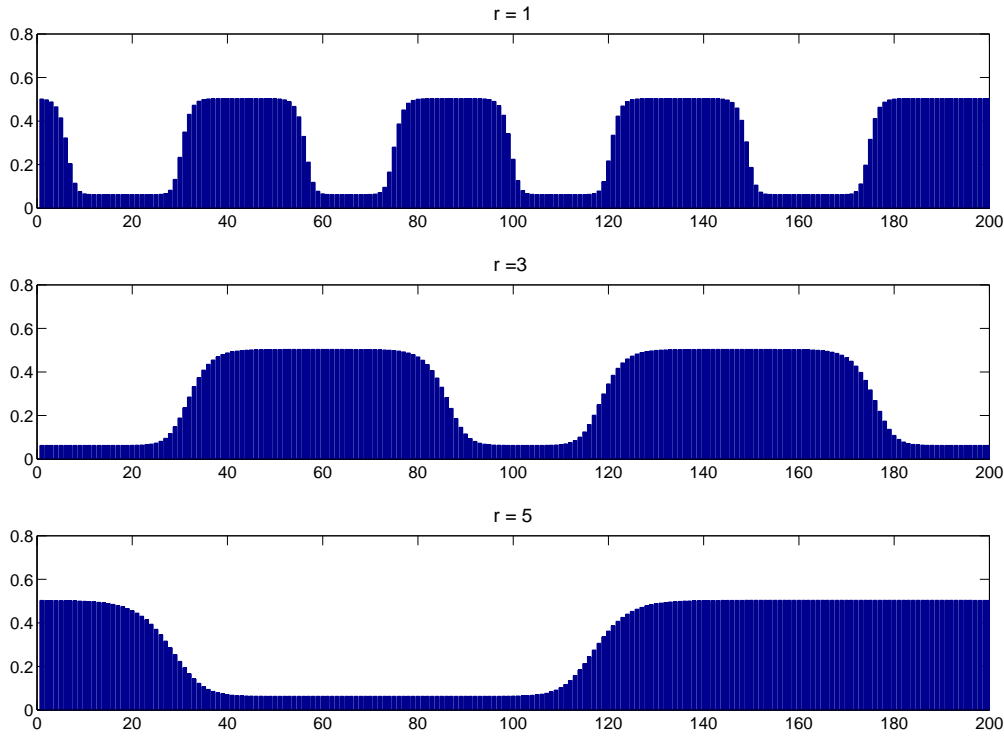


Figure 5.15: Numerical simulations of the long-range sensing model with crowding effects. Simulations show systems of 200 lattice points at equilibrium, for various values of the sensing radius r . Parameters: $M = 60, q = 100, a = 0.01, b = 1.0$.

the sensing radius, which is the size S plotted in figure 5.16, and does not increase further. Subsequent merging of the aggregations results in more cells occupying the same space, making the final peaks longer rather than wider, in contrast to the long-range local sensing models R1 and R2.

Relation to total cell density

We have explored the effect of the total cell density available, to the pattern produced. The crowding model exhibits the same behaviour as the strictly local sensing model: An increase in M corresponds to an increase in the number of aggregates formed. Figure 5.17 depicts the various patterns produced for different values M for the long-range sensing opposite model, for $r = 1$, with small random perturbations from homogeneity used as initial condition. For relatively low values of M , we observe a co-relation between the number of peaks ultimately obtained and the total available

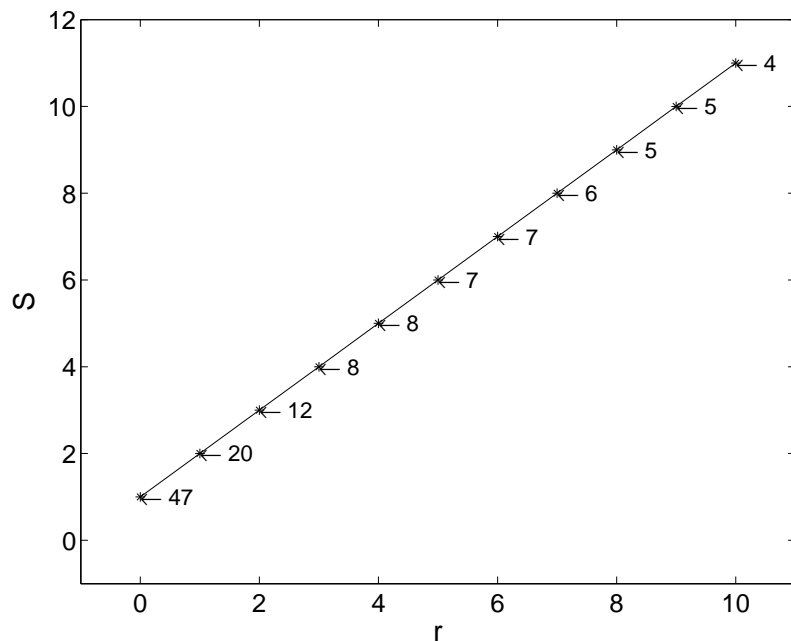


Figure 5.16: Plot of the size of the final aggregation(s) S that compose the steady state reached after numerical simulations, against the sensing radius, for the non-local gradient sensing model (R5). S is defined as the number of consecutive sites at cell density $u > u_0 = M/N$. The numbers shown next to each data point correspond to the total number of aggregations once equilibrium has been established. All simulations were performed in 200-site domains, using the same small perturbation from a homogeneous cell distribution for $t = 0$. The local gradient model is also included ($r = 0$). S is increasing linearly with r , and the final aggregations increase in size in 1-site steps. Similar results are obtained for models R3 and R4. Parameters: $M = 40, a = 1.1, b = 1.0, \gamma = 0.01$

cell density. However, for relatively large values of M , this co-relation breaks down, and irregular aggregations are formed comprised with fewer peaks. Similar behaviour is observed in the non-local gradient model. Linear analysis of the model shows that the last point of intersection of $\lambda(w)$ with the w -axis moves to the right as M increases. That is, as the total cell density increases, the wavelength of the first unstable mode as well as of the fastest growing mode increase as well. If a certain threshold of M is exceeded, low-wavelength modes become stable. Thus, beyond a certain value of M , only patterns of large wavelengths are possible.

We should note at this point, that the width of the aggregates of the final patterns observed in the models (R3)-(R5), is constant and independent of the number of aggregates, depending only on the size of the sensing radius. This contrasts with

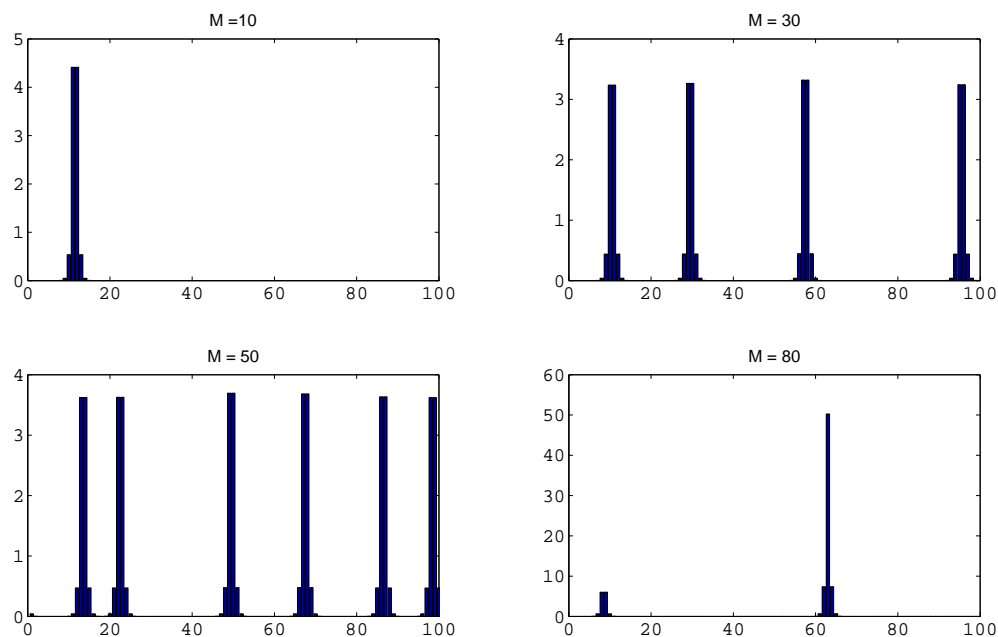


Figure 5.17: Numerical simulations showing the relation between the final pattern obtained and the total cell density for the non-local sensing opposite model. Similar results are obtained for the non-local gradient model. As M increases, so does the number of cell aggregations forming the pattern at equilibrium. For relatively large values of M however, this relation breaks down and the final pattern is comprised by fewer peaks. Parameters: $r = 1, b = 1, a = 0.1, q = 100$.

the findings of section 5.2.3, where we showed that it is the maximum density that remains constant while the width varies. In other words, in these models, cells are accumulated over a set number of sites dictated by the sensing radius. This fact may offer an explanation for the behaviour seen in figure 5.17: Since all cell aggregations are of the same size, there is a maximum number of cell aggregates that can be accommodated in a certain domain. Therefore, if the total cell density exceeds a certain threshold, the relation between M and the number of density peaks cannot be sustained.

5.4 Summary

In this chapter we have extended the models presented in chapters 3 and 4 to allow for long-range sensing by incorporating a sensing radius. In chapter 3 we introduced the discrete local models (M1)-(M5) by considering a variety of ways by which cells

respond to their environment by sensing the cell density in their local neighbourhood. Our aims were to derive continuous models using an approach similar to [66], and explore the effectiveness of both discrete and continuous models to describe an adhesion-type process. The three basic requirements of our models were highlighted in table 3.1: To successfully describe an adhesion-type process a model should be able to (i) allow aggregating behaviour, (ii) exhibit multiple cell aggregates, and (iii) produce cell aggregates of multiple cell widths.

As far as the derivation of continuous models is concerned, we showed in chapters 3 and 4 that the models derived become ill-posed in the region where instability of the homogeneous steady state is predicted. Blow-up is expected under the conditions for instability, rendering the continuous models unusable. However, the continuous models do, at some level, predict aggregation since patterning conditions can be obtained from the linear analysis, which correspond to the equivalent conditions for the discrete models, and blow-up behaviour can be viewed as an aggregation phenomenon. One could expect that by incorporating non-local sensing in the models, this behaviour can be avoided. However, the results of chapter 5 in which non-local interactions were included showed that ill-posedness is still an issue.

Derivation of continuous models from an underlying discrete model can be very useful since it offers a connection between microscopic and macroscopic properties. Thus, macroscopic parameters, such as diffusion coefficients, can be determined from the equivalent measurable microscopic parameters, such as cell velocities. A continuous model has the advantage of being analytically tractable and, especially when large populations of particles are studied, less computationally intensive. Discrete models, on the other hand, are desirable since they allow the incorporation of interactions at a cellular level. It is therefore highly desirable to develop continuous models that retain the underlying characteristics of their discrete counterparts.

The ill-posed nature of continuous models generated using the same approach is also observed in similar local sensing models (e.g. [7, 73]), while in [99] a master equation/Potts model was taken to its continuous limit. Our results in chapter 5, indicate that non-local information inherent in the discrete model is lost upon transformation into a continuous model, an observation also made in [99]. However, the illposedness

of the continuous models may be a product of the scalings and the limit used. Therefore it is possible that different forms of discrete models or the use of different scalings could lead to a well-posed and therefore usable continuous model.

Due to the ill-posed nature of the continuous models we focused our analysis to the discrete models. The analysis of chapter 4 revealed that the discrete models (M1)-(M5) were capable of producing regular patterns if a random migration or a crowding term were included. We also demonstrated that despite some variation in the models' behaviour, the discrete model formulation is relatively insensitive to differences in the precise nature of the sensing mechanism. The drawback of these models is that they cannot exhibit patterns of multiple cell diameters. By including a sensing radius we demonstrated that the extended models (R1)-(R5) retained the desirable characteristics of their local sensing counterparts. Additionally, we showed that through the modifications applied in this chapter multicell patterns are possible, making the models analysed capable of reproducing adhesion mediated aggregating behaviour under the requirements we imposed in table 3.1.

A straightforward extension to the models developed here would be to consider multiple cell populations with different adhesive properties. As we have discussed in section 3.2.2, the Differential Adhesion Hypothesis predicts several cell sorting scenarios (see figure 3.3), and a model of cell-cell adhesion should be able to reproduce these behaviours.

Cell-cell and cell-matrix adhesion is present and plays a key role in a variety of biological processes, including cancer invasion, wound healing, angiogenesis and development of the slime mould *Dictyostelium discoideum*. Numerous attempts of mathematical modelling of these phenomena exist that have taken adhesion into account. Examples include [76] for *Dictyostelium* and [31] for cancer invasion. Our models can be extended to include additional processes such as chemotaxis in order to model cell movement and pattern formation in developmental biology, and further study the interaction of the two processes. We consider one such application in the following chapter, in which we will use the discrete model with non-local sensing approach in order to apply it to modelling a specific example of adhesion mediated pattern formation.

Chapter 6

Application of adhesion modelling: Sympathetic ganglia formation

In this chapter we will consider a specific biological application in which cell-cell adhesion plays an important role: the formation of sympathetic ganglia (figure 6.1). We will first give an account of the biological background. In order to model this phenomenon we will examine both a continuous and a discrete formulation. For the discrete model we will accordingly adapt the discrete master equation-model (R2) proposed and demonstrated to successfully capture the characteristics of adhesive populations in the previous chapter. Since this model was unable to generate a “usable” continuous model we will fall back on an established continuous model for cell adhesion, developed by Armstrong et al. [8]. A brief description of this model will be given, along with a review of analytical results. Finally, we will present the full ganglia formation model, and its analysis.

6.1 Introduction

6.1.1 Biological Background

Sympathetic ganglia are structures of the autonomic part of the peripheral nervous system. They are divided into two subtypes: the paravertebral ganglia and the prevertebral ganglia. The former are located on either side of the spinal chord and form

long chains (the sympathetic chains), while the latter are found in the abdominal cavity [87]. Sympathetic ganglia play an important role in the function of the autonomic peripheral nervous system.

Sympathetic ganglia formation is initiated in early development when *trunk neural crest cells* migrate from the neural tube. Neural crest cells migrate and generate a variety of differentiated cell types. The trunk neural crest cells disperse from the neural tube and follow two principal pathways: cells that migrate dorsally underneath the ectoderm ultimately differentiate into skin pigment cells (melanocytes). Cells that follow the ventral pathway give rise to the *dorsal root ganglia* and sympathetic ganglia [34]. Sympathetic ganglia are formed after a subpopulation of these cells continue their journey past the dorsal root ganglia formation site, and disperse along the dorsal aorta. A striking difference between the two pathways is that in the former case migration is unsegmented, while cells following the ventral pathway move through the somites in a patterned fashion: they selectively enter the rostral part of the somite and avoid the caudal portion [14] (figure 6.2). Experimental evidence suggests the existence of guidance cues located in the somites, responsible for the migration of neural crest cells [15]. Therefore, it was believed that sympathetic ganglia formation is a result of the patterned migration. However, a recent study [45] showed that when

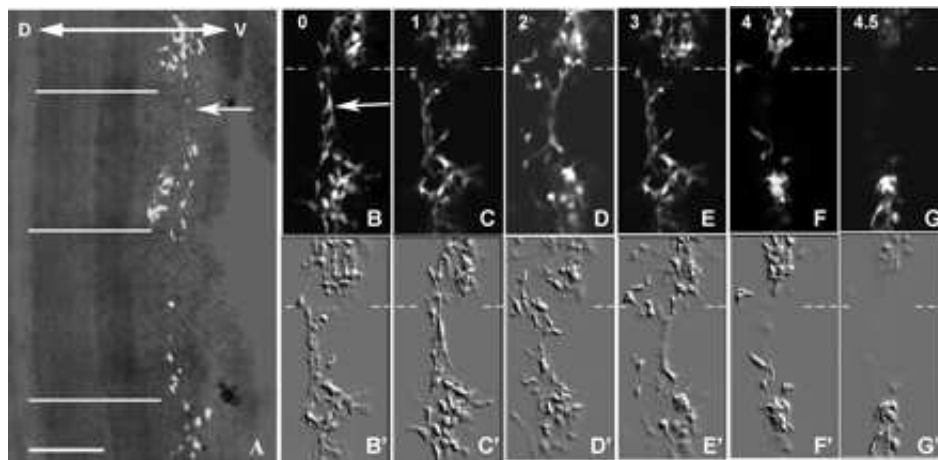


Figure 6.1: Formation of sympathetic ganglia. A: neural crest cells initially dispersed along the dorsal aorta. Lines indicate somite borders. Dorsal (D) and ventral (V) directions shown. Figures B-G and B'-G' show the cells migrating away from the interganglionic regions and aggregate into sympathetic ganglia. Scale bar: $50\mu\text{m}$, times in hours. Figure taken from [45].

cells arrive at the sympathetic ganglion sites, the segregated pattern ceases to exist and cells undergo further re-sorting in order to form discrete ganglia (see figure 6.1).

Further studies by Kasemeier-Kulesa et al [44] provided experimental evidence that the interplay between two mechanisms drive sympathetic ganglia formation. The authors were able to demonstrate: (1) that cell-sorting occurs as a result of a repulsion mechanism mediated by the expression of *ephrinB1* in the inter-ganglionic regions and its receptor *EphB2*, and (2) that cell-adhesion mediated by *N-cadherin* plays a major role in the aggregation process as well as in controlling the ganglion size. As cells migrate away from the inter-ganglionic regions due to the inhibitory signals, cells adhere to one another, thus forming discrete ganglia. This process is schematically depicted in figure 6.2: Neural crest cells migrating from the neural tube pass through the rostral somite and disperse along the dorsal aorta. Ephrin expression is manifested in the interganglionic regions, forcing the cells to move away from them. Cells adhere to each other by forming homophilic N-cadherin bonds and form discrete sympathetic ganglia.

In the following sections we will attempt to model the sympathetic ganglia formation process based on the findings of Kasemeier-Kulesa et al [44]. To do this, we will employ both a discrete and continuous approach. For the discrete model we will extend one of the non-local models for cell adhesion (model (R2)), developed and demonstrated to capture the characteristics of adhesive populations in chapter 5. As discussed in chapter 5, the continuous model derived from the discrete model is ill-posed. For the continuous formulation we will therefore use a more detailed continuous model for cell-cell adhesion proposed in [8]. Our aim is to propose a model that can account for the phenomena described in [44] and make predictions about the biological system. Furthermore, we test the ability of the model for cell adhesion proposed in chapter 5 to model a specific biological application and compare it to the more established continuous model.

We will first give an account of the continuous model for cell adhesion developed in [8] and subsequently present both the full adhesion-repulsion models and their analysis in sections 6.2 and 6.3.

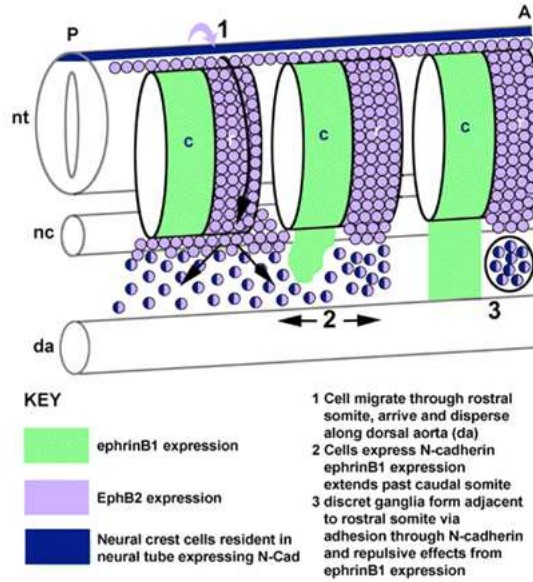


Figure 6.2: Schematic representation of discrete sympathetic ganglia formation, highlighting the key processes: 1. Neural crest cells migrate from the neural tube (nt) through the rostral somites (r), avoiding the caudal part of the somites (c). 2. Neural crest cells disperse adjacent to the dorsal aorta (da). ephrinB1 expression is established in inter-ganglionic regions between developing ganglia. 3. Interplay between N-cadherin mediated adhesion and ephrinB1 repulsion drives discrete ganglia to form adjacent to the ventral edge of a rostral somite. A, anterior; P, posterior; Figure taken from [44]

6.1.2 Mathematical Background

In this section we present and discuss the continuous model for cell adhesion developed in [8]. This model will be extended in section 6.2 in our model formulated to describe sympathetic ganglia formation. The authors assumed no cell birth or death in the system and used a mass conservation approach to derive the model:

$$\frac{\partial u(x, t)}{\partial t} = -\frac{\partial J}{\partial x}, \quad (6.1)$$

where $u(x, t)$ is the cell population density at position x and time t , and J , the cell flux, is taken to be:

$$J = J_d + J_a, \quad (6.2)$$

where J_d and J_a are the contributions due to diffusion and adhesion respectively. Fickian diffusion was assumed: $J_d = -D\frac{\partial u}{\partial x}$, while the adhesive flux is given by:

$$J_a = \frac{\phi}{R}u \int_{-R}^R \alpha g(u(x+x_0))\omega(x_0)dx_0. \quad (6.3)$$

The specific form of J_a shown in (6.3) is derived in [8]. The integral represents the sum of local adhesion forces exerted at cells at position x due to the presence of cells at a distance x_0 . R is defined as the maximum distance x_0 within which cells can sense the adhesive force, and termed the “sensing radius”. As we have discussed in the previous chapters, R minimally represents the physical cell size, but in practice is likely to be somewhat larger in order to include the distance covered by cell protrusions such as filopodia or lamellipodia.

The nature of the adhesive forces and their dependence on cell density is described in (6.5) by $g(u(x+x_0))$, the specific form of which will be discussed later. The strength of adhesion is modelled by the parameter α , and $\omega(x_0)$ models the direction and magnitude of the force according to the location of the cells. Finally ϕ is a constant of proportionality related to viscosity. The model (in one space dimension) is then as follows:

$$\frac{\partial u}{\partial t} = D\frac{\partial^2 u}{\partial x^2} - \frac{\partial}{\partial x}(uK(u)), \quad (6.4)$$

where

$$K(u) = \frac{\phi}{R} \int_{-R}^R \alpha g(u(x+x_0))\omega(x_0)dx_0. \quad (6.5)$$

In (6.4) $u(x, t)$ is the cell population density at position x and time t . The first term in the right hand side accounts for random cell motility (with D the diffusion coefficient), whereas the second term, containing the integral, models movement due to cell adhesion. Regarding the specific forms of $g(u(x+x_0))$ and $\omega(x_0)$, the authors in [8] assume that the adhesion forces are attractive and increase with cell density, since a cell is likely to create more adhesive bonds at higher densities. They propose a simple linear form:

$$g(u(x+x_0)) = u(x+x_0), \quad (6.6)$$

or a form that incorporates crowding effects, assuming that adhesion forces decrease once the cell density exceeds a certain threshold:

$$g(u(x+x_0)) = \begin{cases} u(x+x_0)(1-u(x+x_0)/M) & \text{if } u(x+x_0) < M \\ 0 & \text{otherwise,} \end{cases} \quad (6.7)$$

where M represents the crowding threshold. Finally, $\omega(x_0)$ is given by:

$$\omega(x_0) = \begin{cases} -1 & -R < x_0 < 0, \\ 1 & 0 < x_0 < R. \end{cases} \quad (6.8)$$

As discussed, $\omega(x_0)$ models the force's direction according to the location of the cells. This is the simplest form for $\omega(x_0)$, though a more realistic assumption would be that the magnitude of the adhesion force varies with distance, e.g. to reflect decreased likelihood of forming bonds with distance from cells.

In the following sections we will employ the model (6.4) with the density dependent form of g (equation (6.7)) in order to describe cell-cell adhesion in our model for sympathetic ganglia formation. We scale the cell density u by the crowding capacity M , so that $u^* = u/M$. Incorporating parameter ϕ into the adhesion strength parameter α yields $\alpha^* = \alpha\phi M$, so that the model reads

$$\frac{\partial u}{\partial t} = D \frac{\partial^2 u}{\partial x^2} - \frac{1}{R} \frac{\partial}{\partial x} \left(u \int_{-R}^R \alpha u (1-u) \omega(x_0) dx_0 \right), \quad (6.9)$$

where we have dropped the stars for notational convenience. The parameter choices will be discussed in the following sections.

The authors in [8] have analysed the model presented above by performing linear stability analysis and numerical simulations both in one and two dimensions. The linear stability analysis predicts that aggregating behaviour is possible in the model, and offers a criterion for the strength of the adhesion parameter required in order for aggregations to form. In section 6.3.1, we present the linear analysis in one dimension undertaken in [8]. Numerical simulations confirmed that the model captures cell aggregation. Furthermore, by extending the model to study two adhesive cell popu-

lations, Armstrong et al. [8] showed that the model can reproduce the experimental results of Steinberg and capture cell sorting behaviour.

6.2 Sympathetic ganglia formation modelling

6.2.1 Continuous Model

In order to model the formation of sympathetic ganglia, we consider a cell density $u(x, t)$ at position x and time t of sympathetic ganglia precursor cells that are initially homogeneously distributed along the dorsal aorta. We consider a 1-dimensional domain of size L : $x \in [0, L]$, where x describes the position along the longitudinal axis of the dorsal aorta (see figure 6.2). If J denotes the flux of the cells, mass conservation implies:

$$\frac{\partial u}{\partial t} = -\frac{\partial J}{\partial x}.$$

Movement of cells is assumed to occur due to random migration, cell-cell adhesion as a result of N-cadherin, and movement in response to the Eph-Ephrin repulsive forces, so that $J = J_d + J_a + J_r$, where J_d , J_a , and J_r are the corresponding contributions to the total flux due to each type of movement. We will utilise the model proposed in [8] and discussed in 6.1.2 to describe the contributions J_d and J_a . In order to model Ephrin mediated repulsion, we assume that cells respond to the distribution of EphrinB1 located in the interganglionic region by moving down its gradient. Adopting the classical approach of modelling taxis type terms [61], we therefore take:

$$J_r = -\beta u \frac{\partial \rho}{\partial x}, \quad (6.10)$$

where β is the (constant) chemo-repulsion sensitivity, and $\rho(x)$ denotes the EphrinB1 distribution. Experiments [44] suggest that EphrinB1 expression is restricted to the caudal portion of each somite. Furthermore, it was demonstrated that EphrinB1 expression in the interganglionic regions coincides with the movement of neural crest cells away from these regions, and that EphrinB1 is still expressed after the cells have formed discrete ganglia (figure 6.2). To model these findings we assume a periodic

spatial distribution of EphrinB1, to account for the fact that its expression is localised in each caudal somite. We also assume that directed movement of cells due to repulsion forces begins after EphrinB1 expression is established, and therefore make the simplifying assumption that the chemical's distribution is constant in time. Assuming the chemical concentration is high at the location of the caudal somite, and low at the rostral somite, we can rewrite (6.10) as:

$$J_r = \beta u \Lambda(x). \quad (6.11)$$

We will use $\Lambda(x) = \sin(\frac{2n\pi x}{L})$, where L is the domain size and n is an integer corresponding to the number of somites present in the domain in question. The assumption behind this form of $\Lambda(x)$ is that the Ephrin concentration is fixed in space and does not diffuse, which is supported by the experiments.

The full model reads:

$$\frac{\partial u}{\partial t} = D \frac{\partial^2 u}{\partial x^2} - \frac{\partial}{\partial x} \left(u K(u) \right) + \frac{\partial}{\partial x} \left(\beta u \sin\left(\frac{2n\pi x}{L}\right) \right), \quad (6.12)$$

with

$$K(u) = \frac{1}{R} \int_{-r}^r \alpha u (1-u) \omega(x_0) dx_0, \quad (6.13)$$

where parameters α and β model the strengths of the adhesive and repulsive forces respectively, D is the random motility coefficient and R is the sensing radius. Biologically, α represents the level of N-cadherin activity in the cells, while β the level of Ephrin activity. We have used the (scaled) volume-filling form of $g(u)$ (equation (6.7)), while $\omega(x_0)$ is given by (6.8).

6.2.2 Discrete Model

In this section we approach the problem of sympathetic ganglia formation using the discrete modelling formulation introduced in chapters 3- 5. Specifically, we will use a modified version of the long range crowding model described in sections 3.5.2 and 5.1.2. In this model, the transition probabilities per unit time of a jump from n to $n \pm 1$ are

given by:

$$T_n^\pm = [d + af(U_n)](1 - u_{n\pm 1}), \quad (6.14)$$

where u_n is the cell density at site n which now represents a discrete location along the dorsal aorta, $U_n = \sum_{i=n-r}^{n+r} \frac{u_i}{2r+1}$, $f(U) = \frac{1}{1+qU^2}$, r is the sensing radius, and d, a, q are positive constants. The main assumptions of this model are that the probability of a cell moving from a specific site depends on the cell density at the site and random migration. The latter is modelled by d , whereas a models the adhesive strength. We also assume that there is a crowding threshold in cell density. Analysis of this model was presented in chapter 5.

In order to model sympathetic ganglia formation, we need to modify (6.14) in order to include the contribution of the repulsion mechanism. The presence of Ephrin in specific locations along the lattice should be accompanied by a corresponding increase in the likelihood of a cell located at these sites performing a jump. The modified transition probabilities read:

$$T_n^\pm = [d + af(U_n) + b \sin(\frac{2m\pi n}{N})](1 - u_{n\pm 1}), \quad (6.15)$$

where N is the total number of sites, b is a constant corresponding to the strength of the repulsion, and m corresponds to the number of somites in the lattice.

Table 6.1 below shows the correspondence between the parameters of the continuous and discrete models.

Process	Continuous	Discrete
Random Motility	D	d
Cell Adhesion	α	a
Repulsion	β	b

Table 6.1: Key parameters of the ganglia formation models. Corresponding parameters between the discrete and continuous models are shown.

6.3 Analysis

6.3.1 Continuous Model Analysis

I: No repulsion forces

In this section we analyse the model (6.12) in the absence of the repulsion forces, i.e. we set $\beta = 0$ in (6.12). We present the linear stability analysis undertaken for (6.9), first presented in [8]. The analysis serves as an indication of whether the model can develop cell aggregation patterns when adhesion alone is operating, and investigate the criteria under which this is possible. Furthermore, these criteria will assist in estimating the parameter α to be used in our subsequent simulations. The experimental procedure equivalent to the case we analyse here, would be to artificially disable the Eph/Ephrin repulsion mechanism, which was undertaken in [44]. This experimental procedure resulted into no ganglia forming, and the cells remaining homogeneously distributed along the dorsal aorta.

We begin by linearising around the homogeneous steady state U , by setting: $u(x, t) = U + \tilde{u}(x, t)$, where $\tilde{u}(x, t)$ is a small perturbation. Substitution into (6.9) yields:

$$\frac{\partial \tilde{u}}{\partial t} = D \frac{\partial^2 \tilde{u}}{\partial x^2} - \frac{\alpha U(1 - 2U)}{R} \frac{\partial}{\partial x} \left(\int_{-R}^R \tilde{u}(x + x_0) \omega(x_0) dx_0 \right), \quad (6.16)$$

where we have neglected non-linear terms in \tilde{u} . We look for solutions of the form: $\tilde{u} \propto e^{ikx + \lambda t}$. Upon substitution into (6.16), we obtain the following dispersion relation:

$$\lambda(k) = -Dk^2 - \frac{2\alpha U(1 - 2U)}{R} (\cos(Rk) - 1). \quad (6.17)$$

For cell aggregations to develop we require $Re(\lambda(k)) > 0$, which leads to the following criterion:

$$\alpha > \frac{DRk^2}{2U(1 - 2U)(1 - \cos(Rk))}. \quad (6.18)$$

Expression (6.18) demonstrates the ability of the model to produce inhomogeneous patterns on the condition that the adhesion parameter α is sufficiently strong. The authors in [8] have demonstrated the ability of their model to produce aggregating

behaviour through numerical simulations.

The equivalent analysis for the discrete model was undertaken in section 5.3.1, in which the nonlocal model with crowding (R2) was linearised. The condition for patterning is:

$$2(d + af_0)(\cos k - 1) + \frac{2au_0f'_0}{2r + 1}(1 - u_0)\left(\cos[(r + 1)k] - \cos(rk)\right) > 0 \quad (6.19)$$

where u_0 is the homogeneous steady state, and f_0, f'_0 are the function $f = \frac{1}{1+qu^2}$ modelling cell-adhesion, and its first derivative evaluated at u_0 .

II: No adhesion forces

We can also analytically determine the steady states of the model (6.12) without the adhesion contribution. The equivalent experimental procedure was performed by Kasemeier-Kulesa et al. [44], where they suppressed N-cadherin expression in pre-ganglionic cells. Specifically, setting $\alpha = 0$ we obtain at steady state :

$$\frac{\partial}{\partial x} \left(D \frac{\partial u}{\partial x} + \beta u \sin\left(\frac{2n\pi x}{L}\right) \right) = 0,$$

or

$$D \frac{\partial u}{\partial x} + \beta u \sin\left(\frac{2n\pi x}{L}\right) = c_1.$$

Using no-flux boundary conditions yields $c_1 = 0$. Integrating, we obtain:

$$u = A \exp\left(\frac{\beta L}{2\pi n D} \cos\left(\frac{2\pi n x}{L}\right)\right), \quad (6.20)$$

where A is an integration constant that can be determined through a density conservation argument: $\int_0^L u(x, t) dx = \int_0^L u(x, 0) dx = M_0$, with M_0 being the total initial cell density. Equation (6.20) implies that in the absence of adhesion a periodic inhomogeneous steady state is obtained, the period of which is dictated by n , the number of somites in the domain. This is in accordance with the biological experiments in [44], where it was shown that if N-cadherin expression is suppressed sympathetic ganglia do form in the area rostral to the somites. However, ganglia formed under these conditions were found to be malformed: Since adhesive connections were weakened

the discrete ganglia were found to be elongated. This preliminary analysis therefore provides an indication for the magnitude of the relevant parameters. Furthermore we can compare this analytical result to the numerical simulation.

Numerical simulations of the full model (6.12) will be presented in the following section. Our aim is to reproduce the results of Kasemeier-Kulesa et al. [44] and make predictions about the real biological system. Specifically, we will examine the interplay between the repulsive and attractive forces mediated by Ephrin and cell-cell adhesion respectively, and attempt to determine their significance in the formation of sympathetic ganglia. Additionally we will look at the manner the system behaves if longer range signalling is taken into account, through the use of cellular protrusions.

6.3.2 Numerical simulations

Parametrisation and fitting to experimental data

In this section, results of numerical simulations of equation (6.12) are presented. We have used $g(u) = u(1 - u)$, the scaled equivalent of (6.7), which takes crowding effects into account. We solve (6.12) on a domain of length $L = 300\mu m$ discretised into 3000 mesh points, corresponding to approximately three somites (we estimate the length of each somite to be $100\mu m$ [45], leading to $n = 3$). We generally consider a sensing radius of $R = 20\mu m$, which implies that cells can sense their environment within a radius approximately two times their physical size, however a range of values for R will be investigated in order to illustrate how the magnitude of the sensing radius affects the system. Bray [13] estimated the diffusion coefficient of a “typical” animal cell to be $5 \times 10^{-10} cm^2/sec$, whereas the motility coefficient of fibroblast cells was estimated in [88] to be $\sim 0.83 \times 10^{-9} cm^2/sec$. We will use $D = 10^{-9} cm^2/sec$.

Initially we presume that cells are uniformly distributed along the dorsal aorta, following the results in [44], and therefore assume that at $t = 0$ the cell density distribution is homogeneous with a small random perturbation: $u(x, 0) = U + \eta$, where $U = 0.25$, and η is a random perturbation of order 10^{-4} . Periodic boundary conditions were employed in the simulations shown, effectively modelling an arbitrarily long domain. Simulations using no-flux boundary conditions were also performed,

exhibiting no considerable difference in the results. We are interested in patterns forming within a time window of $\approx 10 - 12$ hours, since this is the relevant time period for sympathetic ganglia formation as suggested in [44].

Figure 6.3 shows the simulations performed, for various values of α and β . Details about the numerical method employed can be found in the appendix A.3. In this manner we test the sensitivity of the system to variation of these two parameters. A reference value for parameter α can be obtained from the linear analysis. Equation (6.18) poses a condition for aggregating behaviour to occur in the absence of the repulsion mechanism. Kasemeier-Kulesa et al. [44] report that by inhibiting Ephrin, the cells remained uniformly distributed along the dorsal aorta over the timescale of patterning, i.e. there was no aggregation into the discrete ganglia. Taking this into account, we vary α around the critical α_c that (6.18) predicts.

Using the value of $U = 0.25$ set in the initial condition, we obtain $\alpha_c \approx 8D/R$. Note that $\alpha \gtrsim \alpha_c$ does not necessarily imply that patterns would be observed in the relevant time period. However, for $\alpha \gg \alpha_c$ we would expect to see peaks in the absence of repulsion contradicting the results of [44]. For $\alpha \gtrsim \alpha_c$ inhomogeneities do grow, however they develop very slowly and the system does not deviate significantly from homogeneity within the relevant biological time scale. Of course, pattern formation due to adhesion is observed in the course of the simulation but the time period required is significantly larger. We have chosen $\alpha = 12D/R > \alpha_c$ to be the “normal” value for the adhesion parameter, since the experimental data in [44] suggest that there is minimal motility in the absence of the repulsion mechanism.

For $\alpha < \alpha_c$ and $\beta = 0$, the system returns to homogeneity, as expected. For $\alpha = 0$, there is perfect agreement between the simulations shown and the steady states calculated by (6.20). Therefore, equilibrium has been reached in the course of the simulation. As β increases, the repulsion mechanism becomes more significant. The sympathetic ganglia pattern forms for low values of β , but the cell density of the aggregates is low and they occupy more space when cell adhesion is weak. In other words, the repulsion mechanism however weak, forces cells to move away from the interganglionic areas, but this leads to malformation of sympathetic ganglia if cells form weak or no adhesive bonds at all, since the repulsion mechanism is not sufficient

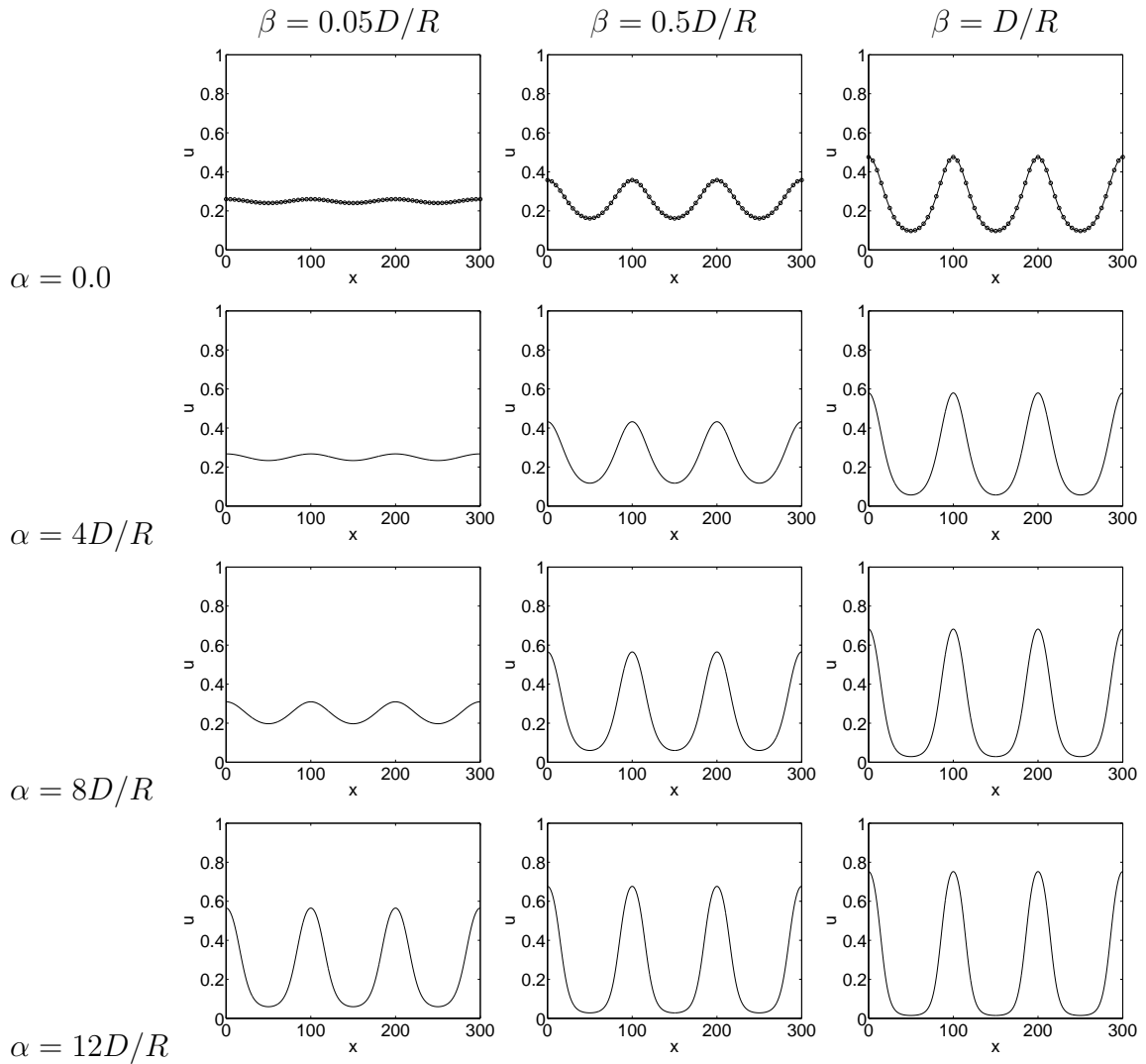


Figure 6.3: Numerical simulations of the full model (6.12) for various values of the adhesion and repulsion strength parameters. All figures depict the patterns obtained at $t = 12h$, in a domain of length $L = 300\mu m$. In absence of adhesive forces ($\alpha = 0$, top row), analytical results of the steady states calculated in section 6.3 (eq. (6.20)) are also plotted, marked with 'o'. Perfect agreement with numerical results indicates that for this case the steady state has been reached. Aggregations do not form in the absence of a repulsive mechanism ($\beta = 0$) for any of the values of α used, in the time the simulation was allowed to run. If cell-cell adhesion is weak, cells tend to move away from the interganglionic areas but the aggregations thus formed are of low density and more elongated. Parameters: $U = 0.25$, $R = 20\mu m$, $D = 10^{-9} cm^2/sec$. For numerical method details see section A.3 of the appendix.

to overcome cell diffusion. This is in agreement with a second experimental procedure presented in [44]. The authors measured the lengths of sympathetic ganglia of a control group to be equal to the length of the rostral somite (i.e. 50% of a somite's length). By blocking N-cadherin expression, cell-cell adhesion is greatly disrupted.

The size of sympathetic ganglia in embryos injected with an N-cadherin antibody was shown to be significantly affected. Since adhesion was weakened, the cells were more loosely aggregated, leading to a significant increase of ganglion length.

In the case where $\alpha > \alpha_c$ and α is significantly large in comparison to β , more peaks emerge due to adhesion driven aggregation. However, if the repulsion is strong enough, the aggregates ultimately merge and form the normal sympathetic ganglia pattern seen in our simulations. This process of peaks merging and moving to the ganglia region might significantly delay the formation process, depending on the relative magnitudes of α and β .

An important conclusion that can be drawn from figure 6.3 is that the sympathetic ganglia formation process is relatively robust. As can be observed, for relatively large values of α and β (bottom right panels in figure 6.3) we obtain very similar patterns. Therefore, ganglia formation is robust to variation of the adhesive and repulsive strengths around their “normal” values.

Predictions

An interesting scenario is the one depicted in figure 6.4, in which the repulsion mechanism is inhibited, while cell-cell adhesion is enhanced. This scenario corresponds to an experiment in which Ephrin receptors in cells are blocked while at the same time N-cadherin is overexpressed. If α is significantly larger than its critical value, pattern formation is observed during the relevant time frame. The patterns formed are composed of multiple cell aggregates, the initial number of which is dictated by the linear analysis (equation (6.17)). Over time, cell communication and movement results in the merging of the aggregations, in common with the discrete adhesion models presented in chapter 5. Therefore, under these circumstances, our model predicts the formation of cell aggregations varying in size, at random locations along the dorsal aorta. Furthermore, if there is a small but non-zero repulsion contribution, it predicts the emergence of multiple cell aggregations that move as a whole, rather than individual cells, and eventually form the sympathetic ganglia pattern. Malformation of sympathetic ganglia is manifested if the aggregations have not merged in the available time, or if they are not found in the correct position. Furthermore, the cells are

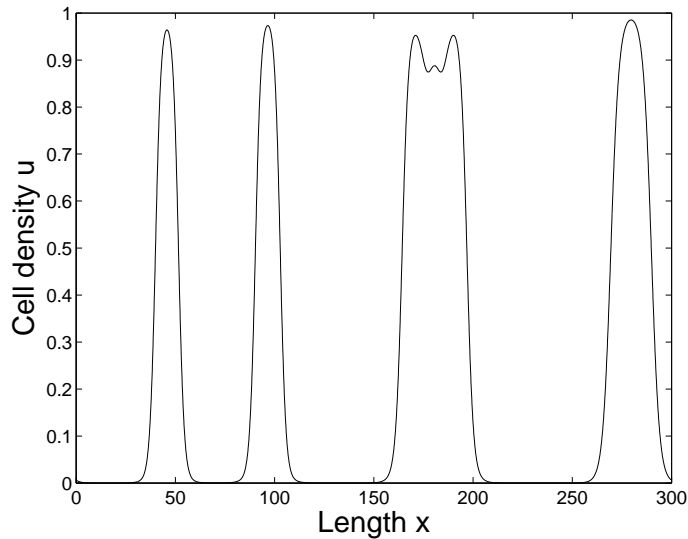


Figure 6.4: Pattern formation occurring in the model when the repulsion mechanism is suppressed ($\beta = 0$) and adhesion is enhanced. The pattern obtained at $t = 12h$ is shown, to allow comparison with figure 6.3. The same parameters and initial and boundary conditions used as in 6.3 except $\alpha = 100D/R$. Multiple peaks emerge initially, and merge as time progresses.

expected to be more densely packed due to the large adhesion forces operating. It would be interesting to assess the validity of these predictions through experimental procedures.

Simulations of the model (6.12) have been carried out in order to determine the role of the magnitude of the sensing radius, in the sympathetic ganglia formation process. Figure 6.5 below shows the results for $R = 10\mu m, 20\mu m$, and $40\mu m$. The simulations show that an increase in the sensing radius results in the accumulation of a larger number of cells in the predetermined ganglionic regions, over a set time period. A similar result was obtained in [9], where the same cell-adhesion model was used. Sympathetic ganglia formation is faster for larger values of the sensing radius, since cells form adhesive bonds with cells located further away, thus increasing the collective cell movement towards the ganglionic areas. However, the difference in ganglia size obtained is small in comparison to the corresponding variation of the sensing radius, suggesting that our model is robust to variation of R .

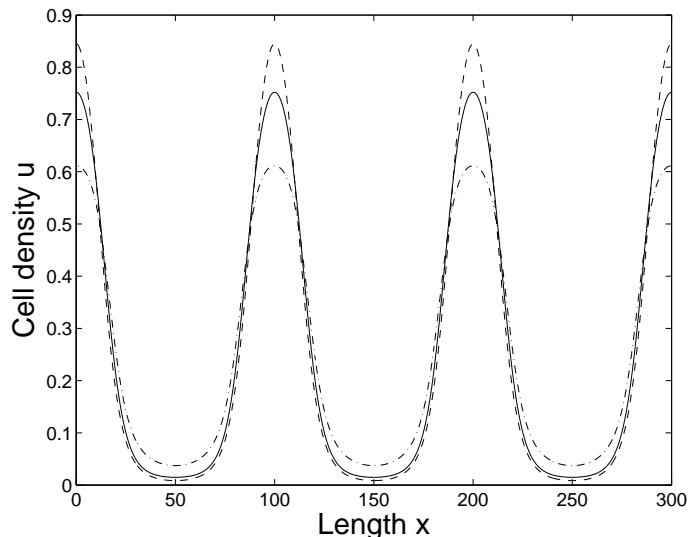


Figure 6.5: Numerical simulations of the full ganglia model (6.12) for different sensing radii: $R_1 = 10\mu m$ (---), $R_2 = 20\mu m$ (-), $R_3 = 40\mu m$ (-.-). Parameters and initial and boundary conditions as in fig. 6.3, with $\alpha = 12D/R_1$, $\beta = D/R_1$, $t = 12h$.

6.4 Discrete modelling of sympathetic ganglia formation

In this section we present numerical simulations performed for the discrete model of sympathetic ganglia formation in order to assess the nonlocal adhesion model of chapter 5 by using it to model a specific application and comparing it to the continuous model.

We have performed numerical simulations in lattices composed of 300 sites, such that one lattice site corresponds to a length of $1\mu m$, for various parameter values, using periodic boundary conditions. Figure 6.6 depicts the results for a sensing radius $r = 10$, so a cell senses over a length of $20\mu m$. The system exhibits very similar behaviour to that observed for the continuous model (see figure 6.3 for comparison). Pattern formation depends on the competition between the homogenising effects of random migration and the aggregating effects of cell-adhesion and the repulsion mechanisms. If the adhesion mechanism is disrupted or weak, the patterns formed are generally composed of lower density peaks extending over more lattice sites. Increasing the adhesion contribution leads to the formation of cell aggregations that are more compact and increases their cell density. However, when b , the repulsion strength

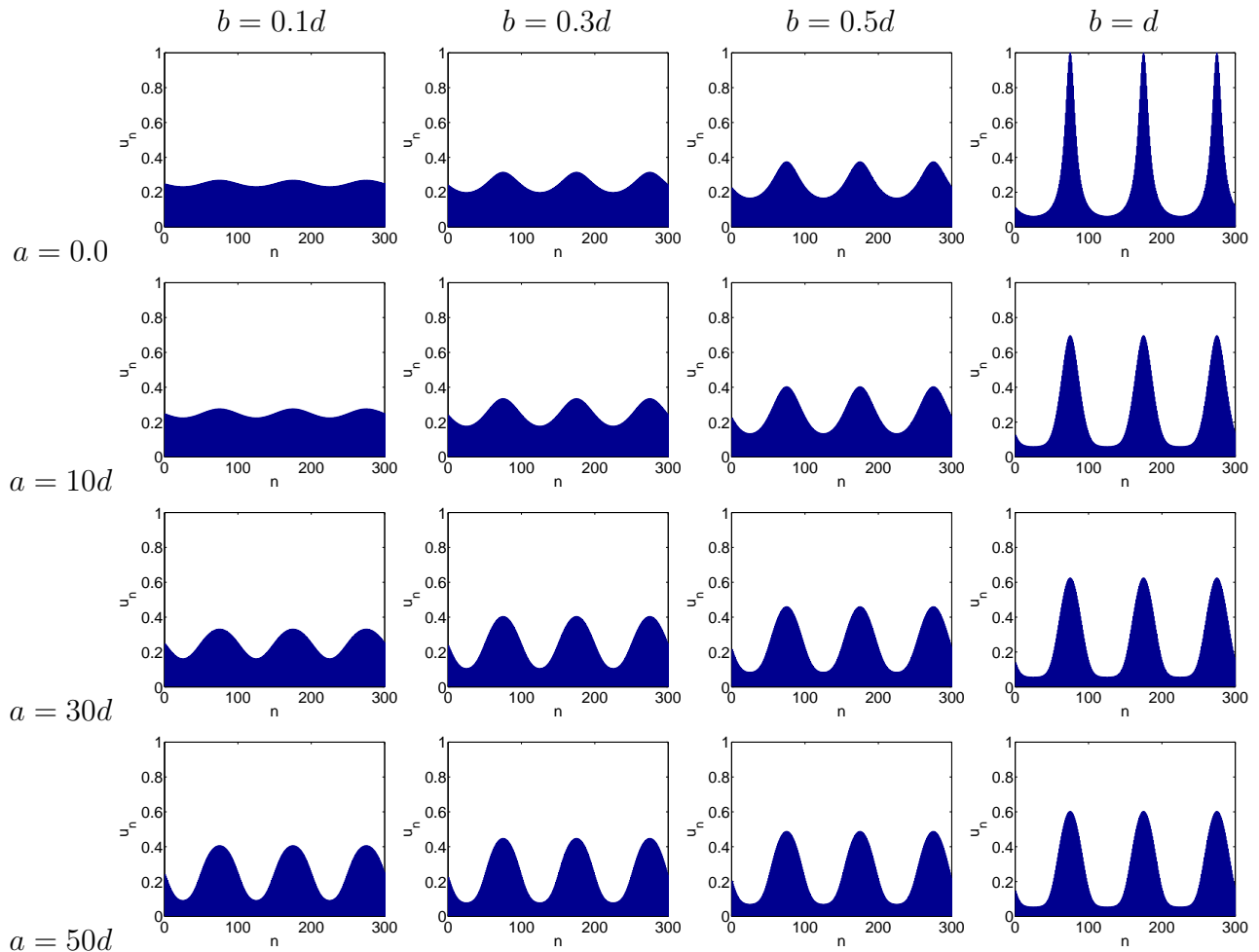


Figure 6.6: Numerical simulations of the discrete sympathetic ganglia formation model. The random migration term d is kept constant, while the adhesion and repulsion strength parameters are varied in order to reveal the interplay between the two mechanisms. No inhomogeneous patterns are obtained in the simulation time for $a \leq 30d$. The model exhibits behaviour similar to the continuous model analysed in section 6.3. Specifically, an increase of a , the adhesive component, enhances ganglia formation. However, when the repulsion parameter is sufficiently strong, increasing a has the opposite effect.

approaches values close to d , the random migration contribution, this behaviour is reversed. We observe that for $b \approx d$, increasing a leads to a slight decrease in the cell density of the aggregations.

This behaviour is more apparent in figure 6.7, in which the patterns obtained for various values of the sensing radius are compared. Here, we observe that increasing the sensing radius results in less pronounced peaks, in contrast to the findings of the continuous model.

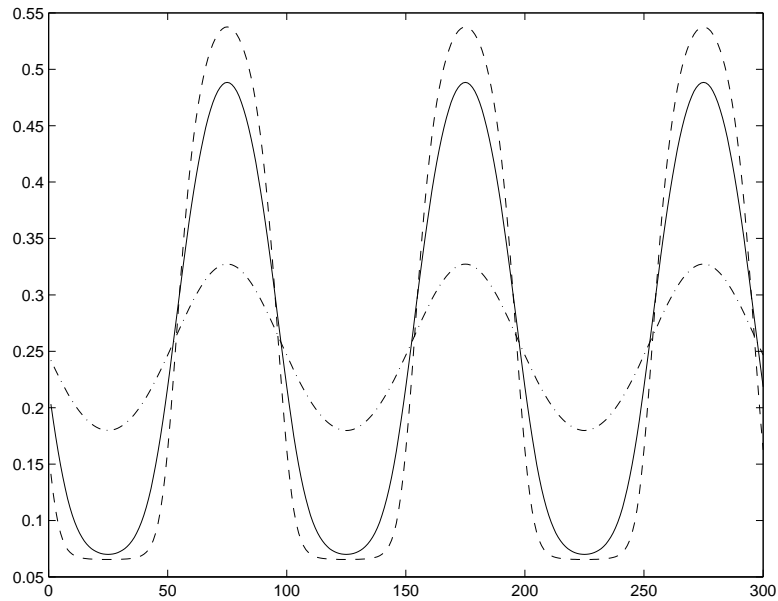


Figure 6.7: Comparison of the patterns obtained for varying values of the sensing radius in the discrete model for sympathetic ganglia formation. $r = 5\mu m$ (--), $r = 10\mu m$ (-), $r = 20\mu m$ (-.-).

The discrete model for cell adhesion was derived by imposing simple rules for the movement of cells in response to cell density variations, and subsequently extended to incorporate nonlocal sensing. Despite the differences discussed above, the results of the discrete model compare well with the equivalent results for the more complex continuous system. Variation of the adhesion and repulsion parameters a and b exhibits very similar behaviours to the corresponding parameter variation of α and β for the continuous model. The discrete model is able to capture the basic aspects of the sympathetic ganglia formation process, i.e. the interplay between the adhesion/repulsion processes, and reproduce the biological experiments. These results reinforce the validity of the discrete cell adhesion models of chapter 5 and demonstrate the impact of incorporating nonlocal sensing in a simple model of cell movement.

6.5 Discussion/Summary

In this chapter we attempted to model sympathetic ganglia formation, a process in which cellular adhesion plays a central role. To this end, we proposed both a discrete and a continuous modelling approach. For our discrete formulation we have used

a model developed in chapter 5 to describe cell adhesion. As shown in chapter 5, the discrete models considered are capable of capturing the fundamental aggregating properties of adhesion-type processes. However, the continuous models derived were demonstrated to be unsuitable. For the continuous modelling of sympathetic ganglia formation therefore, we have employed an established model for cell adhesion.

Our goals were to mathematically describe the process of sympathetic ganglia formation and reproduce the experimental findings of [44], as well as to make predictions about the biological system in question. Furthermore, we were interested to apply the model developed in the previous chapters to a specific biological process and further test its capabilities and limitations by comparing it both with the experimental results and the results of the more established continuous model.

In [44] it was demonstrated that two processes are chiefly responsible for the correct ganglia formation: N-cadherin mediated cell-cell adhesion, and chemorepulsion mediated by Ephrin. We have performed a parameter sensitivity analysis for the two principal parameters of both our models: α (or a for the discrete model) representing the adhesive strength and β (or b) representing the repulsion strength. Both models are capable of capturing the behaviour of the system, and reproduce the experiments undertaken in [44]: In the absence of the repulsion mechanism, no aggregation is possible, while if cell adhesion is suppressed the resulting ganglia are less pronounced. For sufficiently large values of α and β the model exhibits cell aggregations forming corresponding to discrete sympathetic ganglia. Furthermore, when both adhesion and repulsion mechanisms are sufficiently strong, parameter variation has limited effect on the resulting pattern, suggesting that the sympathetic ganglia formation is robust. Additionally, the system was found to be relatively robust to variation of the sensing radius. Increasing the length over which cells can communicate does result in faster ganglia formation and more compact aggregates, however these changes are small in comparison to the large sensing radius length variation.

The discrete model yields very similar results compared to the continuous model. Variation of parameters a and b shows the same qualitative behaviour: loose aggregations are formed when cellular adhesion is weak, while no ganglia formation is possible in absence of the repulsion mechanism. Discrete ganglia are formed for

relatively large values of a and b , while increasing either parameter results in more compact aggregates. However this correlation seems to break down for large parameter values. Overall, this agreement of the discrete model with the continuous model's results demonstrates that despite its simplified nature, the model possesses the essential features necessary to describe biological processes. This reinforces the conclusions of chapter 5 and further demonstrates the impact of non-local sensing.

Chapter 7

Conclusions

In chapter 2 we extended a model for juxtacrine signalling and lateral inhibition [20] in order to include nonlocal signalling. These mechanisms are identified and proved to be responsible for cell fate determination patterning. The model proposed in [20] is incapable of producing the relatively long spaced patterns found in nature. Based on recent experimental results [21], we altered the juxtacrine signalling model to account for long range communication of cells facilitated by the use of filopodia. By considering simple scenarios for the nature of cell signalling we were able to demonstrate that regular long range patterns of different types are possible.

Using standard linear stability analysis we were able to derive the criteria under which pattern formation is possible and highlighted the importance of the strength of the feedback mechanism: Including filopodia signalling corresponds to more cells being contacted. In order for pattern formation to occur a stronger feedback is needed, indicating the existence of a “natural limit” on the possible scale of the patterns that may result. Linear analysis is a useful tool for determining the conditions for patterning and predicting the form of the resulting patterns. However, an accurate prediction of the dominating pattern is not always possible. This is mainly a consequence of the discrete nature of the system: a mode predicted by the linear analysis to be unstable may not correspond to an integer value of wavelength and therefore will not develop.

Numerical simulations demonstrated the variety of patterns that can be obtained by considering different signalling scenarios and confirmed the predictions of the linear analysis. Furthermore, they provided insight to the patterning process. Considering

the more realistic scenario of weighted signalling in one and two-dimensional domains we demonstrated that our results can reproduce the experimental work undertaken in [21].

We have also briefly looked at how a polarised filopodia distribution affects the patterns produced. We demonstrated that polarised signalling can produce striped patterns of alternating cell fates. A more detailed analysis of this phenomenon is an interesting direction of future study. A further extension of the work undertaken in chapter 2 is to consider dynamic filopodia promoted by Delta, as suggested in [19, 21], instead of the constant in time and of set length filopodial distribution considered in this work. Such an extension may be able to reproduce the pattern refinement process reported in [19]. Another future direction for this study would be to undertake a non-linear analysis of the model in order to reveal aspects of it which cannot be fully captured by the linear analysis.

In this study we have chosen to extend the Collier et al. model [20], since its simpler nature offers the possibility of a more detailed analysis. This in turn, provides great insight into the patterning process due to long-range signalling. We remark however, that a more realistic model would have to incorporate a more detailed description of the ligand-receptor binding mechanism, as was the case for the models presented in [68, 69, 100, 101, 102, 103].

In chapter 3 we introduced a framework for modelling contact mediated cell movement. We proposed a number of different discrete models by considering different mechanisms by which cells sense and respond to their environment, and were able to derive continuous models by following the techniques used in [66].

Both discrete and continuous modelling approaches have their benefits and drawbacks. The discrete approach models a biological problem by considering the behaviour and properties of individual cells. A discrete model describes interactions at a microscopic level. Thus, it enables the tracking of individual cells, and allow the use of measurable quantities such as cell velocities. Furthermore, a discrete model offers the advantage of ease of setting up movement rules based on interactions at a cellular level. However, a realistic discrete model quickly becomes analytically intractable and computationally intensive as the number of cells being studied rises, due to the

large number of variables and equations that would be required in order to accurately capture the behaviour of a large system.

Continuous models on the other hand, describe phenomena from a macroscopic point of view. They are formulated in terms of macroscopic quantities such as cell densities and diffusion coefficients. Thus, in contrast with the discrete modelling approach, a continuous model is easier to analyse both analytically and computationally, since it requires significantly fewer variables and equations. However, continuous models may not be able to capture processes taking place on an individual cell scale.

Derivation of a continuous model from a discrete model, offers a link between microscopic and macroscopic properties. Therefore, derivation of a continuous model from an underlying discrete model is highly desirable, since one can combine the strengths of each model form. This is the main reason for the numerous attempts to derive mathematical models in this manner found in the literature (see for example [1, 2, 7, 66, 70, 74, 99]).

In this work we used the framework introduced in [66] in common with a variety of other models (e.g. [7, 40, 72, 74]). The different discrete models formulated were based on different simplifying assumptions about the movement of cells in response to different sensing mechanisms. The movement rules set up in each case were simplistic on purpose in order to investigate the impact different sensing mechanisms have on the models' behaviour. The simple nature of the models makes them more amenable to analyse, compare them to each other, and highlight the importance of several aspects essential to pattern formation. The simple discrete/master equation approach affords a whole set of different possibilities for the way a cell can sense its environment. Consequently, to obtain a detailed understanding into what represents a suitable model for a cell adhesion type process, the approach is to perform a comprehensive analysis by looking at all plausible forms by which a cell can locally respond to the environment.

Analysis of the models was undertaken in chapter 4, where we showed that the continuous models are ill-posed in the region of instability of the homogeneous steady state and therefore cannot be used. Ill-posedness of continuous models derived from underlying discrete models is an issue found in other work similar to ours (e.g. [7, 41]).

We therefore concentrated on the discrete models. The discrete models were shown to be capable of producing patterns comprised of multiple cell aggregates as long as a small random motility term or a crowding term were included. Without the inclusion of these terms, global aggregation was observed, where all the available cell density is localised at a single site. We have also highlighted the importance of the total available cell density in aggregation formation. We showed that aggregations are not possible if the total cell density is below a certain threshold, an observation also made in [7]. Furthermore, it was shown that aggregations are not possible when the total density is too high if random motility or crowding effects are considered.

The aggregates observed however, were of the scale of individual cells, making the models unable to describe the patterns seen in nature, where aggregations are of significantly larger scale. Nevertheless, analysis of the models provided insight to the patterning process and aided in the development and better understanding of the extended models of chapter 5.

It was also demonstrated that the different models considered produced similar results, and the patterns obtained do not exhibit significant differences. We have concluded therefore that the impact of the precise sensing mechanism is not very significant in contrast to the case of chemical signalling as considered in [66]. The precise form of chemical detection actually had a big impact on the behaviour of the system, which implied a significant sensitivity. The conclusion to be drawn from our study is that for adhesion type processes we obtain a type of robustness with respect to the precise sensing mechanism.

In chapter 5 we generalised the models introduced in chapter 3 to include nonlocal sensing. We allowed cells to occupy multiple lattice sites by introducing a sensing radius. The notion of a sensing radius can also be thought to include long range sensing by cellular extensions such as filopodia. There is biological evidence that filopodia do play a role in adhesion processes, as cells extend filopodia to probe for potential adhesive sites [4, 30]. By extending the models of chapter 3, we demonstrated that the models retained the characteristics of the local sensing models while being capable of producing multiple cell aggregations comprised of multiple cell width aggregates, a fundamental requirement for a successful model of cell adhesion mediated patterning.

Inclusion of nonlocal interactions however, could not alter the ill-posed nature of the continuous models. Similarly to [99], we observed that any non-local information existing in the discrete formulation is not present in the continuous models. We remark that derivation of a well-posed continuous model may be achieved by following this procedure for different discrete models or by using a more appropriate combination of scalings and limits.

The approach of Anderson and Chaplain [5] offers an interesting alternative towards the direction of linking discrete and continuous modelling forms. In their work, the authors developed a continuous model for tumor induced angiogenesis comprised of a system of nonlinear partial differential equations. By discretising the continuous system they were able to derive a discrete model similar to the biased random walk models of Othmer and Stevens [66] and the models developed in this work. The discrete model derived describes the motion of an individual cell, by redefining the coefficients of the model to be the probabilities of movement towards a specific direction. The original continuous model can be retrieved following the methods of [66] used in this work. The discrete model derived enabled the authors to track the movement of individual cells as well as to explicitly include specific movement rules. In this manner, the model successfully captures the finer processes of angiogenesis which the continuous model could not account for. A possible approach to link discrete and continuous model formulations of cell adhesion therefore, would be to take the opposite route from the one used in this work. One could derive a discrete model by employing a similar method to the one used in [5], starting from a well-posed continuous model.

The modelling framework developed in this work can be extended in order to model pattern formation in different biological contexts. One possible extension is to modify the models in order to capture cell sorting of multiple cell populations due to differential adhesion, experimentally shown in studies like [86, 90, 91, 92, 93, 95]. A successful model of cell adhesion should be capable of capturing the different cell sorting behaviours predicted by the Differential Adhesion Hypothesis.

Another future direction would be to extend the models to two spatial dimensions, thus considering a more biologically realistic scenario. The models can also be extended in order to include additional processes such as chemotaxis, haptotaxis, or

cell-matrix adhesion. Inclusion of such interactions in our models, in addition to cell adhesion will be helpful in studying the interplay between them and highlighting their importance in relation to each other. The additional processes can be incorporated in the model by altering the movement rules of cells and the transition probabilities accordingly, and considering additional PDEs to describe, for example, the evolution of a chemical signal in the case of chemotaxis. Furthermore, the modified models can be used in order to model cell aggregating behaviour in specific biological contexts. Cell adhesion has been shown to play a significant role in various developmental processes such as vasculogenesis, gastrulation, and cell migration [94]. Other examples include aggregating slime mould, and cancer invasion.

Finally, in chapter 6 we test one of our nonlocal adhesion models in modelling a specific biological process in which cellular adhesion plays a crucial role. We used both discrete and continuous modelling approaches in order to describe the process of sympathetic ganglia formation. We have extended one of the non-local discrete models of chapter 5 for the discrete formulation, and a modified version of the continuous model for cell adhesion presented in [8]. Both approaches were successful in describing ganglia formation through the combination of cellular adhesion and chemical repulsion processes, and highlighting their contributions and interplay. Additionally, our models enable us to make testable predictions about the biological process. Finally, we demonstrated that the discrete nonlocal models developed in chapter 5 compare well with the continuous model.

Overall, by considering different mechanisms of pattern formation, we studied how inclusion of nonlocal sensing affects developmental processes modelling. We showed how it can generate long-scale patterns comprised of multiple cell widths and accelerate the pattern formation process. By incorporating nonlocal information in discrete models of cellular adhesion we were able to derive models that can successfully capture the essential aspects of self-aggregation processes, a claim reinforced by the results of chapter 6.

Appendix A

Numerical Methods

A.1 Juxtacrine Signalling

A.1.1 1-dimensional numerical simulations

Simulations appearing in chapter 2 for the system of equations (2.3)-(2.4), for 1-dimensional lines of cells were produced using FORTRAN. A 4th order Runge-Kutta method for time integration was employed, and the averaging term \bar{l}_j was computed explicitly for every time step. The systems were solved in domains of 100 or 200 cells with time step $dt = 0.01$. The solution was accessed by MATLAB in order to produce the graphic output. We have used either periodic boundary conditions or such that there is no ligand activity outside the domain (specified in the main text). The initial conditions were a homogeneous distribution of ligand and receptor activity with an additional small ($\sim 1\%$) random noise term, unless otherwise stated.

A.1.2 2-dimensional numerical simulations

Numerical solution of the system (2.3)-(2.4) in hexagonal arrays was obtained using a FORTRAN program in which a “signalling regime” is specified (see figure 2.16). This is achieved by computing the coordinates of all the cells, contacted by each cell in the domain. The averaging term is computed for each cell through direct summation of ligand activity in the contacted cells for each time-step. The ROWMAP integrator [104] is used for time-integration, a method that automatically adjusts

the time-step size. Boundary conditions were such that there is no contribution to the averaging term from cells outside the domain, and initial conditions were small perturbations from the homogeneous steady state. Output files were processed by MATLAB to produce the figures presented.

A.2 Cell Adhesion Modelling

Numerical simulations presented in chapters 4 and 5 for the models (M1)-(M5) and (R1)-(R5) were performed using the MATLAB in-built ODE solver ode15s. Periodic boundary conditions were employed throughout. A homogeneous distribution of cell density with a small random noise term was applied initially, except in figure 5.9 where $u_i(0) = u_0 - 0.01 \cos(\frac{4\pi}{N})$ was used.

A.3 Sympathetic Ganglia Formation

The discrete model, equation (6.15) was solved using MATLAB's ode15s in-built solver as in A.2. For the continuous model, equation (6.12), a method of lines was employed. The equation is discretised in space on a mesh of spacing $\Delta x = 0.1$. Time-integration of the resulting ODEs system is performed using the ROWMAP integrator [104] for stiff ODEs. Calculation of the integral term is achieved through direct summation of the grid points enclosed within the set radius. The diffusion term was discretised using a central difference scheme. For the adhesion term, a first-order upwind scheme was employed. Periodic boundary conditions were used for the simulations shown, but no-flux boundary conditions were also used showing no considerable difference. Initially a small random perturbation to a uniform cell density distribution was applied.

Bibliography

- [1] M. Alber, N. Chen, T. Glimm, and P.M. Lushnikov. Multiscale dynamics of biological cells with chemotactic interactions: From a discrete stochastic model to a continuous description. *Phys. Rev. E*, 73:051901, May 2006.
- [2] M. Alber, N. Chen, P.M. Lushnikov, and S.A. Newman. Continuous macroscopic limit of a discrete stochastic model for interaction of living cells. *Phys. Rev. Lett.*, 99:168102, Oct 2007.
- [3] B. Alberts, A. Johnson, J. Lewis, M. Raff, K. Roberts, and P. Walter. *Molecular Biology of the Cell*. Garland Science, 5 edition, November 2007.
- [4] S. Almagro, C. Durmort, A. Chervin-Ptinet, S. Heyraud, M. Dubois, O. Lambert, C. Maillefaud, E. Hewat, J.P. Schaal, P. Huber, and D. Gulino-Debrac. The motor protein myosin-x transports ve-cadherin along filopodia to allow the formation of early endothelial cell-cell contacts. *Mol Cell Biol*, 2010.
- [5] A. R. A. Anderson and M. A. J. Chaplain. Continuous and discrete mathematical models of tumor-induced angiogenesis. *Bulletin of Mathematical Biology*, 60:857–899, 1998.
- [6] A.R.A. Anderson. A hybrid mathematical model of solid tumour invasion: the importance of cell adhesion. *Mathematical Medicine and Biology*, 22(2):163–186, June 2005.
- [7] K. Anguige and C. Schmeiser. A one-dimensional model of cell diffusion and aggregation, incorporating volume filling and cell-to-cell adhesion. *Journal of mathematical biology*, 58(3):395–427, March 2009.

- [8] N.J. Armstrong, K.J. Painter, and J.A. Sherratt. A continuum approach to modelling cell-cell adhesion. *Journal of Theoretical Biology*, 243(1):98 – 113, 2006.
- [9] N.J. Armstrong, K.J. Painter, and J.A. Sherratt. Adding adhesion to a chemical signaling model for somite formation. *Bulletin of Mathematical Biology*, 71:1–24, 2009.
- [10] R. Baker, C. Yates, and R. Erban. From microscopic to macroscopic descriptions of cell migration on growing domains. *Bulletin of Mathematical Biology*, 72:719–762, 2010.
- [11] R. E. Baker, E. A. Gaffney, and P. K. Maini. Partial differential equations for self-organization in cellular and developmental biology. *Nonlinearity*, 21(11):R251–R290, November 2008.
- [12] A.L. Berrier and K.M. Yamada. Cell-matrix adhesion. *Journal of Cellular Physiology*, 213(3):565–573, 2007.
- [13] D. Bray. *Cell Movements: From Molecules to Motility*. Garland Science, 2 edition, November 2000.
- [14] M Bronner-Fraser. Neural crest cell formation and migration in the developing embryo. *The FASEB Journal*, 8(10):699–706, 1994.
- [15] M. Bronner-Fraser and C. Stern. Effects of mesodermal tissues on avian neural crest cell migration. *Developmental Biology*, 143(2):213 – 217, 1991.
- [16] V. Castets, E. Dulos, J. Boissonade, and P. De Kepper. Experimental evidence of a sustained standing turing-type nonequilibrium chemical pattern. *Phys. Rev. Lett.*, 64:2953–2956, Jun 1990.
- [17] A.B. Chitnis. The role of notch in lateral inhibition and cell fate specification. *Molecular and Cellular Neuroscience*, 6(4):311 – 321, 1995.
- [18] E.A. Codling, M.J. Plank, and S. Benhamou. Random walk models in biology. *Journal of The Royal Society Interface*, 5(25):813–834, 2008.

- [19] M. Cohen, M. Georgiou, N.L. Stevenson, M. Miodownik, and B. Baum. Dynamic filopodia transmit intermittent Delta-Notch signaling to drive pattern refinement during lateral inhibition. *Dev Cell*, 19(1):78–89, July 2010.
- [20] J.R. Collier, N.A.M Monk, P.K. Maini, and J.H. Lewis. Pattern formation by lateral inhibition with feedback: a mathematical model of delta-notch intercellular signalling. *Journal of Theoretical Biology*, 183(4):429 – 446, 1996.
- [21] C. de Jussineau, J. Soule, M. Martin, C. Anguille, P. Montcourrier, and D. Alexandre. Delta-promoted filopodia mediate long-range lateral inhibition in *Drosophila*. *Nature*, 426(6966):555–559, December 2003.
- [22] P. De Kepper, V. Castets, E. Dulos, and J. Boissonade. Turing-type chemical patterns in the chlorite-iodide-malonic acid reaction. *Phys. D*, 49:161–169, April 1991.
- [23] E. Dessaud, A.P. McMahon, and J. Briscoe. Pattern formation in the vertebrate neural tube: a sonic hedgehog morphogen-regulated transcriptional network. *Development*, 135(15):2489–2503, 2008.
- [24] C.Q. Doe and C.S. Goodman. Early events in insect neurogenesis: Ii. the role of cell interactions and cell lineage in the determination of neuronal precursor cells. *Developmental Biology*, 111(1):206 – 219, 1985.
- [25] E. Doedel, A. Champneys, F. Dercole, T. Fairgrieve, Y. Kuznetsov, B. Oldeman, R. Paffenroth, B. Sandstede, X. Wang, and C. Zhang. Auto: Software for continuation and bifurcation problems in ordinary differential equations. Technical report, Concordia University, Montreal, 2009.
- [26] D. Duguay, R.A. Foty, and M.S. Steinberg. Cadherin-mediated cell adhesion and tissue segregation: qualitative and quantitative determinants. *Developmental Biology*, 253(2):309 – 323, 2003.
- [27] P. Formosa-Jordan and M. Ibañes. Diffusible ligand and lateral inhibition dynamics for pattern formation. *Journal of Statistical Mechanics: Theory and Experiment*, 2009(03):P03019, 2009.

- [28] R.A. Foty and M.S. Steinberg. Cadherin-mediated cell-cell adhesion and tissue segregation in relation to malignancy. *Int J Dev Biol*, 48(5-6):397–409, 2004.
- [29] R.A. Foty and M.S. Steinberg. The differential adhesion hypothesis: a direct evaluation. *Developmental Biology*, 278(1):255 – 263, 2005.
- [30] C.G. Galbraith, K.M. Yamada, and J.A. Galbraith. Polymerizing actin fibers position integrins primed to probe for adhesion sites. *Science*, 315(5814):992–995, 2007.
- [31] A. Gerisch and M.A.J. Chaplain. Mathematical modelling of cancer cell invasion of tissue: Local and non-local models and the effect of adhesion. *Journal of Theoretical Biology*, 250(4):684 – 704, 2008.
- [32] A. Gerisch and K.J. Painter. Mathematical modeling of cell adhesion and its applications to developmental biology and cancer invasion. In A. Chauvière, L. Preziosi, and C. Verdier, editors, *Cell mechanics: from single scale-based models to multiscale modeling*, Chapman and Hall/CRC mathematical & computational biology series, chapter 12. Chapman & Hall/CRC, 2009.
- [33] A. Gierer and H. Meinhardt. A theory of biological pattern formation. *Biological Cybernetics*, 12(1):30–39, December 1972.
- [34] S. F. Gilbert. *Developmental biology*. Sinauer, 7th edition, 2003.
- [35] J.A. Glazier and F. Graner. Simulation of the differential adhesion driven rearrangement of biological cells. *Physical Review E*, 47(3):2128–2154, March 1993.
- [36] F. Graner and J.A. Glazier. Simulation of biological cell sorting using a two-dimensional extended Potts model. *Physical Review Letters*, 69(13):2013–2016, September 1992.
- [37] B.M. Gumbiner. Regulation of cadherin-mediated adhesion in morphogenesis. *Nature Reviews Molecular Cell Biology*, 6(8):622–634, July 2005.

- [38] J.B. Gurdon, H. Standley, S. Dyson, K. Butler, T. Langon, K. Ryan, F. Stenard, K. Shimizu, and A. Zorn. Single cells can sense their position in a morphogen gradient. *Development*, 126(23):5309–5317, 1999.
- [39] T. Gustafson and L. Wolpert. Studies on the cellular basis of morphogenesis in the sea urchin embryo: Directed movements of primary mesenchyme cells in normal and vegetalized larvae. *Experimental Cell Research*, 253(2):288 – 295, 1999.
- [40] T. Hillen and K.J. Painter. A users guide to pde models for chemotaxis. *Journal of Mathematical Biology*, 58:183–217, 2009.
- [41] D. Horstmann, K.J. Painter, and H.G. Othmer. Aggregation under local reinforcement: From lattice to continuum. *European Journal of Applied Mathematics*, 15(05):545–576, 2004.
- [42] A. Horwitz, K. Duggan, C. Buck, M.C. Beckerle, and K. Burridge. Interaction of plasma membrane fibronectin receptor with talin—a transmembrane linkage. *Nature*, 320(6062):531–3, 1986.
- [43] F. Hsiung, F. Ramirez-Weber, D.D. Iwaki, and T.B. Kornberg. Dependence of drosophila wing imaginal disc cytonemes on decapentaplegic. *Nature*, 437(7058):560–563, 2005.
- [44] J.C. Kasemeier-Kulesa, R. Bradley, E.B. Pasquale, F. Lefcort, and P.M. Kulesa. Eph/ephrins and n-cadherin coordinate to control the pattern of sympathetic ganglia. *Development*, 133(24):4839–4847, 2006.
- [45] J.C. Kasemeier-Kulesa, P.M. Kulesa, and F. Lefcort. Imaging neural crest cell dynamics during formation of dorsal root ganglia and sympathetic ganglia. *Development*, 132(2):235–245, 2005.
- [46] E.F. Keller and L.A. Segel. Initiation of slime mold aggregation viewed as an instability. *Journal of Theoretical Biology*, 26(3):399 – 415, 1970.
- [47] E. Khain and L.M. Sander. Generalized cahn-hilliard equation for biological applications. *Phys. Rev. E*, 77:051129, May 2008.

- [48] E. Khain, L.M. Sander, and C. Schneider-Mizell. The role of cell-cell adhesion in wound healing. *Journal of Statistical Physics*, 128:209–218, 2007.
- [49] I. Lengyel and I.R. Epstein. Modeling of turing structures in the chloriteiodide-malonic acidstarch reaction system. *Science*, 251(4994):650–652, 1991.
- [50] J. Lewis. Neurogenic genes and vertebrate neurogenesis. *Current Opinion in Neurobiology*, 6(1):3 – 10, 1996.
- [51] P.K. Maini. Using mathematical models to help understand biological pattern formation. *Comptes Rendus Biologies*, 327(3):225–234, March 2004.
- [52] P.K. Maini, K.J. Painter, and H. Nguyen Phong Chau. Spatial pattern formation in chemical and biological systems. *J. Chem. Soc., Faraday Trans.*, 93:3601–3610, 1997.
- [53] A.F.M. Marée and P. Hogeweg. How amoeboids self-organize into a fruiting body: Multicellular coordination in dictyostelium discoideum. *Proceedings of the National Academy of Sciences*, 98(7):3879–3883, 2001.
- [54] M. Milán, U. Weihe, L. Pérez, and S.M. Cohen. The lrr proteins capricious and tartan mediate cell interactions during dv boundary formation in the drosophila wing. *Cell*, 106(6):785 – 794, 2001.
- [55] J. Miller, S.E. Fraser, and D. McClay. Dynamics of thin filopodia during sea urchin gastrulation. *Development*, 121(8):2501–2511, 1995.
- [56] K. Mishra-Gorur, M.D. Rand, B. Perez-Villamil, and S. Artavanis-Tsakonas. Down-regulation of delta by proteolytic processing. *The Journal of Cell Biology*, 159(2):313–324, 2002.
- [57] J.C.M. Mombach, J.A. Glazier, R.C. Raphael, and M. Zajac. Quantitative comparison between differential adhesion models and cell sorting in the presence and absence of fluctuations. *Phys. Rev. Lett.*, 75:2244–2247, Sep 1995.
- [58] N.A.M. Monk. Restricted-range gradients and travelling fronts in a model of juxtacrine cell relay. *Bulletin of Mathematical Biology*, 60:901–918, 1998.

- [59] J. Moreira and A. Deutsch. Pigment pattern formation in zebrafish during late larval stages: A model based on local interactions. *Developmental Dynamics*, 232(1):33–42, 2005.
- [60] J. D. Murray, G. F. Oster, and A. K. Harris. A mechanical model for mesenchymal morphogenesis. *Journal of Mathematical Biology*, 17:125–129, 1983.
- [61] J.D. Murray. *Mathematical biology: I. An introduction*. Springer, 3rd edition, 2002.
- [62] J.D. Murray. *Mathematical biology: II. Spatial models and biomedical applications*. Interdisciplinary applied mathematics. Springer, 3rd edition, 2003.
- [63] M.A.T. Muskavitch. Delta-notch signaling and drosophila cell fate choice. *Developmental Biology*, 166(2):415 – 430, 1994.
- [64] H.G. Othmer, K.J. Painter, D. Umulis, and C. Xue. The intersection of theory and application in elucidating pattern formation in developmental biology. *Math Model Nat Phenom*, 4(4):3–82, 2009.
- [65] H.G. Othmer and L.E. Scriven. Instability and dynamic pattern in cellular networks. *Journal of Theoretical Biology*, 32(3):507 – 537, 1971.
- [66] H.G. Othmer and A. Stevens. Aggregation, blowup, and collapse: The abc’s of taxis in reinforced random walks. *SIAM J. APPL. MATH*, 57(4):1044–1081, 1997.
- [67] M.R. Owen. Waves and propagation failure in discrete space models with nonlinear coupling and feedback. *Physica D: Nonlinear Phenomena*, 173(1-2):59 – 76, 2002.
- [68] M.R Owen and J.A. Sherratt. Mathematical modelling of juxtacrine cell signalling. *Mathematical Biosciences*, 153(2):125 – 150, 1998.
- [69] M.R. Owen, J.A. Sherratt, and H.J. Wearing. Lateral induction by juxtacrine signaling is a new mechanism for pattern formation. *Developmental Biology*, 217(1):54 – 61, 2000.

- [70] K.J. Painter. Continuous models for cell migration in tissues and applications to cell sorting via differential chemotaxis. *Bulletin of Mathematical Biology*, 71:1117–1147, 2009.
- [71] K.J. Painter, N.J. Armstrong, and J.A. Sherratt. The impact of adhesion on cellular invasion processes in cancer and development. *Journal of Theoretical Biology*, 264(3):1057 – 1067, 2010.
- [72] K.J. Painter and T. Hillen. Volume-filling and quorum-sensing in models for chemosensitive movement. *Can. Appl. Math. Quart*, 10(4):501–543, 2002.
- [73] K.J. Painter, D. Horstmann, and H.G. Othmer. Localization in lattice and continuum models of reinforced random walks. *Applied Mathematics Letters*, 16(3):375 – 381, 2003.
- [74] K.J. Painter and J.A. Sherratt. Modelling the movement of interacting cell populations. *Journal of Theoretical Biology*, 225(3):327 – 339, 2003.
- [75] E. Palsson. A 3-d model used to explore how cell adhesion and stiffness affect cell sorting and movement in multicellular systems. *Journal of Theoretical Biology*, 254(1):1 – 13, 2008.
- [76] E. Palsson and H.G. Othmer. A model for individual and collective cell movement in dictyostelium discoideum. *Proceedings of the National Academy of Sciences*, 97(19):10448–10453, 2000.
- [77] S.D. Patel, C.P. Chen, F. Bahna, B. Honig, and L. Shapiro. Cadherin-mediated cellcell adhesion: sticking together as a family. *Current Opinion in Structural Biology*, 13(6):690 – 698, 2003.
- [78] C.S. Patlak. Random walk with persistence and external bias. *Bulletin of Mathematical Biology*, 15:311–338, 1953.
- [79] E. Plahte. Pattern formation in discrete cell lattices. *Journal of Mathematical Biology*, 43:411–445, 2001.

- [80] E. Plahte and L. Øyehaug. Pattern-generating travelling waves in a discrete multicellular system with lateral inhibition. *Physica D: Nonlinear Phenomena*, 226(2):117 – 128, 2007.
- [81] S. Pokutta and W.I. Weis. Structure and mechanism of cadherins and catenins in cell-cell contacts. *Annual Review of Cell and Developmental Biology*, 23(1):237–261, 2007.
- [82] H. Qi, D.M. Rand, X. Wu, N. Sestan, W. Wang, P. Rakic, T. Xu, and S. Artavanis-Tsakonas. Processing of the notch ligand delta by the metalloprotease kuzbanian. *Science*, 283(5398):91–94, 1999.
- [83] F.A. Ramirez-Weber and T.B. Kornberg. Cytonemes: cellular processes that project to the principal signaling center in drosophila imaginal discs. *Cell*, 97(5):599–607, 1999.
- [84] F.A. Ramirez-Weber and T.B. Kornberg. Signaling reaches to new dimensions in drosophila imaginal discs. *Cell*, 103(2):189–92, 2000.
- [85] K.A. Rejniak. An immersed boundary framework for modelling the growth of individual cells: An application to the early tumour development. *Journal of Theoretical Biology*, 247(1):186 – 204, 2007.
- [86] S. Roth. Studies on intercellular adhesive selectivity. *Developmental Biology*, 18(6):602 – 631, 1968.
- [87] Y. Schiller. The anatomy and physiology of the sympathetic innervation to the upper limbs. *Clinical Autonomic Research*, 13 (suppl 1):11–15, 2003. 10.1007/s10286-003-1102-6.
- [88] D.I. Shreiber, V.H. Barocas, and R.T. Tranquillo. Temporal variations in cell migration and traction during fibroblast-mediated gel compaction. *Biophysical Journal*, 84(6):4102 – 4114, 2003.
- [89] P. Simpson, R. Woehl, and K. Usui. The development and evolution of bristle patterns in diptera. *Development*, 126(7):1349–1364, 1999.

- [90] M.S. Steinberg. On the mechanism of tissue reconstruction by dissociated cells, i. population kinetics, differential adhesiveness, and the absence of directed migration. *Proceedings of the National Academy of Sciences*, 48(9):1577–1582, 1962a.
- [91] M.S. Steinberg. Mechanism of tissue reconstruction by dissociated cells, ii: Time-course of events. *Science*, 137(3532):762–763, 1962b.
- [92] M.S. Steinberg. On the mechanism of tissue reconstruction by dissociated cells, iii. free energy relations and the reorganization of fused, heteronomic tissue fragments. *Proceedings of the National Academy of Sciences*, 48(10):1769–1776, 1962c.
- [93] M. Takeichi. Cadherins: a molecular family essential for selective cell-cell adhesion and animal morphogenesis. *Trends in Genetics*, 3(0):213 – 217, 1987.
- [94] J.P. Thiery. Cell adhesion in development: a complex signaling network. *Current Opinion in Genetics & Development*, 13(4):365 – 371, 2003.
- [95] P.L. Townes and J. Holtfreter. Directed movements and selective adhesion of embryonic amphibian cells. *Journal of Experimental Zoology*, 128(1):53–120, 1955.
- [96] S. Tsukita, S. Tsukita, A. Nagafuchi, and S. Yonemura. Molecular linkage between cadherins and actin filaments in cell-cell adherens junctions. *Current Opinion in Cell Biology*, 4(5):834 – 839, 1992.
- [97] A.M. Turing. The chemical basis of morphogenesis. *Philosophical Transactions of the Royal Society of London. Series B, Biological Sciences*, 237(641):37–72, 1952.
- [98] S. Turner and J.A. Sherratt. Intercellular adhesion and cancer invasion: A discrete simulation using the extended potts model. *Journal of Theoretical Biology*, 216(1):85 – 100, 2002.

- [99] S. Turner, J.A. Sherratt, K.J. Painter, and N.J. Savill. From a discrete to a continuous model of biological cell movement. *Phys. Rev. E*, 69:021910, Feb 2004.
- [100] H.J. Wearing, M.R. Owen, and J.A. Sherratt. Mathematical modelling of juxtacrine patterning. *Bulletin of Mathematical Biology*, 62:293–320, 2000.
- [101] H.J. Wearing and J.A. Sherratt. Nonlinear analysis of juxtacrine patterns. *SIAM Journal on Applied Mathematics*, 62(1):283–309, 2001.
- [102] S.D. Webb and M.R. Owen. Intra-membrane ligand diffusion and cell shape modulate juxtacrine patterning. *Journal of Theoretical Biology*, 230(1):99 – 117, 2004.
- [103] S.D. Webb and M.R. Owen. Oscillations and patterns in spatially discrete models for developmental intercellular signalling. *Journal of Mathematical Biology*, 48:444–476, 2004.
- [104] R. Weiner, B.A. Schmitt, and H. Podhaisky. Rowmap - a row-code with krylov techniques for large stiff odes. *Appl. Numer. Math*, 25:303–319, 1997.
- [105] M.J. Wheelock and K.R. Johnson. Cadherins as modulators of cellular phenotype. *Annual Review of Cell and Developmental Biology*, 19(1):207–235, 2003.
- [106] M.J. Wheelock, Y. Shintani, M. Maeda, Y. Fukumoto, and K.R. Johnson. Cadherin switching. *Journal of Cell Science*, 121(6):727–735, 2008.
- [107] L. Wolpert. Positional information and the spatial pattern of cellular differentiation. *Journal of Theoretical Biology*, 25(1):1 – 47, 1969.